



**HAL**  
open science

# Unraveling Degradation Patterns in Li-ion Batteries through Electrochemical Analysis Procedures

Valentin Meunier

► **To cite this version:**

Valentin Meunier. Unraveling Degradation Patterns in Li-ion Batteries through Electrochemical Analysis Procedures. Material chemistry. Sorbonne Université, 2023. English. NNT : 2023SORUS354 . tel-04347681

**HAL Id: tel-04347681**

**<https://theses.hal.science/tel-04347681>**

Submitted on 15 Dec 2023

**HAL** is a multi-disciplinary open access archive for the deposit and dissemination of scientific research documents, whether they are published or not. The documents may come from teaching and research institutions in France or abroad, or from public or private research centers.

L'archive ouverte pluridisciplinaire **HAL**, est destinée au dépôt et à la diffusion de documents scientifiques de niveau recherche, publiés ou non, émanant des établissements d'enseignement et de recherche français ou étrangers, des laboratoires publics ou privés.



Distributed under a Creative Commons Attribution - NonCommercial - NoDerivatives 4.0 International License

# Sorbonne Université

Doctoral school 397 – Physics and Chemistry of Materials

*Solid state Chemistry and Energy, Collège de France, UMR 8260*

## **Unraveling Degradation Patterns in Li-ion Batteries through Electrochemical Analysis Procedures**

By Valentin Meunier

Ph.D. thesis of Physics and Chemistry of Materials

Supervised by Dr. Alexis Grimaud

Presented and defended publicly on September 15<sup>th</sup>, 2023

### In front of the Jury:

Dr. Alexandre Ponrouch	Tenure scientist, ICMAB, Barcelona	Referee
Dr. Maxime Blangero	Head of Product R&D, Umicore, Cheonan	Referee
Prof. Christel Laberty-Robert	Professor, LCMCP, Paris	Examiner
Dr. Alexis Grimaud	A. Professor, Boston College, Boston	Director
Prof. Jean-Marie Tarascon	Professor, Collège de France, Paris	Invited member
Dr. Mathieu Morcrette	Research director, LRCS, Amiens	Invited member
Dr. Michael Metzger	A. Professor, Dalhousie University	Invited member





# Sorbonne Université

Ecole doctorale 397 – Physique et Chimie des Matériaux

*Chimie du Solide et de l'Energie, Collège de France, UMR 8260*

## **Mise en Evidence des Schémas de Dégradation des Batteries Li-ion grâce à des Procédures d'Analyse Electrochimique**

Par Valentin Meunier

Thèse de doctorat en Physique et Chimie des Matériaux

Supervisée par Dr. Alexis Grimaud

Présentée and défendue publiquement le 15 septembre 2023

Devant un jury composé de:

Dr. Alexandre Ponrouch	Chercheur, ICMA B, Barcelone	Rapporteur
Dr. Maxime Blangero	Responsable R&D, Umicore, Cheonan	Rapporteur
Prof. Christel Laberty-Robert	Professeur, LCMCP, Paris	Examinatrice
Dr. Alexis Grimaud	A. Professeur, Boston College, Boston	Directeur
Prof. Jean-Marie Tarascon	Professeur, Collège de France, Paris	Membre invité
Dr. Mathieu Morcrette	Directeur de recherche, LRCS, Amiens	Membre invité
Dr. Michael Metzger	A. Professeur, Dalhousie University	Membre invité





*A ma famille, mes amis.*



# Acknowledgement

I would like to express my sincere gratitude to my thesis director, Alexis Grimaud, for his supervision throughout these three years of Ph.D. research. It has been a pleasure to work with you, both from a scientific and managerial perspective. Your constant availability has been invaluable as a student. Moreover, you went above and beyond to provide me with the opportunity to spend part of my third year of Ph.D. at Boston College. I truly appreciate it.

I also want to acknowledge Professor Jean-Marie Tarascon for giving me the chance to conduct research at the Chemistry and Solid State Chemistry lab. Your advices, achievements, and vision in the field of batteries have been truly inspiring. Throughout these three years, I have confirmed that hard work and dedication are key, and I am certain this thesis would not have been the same without the great team spirit and available resources at CSE.

Many thanks to Ivette for your invaluable help throughout this three-year challenge. Whenever I had doubts about the ICP or anything else, you were there, and I genuinely appreciate it. I thank Romain for teaching me about the testing background with the potentiostat, testing tips, and analysis methods. Also, a big thanks to Matheus, Ph.D., for working together and co-signing research articles. Your rigor and organization have been truly motivating in helping me conduct the work in BIG-MAP. I am sincerely grateful to the XPS collaborators for this thesis, Federico and Rémi, with whom I had interesting discussions about science during synchrotron nights in Lund. Thanks to Mathieu Morcrette for his expertise in reading battery degradation. Your experience in this matter truly helped me and provided me with the necessary knowledge to continue. I acknowledge Jessica for her incredible efficiency in handling all administrative procedures and her invaluable help during the business trips

Thanks to Damien with whom I had numerous debates on science and societal topics. I appreciate the time spent together visiting the US. Thanks to my officemate, Sathiya, for engaging scientific discussions with me and bringing your taunting sense of humor. Special thanks to the running Team composed of Jacques, Damien, and Fu. We had great runs along the Seine River and challenged ourselves with a half marathon. Finally, I thank all the team members of CSE, both former and current, who contribute every day to the atmosphere of mutual assistance and well-being in the laboratory. Special thanks to Dorian, Ezzoubair, Jacques, Damien, Julien, and Thomas for your unwavering good mood and sense of humor.

Quelques mots en français pour remercier ma famille de son inestimable soutien. J'arrive en fin de cursus académique avec la fierté d'avoir réussi et suis profondément reconnaissant de votre aide. Je vous dédie ce travail.

Last but not least, I extend my heartfelt gratitude to the jury members, Dr. Alexandre Ponrouch, Dr. Maxime Blangero, Prof. Christel Laberty-Robert, Dr. Michael Metzger, and Dr. Mathieu Morcrette, for taking the time reading the thesis and provide valuable manuscript corrections.

# OUTLINE

<b>CHAPTER I: INTRODUCTION OF THE THESIS .....</b>	<b>11</b>
I.1. BROAD INTRODUCTION .....	13
I.2. THE ROLE OF ELECTRIC MOBILITY IN THE ENERGY TRANSITION .....	15
I.2.1. Market of electric mobility .....	15
I.2.2. Success story of LIBs in electric mobility .....	15
I.2.3. Ongoing challenges for further market expansion .....	16
I.3. FUNDAMENTALS OF LI-ION BATTERIES .....	17
I.3.1. General functioning .....	17
I.3.2. Usual descriptors of battery performance .....	19
I.3.3. Architecture of Li-ion batteries .....	22
I.3.4. Chemistry of cell components .....	25
I.4. DESIGN OF POSITIVE ELECTRODE MATERIALS .....	29
I.4.1. Ni-rich materials: a solution to higher energy .....	29
I.4.2. Consequences of high voltages on Ni-rich materials .....	30
I.4.3. Stabilization of bulk materials .....	33
I.5. THE CHALLENGES OF NI-RICH ELECTRODE/ELECTROLYTE INTERFACE .....	35
I.5.1. Degradations at electrode surface .....	35
I.5.2. Solutions based on additives .....	38
I.5.3. Solution based on electrolyte design .....	40
I.6. CONTEXT OF THE PH.D. ....	47
I.6.1. Study of interfacial degradations at European scale .....	47
I.6.2. Bottlenecks for studying interfaces in BIG-MAP .....	47
I.6.3. Contribution of this Ph.D. ....	48
<b>CHAPITRE II: STANDARDIZATION OF CELL ASSEMBLY AND TESTING .....</b>	<b>50</b>
II.1. DRAWING INSPIRATION FROM INSPIRATION FORM INDUSTRY TO ESTABLISH STANDARDS IN ACADEMIA .....	52
II.1.1. Outcomes of standardization .....	52
II.1.2. Challenges .....	53
II.1.3. Pending obstacles .....	55
II.2. IMPLEMENTATION OF ASSEMBLY STANDARDS .....	56
II.2.1. Standardization of cell components .....	56
II.2.2. Standardization of chemistry .....	59
II.2.3. Efforts that worth it .....	63
II.3. ASSESSING CELL PERFORMANCE IN BIG-MAP .....	64
II.3.1. First tier testing protocols .....	64
II.3.2. Second tier testing protocols .....	68
II.3.3. Storage of data .....	72
CONCLUSION OF CHAPTER II .....	74
<b>CHAPTER III: DESIGN OF ANALYSIS WORKFLOWS FOR DETECTING DEGRADATIONS .....</b>	<b>76</b>
INTRODUCTION OF CHAPTER III .....	78
III.1. FUNDAMENTALS OF BATTERY ANALYSIS .....	80
III.1.1. Consequences of degradations in LIB .....	80
III.1.2. Commonly employed analysis methods .....	81
III.2. THE COMPLEXITY OF KNEE POINT .....	87
III.2.1. Knee points: definition and types .....	87
III.2.2. Origins of knee points .....	88
III.2.3. Motivations for constructing analysis workflows .....	89
III.3. WORKFLOWS .....	90
III.3.1. Detection of shuttling events .....	91
III.3.2. Detection of chemical crosstalks .....	93
III.3.3. Detection of crosstalk associated to voltage window shift .....	96
CONCLUSION OF CHAPTER III .....	100

<b>CHAPTER IV: ASSESSING THE EFFECTS OF DISSOLVED TRANSITION METALS IN GRAPHITE/LINIO<sub>2</sub> CELLS PERFORMANCE .....</b>	<b>102</b>
INTRODUCTION OF CHAPTER IV.....	104
IV.1. NICKEL CROSSTALK AND RESULTING CELL PERFORMANCE .....	105
IV.1.1. Graphite LiNiO <sub>2</sub> cell performance.....	105
IV.1.2. In-depth analysis of degradations .....	107
IV.1.3. Mechanism of Ni incorporation in the SEI.....	111
IV.2. BENCHMARK OF TRANSITION METAL EFFECTS .....	113
IV.2.1. Effect of TM on cell performance .....	113
IV.2.2. Graphite staging jump .....	115
IV.2.3. Short-lived benefits.....	116
IV.3. EFFECTS OF METALS AT THE GRAPHITE ELECTRODE .....	117
IV.3.1. Method introduction.....	117
IV.3.2. Influence of TM in the SEI .....	119
CONCLUSION OF CHAPTER IV .....	122
<b>CHAPTER V: HIGHLY CONCENTRATED ELECTROLYTES AND CASCADING SIDE REACTIONS IN GRAPHITE/NMC811 CELLS .....</b>	<b>124</b>
INTRODUCTION OF CHAPTER V.....	126
V.1. CASCADING DEGRADATIONS .....	128
V.1.1. Cell performance with HCE .....	128
V.1.2. Determining the cause of instability.....	132
V.1.3. Li plating as a consequence of side oxidation.....	136
V.2. MITIGATING THE SIDE REACTIONS .....	138
V.2.1. Outcome of higher cycling temperatures.....	138
V.2.2. Formation of SEI and CEI.....	139
V.2.3. Electrolyte optimization.....	144
V.3. LOCALIZED HIGH CONCENTRATION ELECTROLYTE .....	147
V.3.1. Finding the ideal composition.....	147
V.3.2. Stability limits at high voltages .....	152
V.3.3. Overview of electrolyte degradations .....	155
CONCLUSION OF CHAPTER V .....	158
<b>CONCLUSION AND PERSPECTIVE .....</b>	<b>160</b>
ANNEX 1 – INTERNAL STACK HEIGHT CALCULATION TOOL.....	169
ANNEX 2 – ELECTROLYTE VOLUME CALCULATION TOOL.....	170
ANNEX 3 – EXPERIMENTAL SECTION OF CHAPTER III.....	171
ANNEX 4 – EFFECT OF CONTROL CYCLES ON CELL PERFORMANCE .....	174
ANNEX 5 – FITS OF CONTROL 0 FOR 4.5 AND 4.8 V CELLS.....	175
ANNEX 6 – ICA OF LNO HALF CELLS .....	176
ANNEX 7 – FITS OF 4.2 V CELLS USING LP57 + Ni <sup>2+</sup> ELECTROLYTE .....	177
ANNEX 8 – EXPERIMENTAL SECTION OF CHAPTER IV.....	178
ANNEX 9 – RELATIVE DISCHARGE CAPACITIES AND CORRESPONDING LLI .....	182
ANNEX 10 – EVOLUTION OF CELL POLARIZATION AT 25°C AND 55°C .....	183
ANNEX 11 – FITS OF dV/dQ CURVES WITH CELLS USING LP57 VC AND HCE DMC .....	184
ANNEX 12 – LIMITED OXIDATION OF ALUMINUM USING HCE DMC .....	185
ANNEX 13 – OXIDATION PRODUCTS OF HCE DMC USING STAINLESS STEEL FOIL .....	186
ANNEX 14 – PHOTOGRAPH OF LI PLATING ON GRAPHITE ELECTRODE USING HCE DMC..	187
ANNEX 15 – HAXPS DATA OF GRAPHITE ELECTRODES RECORDED AT 6.9 KEV.....	188
ANNEX 16 – TM QUANTIFICATION BY ICP-MS OF GRAPHITE ELCTRODE USING HCE EC....	189
ANNEX 17 – ICA OF LHCE WITH ADDITIVES FOR SEI (2%WT VC AND 2WT% FEC) .....	190
ANNEX 18 – ICA OF LHCE WITH ADDITIVES FOR CEI (2WT% FB AND 2WT% TMP) .....	191
LEXICON.....	193
TABLE OF FIGURES .....	195
<b>REFERENCES .....</b>	<b>197</b>
<b>RESUME DE THESE EN FRANCAIS.....</b>	<b>209</b>

# **CHAPTER I: INTRODUCTION OF THE THESIS**



## I.1. BROAD INTRODUCTION

The advancement of industrial societies is heavily dependent on the extensive utilization of energy for operating production machinery and maintaining certain comfort in everyday life. In 2021, 180 PWh ( $10^{15}$  Wh) of energy was consumed worldwide for powering transport (30%), industry (29%), residential (21%), tertiary (8%) or farming (2%), of which 80% stems from the combustion of fossil fuels [1]. Although fossil fuels, including oil, coal and gas, benefit from high gravimetric energy ( $\sim 10 \text{ kWh.kg}^{-1}$ ) at cheap price ( $< 0.5 \text{ \$.kg}^{-1}$ ) [2], they have two main drawbacks. Firstly, these are finite resources and supply will not be sufficient to meet the world's growing energy demand of +1.4% per year [2]. Conventional oil already reached its production peak in 2006 and similar scenario are envisioned for gas by 2035 and coal between 2050 and 2150. In the face of this countdown, there is an urgent need to consider sustainable energy resources for the future.

Secondly and more importantly, the combustion of fossil fuels releases carbon dioxide ( $\text{CO}_2$ ), the greenhouse gas that contributes the most to global warming. Since pre-industrial age, the increase of  $\text{CO}_2$  concentration in the atmosphere is purely anthropogenic and reached 412 ppm in 2020, *i.e.* an increase of +145% [2]. Those levels will cause an increase of the average Earth temperature by +1.1°C by 2030, independently of current environmental policies. As a reminder, the goals of Paris' agreement are to limit global warming below +1.5°C, corresponding to  $\text{CO}_2$  concentration lower than 450 ppm by 2100 [3]. At current emission rates,  $\text{CO}_2$  level will reach this threshold by 2045, threatening ecosystems and human being. Regions, in particular near the equator, will become inhabitable for human being while desertification will modify the establishment of vegetal and animal species. Direct consequences are droughts and a drop of crop yields, precipitating malnutrition and poverty level in some regions. On the other side, the melting of polar ice cap will cause an increase of sea level of 1.5 cm per year, threatening coastal populations and modifying ocean streams. Finally, global warming will also enhance temperature gradient in seas and atmosphere, increasing the intensity and frequency of natural disasters such as tornado, hurricane and typhoons [4]. Nevertheless, above-mentioned effects are solely the tip of the iceberg, as climate change will likely disrupt geopolitical equilibrium, which consequences are delicate to anticipate. Among them, 216 million people will migrate internally in their country for economic reasons or to more favorable environmental locations [5]. Climate change could also lead to economy recession, increasing poverty and disrupting the geopolitical stability. The 20<sup>th</sup> century bears witness numerous conflicts triggered by wealth inequalities, food insecurity, and rise of nationalism regimes.

The reliance of modern societies to fossil fuels faces stakes that go beyond a matter of supply, as it disrupts the environmental and geopolitical global balance. On the positive side, climate challenge is mainly an energy challenge where recent awareness and democratization of the urgency have sparked unprecedented momentum for actions [3]. In 2021, the international energy agency have edited the net zero emission (NZE) roadmap that aims to reach carbon neutrality by 2050, which most prominent levers are renewable energies, consuming habits and building insulation [3]. In each sector, NZE roadmap proposes milestones and ideal development rates. While the deployment of renewables energies is on track, total production only represents 1/3 of expected levels in NZE scenario by 2030 and similar conclusions are drawn in road transport accounting for 16% of global CO<sub>2</sub> [6]. Efforts have to intensity to reach carbon neutrality and intermediate goals by 2030 as shown in Figure 1.

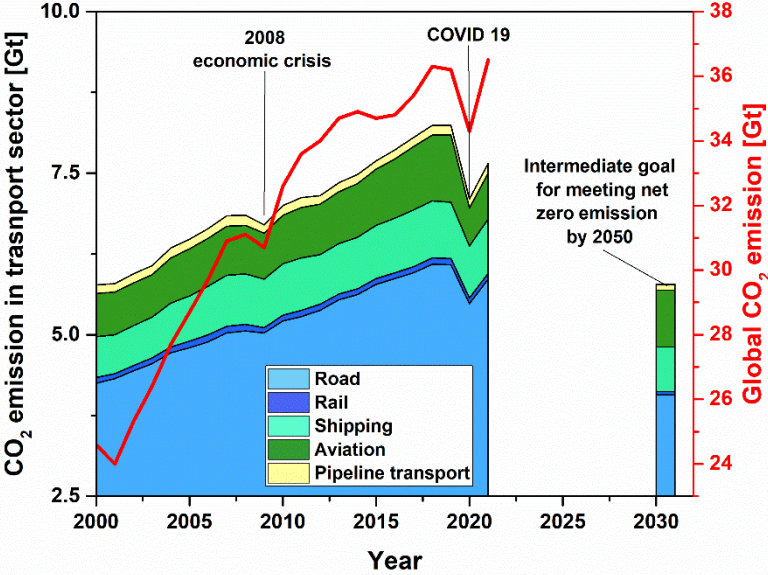


**Figure 1 – Evolution of CO<sub>2</sub> emission over the last twenty years**

*Evolution of global CO<sub>2</sub> emission during the last twenty years (right), which 16% is attributed to road sector. The breakdown of CO<sub>2</sub> emission in transport sector is provided on the left y-axis. To meet NZE milestones, CO<sub>2</sub> emission have to drop by 30% by 2030 pushing for the widespread adoption of sustainable mobility solutions.*

## **I.2. THE ROLE OF ELECTRIC MOBILITY IN THE ENERGY TRANSITION**

### **I.2.1. Market of electric mobility**

To reach carbon neutrality, road transport emissions have to be reduced by 30% by 2030, pushing for the widespread adoption of low-carbon mobility solutions [6]. Electric vehicles (EVs), powered by Li-ion batteries (LIBs), are a key factor in promoting sustainable mobility, offering a carbon footprint that is 70% lower compared to diesel engines when charged with low-carbon electricity [7]. Furthermore, with no pipe tail emissions, EVs help reducing air pollution-related premature deaths due to NO<sub>x</sub>, SO<sub>x</sub> and fine particles [5]. The EV and hybrid sector have thus become very dynamic in the last decade and represented, in 2020, 13% of global car fleet, *i.e.* 11 million cars [6]. Most dynamic markets are located in China and Europe, representing 77% of global sells combined, followed by the USA with 16%. The success of EVs relies on continuous drop of selling prices, widespread development of charging facilities and the implementation of incentive buying policies [8]. In ten years, EVs have thus become the new standard for sustainable mobility while developing economic growth. Optimistic forecasts predict sell to increase by 6% per year until 2030. Although EVs are an appropriate solution for reducing CO<sub>2</sub> emissions, their deployment must be associated with a change in mobility habits.

### **I.2.2. Success story of LIBs in electric mobility**

Since their initial commercialization in 1991 by Sony, Li-ion batteries (LIBs) have gained popularity for use in portable devices due to their superior performance compared to contemporaneous Ni-Cd or lead-acid batteries. LIB technology has revolutionized energy storage and has been equipping laptops, cell phones, and camcorders for over three decades. As the technology matured, production costs rapidly declined, while performance continuously improved. Between 1995 and 2021, the price of Lithium-ion Batteries (LIBs) decreased significantly by a factor of 38, going from 6,746 USD/kWh to 176 USD/kWh, and at the same time, their capacity doubled, reaching 250 Wh/kg. [9]. These metrics paved the way for new applications in the mobility sector, with the introduction of mainstream EV models such as the Tesla Roadster (2008) or the Nissan Leaf (2013). During the 2010s, there was an annual growth rate of approximately 150% in the average LIB stocks, and in response to the rapidly increasing demand, numerous giga-factories were established (Figure 2). Between 2015 and 2020, LIB production tripled, reaching a capability storage of 160 GWh. As a result, the enthusiasm for batteries has driven manufacturers and academics to continuously enhance

performance and affordability. Toward that goal, a comprehensive understanding of battery fundamentals is necessary.

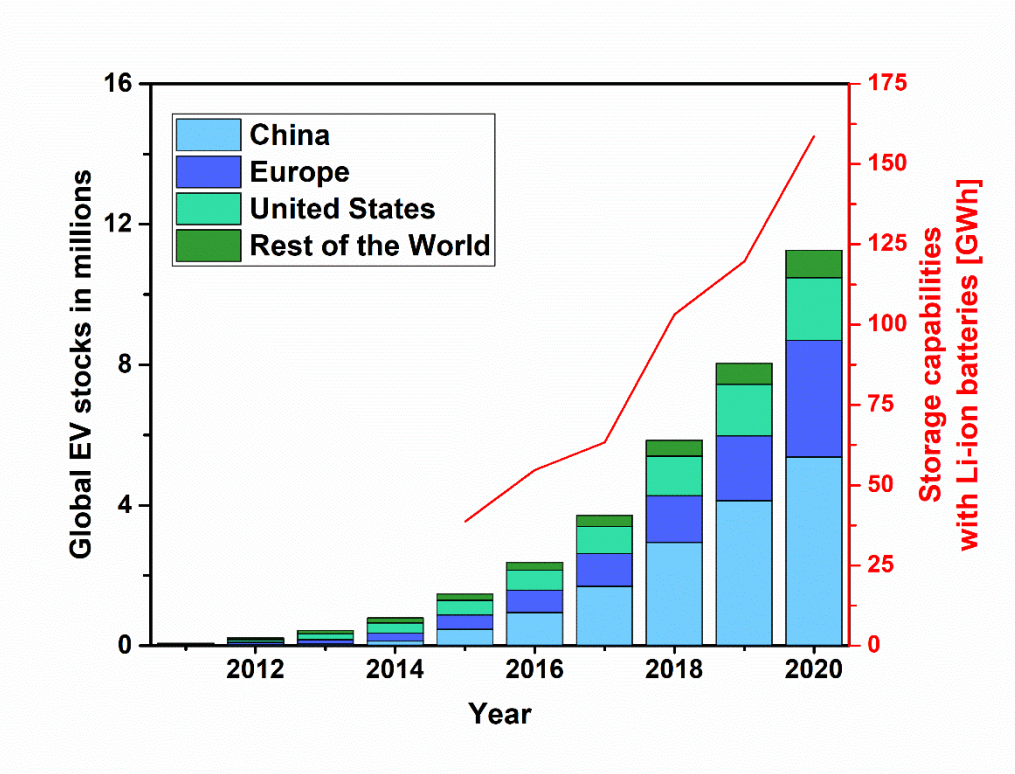


Figure 2 – Evolution of EV stocks over the last ten years

Correlation between global EV stocks and storage capabilities with Li-ion batteries from 2011 to 2020. Source: Global EV Outlook 2022, IEA [6].

**1.2.3. Ongoing challenges for further market expansion**

Powered by Li-ion batteries, EVs still fall short at reaching the 700 km average driving range of combustion engines, maintaining the “range anxiety” in the minds of consumers. At the pack level, LIBs achieve 170 Wh.kg<sup>-1</sup> and US\$ 176 kWh<sup>-1</sup>. The US department of energy estimates that battery packs of 235 Wh.kg<sup>-1</sup> at US\$ 100 kWh<sup>-1</sup> should be achieved for competing with combustion engines [10]. Although production volume, pack design and management of powertrain all help achieving those goals, largest cost and energy gains will come from the chemistry of used materials, in particular, the chemistry of the positive electrode [8]. For now, the range anxiety can be alleviated by fast charging of batteries and the development and densification of charge station network.

## I.3. FUNDAMENTALS OF LI-ION BATTERIES

### I.3.1. General functioning

#### I.3.1.a. Description of an electrochemical cell

A Li-ion cell converts chemical energy to electrical energy in a reversible way thanks to the exchange of lithium ions and electrons between the electrodes (Figure 3). Electrodes are composed of a blend of lithium-host compounds, named active material, along with carbon black additives that are necessary to ensure electronic conductivity. Moreover, a polymer binder is added for maintaining the mechanical properties of the electrode. All components are blended together with solvent to form a slurry that is subsequently casted onto either aluminum or copper foils, depending on the operating voltage required for the electrode. After the electrodes have been dried, they are combined within a cell along with a separator. The separator is thin and porous polymer foil that protects the cell from short-circuits. Eventually, the electrolyte fills the porosity of the separator and electrode pores and ensures  $\text{Li}^+$  transports between electrodes. As per convention, the material with the highest potential is coined as the positive electrode, while the lowest potential material serves as the negative electrode.

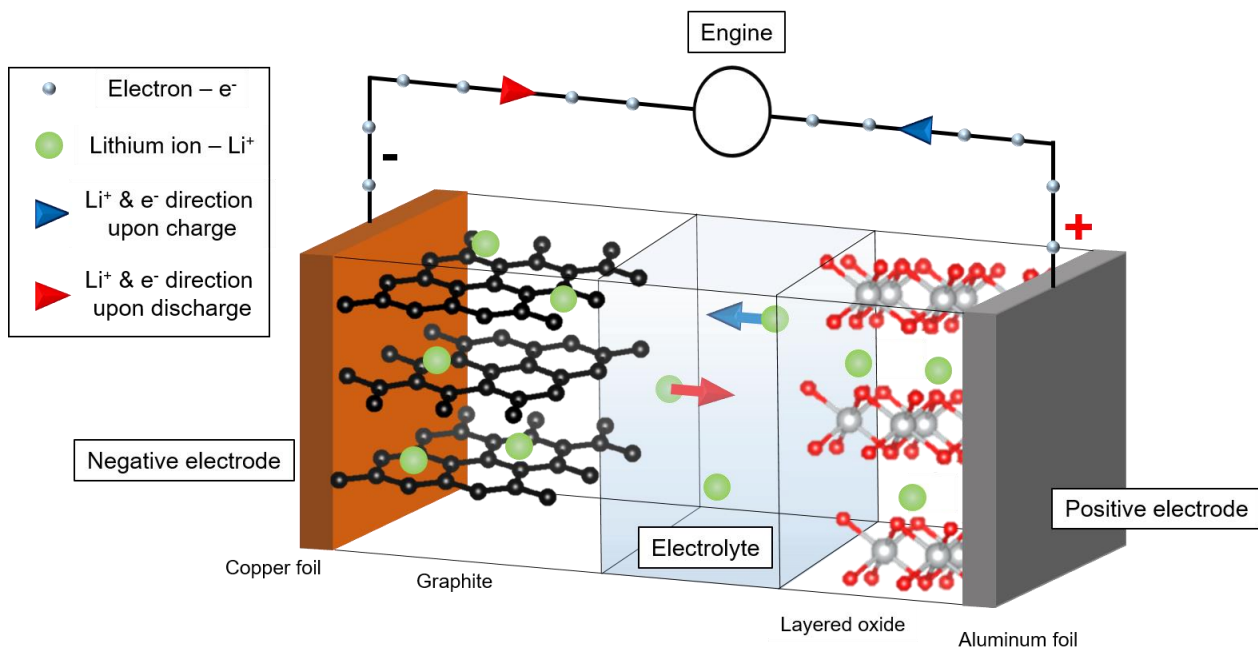


**Figure 3 – Schematic of Li-ion battery**

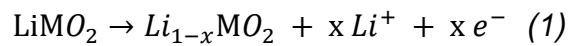
*Schematic view of a Li-ion battery. Upon cycling, lithium ions and electrons migrate reversibly between positive and negative electrodes, on charge or discharge step.*

### I.3.1.b. Electrochemical reactions

In current LIB technology, the typical positive electrode's material is a layered oxide as  $\text{Li}_{1-x}\text{MO}_2$ , where M is a transition metal such as Ni, Co or Mn. On the other hand, the negative electrode is composed of carbonaceous material, specifically graphite ( $\text{C}_6$ ).

Upon charge, the positive electrode (+) is oxidized, *i.e.* releases a given quantity  $x$  of lithium ions (Equation 1), while negative electrode (-) is reduced, *i.e.* inserts  $x$  lithium ions (Equation 2). During this process, the cell voltage increases.

#### (+) Anode

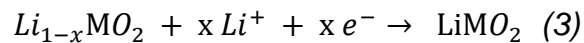


#### (-) Cathode

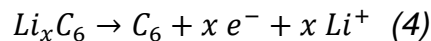


During the discharge, reverse reactions occur spontaneously, allowing the user to retrieve stored energy. The discharge is indeed the thermodynamically favored step during which positive electrode (+) is reduced, *i.e.* inserting back  $x$  lithium ions (Equation 3), while negative electrode (-) releases  $x$  lithium ions via oxidation (Equation 4). As a result, cell voltage decreases.

#### (+) Cathode



#### (-) Anode



In summary, during charge,  $\text{Li}^+$  ions and electrons are transferred from the positive electrode to the negative electrode, whereas during discharge,  $\text{Li}^+$  ions and electrons are transferred from the negative electrode to the positive electrode. It is worth noting that the terms "cathode" and "anode" are often used to refer, despite partially true, to positive and negative electrode, respectively.

### I.3.1.c. Li-ion battery conventions

#### *Electrode nomenclature*

To describe Li-ion cells, the same electrode terminology used in electrochemistry is employed.

1. Working electrode (WE) refers to the electrode where electrochemical half-reaction of interest occurs.

2. Counter electrode (CE) hosts the second half-reaction and closes electrochemical circuit, ensuring electron movement.
3. Reference electrode (Ref) is facultative and serves as potential base in the system. The reference electrode maintains a stable and well-known potential thanks to an equilibrium between fast redox species, which potential is defined by Nernst equation.

In a two-electrode battery, the working electrode is associated to the positive electrode since it determines the overall capacity of the cell, whereas the negative electrode functions as the counter and reference electrode. In a three-electrode cell, a third electrode serves as the reference electrode. Lithium metal possesses the characteristics of a reference electrode, and therefore, potentials are typically measured against the Li<sup>+</sup>/Li redox couple ( $E^\circ(\text{Li}^+/\text{Li}) = 0.00 \text{ V vs Li}^+/\text{Li}$ ), which corresponds to -3.04 V when compared to the standard hydrogen electrode.

### *Voltage*

The cell voltage is determined by measuring the potential difference between the working and reference electrodes (Equation 5), which corresponds to the positive and negative electrodes in full cell, respectively.

$$E_{\text{Cell}} = V_{\text{positive}} - V_{\text{negative}} \quad (5)$$

In the majority of batteries, the positive electrode operates between 2.0 – 2.5 V and 4.1 – 4.45 V vs Li<sup>+</sup>/Li for layered oxides, whereas the negative electrode operates between 1 – 1.5 V to 0.01 V vs Li<sup>+</sup>/Li. As a result, the usual battery voltage ranges between 2.5 to ~4.1 – 4.4 V.

### *Current*

Following the electrochemistry convention, the charge current is positive as electrons flow from the positive to the negative electrode during the oxidation. Conversely, during discharge, the reduction current is negative as electrons flows from the positive to the negative pole.

## **I.3.2. Usual descriptors of battery performance**

### **I.3.2.a. Capacity and energy**

Battery capacity is defined as the total amount of electric charges generated by electrochemical reactions. The total amount of charges is estimated from input and output current in the battery following Equation 6, where  $i$  is the applied current, and  $\Delta T = T_1 - T_0$ , the time in which electrons have passed.

$$Q = \int_{T_0}^{T_1} i. dt = i. \Delta T \quad (6)$$

In battery research, the typical unit for capacity is mAh per gram (mAh.g<sup>-1</sup>), which is normalized by the masses of active materials in the positive electrode. By convention, positive electrodes experience an increase in capacity during the charge (de-lithiation) and a decrease in capacity during discharge (lithiation). In contrast, negative electrodes experience an increase in capacity during discharge (lithiation) and a decrease in capacity during charge (de-lithiation). Voltage as a function of capacity curves (Figure 4) are commonly used to show charge (red) and discharge steps (blue).

The energy of the battery (E) is calculated by multiplying the voltage of the battery V(Q) by the capacity of electrochemical reactions (dQ). Energy is expressed in Wh per kilogram (Wh.kg<sup>-1</sup>) and corresponds to the area under the voltage-capacity curve (Equation 7). As an approximation, energy corresponds to average voltage V<sup>av.</sup> times the capacity. It is worth noting that the increase of cell voltage ensures more energy for similar capacity.

$$E = \int_{Q_0}^{Q_1} V(Q). dQ \sim V^{av.} . \Delta Q \quad (7)$$

### **I.3.2.b. C-rate**

Since LIBs must function effectively across a range of current levels, their performance is typically evaluated at various currents using C-rate definition. C-rate determines how fast the cell can deliver energy based on their nominal capacity. The standard notation for C-rate is expressed as C/N, where C refers to the capacity to be reached (mAh or Ah) and N represents the number of hours (h) required to achieve full (dis-)charge. The value of C can be calculated using either the theoretical capacity of the working electrode material or through experimental testing at a low current. For this thesis, the C-rate is always determined using the theoretical capacity, as per the following formula (Equation 8), where Q is the theoretical capacity in mAh.g<sup>-1</sup>, n is the number of exchanged lithium ions, F represents the Faraday constant in A.s.mol<sup>-1</sup>, M denotes the molecular weight of the material in g.mol<sup>-1</sup>, and the 3.6 factor is used to convert seconds into hours and ampere to miliampere.

$$Q = \frac{n \times F}{3.6 \times M} \quad (8)$$

Using the theoretical capacity offers the advantage of accommodating the fluctuations in the electrode loading, as the mass of each active material is measured during assembly.

### I.3.2.c. Polarization

When a cell is cycled at constant current, cell voltages of charge and discharge differ from thermodynamic voltages measured under open circuit conditions. This is because the (de-)lithiation reactions are hindered by resistances and a voltage bias is necessary to overcome them. The voltage bias corresponds thus to the voltage difference between the equilibrium voltage and the recorded (dis-)charge voltage, and is linked to the internal cell resistance (Figure 4). It is thus common to estimate internal resistance by measuring the cell polarization  $\Delta V$ .  $\Delta V$  is the difference between the average charge and discharge voltages, providing an estimation of the cell Ohmic drop ( $Ri$ ), where  $i$  is the applied current and  $R$  is the Ohmic resistance (Equation 9). The factor “2” in equation 9 arises from the polarization during charge and discharge. The increase of  $\Delta V$  may indicate lower kinetic, change in temperature or appearance of resistive layers on electrodes.

$$\Delta V = V_{Charge}^{Mean} - V_{Discharge}^{Mean} = 2 * Ri \quad (9)$$

In addition to polarization, electrodes can experience upon charge and discharge, electrochemical reactions that use electrons for purposes other than  $\text{Li}^+$  intercalation. Although

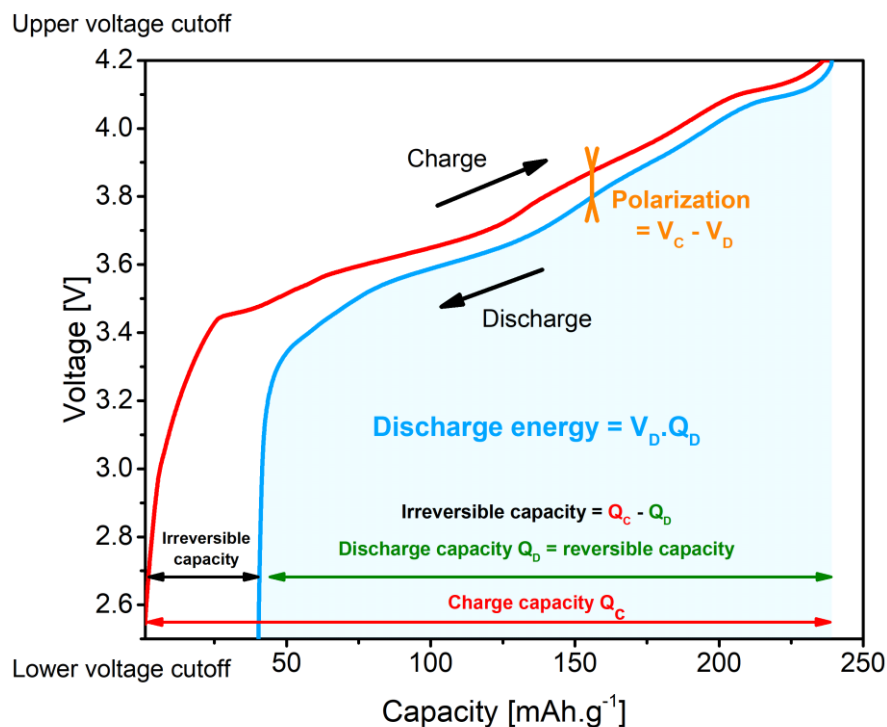


**Figure 4 - Overview of common descriptors of cell performance**

The electrochemical cycling curve of a graphite/NMC811 cell depicts the commonly used metrics for evaluating cell performance. The discharge energy corresponds to the area beneath the blue line on the discharge curve, while the voltage difference between charge and discharge is referred to as cell polarization.

these side reactions do not necessarily result in cell polarization, they can reduce the reversibility of the energy storage and retrieval process, thereby reducing cell performance.

#### **I.3.2.d. Coulombic efficiency**

Coulombic efficiency (CE) estimates the reversibility of lithium (de-)insertion upon cycling and is calculated from the ratio between charge  $Q_C$  and discharge capacities  $Q_D$  (Equation 10). CE is ideally equal to unity, which would indicate absence of side reaction in the electrochemical cell. However, in practice, part of charge capacity cannot be retrieved upon discharge, which is known as irreversible capacity (Figure 4), thereby leading to  $CE < 1$ . For instance, to reach the commercial standard 80% initial state of charge (SOC) over 1,000 cycles, mean CE should be higher than 0.9998.

$$CE = \frac{Q_D}{Q_C} \quad (10)$$

### **I.3.3. Architecture of Li-ion batteries**

#### **I.3.3.a. Cell configuration**

Half-cell refers to the configuration where lithium metal is used as CE and reference electrode while working (positive) electrode is the material of interest. The half-cell configuration benefits from lithium metal exhibiting characteristics of a reference electrode, maintaining a stable and fixed potential at 0.00 V vs Li<sup>+</sup>/Li. By employing the half-cell configuration, the electrochemical response observed is solely attributed to the positive electrode material, making it suitable for material studies and electrochemical characterizations.

Full cell refers to a configuration that employs a finite quantity of Li<sup>+</sup> ions, without a reference electrode. Considered as a full cell, symmetric cell is a configuration in which similar intercalation compounds are used for both positive and negative electrodes without a reference electrode.

#### **I.3.3.b. Commercial format**

Nowadays, three main formats are available for commercial batteries: cylindrical, prismatic and pouch. Although the casing is different, inner structure remains similar, i.e. a lithium-ion battery pack is comprised of modules, gathering lithium-ion cell arrays. In the cells, the positive and negative electrodes are double sided casted on current collector and paired on top of each other with a separator in between. The obtained structure is then rolled to form a jellyroll and is placed in the cell casing, filled with electrolyte. Sometimes double-coated electrodes are placed on top of each other, with a separator between them to form a stacked

format. The choice of electrode geometry depends on the needs, in terms of space, energy density and lifetime.

*Cylindrical cell*

In cylindrical cell, the jellyroll is inserted in cylindrical shaped stainless-steel can giving the name to the cell format (Figure 5a). Panasonic commercialized in 1994 the first 18650-cylindrical cell (18 mm diameter x 65 mm height) that have rapidly become the most popular format among cylindrical formats. However, larger size 21700 cells progressively replace 18650 and equip new vehicles thanks to higher energy densities while decreasing production cost associated to handling work as jellyroll insertion, closing and welding [11]. For instance, cylindrical cells mostly equip Tesla model S, 3 and X.

*Prismatic cell*

In the prismatic cell, the jellyroll is shaped oblongly using flat mandrel to fit into a prismatic case (Figure 5b). Cells are attractive in volume-sensitive applications because the size of the cells can be easily customized, ensuring denser packaging. Furthermore, prismatic cells allow for an easier connection between packs. A standard format for prismatic cell in EV measures 30 mm thick x 120 mm wide x 320 mm long [12]. Associated with higher energy density than cylindrical cells, prismatic cells are the standard format used in the EV industry. However, the electrodes have lower mechanical stability due to lower internal pressure, resulting in delamination of the material coating [13].

*Pouch cell*

Pouch cell geometry is similar to prismatic ones, except that pouch cells have a composite casing, which is composed of a trilayer of polypropylene / Al foil / polypropylene laminated by heat (Figure 5c). To connect pouch cells, positive and negatives electrodes are bundled together by tabs that protrude from the packaging. Pouch cells provide the highest energy density among other formats thanks to the thinness and lightness of the envelope. On the other hand, the polymer foil fails at maintaining proper mechanical hold, which emphasizes the issue of material delamination observed in prismatic format [12].

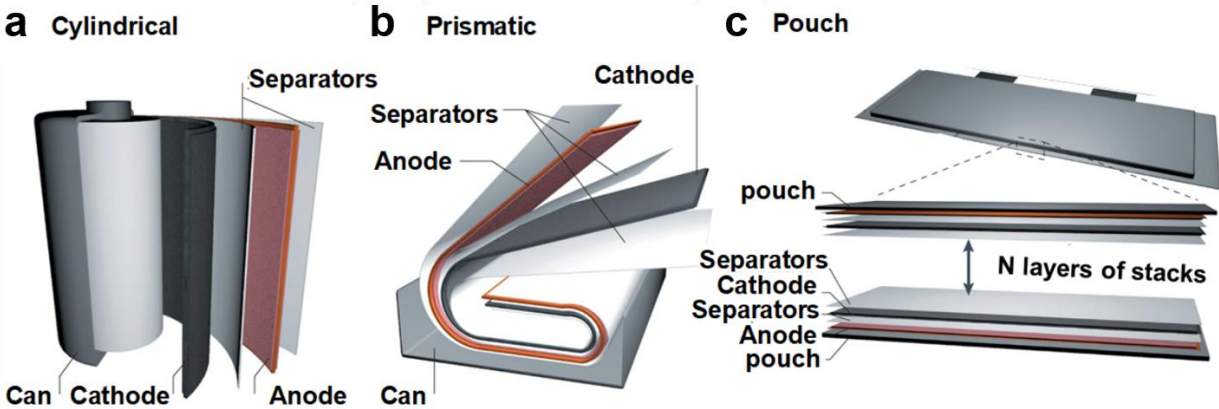


Figure 5 – Available commercial cell formats

Cylindrical (a), prismatic (b), and pouch formats (c) are commonly used in the industry.

### I.3.3.c. Academic format

While mass production of batteries drops down the production costs, commercial cell assembly necessitates costly production lines and large amount of active materials that is not adapted to academic research. Electrodes and electrolyte design are thus tested in smaller cell formats.

#### *Swagelok®*

Initially used as gas pipe connector, Swagelok® type cell shows various electrochemical testing applications in two or three-electrode configurations. The body of the cell can embed powder or electrodes maintained by stainless plungers. Nuts at the ends of the cell hold the plungers and spring in place to ensure a correct internal pressure. A plastic foil named Mylar covers the inner part of the cell body, and a separator is placed between the electrodes to prevent short-circuits (Figure 6a). If the connector has three heads, the third hole can be used to insert a reference electrode. Additionally, certain Swagelok® models enable the detection of any released gas [14].

#### *Coin cell*

Whilst coin cell format has some applications in domestic sector as primary batteries, e.g. in hearing aids, calculators or pacemakers, commercial LIB in coin cells are not available. Coin cells are commonly used in academia because they provide a quick testing option for low sample quantities. Furthermore, electrodes can be used as well, if coated on one side and cut into round shapes to fit the standard 2032 or 2025 dimensions (20 mm diameter x 32 or 25

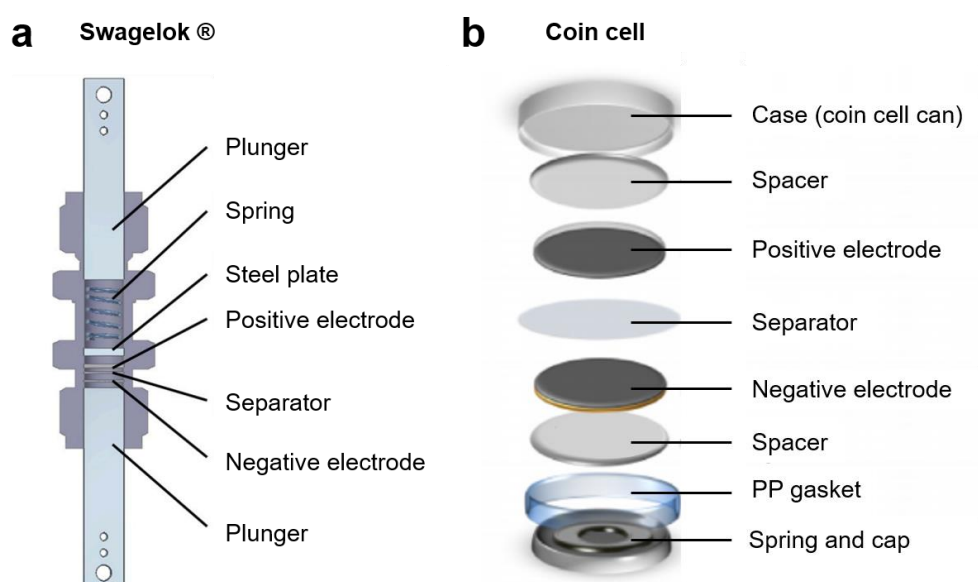


**Figure 6 – Widespread used academic cell formats**

Schematics of Swagelok® a) and coin b) cell formats that are commonly used in academia. Used components are similar for both cell formats.

mm thick). When the cell is closed, internal spring clamped stack holds the electrodes face to face, and stainless steel holders called spacers keep them in place (Figure 6b).

### I.3.4. Chemistry of cell components

#### I.3.4.a. Electrolyte

Electrolytes are a centerpiece of electrochemical cells, providing the necessary ionic transport to support redox reactions at electrodes. In most commercial batteries, electrolytes are liquid to ensure high active material wettability and electrode pore filling, and thus the most efficient charge transport [15]. Electrolytes are composed of a combination of lithium salt and polar organic solvents, wherein the solvent molecules solvate ions following a solvation sheath. Typically, the solvents used are a combination of cyclic carbonates (high dielectric constant, high viscosity) and linear carbonates (low dielectric constant, low viscosity) to achieve the best compromise between high lithium solvation while maintaining low electrolyte viscosity. For instance, ethyl carbonate (EC) and propyl carbonate (PC) have a high dielectric constant of 95.3 and 65.5 [16], respectively, which makes them good at coordinating with Li<sup>+</sup> ions, but they also have a high viscosity of 1.9 mPa.s. The addition of linear carbonate like ethylmethylcarbonate (EMC), which has a viscosity of 0.544 mPa.s, significantly reduces the overall electrolyte viscosity to approximately 2.8 mPa.s [17] and facilitates the transport of Li<sup>+</sup> to the interfaces. Other solvents like dimethylcarbonate (DMC), diethylcarbonate (DEC), or ethyl acetate (EA) are also often used.

Name	Solvent mix (molar ratio)
<b>LP30</b>	EC–DMC (0.5/0.5)
<b>LP40</b>	EC–DEC (0.6/0.4)
<b>LP47</b>	EC–DEC (0.4/0.6)
<b>LP50</b>	EC–EMC (0.55/0.45)
<b>LP57</b>	EC–EMC (0.3/0.7)
<b>LP71</b>	EC–DEC–DMC (0.4/0.3/0.3)
<b>LP81</b>	EC–DMC–EA (0.4/0.3/0.3)

**Table 1**

*List of widespread used LiPF<sub>6</sub>-carbonate based electrolytes known as LP class.*

Typically, the electrolyte solution for lithium-ion batteries contains lithium hexafluorophosphate ( $\text{LiPF}_6$ ) salt, with a concentration of approximately 1 M. This concentration strikes a balance between achieving the highest possible ionic mobility and keeping the electrolyte viscosity low, which in turn maximizes ionic conductivity  $\sim 10^{-2} \text{ S}\cdot\text{cm}^{-1}$  [18]. Electrolytes using 1 M  $\text{LiPF}_6$  are denoted by the abbreviation “LP + number”, and can be associated to various solvent compositions as shown in the Table 1.

#### **I.3.4.b. Electrolyte interphase**

The current operating voltage range of 2.0 to 4.4 V of LIBs falls beyond the thermodynamic stability range of LP-type electrolytes. Indeed, carbonate solvents experience reduction below 0.8 V vs  $\text{Li}^+/\text{Li}$  and oxidation above 4.2 V vs  $\text{Li}^+/\text{Li}$  and this reactivity is likely to result in a premature battery end of life. However, the proper operation is ensured owing to a passivation mechanism [15], where solvents, salt, additives are decomposed upon lithium (de-)insertion at electrode surfaces. On the negative electrode, solvents and salt reduce and deposit, forming a layer called the solid electrolyte interphase (SEI) [19]. *J. Dahn et al* correlated the SEI formation with a loss of available lithium in the system, resulting in a capacity loss [20], [21]. Although SEI formation can lead to a reduction in capacity, it is still essential for passivating the electrode surface and preventing additional electrolyte reduction during battery cycling. A thickness of approximately 45 Å is thought to be effective in preventing electron tunneling [21]. *E. Peled et al* first proposed in 1979 a model describing the SEI as a mosaic structure composed of organic and inorganic components [22]. Organic components are mainly lithium ethyldicarbonate (LEDC) and polyolephines stemming from the decomposition of EC, EMC or DMC solvents. Salt degradation in contrast leads to the formation of inorganic components such as  $\text{LiF}$ ,  $\text{Li}_2\text{O}$  and  $\text{Li}_2\text{CO}_3$ . The different components are distributed following a bilayer structure, with an inorganic and dense layer near the electrode surface and a porous outer layer composed of organic components. Ideally, the SEI must be a good  $\text{Li}^+$  conductor blocking electron transport to avoid further decomposition of the electrolyte. Moreover, the ideal SEI forms only during the first few cycles, to reduce the consumption of electrolyte over cycling, and the passivating power is sustained during long-term operation. To achieve this goal, electrolyte additives like vinylene carbonate (VC), fluoroethylene carbonate (FEC) are often added into the electrolyte; their reduction occurs before the one of conventional carbonate solvent [23]–[25].

At the positive electrode, a similar passivating layer has been observed, named cathode electrolyte interphase (CEI). The formation of this layer stems from the anodic decomposition of the electrolyte. Although CEIs are thinner than SEIs, they fulfill similar functions: good passivation while sustaining high  $\text{Li}^+$  conductivity.

### **I.3.4.c. Electrodes**

#### *Negative electrodes*

The most prominent material used as negative electrode is graphite, with a practical capacity of  $360 \text{ mAh.g}^{-1}$ . Upon cycling, lithium inserts reversibly into graphitic layers, forming successively different intermediate phases with composition varying from  $x = 0$  to  $1$  in  $\text{Li}_x\text{C}_6$ . Three distinct domains are clearly visible at fixed potentials of 200, 110 and 90 mV vs  $\text{Li}^+/\text{Li}$ ; they are referred to as stage III, II and I, respectively [26].

Silicon is a promising material for next generation of negative electrode materials. In contrast with graphite, where lithium experiences intercalation reactions, silicon reacts with lithium by forming  $\text{Li}_x\text{Si}$  alloys, this alloying reaction offers ten times more capacity than intercalation in graphite ( $3,579 \text{ mAh.g}^{-1}$ ). However, (de)-alloying reactions cause massive volume changes of  $\pm 280\%$ , leading to severe particle fractures, pulverization and loss of electric contact [27]. Moreover, the appearance of particle cracks reveals new silicon surfaces that react with the electrolyte since silicon operates within the range of 1 to 0.05 V vs  $\text{Li}^+/\text{Li}$ , thus below stability limit of LP electrolytes. Currently, a tradeoff is found by using composite electrode composed of up to 35% Si with graphite that limits cracking. Composite electrodes are further used in combination of self-healing binders and/or electrolyte additives, which enhance mechanical stability [28].

Lithium metal offers high-energy density and a quasi-infinite lithium reservoir when used as negative electrode. However, plating/stripping reactions of lithium causes continuous changes of surface morphologies that leads, when uncontrolled, to the appearance of lithium dendrites [29], [30]. Furthermore, the highly reactive nature of lithium triggers numerous side reactions, consuming electrolyte and forming poor passivating layer [31].

#### *Positive electrode*

Fundamental works on positive electrode materials started in the early 1970s with the study of intercalation compounds such as  $\text{NbSe}_3$ ,  $\text{TiS}_2$  or  $\text{MoS}_2$ . Although companies attempted to commercialize these materials, such as Moli Energy with  $\text{MoS}_2$ , only the introduction of lithium-containing oxides by J.B. Goodenough (Nobel Prize 2019) in 1979 led to materials that have dominated market share for decade:  $\text{LiCoO}_2$  (LCO) [32]. The lamellar oxide provides reversible capacity of  $140 \text{ mAh.g}^{-1}$  at 4.0 V vs  $\text{Li}^+/\text{Li}$ . However, the cycling of LCO is constrained to utilizing only half of its capacity due to degradations occurring beyond 4.0 V, thus limiting the total amount of cyclable lithium in the cell. The incorporation of electrolyte additives and material coatings assisted in overcoming partially this limitation, cycling up to 4.4 V versus graphite. In 1980's, Thackeray and coworkers broadened the chemical space of intercalation compounds to spinel structures, with the study of  $\text{LiMn}_2\text{O}_4$  which has higher thermal stability and circumvent the use of costly cobalt mineral [32]. Later

on, Goodenough and his group demonstrated that  $\text{LiFePO}_4$  (LFP), with an olivine structure, has a remarkable stability, with reversible capacity of  $145 \text{ mAh.g}^{-1}$  at 3.45 V vs  $\text{Li}^+/\text{Li}$ . Thanks to their extended lifespan, LFP-based batteries continue to be used and remain a viable choice for long-term applications.

In 1990, *Dahn et al.* first proposed the lamellar oxide  $\text{LiNiO}_2$  (LNO) with a capacity of  $220 \text{ mAh.g}^{-1}$  at 4.2 V vs  $\text{Li}^+/\text{Li}$  [33], but similarly to LCO, the LNO structure becomes unstable at high voltage. As a result, practical applications restrain voltage to 4.1 V vs  $\text{Li}^+/\text{Li}$ , corresponding to 70% of lithium extraction and reversible capacity of  $190 \text{ mAh.g}^{-1}$ . By substituting Ni with Al and Co, new LNO variants were developed, achieving safer battery compared to pure LNO. This resulted in the creation of  $\text{LiNi}_x\text{Co}_y\text{Al}_z\text{O}_2$  (NCA) with  $x + y + z = 1$ ,  $0 < x, y, z < 1$ , which is extensively employed nowadays in electric and hybrid vehicles [34]–[36]. Another significant LNO variant arrived in 2003, when *Ohzuku et al.* synthesized stoichiometric  $\text{LiNi}_{1/3}\text{Mn}_{1/3}\text{Co}_{1/3}\text{O}_2$  (NMC333), phase by substituting Ni with Co and Mn [37]. NMC333 phases provide reversible capacity of  $150 \text{ mAh.g}^{-1}$  at 4.2 V vs  $\text{Li}^+/\text{Li}$ , but the increase of Ni content in phases ensures higher discharge capacities. As a result, NMC materials,

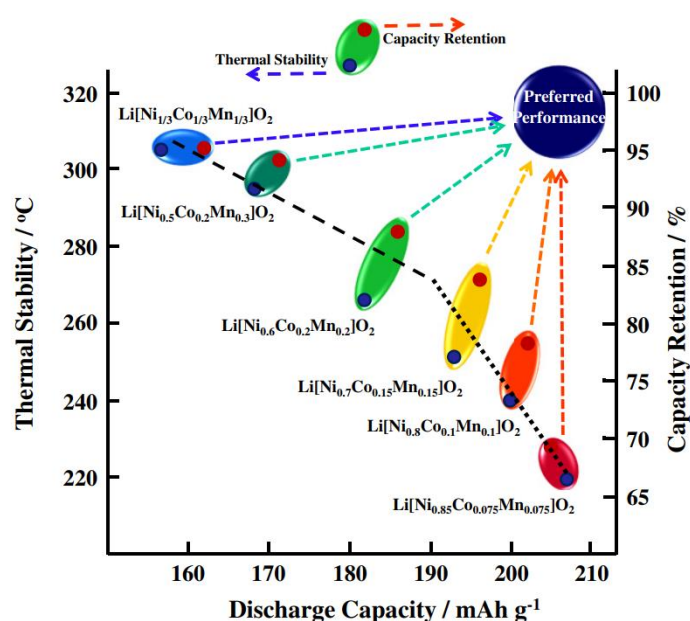


**Figure 7 – Stability of NMC compounds**

*Map of thermal stability, discharge capacity and capacity retention for NMC materials at different nickel content. Extracted from [38].*

general composition  $\text{LiNi}_x\text{Mn}_y\text{Co}_z\text{O}_2$ ,  $x + y + z = 1$ ,  $0 < x, y, z < 1$ , progressively shifted in the last decade from NMC 333 to NMC 532, NMC 622 and finally NMC 811, achieving a reversible capacity of  $200 \text{ mAh.g}^{-1}$  at 4.2 V [38] (Figure 7). Similarly, the current Ni content in NCA is approximately  $x = 0.8$ , providing specific capacity of  $200 \text{ mAh.g}^{-1}$  at 4.2 V vs  $\text{Li}^+/\text{Li}$ .

## I.4. DESIGN OF POSITIVE ELECTRODE MATERIALS

### I.4.1. Ni-rich materials: a solution to higher energy

Enhancing the energy density, and thus the autonomy of LIBs, requires improving two factors: first improving the material's capacity and second, increasing the operating voltage (Equation 7). Over the past decade, the increase of nickel content in lamellar oxides has gained popularity as material fulfills both conditions, ensuring high capacity ( $> 200 \text{ mAh.g}^{-1}$ ) at elevated operating voltage ( $> 4.2 \text{ V}$ ) [32]. Beside energy density, Ni-rich materials reduce the dependence to costly and scarce cobalt mineral, which estimated stocks cannot sustain the forecasted mineral demand for EVs [10]. In addition, cobalt mining is disrupted by poor labor conditions that exposes the supply chain to upcoming scandals. Altogether, these stakes push for the development of Ni-rich phases ( $x \geq 0.8$ ) and last decade has seen growing interest for NMC811, while LNO regains some attention. Ni-rich layered compounds are expected to be the primary materials for positive electrodes in the years to come [8], though it is possible to debate that assertion, considering that graphite/NMC532 technology is still being envisioned to achieve an ultra-long lifespan of 1 million miles in 2019 [39]. Actually, these technologies complement each other, serving distinct market segments: the energy and long-life applications.

To extract the maximal amount of lithium from Ni-rich phases and thus benefits the highest energy, operating voltages above 4.2 V are required. For instance, LNO exhibits a considerable interest in reaching the final capacity plateau at 4.2 V vs  $\text{Li}^+/\text{Li}$ , which provides an additional  $40 \text{ mAh.g}^{-1}$  (Figure 8a). Similarly, at 4.3 V versus  $\text{Li}^+/\text{Li}$ , all recoverable  $\text{Li}^+$  is obtained, and no additional capacity can be achieved. (Figure 8b). Nevertheless, cycling above 4.2 V has a clear negative impact on cell lifespan and increases the risk of premature cell failure, as shown in Figure 8c for graphite/LNO cells, which degradations increase as the operating voltage increases. Similarly, graphite/NMC811 cells age faster above 4.2 V. It should be emphasized that the gain in discharge capacity for graphite / NMC811 cells at 4.3 V compared to 4.2 V is temporary and lasts for only 40 cycles before experiencing a sudden decrease (Figure 8d). As a result, the current dilemma is either to lower the upper voltage limit, which challenges the benefits of Ni-rich materials, or to stabilize the Ni-rich materials. Many studies thus focused on the stabilization of LNO and NMC811 materials and it is worth noting that no more capacity is obtained above 4.5 V, which limits the challenge of stabilization in range 4.2 – 4.5 V.

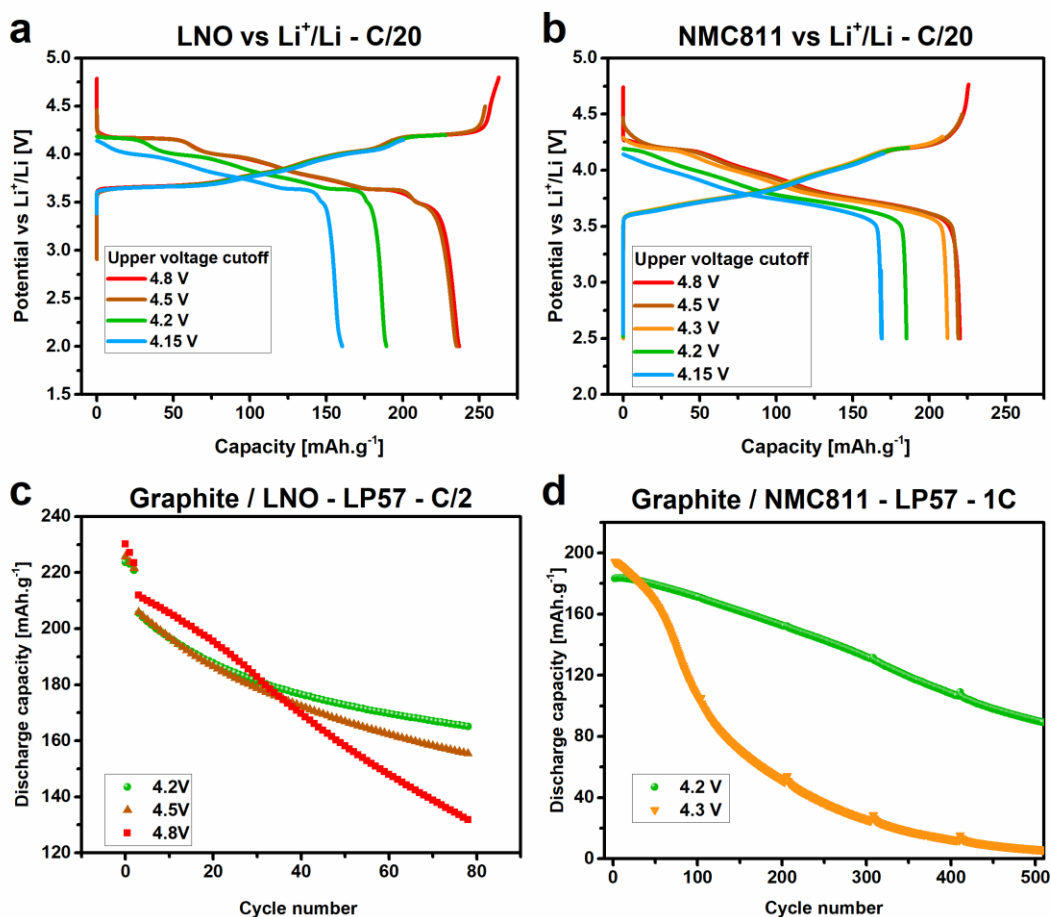


**Figure 8 – Performance of LiNiO<sub>2</sub> and NMC811 materials**

*Electrochemical curves of LNO a) and NMC811 vs Li<sup>+</sup>/Li b) that shows the capacity gain when cycling material above 4.2 V vs Li<sup>+</sup>/Li. However, beyond this voltage threshold, discharge capacities for both LNO c) and NMC811 d) materials rapidly fade, which highlights the need for the development of stabilizing solutions.*

#### **I.4.2. Consequences of high voltages on Ni-rich materials**

Layered Ni-rich oxides are considered as a viable solution for energy dense positive electrodes. However, these materials may experience significant performance degradation, especially under stressful operating conditions such as high temperature and voltage above 4.2 V vs Li<sup>+</sup>/Li. To gain a deeper comprehension of the degradations of layered oxides, it is first important to have a clear understanding of their structure. Lithiated layered oxides exhibit a structure of O3 type (R-3*m* space group), with a stacking pattern of AB CA BC, where the layers alternate between lithium cations and transition metals (TM) atoms (Figure 9a). The letter "O" refers to the octahedral coordination of lithium, while the number "3" is associated to the number of TMO<sub>2</sub> slabs necessary to describe the unit cell [40]. Upon charge, some layered compounds can undergo phase transition to O1 structure (P-3*m*1 space group), which is characterized by the AB AB stacked oxygen layers and one TMO<sub>2</sub> slab per unit cell (Figure

9b). In the coordinate system, slabs are oriented in the  $ab$  plane while the  $c$  axis is perpendicular to the layers. However as most of the phase transitions in layered compounds occur within the O3 type structure, it becomes necessary to use an alternative nomenclature to describe them. This alternative notation involves naming the structures based on a hexagonal and monoclinic structures denoted by “H” and “M”, respectively [41]. Consequently, the initial structures of pristine LNO, NMC, and NCA are designated as "H1". Following delithiation, stage observed in the hexagonal structure is referred to as "M", then “H2”. Upon charge, LNO shows H1  $\rightarrow$  M  $\rightarrow$  H2  $\rightarrow$  H3 phases, while all phase remains in O3 stacking sequence (Figure 9c). It is worth noting that H3  $\rightarrow$  H4 (corresponding to O3  $\rightarrow$  O1 ) phase transition can occur for LNO at 4.45 V vs Li<sup>+</sup>/Li at very low current after potentiostatic hold for hundreds of hours [42]. For NMC811, while the electrochemical curve has some similarities with LNO and shows H1  $\rightarrow$  M  $\rightarrow$  H2 transitions, there are no observable H2  $\rightarrow$  H3 transition in the material [40]. Therefore, it is misleading to use electrochemical curves as direct evidence for the presence of phase transformations. Despite different crystallographic behaviors, Ni-rich materials exhibit comparable degradations to LNO, which occur at similar delithiation state of 70% or 4.2 V vs Li<sup>+</sup>/Li. The following sections provide an overview of these structural degradations.

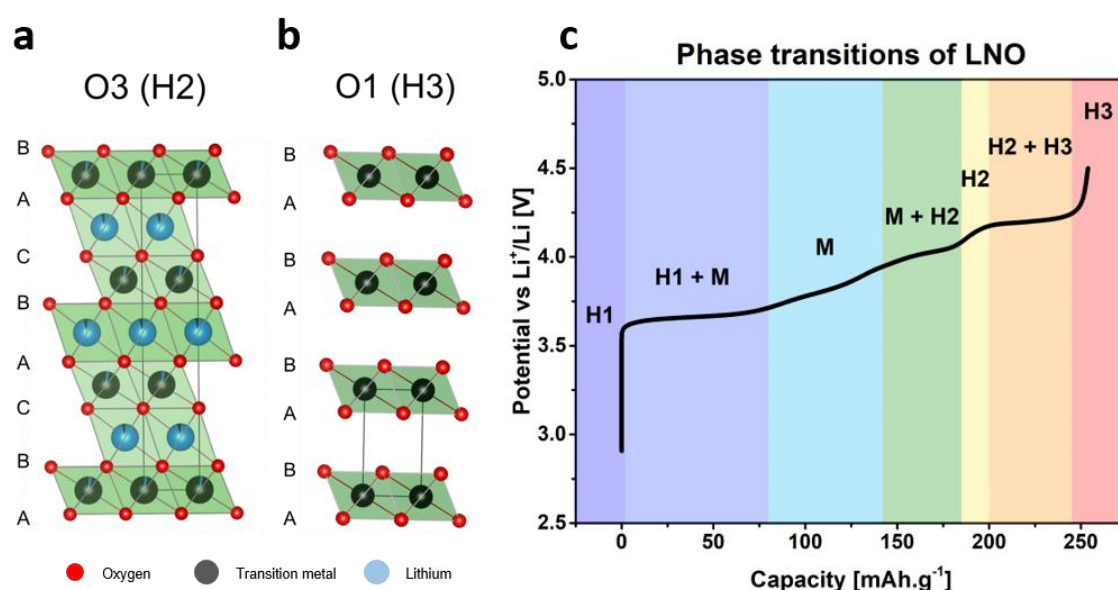


**Figure 9 – Phase transitions of LiNiO<sub>2</sub>**

*Schematic of crystal structures of Ni-rich layered materials. Structures of O3 a) and O1 b) phases are viewed parallel to the layer direction to highlight the stacking regimes. The oxygen planes are labelled to indicate stacking sequences. The LNO materials exhibit various phase transitions c), among which the H2  $\rightarrow$  H3 transition is identified as harmful.*

#### **I.4.2.a. Anisotropic deformation of the lattice**

For LNO, the onset of degradation corresponds to H2 → H3 transition for which a massive drop of distance between TMO<sub>2</sub> slabs is observed, causing the decrease of c-parameter [43]. Although no phase transition is observed for Ni-rich NMC, similar shrinkage of cell unit is observed at delithiation state above 70% corresponding to ~4.2 V. With repeated charges and discharges, the significant variation of the c-parameter can create substantial strains within the lattice, which may result in cracking both within and between the particles [44]–[46]. At the lattice level, strains cause bulk fatigue and buildup of stacking faults that hampers lithium diffusion in the material [43]. At the particle or agglomerate level, successive changes of material's volume by 5-10% leads to inter-granular cracking and electronic disconnection between particles, both becoming more pronounced with increasing Ni content [47], [48].

#### **I.4.2.b. Structural reconstruction**

Ni-rich materials experience structural reconstruction from layered to denser structure when exposed to electrolyte. The formed structures are spinel or rock-salt phases and hinder the lithium diffusion as well as electron transport in the structure. As a result, these inactive phases cause a direct loss of active material in addition to increasing cell impedance [41]. The increase of polarization observed in Ni-rich cells, and the subsequent capacity loss plateau at approximately 4.2 V on capacity curves in Figure 10, can be attributed in part to structural reconstruction and particle cracking. Furthermore, the grinding of particle heightens the phenomena, creating new surfaces that, once exposed to the electrolyte, experience structural reconstruction and deplete the electrolyte. *Dahn* and colleagues propose that the primary cause of degradation could be the high reactivity of particle surfaces, rather than structural alterations [49]. It is worth noting that the structural reconstruction of layered to rock-salt or spinel at the surface necessitates the loss of oxygen from the lattice [41], [50], the extent of oxygen release increases with the Ni content in NMC phases and material SOC [38].

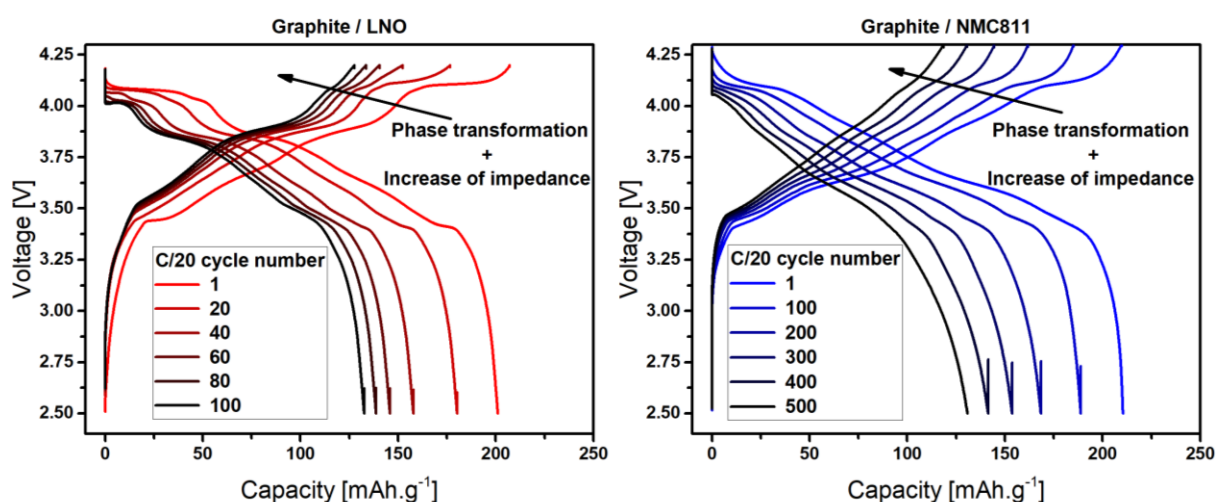


**Figure 10 – Degradation of Ni-rich compounds at high voltage**

*Degradations of NMC and LNO at high voltage include structural deformation and phase reconstruction, both of which lead to an increase in polarization.*

Besides phase reconstruction, materials can show some defects where TM and lithium cations exchange between octahedral sites leading to Ni<sup>2+</sup> in the Li layers for LNO, as well as NCA and NMC analogous. The similarity in radius between Li<sup>+</sup> (0.76 Å) and Ni<sup>2+</sup> (0.69 Å) is responsible for this TM/Li mixing, in part due to synthesis conditions. The quantity of defects in LNO and derivatives has a significant effect on various properties, such as electrochemical performance, electronic and magnetic characteristics, as well as phase behaviors.

### I.4.3. Stabilization of bulk materials

To counteract surface reconstruction and bulk degradations, strategies involving doping or surface coating were pursued.

#### I.4.3.a. Doping

One of the most commonly employed techniques for developing improved layered materials involves the substitution of an element within the bulk material structure with another one [51]. Cation substitution in Ni-rich layered oxides has vastly contributed to improve their performance and their structural stability [51], [52]. Indeed, the substitution of TM by extrinsic element was shown to reduce TM migration to Li<sup>+</sup> interlayers and strengthen bonds between oxygen that mitigates oxygen release. For instance, the substitution by Mn can help stabilize the transition-metal oxide framework, as Mn valency remains unchanged during charge and discharge. Furthermore, dopants can prevent surface reconstruction to spinel or rock salt phases, maintaining suitable lithium diffusion in interlayers upon cycling. Various elements

have been successfully incorporated, such as Aluminum [53], [54], Magnesium [55], Tin [56], Iron [57], [58], Titanium [59], Zirconium [52] or Niobium [51]. Concentrations of these elements remain below 5% to benefit from positive effects of dopants while maintaining high capacity of Ni-rich phase.

#### **I.4.3.b. Core-shell structure**

The design of core-shell structure is an auspicious solution to design high-energy particles: for instance, particles with a Ni-depleted shell encapsulating a Ni-rich core were developed to protect surface from electrochemical degradations while maintaining high energy density [60]. In 2005, *Amine* and colleagues achieved a significant advancement by creating a core-shell structure that integrated the high-energy NMC811 with the favorable thermal stability of  $\text{Li}[\text{Ni}_{0.5}\text{Mn}_{0.5}]\text{O}_2$  [61], [62]. To date, progress continued and *Dahn et al*, recently proposed a Ni-rich core material with Mn-rich shell, demonstrating a capacity of  $220 \text{ mAh.g}^{-1}$  while being suitable regarding safety standards of automotive industry [63]. However, due to lattice mismatch and volume changes between the core and the shell, the structure delaminates upon cycling to form voids that precipitate capacity drop. To reduce the structural mismatch between the core and the shell structure, Ni content is reduced from center to the surface while the relative content of Co or Mn increase gradually. The method, referred to as gradient strategy, maintains protection not only at the outer part of the particle but gradually to the center [64], [65].

#### **I.4.3.c. Material coating**

Surface coating of particles proves to be efficient in protecting Ni-rich compounds, in particular at highly delithiated state. Surface coatings act as physical barrier between the active material and the electrolyte, suppressing side reactions and preventing surface reconstruction to spinel or rock-salt phases. In addition, coatings can act as HF scavengers, with  $\text{TiO}_2$  coatings being more energetically favorable for HF reaction than Ni-rich compounds, effectively preventing the dissolution of transition metals [66]. Wide variety of coatings, including  $\text{ZrO}_2$  [67],  $\text{Al}_2\text{O}_3$  [52], [68],  $\text{SiO}_2$  [69] or  $\text{TiO}_2$  [70], show high stability but lower  $\text{Li}^+$  conductivity, highlighting the need for optimizing the coating thickness and homogeneity to achieve the best performance. Moreover, inorganic coatings have a poor adhesion to active material, causing premature coating delamination upon aging.

## I.5. THE CHALLENGES OF NI-RICH ELECTRODE/ELECTROLYTE INTERFACE

### I.5.1. Degradations at electrode surface

#### I.5.1.a. Electrolyte oxidation

In high voltage applications, the carbonate solvents present in LP electrolytes experience parasitic oxidation, with cyclic carbonates such as EC being the first to oxidize ( $\sim 4.2$  V vs  $\text{Li}^+/\text{Li}$ ) followed by linear ones like DMC ( $\sim 4.5$  V vs  $\text{Li}^+/\text{Li}$ ) [71]. This indicates that all solvents are vulnerable to parasitic oxidation. These oxidation events negatively affect the performance and longevity of the battery. First, oxidation of conventional carbonate solvents forms  $\text{O}_2$ ,  $\text{CO}_2$ ,  $\text{H}_2$ ,  $\text{CO}$  or  $\text{C}_2\text{H}_4$  gases [72], [73], [74], where large amounts can swell the cell casing up to its rupture, or trigger internal safety switch. Second, released gases can further react at electrode surface, consuming electrolyte molecules or species composing the SEI/CEI, both effects being associated with a loss of lithium [75]. At last, oxidation products can deposit on positive electrode surface, forming a resistive CEI that reduces interfacial kinetic and increases overall cell impedance.

Recent results have shown two possible routes for electrolyte oxidation, either chemical or electrochemical. Between these two mechanisms, evidences exist that the chemical route is triggered from a certain threshold voltage, while the oxidation current associated with the electrochemical reaction follows the applied potential, in agreement with Butler-Volmer equation [76]. The chemical oxidation is triggered from the release of gaseous oxygen upon surface reconstruction of the positive electrode material that reacts with carbonate solvent [77]–[79]. Following this mechanism, the oxygen evolution is attributed to the oxidation of the lattice oxygen including several active oxygen intermediates such as peroxides, radicals and oxygen singlets [38], [76]. The chemical oxidation is thus intrinsically linked to the degradation of positive electrode material, which onset potential decreases with higher Ni content, for example, at  $\sim 4.6$  V vs  $\text{Li}^+/\text{Li}$  for NMC111 but as low as  $\sim 4.2$  V vs.  $\text{Li}^+/\text{Li}$  for NMC811 [72], [77]. Upon electrochemical reaction, oxidation is a faradaic process, i.e. electrons are exchanged between the electrode and solvent molecules. Although oxidation current contributes overall less to anodic decomposition of the electrolyte, the onset of electrochemical reactions occurs before 4.2 V, thus before chemical oxidation [71].

In summary, electrolyte oxidation is at the origin of a multitude of degradations, the consequences of which affect both electrodes. Involved mechanisms and associated onset of oxidation potential heavily depend on the reactivity of the surface materials.

### **I.5.1.b. Transition metal dissolution**

Increasing the nickel content of NMC phases destabilizes the material structure, leading to more severe dissolution of TMs. *Thackarey* and *Tarascon's* group conducted the first studies on the effects of TM dissolution on LMO spinel [80]. It was observed that at high temperatures [81] and operating voltages [82], Mn dissolution is significantly enhanced. The Hunter disproportion mechanisms explain this phenomenon by forming more soluble  $Mn^{2+}$  from  $Mn^{4+}$  [83]. Furthermore, positive electrodes are chemically etched, releasing TM ions, a phenomenon accelerated in the presence of water traces. Indeed, water reacts with  $LiPF_6$  salt, forming hydrofluoric acid HF. Additional etching agents can participate to TM dissolution, such as ketones or acetates [84], [85], both formed by electrolyte decomposition. More recently, the degradation pathways of NMC, such as  $O_2$  release, was found to create favorable conditions for subsequent TM dissolution. Oxygen loss indeed leads to surface reconstruction and oxygen vacancy formation, forcing TM migration from bulk to surface sites and interlayers that destabilizes the structure and favor subsequent dissolution [86].

### **I.5.1.c. Crosstalking phenomena**

Considering the various degradation phenomena mentioned earlier, certain species may be liberated into the electrolyte following the effects of working voltage and temperature. Once these species are released, they can interfere with the operation of the other electrode through a mechanism known as crosstalking phenomena. In particular, Ni-rich electrodes are prone to trigger crosstalking damages at the negative electrode, of which most prominent example is the transition metal migration. Upon TM dissolution, TMs are solvated and migrate through the electrolyte to the negative electrode where they can incorporate into the SEI as ions [86]–[88] or reduce at electrode surface [89]–[91]. *Tornheim et al.* and *Wang et al.* showed that TMs are more preferably solvated by EC, TFSI<sup>-</sup> or  $PF_6^-$ ; these interactions make chemical decomposition and activation for electrochemical reduction at the anode energetically more favorable [92]–[94]. Although there is no clear consensus on the involved mechanisms, reactions at the interface are associated to  $Li^+$  losses that reduce battery lifespan. *Delacourt* and colleagues proposed that TMs in the SEI decrease passivation properties of the SEI, hence favoring electrolyte reduction and further  $Li^+$  losses [88]. *Joshi et al.* described that TMs in the SEI lead to decomposition of LEDC, following mechanisms shown in Figure 11a, revealing fresh graphite surface and triggering more electrolyte reduction [94]. *Leung* proposed that TMs serve as electrocatalytic centers, where complexed carbonate anions are reduced to alkoxides and then to carbon dioxide radicals ( $CO_2^{\cdot-}$ ). As the alkoxides are continuously replaced by new carbonate species, a turnover of species occurs, which is responsible for initiating the catalytic loop [92], [93]. *Gasteiger's* group further confirmed the electrocatalytic mechanism while linking it reaction to gassing events [95]. On the other hand, *Klein et al.*

showed that reduced TMs at electrode surface lead to highly electronic conductive spots that trigger lithium plating (Figure 11b) and can ultimately lead to dendrite formation and short-circuit [96], [97].

To summarize, the presence of TMs in the SEI can lead to various side reactions that can be classified into SEI growth and lithium plating. However, both of these reactions result in the loss of lithium and decomposition of the electrolyte, making it challenging to distinguish between SEI growth and Li plating without conducting post-mortem analyses. Furthermore, highlighting the plating phenomenon through post mortem analyses can be tedious since the presence of metallic lithium can be hidden as lithium can re-intercalate into graphite during relaxation time [98]–[100]. Therefore, *Waldmann et al.* proposed experimental strategy that consists in determining activation energies of Li plating and SEI growth reactions [101]. For that, degradation rates of cells are plotted as the reciprocal of the working temperature, i.e. Arrhenius plot in Figure 11c, and two regimes are obtained with different activation energies. A first regime at high temperature with a positive activation energy is associated to the SEI growth, while the second one with a negative activation energy is associated to lithium plating. As a result, the two degradation regimes can be distinguished to determine prevailing degradation mechanisms as a function of temperature [102].

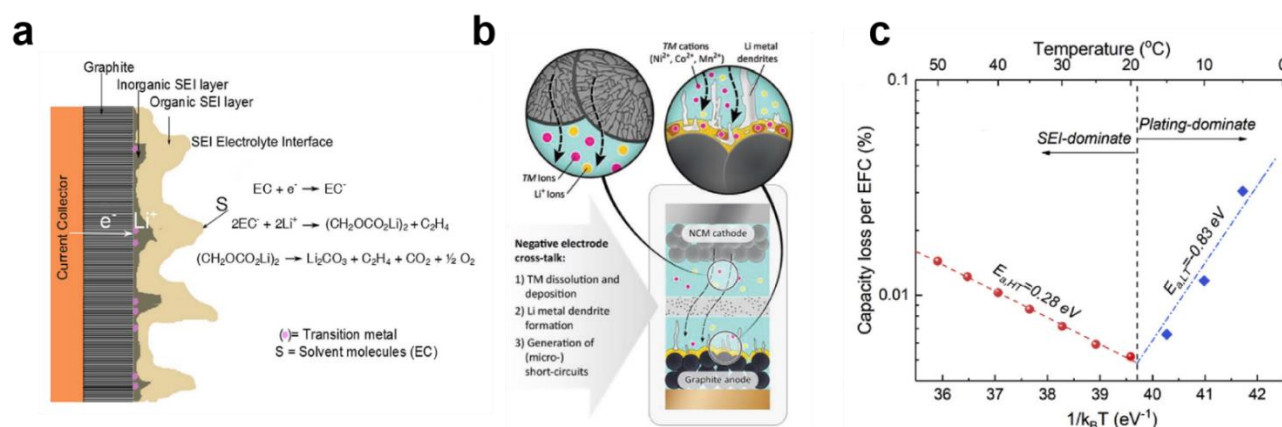


**Figure 11 – Competition between Li plating and SEI growth depending on temperature**

*Proposed mechanism of LEDC decomposition through TM [94] a). TM at the negative electrode favoring lithium plating and the growth of dendrites b) [96]. Arrhenius plot of degradation rates allowing to distinguish between two regimes: SEI growth and lithium plating c) [221].*

In addition to transition metals, there are additional chemical crosstalks at play in degradation. The aging of Ni-rich materials and the electro-oxidation of surface impurities form highly reactive species as radicals or superoxide, which further react with the electrolyte [75]. Similarly, electrolyte oxidation can also form highly reactive CO<sub>2</sub><sup>-•</sup> radicals, damaging solvent molecules. Furthermore, parasitic oxidation at the positive electrode leads to the formation of

high molecular weight molecules that can deposit on negative electrode surface and cause kinetic limitation, and even become ion blocking [103], [104].

In summary, crosstalking phenomena are responsible for the complex degradations, which can be challenging to evaluate. The studies mentioned earlier demonstrate that the positive and negative interfaces cannot be studied separately and more attention should be paid to the interactions pushing for the development of adapted analysis methods.

## **I.5.2. Solutions based on additives**

### **I.5.2.a. Additives for the CEI**

The use of additives is an efficient and cost-effective method to stabilize the interface of positive electrodes for high voltage operations. Additives can be sacrificial, i.e. additives that are electrochemically decomposed at the positive electrode to participate to the CEI formation, or added for their higher stability or used as scavengers.

First, various sacrificial additives have been tested, including unsaturated carbonate [105], fluorine- [106], boron- [105], silicon- [107] or phosphorous- [108] containing species. Among them, boron-based additives like tris(trimethylsilyl)borate, trimethylborate or triethylborate showed very efficient in stabilizing positive interface [109], [110]. Indeed, boron is an electron deficient element, which coordinates salt anions and lower their oxidation potential in the electrolyte. Therefore, and contrary to general wisdom, salts also participate to the formation of stable CEI through decomposition of counter anion, forming a salt-derived CEI, which is more robust and passivating thanks to B – F species. As a result, borates have efficiently stabilize nickel rich interfaces as NMC811 to 4.5 V [111].

Since borate counter anions contribute to the formation of robust CEI, borate lithium salts have been further studied, including lithium bis(oxalato)borate (LiBOB) and lithium difluoro(oxalato)borate (LiDFOB). Although decomposition mechanism needs further investigation, additives ensure stable cycling up to 5 V for NCA [112], NMC811 [113] or Li-rich positive electrodes [114]. LiDFOB efficiently stabilizes LiNiO<sub>2</sub> to 4.4 V with capacity retention of >80% after 400 cycles [115], compared to less than 100 cycles in carbonate-based electrolytes. Improved performance is associated to the CEI, which is composed of Li<sub>x</sub>BO<sub>y</sub>F<sub>z</sub> and fluorine-derived species that effectively suppress further reaction with the electrolyte at particle surface. Furthermore, combining different salts offers synergetic effects that are often beneficial for cell performance at high voltage, for instance LiTFSI – LiBOB [116] or LiBOB – LiBF<sub>4</sub> [117]. In addition to forming better CEI, LiDFOB proved to be an inhibitor of Aluminum corrosion, forming Al – F, B – O, B – F species and Al<sub>2</sub>O<sub>3</sub> that passivate the current collector surface [118]. Overall, additives enrich the toolbox for stabilizing positive interface and remain an asset for designing high voltage electrolytes.

### **I.5.2.b. Anti-oxidation additives**

The use of conventional carbonate-based electrolytes that oxidize starting at 4.2 V hamper the full exploitation of Ni-rich materials [72]. To postpone the oxidation onset of the electrolyte, fluorinated solvents have been widely envisioned thanks to their superior oxidation stability up to 5.0 V [119]. *Wang et al.* showed an all-fluorinated electrolyte ensuring cycling NMC811 half cells to 4.5 V with 99.3% capacity retention after 1,000 cycles thanks to the formation of a robust and thin CEI (~9 nm) [120]. Although fluorinated solvents have higher oxidation stability, they also reduce at higher potential at the negative electrode, which may limit the practicality of all fluorinated solvent strategies in full cells [121]. Furthermore, a too high degree of solvent-fluorination hampers the solvation of Li<sup>+</sup>, suggesting the need to adjust the fluorination degree of the solvent to strike a balance between stability and solvation capability [122].

Moreover, sulfones exhibit higher oxidation stability to 5.0 V with enhanced reduction stability at the graphite anode, resulting in 81% capacity retention in graphite/NMC622 cells after 400 cycles at 4.5 V [123]. The decomposition of sulfones leads to sulfur-rich CEI composed of polymerized species. Similarly, nitriles demonstrated high stability versus oxidation, among which the most prominent example is succinonitrile forming N-derived thin CEI [124].

### **I.5.2.c. Scavenging additives for high voltages**

Besides interfacial stabilization, additives can scavenge reactive species resulting from the decomposition of the electrolyte or electrodes and suppress subsequent side reactions, including TMs dissolution. Among the chelating agents, pyridine and phosphates show efficient in counteracting the negative impact of TMs at the negative electrode [96]. However, chelating agents can be electrochemically decomposed at the electrodes, which reduces the lifetime of the additives. Therefore, the development of stable chelating agents is essential. Bulky phenyl agents like 1,2-bis(diphenylphosphino)ethane (DPPE) demonstrated high chelating properties thanks to bidentate phosphine moieties, while remaining stable at electrode interfaces [125]. Finally, when chemistry of the separator is optimized, chelating structures using carbonates [126] or pyridine functions [127] can be directly anchored to polymer network.

Instead of dealing with the consequences, additives can also address the causes of TM dissolution. First strategy is to remove water impurities, as the water breaks down PF<sub>6</sub><sup>-</sup> anions, producing HF, a powerful etching agent for the positive electrode. In that regard, Lewis bases such as tris(trimethylsilyl)phosphite (TMSPi) showed efficient since P atom has high binding affinity with water [128]. Furthermore, additives containing Si – N or Si – O bonds can react with water, HF or radicals O<sub>2</sub><sup>-</sup> from oxygen release of positive electrodes [129].

### I.5.3. Solution based on electrolyte design

#### I.5.3.a. Highly concentrated electrolyte

##### *Success story of HCE*

Although additives show efficient in extending the battery lifespan, they often cannot fully prevent degradations of solvents and salts. As a result, for high voltage applications, it can be more advantageous to use stable electrolytes directly, rather than relying on the conventional approach based on additives in carbonate electrolytes. Many efforts have been carried out on polymers, ionic liquids and solid electrolytes but intrinsic issues hamper their widespread adoption [130]. Revisiting organic electrolytes thus remains the more realistic solution at short term for superior battery performance. In that regard, highly concentrated electrolytes (HCE) received particular attention in the last decades as they offer interesting properties. First success dates from 1985, where *Mc Kinnon et al.* and *Dahn et al.* demonstrated that saturating  $\text{LiAsF}_6$  in PC successfully suppresses co-intercalation of PC into  $\text{ZrS}_2$  positive material [131]. However, the poor ionic conductivity and high viscosity of HCE hampered high battery rate performance [132] and HCE have been left aside for this reason. Inspired from the pioneering work from late 80's, *Ogumi et al.* reignited the interest of HCE in 2000's showing that high salt concentration mitigates inherent issue of PC intercalation into graphite [133], [134]. At the same time, new salts such as lithium bis(fluorosulfonyl)imide (LiFSI) and lithium bis(trifluoromethanesulfonyl)imide<sup>1</sup> (LiTFSI) were introduced and demonstrated high intercalation kinetic associated to high solubility, which is adapted for HCE design [135]. As a result, imide-based HCE finally achieved high rate performance in addition to high quality of Li plating/stripping in half cells [136]. This reversibility of lithium plating was further confirmed by *Suo et al.* [137] and *Qian et al.* [138], where lithium surfaces exhibited round shaped-edge nodules at the origin of a smooth plating. Finally, the SEI derived from HCE proved to be passivating, dense and inorganic while having high ionic conductivity. Although HCE were first studied for their high reversibility of Li plating/stripping and SEI quality, HCE also show promise for stabilizing high voltage positive electrodes for three reasons. First, HCE inhibit the dissolution of aluminum current collectors above 4.2 V. *Matsumoto et al.* first demonstrated that 1.8 M LiTFSI in EC/DEC efficiently suppresses aluminum corrosion and rationalized the observations with the formation of insoluble LiF at aluminum surface [139]. *McOwen et al.*, *Zheng et al.* and *Yamada et al.* later proposed an additional mechanism, where the solvation of  $\text{Al}^{3+}$  by solvent molecules is energetically less favored in HCE than in 1 M regime, as shown in Figure 12a [140]–[142]. Second, HCEs significantly reduce the dissolution

---

<sup>1</sup> Can be written bis(fluorosulfonyl)amide LiFSA and bis(trifluoromethanesulfonyl)amide LiTFSa, since an imide is a secondary amide.

of TM from the positive electrode that extends the stability windows of materials. Most prominent example is the use of LiFSI 5M in DMC to cycle vanadium halogenates, which was impossible in conventional carbonate based electrolytes due to vanadium dissolution [143]. Similarly, in LIB, graphite electrodes cycled with  $\text{LiMn}_{1.5}\text{Ni}_{0.5}\text{O}_4$  at 4.7 V show no TM at the surface with energy dispersive X-ray spectroscopy (EDS) when HCE was used (Figure 12b). Results suggest that crosstalking phenomena and associated side effects are mitigated, explaining the diminished capacity fading [144]. Quantification of TM amounts at the negative electrode by inductive coupled plasma mass spectroscopy (ICP-MS) further confirmed the decrease of TM solubility [145]. Finally, the use of LiFSI or LiTFSI, chemically more stable salts than  $\text{LiPF}_6$ , circumvents the formation of HF and subsequent TMs release from positive electrode.

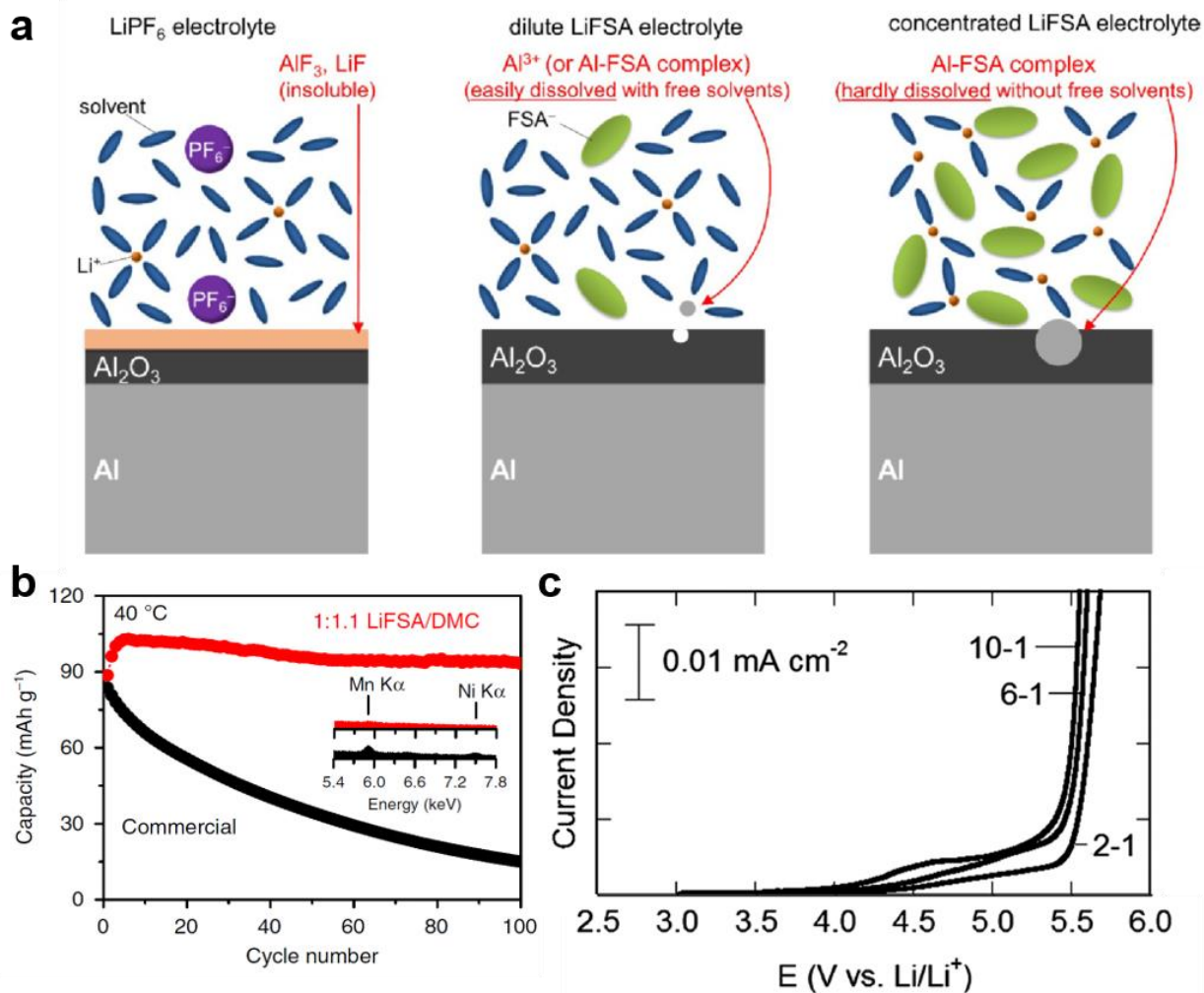


**Figure 12 – Performance and properties of HCE**

a) Schematic of Aluminum corrosion using from left to right: dilute LiPF<sub>6</sub> based electrolyte, dilute LiFSI based electrolyte and HCE. HCE inhibits the dissolution of aluminum current collector [140]. b) Performance at 4.7 V of graphite/ LiMn<sub>1.5</sub>Ni<sub>0.5</sub>O<sub>4</sub> cells 1.0M LiPF<sub>6</sub>/ EC:DMC 1:1 by vol. (black) and 5.5M LiFSI in DMC (red). The inset shows EDS spectra of graphite area 200x200 μm<sup>2</sup> after 100 cycles in full cells. c) Cyclic voltammetry between Pt electrode and Ag<sup>+</sup>/Ag reference (25°C, 5.0 mV/s) for EC– LiFSI electrolyte at different mole ratio 10 : 1, 6 : 1 and 2 : 1. EC oxidation is not completely suppressed below 4.5 V vs Li<sup>+</sup>/Li [141].

Third and last reason, HCEs have demonstrated oxidation stability up to 4.5 V vs Li<sup>+</sup>/Li [146], although parasitic oxidation is not completely suppressed as shown with residual oxidation current in Figure 12c [141]. This enhanced stability is ascribed to the thin and inorganic-rich CEI formed from the decomposition of anions [144], [145].

The advantages mentioned earlier are limited by the costs linked to a high salt concentration, hindering broad implementation in real-world scenarios. Furthermore, the elevated salt concentration allows for 3 to 5-times more lithium in the electrolyte, often surpassing the quantity present in positive electrode materials. Consequently, this conceals degradation phenomena in the studies, as discussed in Chapter 5. Lastly, reduced conductivity hampers the ability for rapid charging.

### *Chemical considerations*

Properties of HCE lie in the solvation structure of salt at high concentration regime. In HCE, the number of salt molecules is voluntary too high compared to solvent ones, leading to an imperfect ion solvation [130]. Unlike in dilute 1 M regimes, where the “classical” three-layer solvation sheath is observed (Figure 13a), the number of free solvent is too limited for concentrations above 3 M to solvate all Li<sup>+</sup> ions [144]. As a result, anions participate to the solvation structure (Figure 13b) forming contact ion pairs (one anion solvating one Li<sup>+</sup>) or aggregates (one anion solvating two Li<sup>+</sup>) [147] that induce a series of new properties including new interfacial chemistry and thermal, mechanical and (electro)-chemical stability. In HCE, energy levels of electrolyte components are modified for both the lowest unoccupied molecular orbital (LUMO) and highest occupied molecular orbital (HOMO). In HCE, the LUMO of the solvent, i.e. the orbital that is thermodynamically the most likely to receive electrons and thus reduce upon charge, is lowered relative to the anions, resulting in the reduction of anions and the formation of an anion-based passivation layer. Similarly, the HOMO of solvent, i.e. the orbital that is thermodynamically the most susceptible to lose an electron, is also decreased, leading to enhanced stability against oxidation [130].

### **I.5.3.b. Localized highly concentrated electrolyte**

#### *Chemical considerations*

In recent years, localized high concentration electrolytes (LHCE) showed extensive attention because they demonstrate similar stabilization properties of Ni-rich electrodes than HCE at lower viscosity and price [148]. LHCE consists in diluting HCE with a co-solvent that has a low viscosity, low cost and adequate coordination properties that do not disrupt the imperfect solvation of HCE. Ideally, co-solvent is also non-flammable for safety concerns and is inert in the electrochemical window. *Watanabe et al.* first introduced 1,1,2,2-tetrafluoroethyl-

2,2,3,3-tetrafluoropropylether (TTE) that meets all above-mentioned properties and decreases electrolyte concentration to ~1 M and viscosity down to 3 mPa.s (110 initially) relative to 2.8 mPa.s for LP57 [149]. Furthermore, the low dielectric constant of the fluorinated chains prevents TTE co-solvent from participating to the Li<sup>+</sup> solvation, thus segregating HCE into micro-domains as shown in Figure 13 [150]–[152]. Additional co-solvents such as bis(2,2,2-trifluoroethyl)ether (BTFE) [132], [153], [154] or tris(2,2,2-trifluoroethyl)orthoformate (TFO) [155] have been tested and although the chemistry difference between co-solvent is minor, the electrochemical performances are not equivalent. Recent benchmark showed that TTE-based LHCE has higher performance in full-cells than electrolytes using BTFE [156].

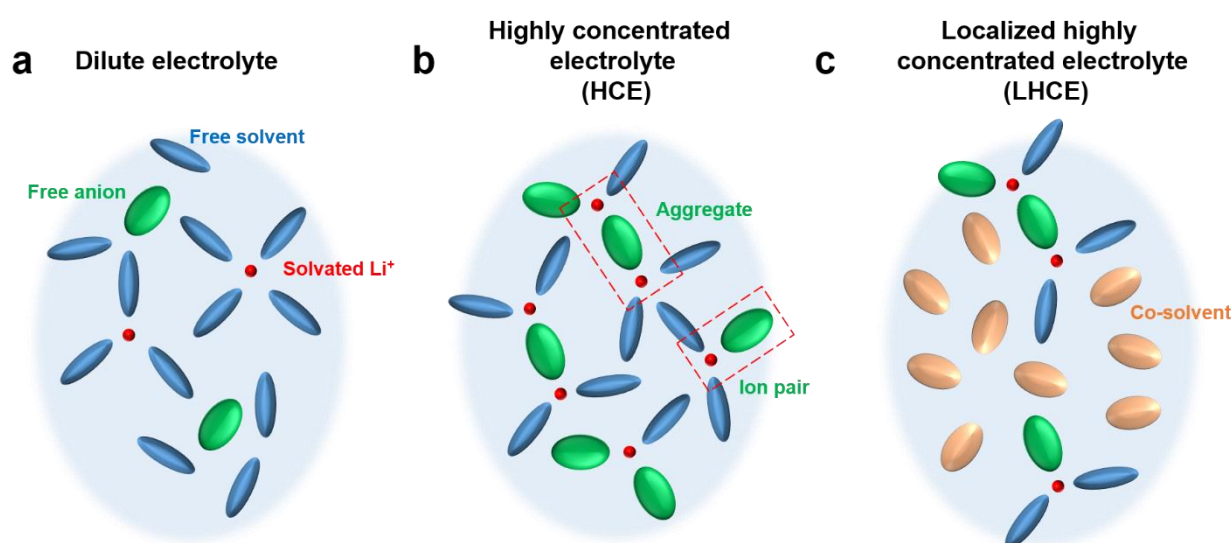


**Figure 13 – Schematic of solvation structures in HCE and LHCE**

*Schematic representation of electrolyte structures: dilute, highly concentrated and locally highly concentration electrolyte.*

### **Performance**

LHCEs have demonstrated high performance versus lithium metal batteries using Ni-rich materials. For instance, *Manthiram* and colleagues showed that Li/LNO cells retain 92% of initial capacity after 200 cycles at 4.4 V vs Li<sup>+</sup>/Li when using TTE-based LHCE, compared to 56% capacity retention in baseline electrolyte (Figure 14a) [157]. Furthermore, LHCEs stabilize NMC811 interface to 4.4 V vs Li<sup>+</sup>/Li with 88% retention after 200 cycles, even when using lean electrolyte conditions, i.e. low electrolyte volume close to that in industrial applications (Figure 14b). The beneficial effect of additives adds to the LHCE, e.g. LiDFOB extends the battery life by more than 50 cycles compared to virgin LHCE [158]. It is also worth noting that LHCEs sometimes achieve longer lifespan than sole HCE, which confirms HCEs are not necessary the ideal solution for stabilizing Ni-rich at high voltage.

Similarly to HCE, few studies confirmed the practicality of LHCE in graphite/Ni-rich cells at high voltages. *Xu et al.* used LiFSI / DMC / EC / TTE electrolyte to stabilize graphite/LiNi<sub>0.96</sub>Mg<sub>0.02</sub>Ti<sub>0.02</sub>O<sub>2</sub> cells and achieve 97.2% capacity retention after 200 cycles at 4.4 V [151]. Graphite/NMC811 cells showed 98.6% capacity retention after 400 cycles at 25°C (Figure 14c) [159], while similar cells tested at 60°C sustain high performance for 100 cycles (Figure 14d). To rationalize the result, XPS measurements of SEI and CEI were conducted and revealed that interphase composition does not change with the elevation of temperature, demonstrating the high quality of formed interphase. As a result, LHCEs suppress continuous electrolyte decompositions and mitigate the dissolution of TM thanks to the formation of more protective SEI/CEI, which in turn, lead to significantly improved cycling stability, event at high temperatures [160].

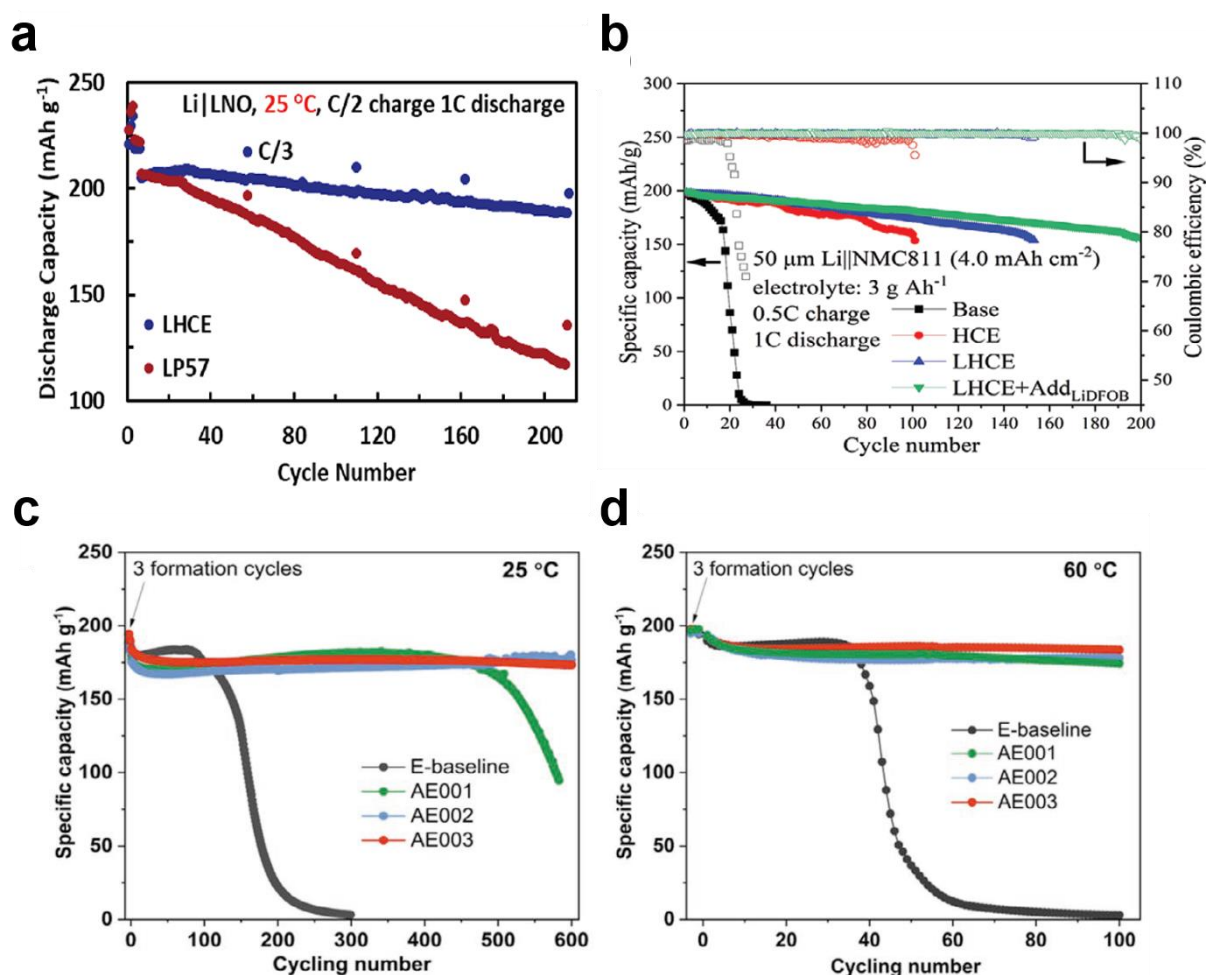


**Figure 14 – Outcomes of LHCE with Ni-rich materials**

*Beneficial effects of LHCE to Ni-rich positive electrode. a) Benchmark between carbonate based LP57 and LHCE in Li/LNO cells at 4.3 V [157]. LHCE = LiFSI-DME-TTE (1:1.2:3 by mole) b) Li/NMC811 cells with controlled amount of electrolyte show higher performance with LHCE + LiDFOB additives. LHCE = LiFSI-FEC-TTE (1:0.1:1.4 by mole) [158] c) Different LHCE graphite/NMC811 full cell at 4.3 V at 25 and 60°C [159]. Baseline = LP57 +2%VC, AE001 = 1.4 M LiFSI in DMC-TTE (2.2:3 by mole), AE002 = 1.4 M LiFSI in DMC-VC-TTE (2:0.2:3 by mole), AE003 = 1.4 M LiFSI in DMC-EC-TTE (2:0.2:3 by mole).*

### I.5.3.c. Remaining challenges of HCE and LHCE

Although HCE and LHCE demonstrated auspicious performance at high voltage, works focusing on lithium metal batteries certainly dominate those reported in the literature. Indeed, the high reversibility of lithium plating/stripping renews promises of CE higher than 99.99% that is of particular interest for battery lifetime [31]. As a result, the number of studies using HCE and LHCE for stabilizing Ni-rich materials, suppressing Al corrosion or enhancing oxidation stability represents only ~20% of works done in the state of the art of 2019 made by *Yamada et al.* [161] (Red highlights in Figure 15). When HCE and LHCE are tested in full cells, aging rarely exceed 200 cycles and cycling conditions are unrealistic for application in commercial formats, i.e. absence of constant voltage step at the end of charge and large excess of electrolyte. More importantly, degradations in HCE or LHCE are less studied than in conventional electrolytes and thus requires additional efforts in understanding interfacial phenomena. This pushes for the use of adapted analysis methods. For instance, *Xu et al.* ascribed an increase of capacity upon cycling number related to an “activation process and [due to] the reversible formation of electrode surface films by the kinetically activated electrolyte degradation” [151]. Adapted electrochemical analysis methods might confirm the statement and clarify the appearance of this bump in capacity retention curve that has already

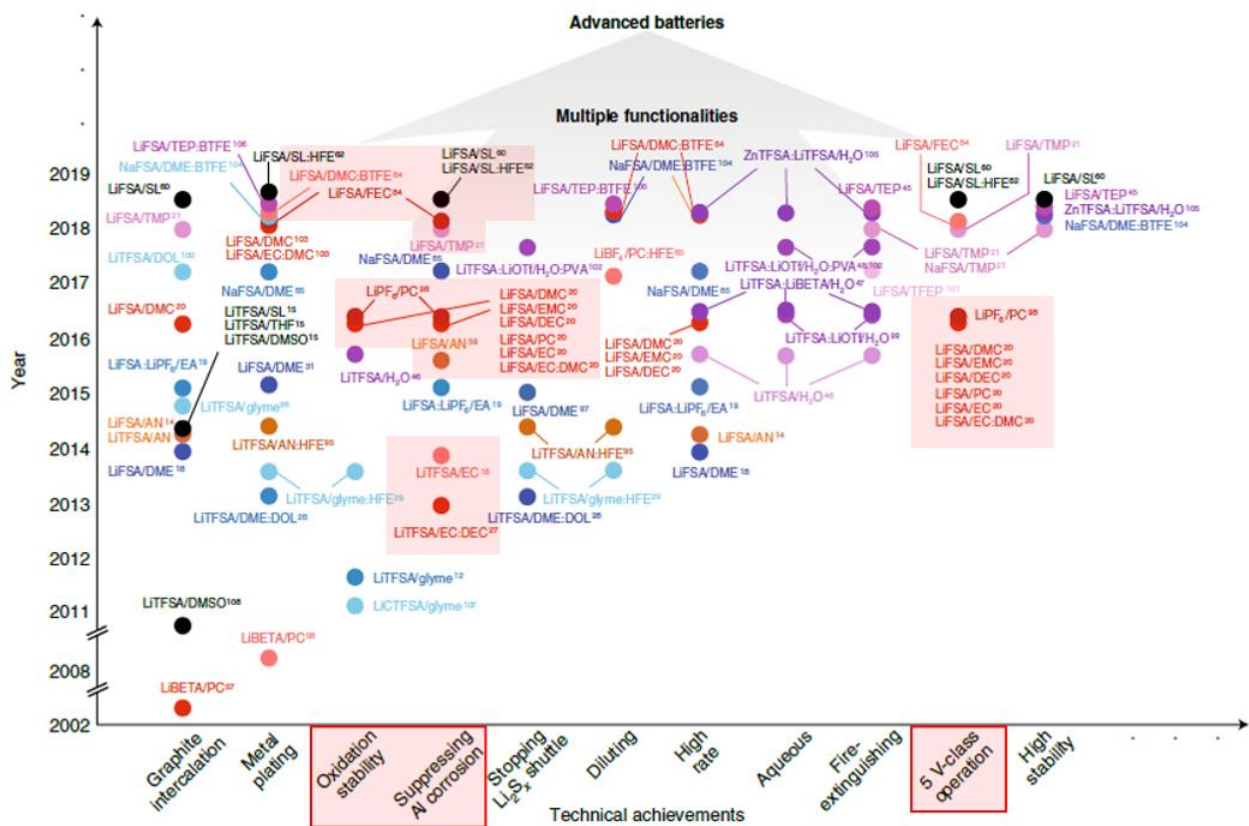


Figure 15 – Overview of tested HCE compositions and outcomes

State of the art dating 2019 of used HCE and LHCE for specific properties. Electrolytes dedicated to high voltage applications are highlighted in red and represent ~20% of total studies in 2019 [161].

been reported for several LHCE studies [162], [163]. At last, very little is known regarding the thermal stability of the HCE/LHCE and battery tests should be actively conducted at high/low temperatures to demonstrate the practicability range. It is worth noting that best battery performance is achieved using LiFSI salt with carbonate solvents such as PC, EC, DEC, EMC or DMC, (and TTE if co-solvent is needed), which provides a strong baseline for future electrolyte designs in this PhD.

In conclusion, HCE/LHCE performance has rarely been tested in full cell configuration that hampers the establishment of strong conclusions regarding the stabilization of graphite/Ni-rich at high voltage. We believe the practical application of these electrolytes in LIBs requires to consider the compatibility with the graphite electrodes through the formation of high quality SEI and the evaluation of crosstalking phenomena. Therefore, one of the objectives of this thesis is to check the full-cell compatibility of HCE and LHCE designs that have been announced as promising versus lithium.

## **I.6. CONTEXT OF THE PH.D.**

### **I.6.1. Study of interfacial degradations at European scale**

In 2020, European Union introduced BATTERY 2030+ road-map to support projects in sustainable batteries development. Among them, BIG-MAP project aims to understand degradations at electrode-electrolyte interfaces that is crucial to ensure long term performance of Ni-rich materials. The project combines experimental data of battery interfaces with machine learning to achieve accurate comprehension of degradations. BIG-MAP is thus a two steps project. Initially, electrochemical data and ex-situ interface characterizations are gathered to develop a "big interface genome" (BIG). Subsequently, the project utilizes automated analysis to uncover crucial aging parameters and establish models for lifetime prediction. The outcomes aim to implement efficient solutions that can enhance the "material acceleration platform" (MAP) in BIG-MAP, thereby increasing general performance. Overall, the implemented strategies might improve the understanding of interfacial degradation and increase the testing rate of mitigating strategies. Furthermore, BIG-MAP goes beyond academic applications and aims to provide results closer to industrial standards. Funded by this project, the PhD work aims at developing accurate electrochemical protocols to test improvements made in stabilizing Ni-rich interfaces while contributing to the development of the BIG-MAP infrastructure.

### **I.6.2. Bottlenecks for studying interfaces in BIG-MAP**

For more than two decades, numerous stabilization strategies have made promising inroads towards higher energy densities and longer lifetimes. Despite the undeniable

performance improvements, the testing approach sometimes uses conditions that hinder the accurate assessment of the overall benefits derived from the applied strategy. First, testing in academic field is subject to high variability in results from one cell to another, associated with different assembly and testing procedures (i). Since testing conditions can significantly modulates the (dis-)appearance and rates of degradations [164], the 34-partners of BIG-MAP shall homogenize testing procedures to avoid misleading interpretations and wrong data models. The second pitfall is to consider one single degradation event as an insulated mechanism, free of interconnection with the rest of the cell (ii). Most of the degradation mechanisms are intertwined, and effects are building up upon aging until triggering premature cell death. Considering consequences of positive electrode degradations as an interconnected ensemble is necessary to gain a general picture of cell behavior and to ensure building an aging model adapted to commercial conditions. At last, degradations are most of the time assessed with conventional metrics such as discharge capacity and CE vs cycle numbers, which, although efficient at predicting aging rates, fall short at capturing the complexity of aging mechanisms (iii). These indicators indeed do not provide information on the nature of degradations and at which electrode they occur, drastically limiting our comprehension of cell degradations and to larger extend limiting the accuracy of aging models in BIG-MAP. Therefore, the project needs adapted analysis workflows, upon which machine learning and AI algorithm can be developed to rationally design solutions for high voltage batteries.

### **I.6.3. Contribution of this Ph.D.**

This Ph.D. work provides adapted analysis workflows to comprehend interfacial degradations associated to high voltage and give the necessary knowledge for judiciously assessing the benefits of novel mitigating solutions. Methods introduced in this work are based on electrochemical analysis that require rigorous testing conditions and particular care during the analysis. Being part of a European project, battery testing must follow homogenized procedures to ensure knowledge transferability and data compatibility between the 34-partners. Evidently, standardization of battery testing will layout the PhD work and give access to high-quality data to further deploy electrochemical analysis. The effort in standardizing and adapting analysis methods has proved effective in achieving an advanced level of understanding of degradation in batteries. After Chapter I, which introduces the broad battery context and justifies the research need, the outline is as follows:

Chapter II introduces key parameters for achieving high reproducibility of battery assembly. Then, the discussion will focus on the necessary actions taken during electrochemical cycling, including the formation step as well as the constant voltage charge step.

Chapter III introduces common degradation types in Li-ion cells and describe the methods to detect them. Analysis methods particularly emphasize the interconnection existing between complex degradation phenomena.

Chapter IV discusses the consequences of TM migration from  $\text{LiNiO}_2$  to the SEI. Two major mechanisms are considered between the catalytic growth of the SEI and lithium plating.

Chapter V demonstrates the instabilities of HCE in graphite/NMC811 cells at 4.3 V, where cell performance is artificially sustained by parasitic oxidation. The performance of LHCE as a promising solution for high-voltage applications is further tested in this chapter.

Lastly, the conclusion will provide a summary of all significant findings and propose ideas for future research endeavors.

# **CHAPITRE II: STANDARDIZATION OF CELL ASSEMBLY AND TESTING**



## **II.1. DRAWING INSPIRATION FROM INSPIRATION FORM INDUSTRY TO ESTABLISH STANDARDS IN ACADEMIA**

### **II.1.1. Outcomes of standardization**

Various research fields have long benefited from the establishment of standards and protocols for testing. Among them, testing of photovoltaic cells are dictated by standard procedures (National Institute of Standards and Technology) both for certifying efficiencies and for reporting data in scientific publications [165]. Notoriously, the field of rechargeable batteries has suffered from a reproducibility crisis, severely amplified by the current lack of standardized protocols for battery research at lab level. This shortcoming is increasingly problematic with the recent growth of overly ambitious short-term goals, doubtful performance and false promises motivated by the vertiginous growth of battery market. In this respect, scientific publishers and researchers have called for more transparency with the introduction of good practices and standard methods for reporting electrochemical data [166], [167]. However, it is crucial to continue further standardization efforts in order to accelerate academic research. First, standardization ensures the proper benchmarking of the battery performance between different laboratories (i), particularly in BIG-MAP as it guarantees the strict homogeneity of cycling conditions between the 34 partners. Making the cell assembly and cycling conditions uniform is the key to produce data that are readable and accessible for processing by machine learning and artificial intelligence algorithms. Second, standardization plays a key role in generating high quality data, which is fundamental for conducting in-depth electrochemical analysis, as pursued in this thesis (ii). Developing a thorough comprehension of battery degradation and creating accurate automated analysis through the use of machine learning applications is only achievable by utilizing high quality data. Third, it is essential to adopt suitable testing practices within academia in order to effectively implement innovative approaches aimed at extending battery lifespan in the industry (iii). If academic tests are conducted in a suboptimal manner, cell can benefit from advantageous testing conditions that might hide degradations while promoting false positive solutions or accentuating benefits of an additive. This phenomenon can be attributed to several factors, namely the cell formats employed, variations in electrode composition, and the excessive amount of electrolyte utilized in academic cells. These factors collectively reduce the sensitivity of academic cells to SEI instability, side reactions that consume lithium ions, or drying out. Furthermore, the conventional practice of conducting 1C charge-discharge cycling in laboratory settings fails to fully capture the complex and challenging conditions experienced during practical usage of batteries. Commercial cells are subjected to significant temperature variations and endure harsh voltage or current profiles, making it crucial to minimize any loss of lithium due to side

reactions. Consequently, when considering batteries with the same chemistry, it is highly likely that battery failures observed in academic settings will differ from those observed during practical usage. To a greater extent, the prediction of battery death in industry cannot directly be deduced from academic tests. Therefore, the successful transfer of solutions from academia to industry is incremental and requires testing conditions that closely resemble those encountered in the industry, while incorporating adapted control steps and analysis methods to understand the deteriorations in cells. Standardization is a way to achieve it.

In conclusion, the implementation of standardized testing conditions within academia offers a chance to streamline the evaluation of novel solutions and develop AI-supported models for battery degradation. To reach this goal, the subsequent section provides details on the key parameters recognized as crucial for correctly testing cells. Subsequently, drawing inspiration from the aforementioned discussion, a dedicated part focuses on the solutions implemented in the BIG-MAP project to ensure the generation of high-quality and reproducible data. Lastly, the third part of this chapter introduces the standardized protocols for recording and testing the performance of cells.

### II.1.2. Challenges

It is well-established that the performance of batteries can be affected by assembly parameters, with the most common ones being electrode composition and electrolyte volume. The following sections will show how these parameters impact performance, before moving on to show potential solutions to tackle these challenges.

#### II.1.2.a. Electrode composition

The composition of electrodes in academia sharply differs with respect to masses of active material and additive percentages compared to industrial electrodes. First, lab-scale electrodes are usually prepared with relatively low mass loading ( $< 2 \text{ mg/cm}^2$ ) and thin coating ( $< 20 \mu\text{m}$ ) that favors the impregnation of the electrolyte in porosities. However, commercial electrodes typically operate with loadings of approximately 5 to 10  $\text{mg.cm}^{-2}$ , corresponding to 1 – 3  $\text{mAh.cm}^{-2}$  [168], which shifts away from the testing conditions used in academic settings. Additionally, forthcoming energy-dense batteries will utilize electrodes with loading of 10 to 25  $\text{mg.cm}^{-2}$ , i.e. 3 – 7  $\text{mAh.cm}^{-2}$ . The progressive rise in electrode mass loading has an impact on the cell's C-rate capability, as illustrated in Figure 16a by *Bataglia et al.* [169]. When NMC33 electrodes are subjected to an increased charging current density from C/10 to 5C, the discharge capacity of the 3.5  $\text{mAh.cm}^{-2}$  electrode (100  $\mu\text{m}$  thick) drops significantly by 77% compared to its original capacity. In contrast, a thinner electrode – 24  $\mu\text{m}$  – with a loading of only 0.8  $\text{mAh.cm}^{-2}$  maintains its performance up to 10C. This observation suggests that thick

electrodes increase the polarization of the cell as a result of poor ionic transport in electrode porosities. Second, laboratory-produced electrode slurries frequently incorporate substantial quantities of carbon additives and binders to improve electronic conductivity and mechanical stability. However, this comes at the cost of energy density. The excessive use of binders, such as polyvinylidene fluoride (PVDF), reduces electrolyte percolation and ion transport due to decreased electrode porosity, as shown by *Marbella et al.* [170] and reproduced in Figure 16b. When the PVDF content in NMC333 slurries is increased from 5% to 10%, as is common in academic research, discharge capacity decreases by 15% at 1C, as a result of lower electrolyte percolation in electrodes.

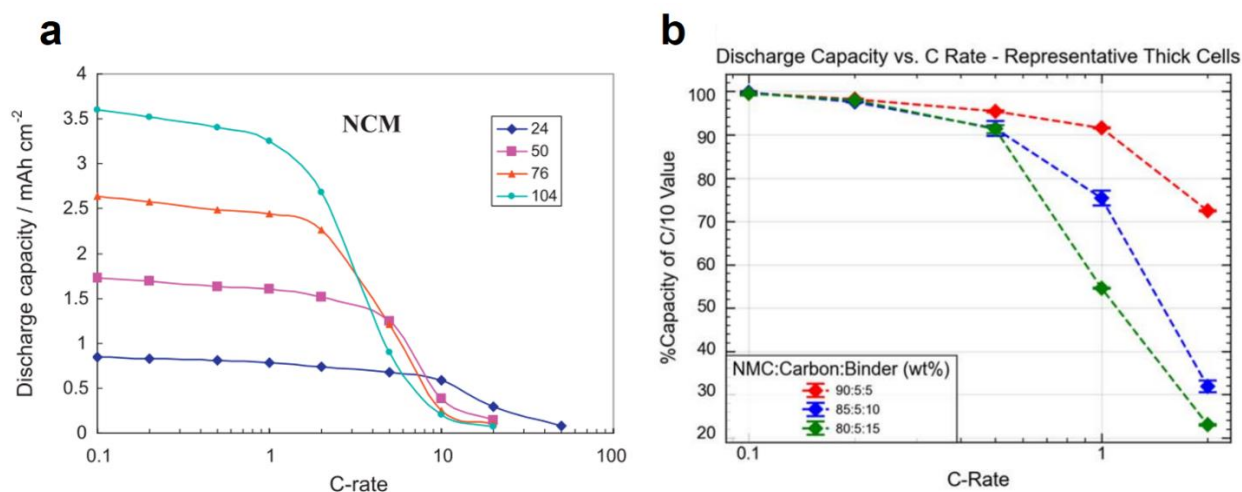


**Figure 16 – Effect of electrode loading and composition on cell performance**

a) Performance of NMC333 half-cells at different C-rates using various electrode mass loadings, with thicknesses ranging from 24  $\mu\text{m}$  for electrodes with a loading of 0.8  $\text{mAh}\cdot\text{cm}^{-2}$  to 104  $\mu\text{m}$  for those with a loading of 3.5  $\text{mAh}\cdot\text{cm}^{-2}$ . Reproduced from [169]. b) Benchmark of discharge capacity of thick NMC333 electrodes (120  $\mu\text{m}$  thick and 24.5  $\text{mg}\cdot\text{cm}^{-2}$ ) relative to their discharge capacity at C/10 rate, within a voltage range of 2.7 to 4.3 V. The cells being tested have different binder compositions, including samples with 5% (red), 10% (blue), and 15% (green) PVDF binder content. Dotted lines have been added to connect the data points and show the overall trends. Reproduced from [170].

Altogether, the results indicate that both the composition and mass loading of the electrode play a significant role in determining cell performance, particularly at C-rates higher than 1C. Therefore, to develop energy-dense LIBs, it is essential to prioritize research done using higher loading and thickness, to reduce the gap with electrodes used in industrial cells.

### II.1.2.b. Electrolyte volume

Besides electrode composition, the electrolyte amount determines cell lifetime and performance. If added volume is too low, electrolyte does not sufficiently fill the pores in electrodes and in separator, ionically insulating part of the active material and decreasing the cell capacity. On the opposite, a large excess of electrolyte artificially extends cell lifetime,

where electrolyte acts as a lithium reservoir and buffers  $\text{Li}^+$  losses associated to side reactions [164]. In results, high volumes postpone cell failure in addition to increase overall cost. Battery makers use an average of  $\sim 1.3$  g of electrolyte per 1 Ah of positive electrode as optimized electrolyte volume [164]. However, for academic cell formats, the community often does not report the exact amount of electrolyte volume utilized and instead only specifies the number of drops or that sufficient volume was added to wet the separator. Typically, academic researchers use an excessive amount of electrolyte, which can be as much as 100 times greater than that used in commercial cells. For instance, an average of 100  $\mu\text{L}$  is used for coin cells or Swagelock cells using 1 mAh electrode, or roughly 130 g/Ah, rendering academic cells less representative of practical performance. A fine control of electrolyte volume is thus required to limit erroneous conclusions regarding coin cell lifetime, by remaining closer to practical applications.

### II.1.3. Pending obstacles

The performance of academic cells is overestimated in comparison to performance reached in commercial cells, despite similar testing conditions. For instance, the calculations made by *Betz et al.* [5] demonstrate, step by step, the effect in scale when it comes to 18650 battery format. For that, NCA chemistry is used, with a theoretical energy density of  $\sim 770$  Wh.kg<sup>-1</sup> and 3,600 Wh.L<sup>-1</sup> [171].

When NCA is tested in a full cell versus graphite, the theoretical energy content is calculated based on complete delithiation of NCA (i.e. 279 mAh.g<sup>-1</sup>) and lithiation of graphite (i.e. 372 mAh.g<sup>-1</sup>). By taking the difference of the theoretical redox potentials of 3.8 V versus graphite (approximately 3.9 V vs  $\text{Li}^+/\text{Li}$ ) [172], the theoretical energy content of the full cell assembly at the active material level now amounts to 606 Wh.kg<sup>-1</sup> (a reduction of -21% in regard to pristine material) and 1,928 Wh.L<sup>-1</sup> (-46%) at the end of step 1.

While the theoretical capacity of graphite can be almost fully utilized at 360 mAh.g<sup>-1</sup>, only  $\sim 70\%$  of lithium is removed from the positive electrode (i.e. 200 mAh.g<sup>-1</sup>) due to limited upper voltage cutoff of 4.3 V and initial material irreversibility [173]. Additionally, the capacity ratio between the two electrodes must be balanced to avoid lithium plating and improve battery safety, typically with a negative to positive electrode capacity ratio of  $N/P = 1.1$  [174]. As a result of step 2, the energy content for graphite/NCA cells is reduced to 447 Wh.kg<sup>-1</sup> (-26% reduction from step 1) and 1,480 Wh.L<sup>-1</sup> (-23%)

In addition, the cell contains a minimal amount of electrolyte for operation, and additional volume is added to prevent electrolyte dry-out, resulting in energy densities of 365 Wh.kg<sup>-1</sup> and 915 Wh.L<sup>-1</sup>. Furthermore, inactive materials like binder (3w% of electrode) and carbon additives (1w%) are necessary to ensure mechanical and conductivity properties [8], [171], and the volumetric expansion of graphite and NCA shrinkage is also considered. Upon

implementing the adjustments outlined in step 3, energy densities are even more reduced to  $314 \text{ Wh.kg}^{-1}$  (-30%) and  $773 \text{ Wh.L}^{-1}$  (-48%).

In the last stage of the calculation process, composite electrode slurries are applied onto current collectors, thereby adding to the weight and volume of inactive materials within the battery. Furthermore, the components of the cell housing, such as the steel can, insulator disks, positive and negative poles, are necessary to assemble the cylindrical cell and are included in the calculations, resulting in a practically attainable energy density of  $264 \text{ Wh.kg}^{-1}$  (-16%) and  $635 \text{ Wh.L}^{-1}$  (-18%) for an NCA/graphite-based LIB at the 18650-type cell level. Consequently, the practical energy provided by an 18650 type Li-ion battery is on average three to four times lower compared to the theoretical performance of the positive electrode material, a rule of thumb generally accepted by the community [5].

## II.2. IMPLEMENTATION OF ASSEMBLY STANDARDS

After identifying the main factors contributing to cell-to-cell variability, our current focus lies on the preliminary experiments to conduct before implementing standards in the BIG-MAP project. The tests we perform in the following provide a rationale for the subsequent choices made within the project and throughout this thesis.

### II.2.1. Standardization of cell components

#### II.2.1.a. Coin cell: format of choice

The first step to standardize battery assembly and testing for lab-scale cells is to choose an appropriate cell format and fine-tune its assembly parameters. Subsequently, the standardization of the chemistry such as electrolyte volume and electrodes can be carried out. Among the different cell formats used in academic laboratories, coin cell is the most widely-spread format thanks to its convenience and high repeatability. In particular, when special care is paid in cell assembly, high repeatability of results and reproducibility can be achieved between different laboratories and operators, as previously demonstrated [175]. As a result, all subsequent studies and standardization efforts will be based on 2032-coin cells, with the list of components provided in Table 2. Furthermore, in order to investigate degradation at interfaces, full-cell configuration was preferred over half-cell, as it enables the detection of any loss of lithium associated with electrolyte consumption and structural damage.

Component	Dimension
<b>Negative case with polypropylene gasket</b>	19.3 mm diameter
<b>Wave spring</b>	14.5 mm diameter 1.42 mm thick
<b>Stainless steel spacer n°1</b>	15.8 mm diameter 1.0 mm thick
<b>Stainless steel spacer n°2</b>	15.8 mm diameter 0.5 mm thick
<b>Polypropylene separator Celgard 2500</b>	25 $\mu$ m thick 55% porosity
<b>Positive can</b>	20 mm diameter

**Table 2**

*Roster of 2032-format coin cell components suggested to the partners of BIG-MAP.*

### **II.2.1.b. Selection of chemistries tested in the BIG-MAP project**

Even though the standardization effort is not specific to any particular chemistry, BIG-MAP project has prioritized certain chemistries in order to demonstrate the implementation of high throughput testing and machine learning algorithms. First objective is to enhance the stability of Ni-rich electrodes at high potentials, more specifically NMC811 and LNO above 4.2 V, when used in full-cell against graphite negative electrode. The second tier of chemistries targeted in BIG-MAP is to then match high potential Ni-rich materials with silicon-graphite composite negative electrodes (Si-Gr). Similarly, LP57 has been selected as benchmark electrolyte, either with or without additives (VC and FEC). The use of common chemistries allows first to compare advancements made in BIG-MAP towards new electrolyte chemistries (Work package 4, WP4) and novel coating strategies (WP6) to improve battery lifetime and stability. Furthermore, it is necessary to establish reliable standardized cell assembly and testing procedures before implementing advanced analytical methods for uncovering complex degradation phenomena, as carried in WP8 and in this thesis.

### **II.2.1.c. Control of internal pressure in coin cells**

In order to accurately record performance using coin cells, first thing to ensure is that the internal pressure is sufficiently high. Insufficient pressure increases the risk of poor electrical conductivity between the electrodes and external caps that decrease overall capacity. The control of internal pressure in coin cells is indirectly ensured by the height of components that apply forces upon cell crimping and maintain the electrodes. When component sizes are adapted, electrodes are pressed together and stack ensures the good electronic conductivity. Typically, crimped coin cell has an internal void of 2.9 mm between the positive and the negative caps, of which free volume has to be filled by spring, electrodes and spacers (list of components provided in Table 2). During the cell assembly, electrode and

separator thicknesses using BIG-MAP standard components is 0.225 mm and the spring is 1.4 mm thick. Therefore, when excluding spring deformation, a minimum of 1.275 mm is left to be filled by spacers ( $2.9 - 0.225 - 1.4 = 1.275$  mm), using the appropriate number and thickness. Calculations are shown in Annex 1.

To test the effect of internal pressure, four cell configurations using different spacer heights and numbers have been tested in graphite/NCM811 cells at 4.2 V using non-optimized electrolyte volume of 60  $\mu\text{L}$  (Figure 17). When a single 0.5 mm spacer was used, the cell was unable to cycle, indicating that the components were not in contact with both sides of the cell due to low internal pressure. With two spacers of 0.5 mm, the cell capacity measured at 1C was 160  $\text{mAh.g}^{-1}$ , which is 30  $\text{mAh.g}^{-1}$  lower than the expected value for graphite/NMC811 cells cycled at this rate, while the CE was lower than 99.8%. Furthermore, the poor reproducibility observed across the different cells evidences inadequate use of spacers. When two spacers of 1 + 0.5 mm were used, results recorded across different cells were perfectly reproducible, and higher CE were obtained. In other words, the overall thickness of the cell prior to crimping should be at least 5% greater than the thickness of the empty crimped coin cell. Although similar performances are obtained with 1 + 1 mm spacers, cycling conditions were not ideal, as the cell casing was found deformed upon crimping. In conclusion, the optimal configuration was achieved using a combination of 0.5 + 1 mm spacers in 2032 coin-cells with

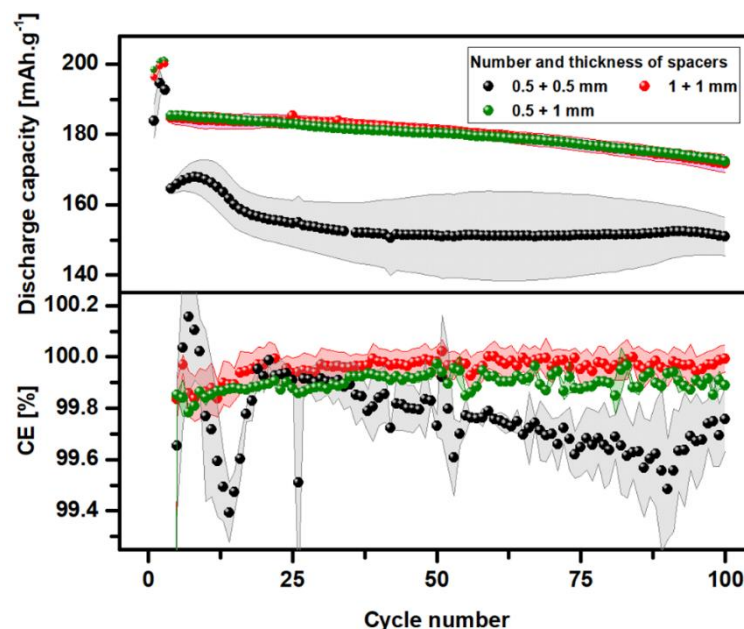


**Figure 17 – Effect of spacers on coin cell internal pressure**

*Effects of the quantity and thickness of spacers on the repeatability of cell assembly. Benchmark has been carried out for graphite/NMC811 cells using an excess of LP57 electrolyte (60  $\mu\text{L}$ ) and cycled between 2.5 and 4.2 V at 1C at a temperature of 25°C. Error bars indicate one standard deviation of error between two samples measured.*

a Celgard separator and casted electrodes. This finding is consistent with recently published research [176].

## II.2.2. Standardization of chemistry

### II.2.2.a. Homogeneity of electrodes

In addition to the standardization of cell components, the most influential components, *i.e.* the electrodes, must be standardized, more specifically their loading, thickness, and porosity as they directly affect the output capacity and rate performance. Therefore, within the context of the BIG-MAP project, all tested electrodes were produced by industrial partners, with high repeatability, to ensure the strict homogeneity of tested electrodes between partners. Two capacity loadings were tested, they are referred to as low and high loadings and are used to study rate capabilities and energy densities, respectively. High loading (HL) electrodes consist in a set of 3.0 mAh.cm<sup>-2</sup> positive electrode and 3.3 mAh.cm<sup>-2</sup> negative electrode, while low loading (LL) ones are 1.0 mAh.cm<sup>-2</sup> for positive electrode and 1.1 mAh.cm<sup>-2</sup> for negative electrode. The composition of NMC811 electrode consists of 95% by weight of active material, 3% C65 carbon, and 2% PVDF. For LiNiO<sub>2</sub>, the composition includes 94% by weight of active material, 3% C65 carbon black, and 3% PVDF. The negative electrode comprises graphite, with a composition of 94% 15-4 graphite, 2% C45 carbon black, 2% styrene butadiene rubber (SBR), and 2% carboxymethyl cellulose (CMC). Properties of NMC811, LNO and graphite electrodes are shown in Table 3, Table 4 and Table 5, respectively. Besides loadings, positive and negative electrodes are punched to 14 mm and 15 mm diameter, respectively. The negative area is thus oversized by +15% compared to positive electrode to ensure the optimal alignment. Indeed, even a very minor misalignment can result in significant performance losses, as shown by *Dahn et al* [177]. *Bloom et al.* showed that a 1 mm diameter difference totally suppresses the issue [175]. As a result, a capacity balancing between negative and positive electrode of N/P = 1.27 is attained in this project and thesis. While electrode balancing shifts away from industry standard of 1.05 – 1.1, one can argue that this tradeoff was necessary to achieve high cell repeatability using coin cells.

Electrode capacity loading (mAh/cm <sup>2</sup> )	Electrode weight loading (mg/cm <sup>2</sup> )	Total thickness (μm)	Coating thickness (μm)	Density (g/cm <sup>3</sup> )	Porosity (%)
1.0	5.4	39	19	2.96	32.6
3.0	15.1	70	50	3.20	27.1

**Table 3**

*Properties of NMC811 electrodes available in BIG-MAP project.*

Electrode capacity loading (mAh/cm <sup>2</sup> )	Electrode weight loading (mg/cm <sup>2</sup> )	Total thickness (μm)	Coating thickness (μm)	Density (g/cm <sup>3</sup> )	Porosity (%)
1.0	4.4	25	15	2.93	36
3.1	13.9	63	43	3.23	30

**Table 4**

*Properties of LiNiO<sub>2</sub> electrodes available in BIG-MAP project.*

Electrode capacity loading (mAh/cm <sup>2</sup> )	Electrode weight loading (mg/cm <sup>2</sup> )	Total thickness (μm)	Coating thickness (μm)	Density (g/cm <sup>3</sup> )	Porosity (%)
1.1	3.0	39	30	1.16	48.0
3.4	9.4	82	73	1.43	36.0

**Table 5**

*Properties of graphite electrodes available in BIG-MAP project.*

To demonstrate how electrode loading affects the performance of a graphite/NMC811 cell, electrodes with high loading (HL) and low loading (LL) were employed along with a large excess of electrolyte. When HL electrodes are cycled at 1C, the discharge capacity is measured 4 – 5 mAh.g<sup>-1</sup> lower when compared to LL electrodes, a phenomenon that stems from the poorer electronic percolation and from electrolyte diffusion limitations (Figure 18). Furthermore, capacity fading is faster with HL electrodes, suggesting that higher surface of material significantly reacts, thus forming a thicker SEI and consuming more Li<sup>+</sup>. Therefore, in order to achieve consistent studies and benchmarks, similar electrode loading will be used throughout the work.

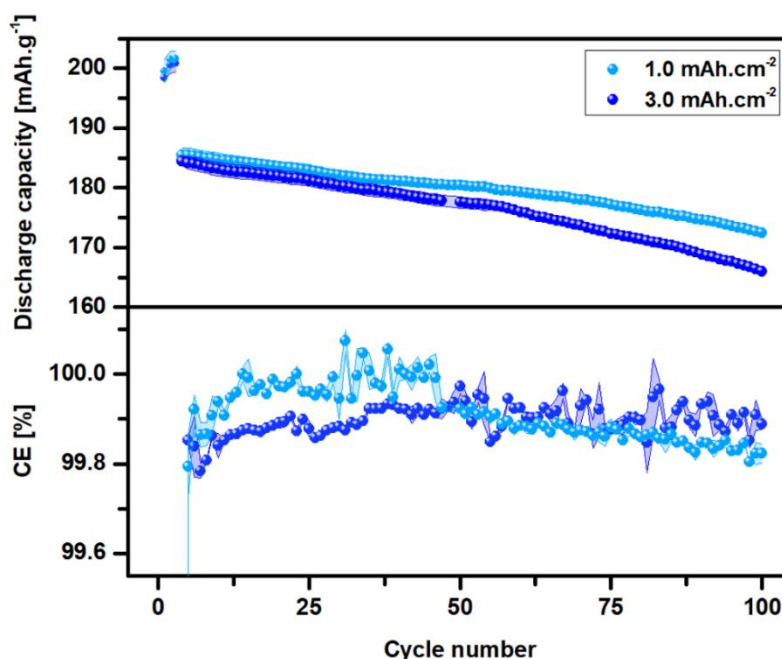


**Figure 18 – Performance of low and high loading electrodes in BIG-MAP**

*Effect of electrode loading on cell performance. High loading intensifies cell polarization and deteriorates performance, leading to more rapid decline in capacity. Benchmark has been carried for graphite/NMC811 cells using LP57 electrolyte (32.6  $\mu\text{L}$ ) and cycled between 2.5 to 4.2 V at 1C at a temperature of 25°C. Error bars indicate one standard deviation between two samples measured.*

### **II.2.2.b. Electrolyte amount**

Electrolyte sets the boundaries for cell energy, safety and lifetime; adapting its volume is thus an exercise of compromises. The objective of optimizing electrolyte volume is to make it applicable to all types of chemistry, and to achieve this, a readily available electrolyte - the commercial LP57 - has been utilized. To determine the optimal electrolyte volume using BIG-MAP electrodes, graphite/NMC811 coin cells were assembled using LL electrodes and 1 + 0.5 mm spacers. Previous studies dedicated to optimizing the electrolyte volume in coin cells showed that coin cell format has an inner geometry with a lot of free volumes, where electrolyte can flow upon the assembly. As a result, the optimized volumes were found to be higher than what is typically observed in the industry, with the reported amounts in coin cells ranging from 10  $\text{g.Ah}^{-1}$  [177] to 22  $\text{g.Ah}^{-1}$  of positive electrode capacity [175]. Therefore, electrolyte quantities were screened with 13.2, 19.8, 26.4 and 33.0  $\text{g.Ah}^{-1}$ , and results are shown in Figure 19a. When the lowest amount of electrolyte is added, *i.e.* 13.2  $\text{g.Ah}^{-1}$ , discharge capacity reaches 178  $\text{mAh.g}^{-1}$  in average during the first cycles that is 4% lower than that expected for NMC811 cycled at 1C with an upper cutoff voltage of 4.2 V. However, gradually increasing the volume, performance becomes maximal when reaching 26.4  $\text{g.Ah}^{-1}$ , with a capacity of 185  $\text{mAh.g}^{-1}$  and

a CE of 99.8%, both associated to lower cell to cell variability. Beyond 26.4 g.Ah<sup>-1</sup>, cells performance does not improve, indicating that the optimal electrolyte quantity is around 26.4 g.Ah<sup>-1</sup>, equivalent to 31.3 μL, for the coin cell assembly conditions listed above and using the LL electrodes. The value is at the upper end of what was found in previous studies, which may seem surprising at first. However, capacity of the positive electrode is not the sole descriptor for the optimization of electrolyte amounts and total pore volumes of electrodes and separator directly influence cell performance. In the BIG-MAP cell configuration, the negative electrode is +15% oversized compared to positive electrode for alignment purposes, this increases the pore volume to be filled by the electrolyte. Once normalized by total pore volume in the cell, 26.4 g.Ah<sup>-1</sup> corresponds actually to four-times the total pore volume of the coin cell, which matches with the equivalent volumes evoked in previous studies, with values ranging between 2-times [177] and 4.7-times [175]. Details for calculations and experimental conditions are detailed in Annex 2.

### II.2.2.c. Electrolyte distribution

Poor cell performance can result from an inadequate distribution of electrolyte, in addition to volume considerations. To investigate this effect, coin cells with similar electrode chemistry and an electrolyte amount of 26.4 g.Ah<sup>-1</sup> were assembled, with two types of electrolyte distribution. In the first assembly, the entire volume of electrolyte was added to one side of the separator, while in the second assembly procedure, the electrolyte volume was

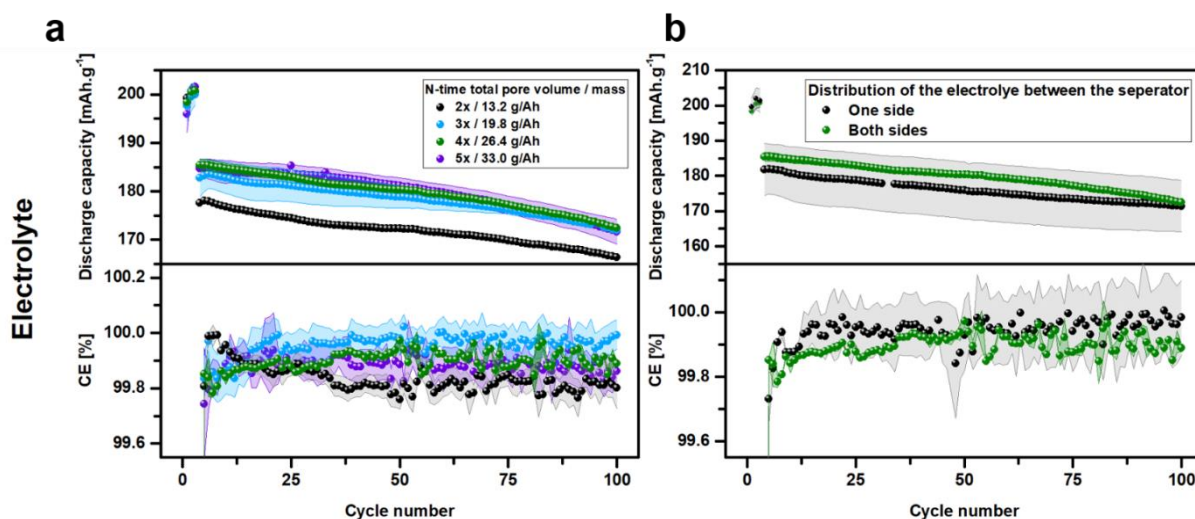


**Figure 19 – Effect of electrolyte volumes in coin cells**

The significance of electrolyte in the standardization of coin cell assembly is highlighted by: a) the identification of the most favorable electrolyte volumes, which correspond to four times the total volume of porosity of the electrodes and separator, and b) the necessity to evenly distribute the electrolyte on both sides of the separator to decrease result discrepancies. Tests have been carried out in graphite/NMC811 cells using LP57 between 2.5 and 4.2 V at 1C at a temperature of 25°C. Formation cycles consist in three consecutive C/10,  $i < C/50$ . Error bars indicate one standard deviation of error between two samples measured.

equally distributed on both sides of the separator (Figure 19b). When the electrolyte is distributed on one side, the cell capacity was lower by 2% compared to the baseline, with higher cell-to-cell variability. Despite leaving all cells at rest for 6 hours before the first cycle, the electrolyte did not fully permeate through the separator to fill the pores of the second electrode. To ensure highest repeatability and performance in coin cell using BIG-MAP electrodes, the following must therefore be respected: first, electrolyte amount must be fixed at  $26.4 \text{ g.Ah}^{-1}$ , corresponding to 4-times the calculated total pore volumes in cell. Second, the electrolyte must be equally distributed on both sides of the separator.

### II.2.3. Efforts that worth it

#### II.2.3.a. Assembly procedure

The following assembly protocol was therefore established and used within BIG-MAP project and throughout this thesis. The assembly process begins from the negative side, with the negative case and the gasket that contains a wave spring and the 1 mm spacer. The negative electrode (15 mm diameter) is then centered on the spacer, and half of the electrolyte is added on top. For instance, using a set of LL NMC811 and graphite electrodes, the total volume to add is  $31.2 \mu\text{L}$ . Care should be taken not to trap any bubbles between the electrode surface and the separator when placing the separator on the negative electrode. The remaining electrolyte is then added, and the positive electrode (14 mm diameter) is centered on top of the negative electrode, thanks to the transparency of the wet separator. Finally, the 0.5 mm spacer is placed, followed by the positive can, and the cell is crimped under a pressure of 800 kg.

#### II.2.3.b. Results

To demonstrate how effective is the standardization, cell performance measured by different BIG-MAP partners before and after the standardization efforts were compared. Beforehand, the work package 8 (Standardization and Protocols) to which we belong requested BIG-MAP partners to provide their own assembly procedures. The different procedures have been reproduced following their instructions, including details such as the number and thickness of spacers, distribution of electrolyte volumes. The results shown in Figure 20a highlight a significant variation in the performance of graphite/LNO cells depending on the assembly methods used. Surprisingly, some configurations fail to achieve the expected  $190 \text{ mAh.g}^{-1}$  capacity at 1C during the initial aging time. For cells with a discharge capacity below  $120 \text{ mAh.g}^{-1}$ , the poor performance is attributed to inadequate pore filling of the electrodes following the addition of electrolyte. Electrolyte volume is either low or added following an uneven distribution. For cells with a discharge capacity between 120 and  $190 \text{ mAh.g}^{-1}$ , electrolyte management is adapted but certain configurations exhibit irregular

retention curves and/or reduced capacity, most likely because of poor electronic conductivity. As a result, the polarization of the cell increases and recorded capacity retention curves is noisy. After the homogenization work, standardized procedure was taught to the different BIG-MAP partners during an event organized by WP8 which aimed at training operators in coin cell assembly. The results are clear, the use of standard protocols significantly improve the data quality and reproducibility between cells (Figure 20b). It is worth noting that although the operators were not accustomed to assembling coin cells, they still achieved remarkable results, highlighting the advantages of reconsidering assembly techniques in academia.

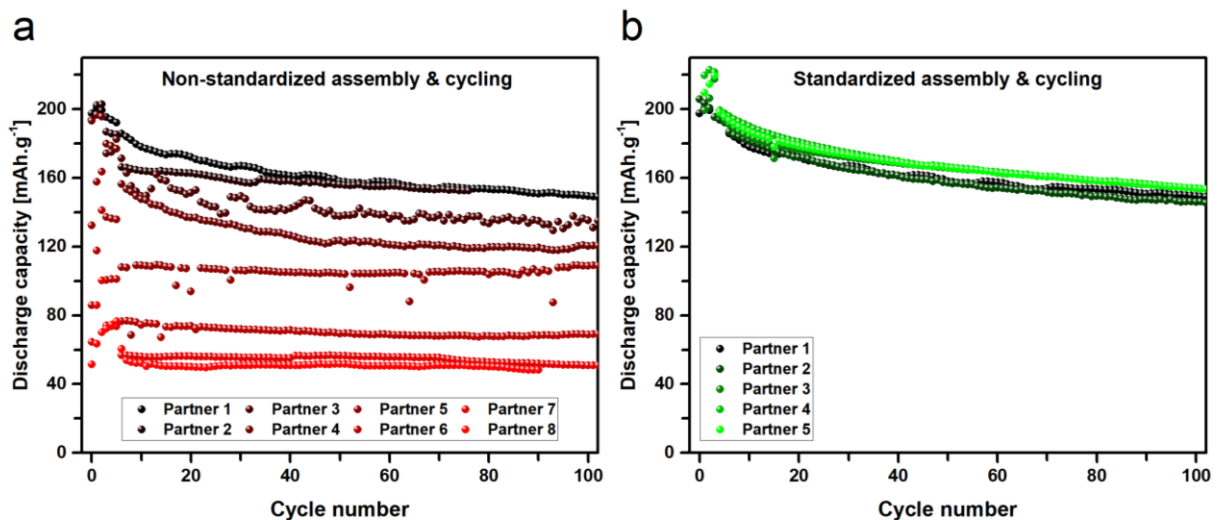


**Figure 20 – Outcomes of cell standardization**

*The evaluation of graphite/LNO cell performance before a) and after b) the establishment of a standardized assembly procedure. Tests have been carried out using LP57 between 2.5 and 4.2 V at 1C at a temperature of 25°C. Formation cycles consist in three consecutive C/10,  $i < C/50$ .*

## II.3. ASSESSING CELL PERFORMANCE IN BIG-MAP

### II.3.1. First tier testing protocols

#### II.3.1.a. Sampling conditions

Although standardization of cell assembly shows efficient, the BIG-MAP initiative strives for consistent data cycling among all partners to facilitate the implementation and processing of machine learning. Therefore, cycling procedures are also subject to the implementation of standardization. In that purpose, the first step involves establishing sampling conditions during cycling, where voltage measurements are taken every 5 mV or 30 seconds for constant current (CC) steps and every 1 mAh or 60 seconds for constant voltage (CV) steps. These sampling conditions strike a balance between the data file size and the precision of the recorded information, ensuring that accurate data analysis is further possible.

### II.3.1.b. Formation cycles

The formation process in a LIB is a necessary step to form passivating interfaces and avoid a continuous consumption of lithium ions associated to side reactions. Formation is a costly step in industry because it requires numerous cyclers, large floor space, and intense energy for the cyclers and environmental chambers. According to calculations carried out by *Wood et al.*, the formation step is estimated to be the most expensive process, with a cost of  $\$7.5 \text{ kWh}^{-1}$ , compared to  $\$2.2 \text{ kWh}^{-1}$  for electrode manufacturing, aside from materials [178]. Furthermore, the formation step is time-consuming because it first ensures that all the electrolyte completely wets the electrodes and separator, which can be particularly lengthy for large commercial cells. Second, most of the interphase is formed during low charge/discharge cycles, such as 3-5 cycles at C/20, before cycling the cells in environmental chambers [179]. As a result, the formation step may take up to 3 weeks, including the degassing step. Therefore, in BIG-MAP and to larger extend in industry, it is important to minimize the time spent for formation, while ensuring highest passivation of interfaces.

To determine the adapted formation step in BIG-MAP, four protocols were tested for graphite/NMC811 cells before aging them at 1C during 100 cycles (Figure 21). When cells were aged directly without formation cycles, the discharge capacity was  $10 \text{ mAh.g}^{-1}$  lower than the expected capacity, indicating that side reactions initially caused higher lithium losses during the first few cycles due to poor quality interphases. It is important to note that during formation, the initial irreversible capacity loss also depends on the capacity ratio between electrodes and the surface and particle size. In addition, the CE averages 99.6% during the 100 cycles of aging, suggesting that lithium is continuously consumed as a result of poorly passivating interphases initially formed. Cycling cells with three formation cycles at C/5, followed by a constant voltage (CV) step until reaching  $i < C/50$ , resulted in an initial capacity recorded at 1C of  $188 \text{ mAh.g}^{-1}$  with high repeatability, indicating efficient interphase formation. However, an increase in capacity fading, accompanied by a drop in CE from the 60<sup>th</sup> cycle onwards, suggests that the interphases are not stable over time, leading to increased lithium ion losses. The third protocol uses reduced cycling current of C/10 and achieved similar initial capacity than with C/5, confirming the efficient formation of interphases. The real benefit is observed during the long-term aging, when capacity fading remains steady after the 60<sup>th</sup> cycles, indicating that the interphases are more stable. It is worth noting that the C/10 CC, CV  $i < C/50$  protocol was not replicated when utilizing three formation cycles at C/20, as faster capacity degradation was recorded. This suggests that the voltage hold at the end of the charge cycle is beneficial for creating a more effective SEI, likely due to the extended period of low potential experienced by the graphite electrode. As a result, the three formation cycles consisting of

$C/10$ ,  $i < C/50$ , have been established as the standard formation protocol for BIG-MAP and complete description is available in Table 6.

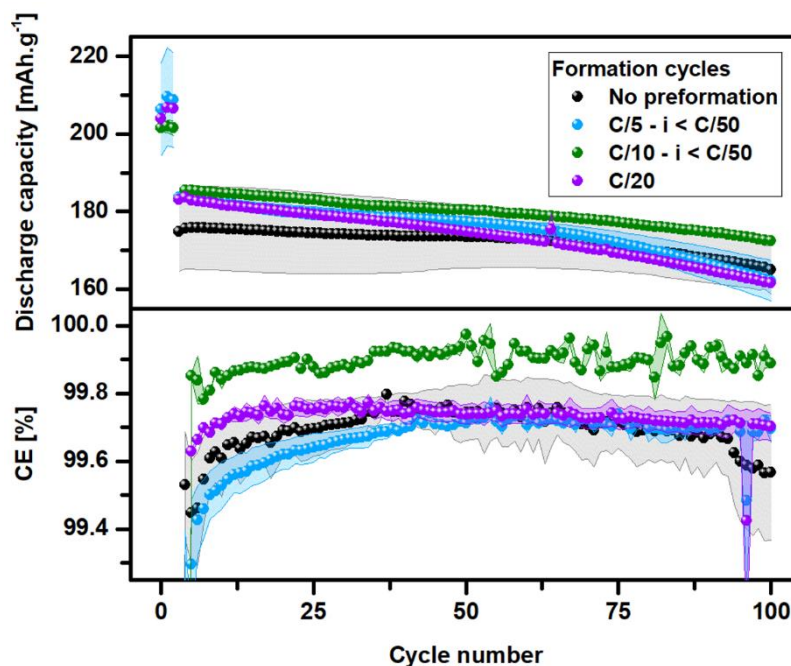


**Figure 21 – Optimizing the formation protocol**

*Formation cycles play a crucial role in developing a passivating interface and ensuring prolonged battery lifespan. The chosen protocol achieves a trade-off between the duration of the process and the resultant stability. Tests have been carried out in graphite/NMC811 cells using LP57 between 2.5 to 4.2 V and 1C at a temperature of 25°C. Formation cycles consist in three consecutive  $C/10$ ,  $i < C/50$ . Error bars indicate one standard deviation of error between two samples measured.*

### II.3.1.c. Regular cycling protocol

Continuous cycling at fixed current density is the straightforward method selected in BIG-MAP to age the cells and evaluate performance over an extended time (Table 6). Additionally, the protocol strives at ensuring that the cycling remains simple to implement. The test is inspired from ISO standards [180], [181], which are used to evaluate the performance of batteries in automotive applications.

1 <sup>st</sup> tier protocols		Procedure
Formation cycling		6h rest at OCV Charge CC: C/10 CV: $i < C/50$ Discharge CC: D/10
		Repeat 3-times
Regular cycling	Formation cycle protocol	Charge CC: 1C CV: $i < C/20$ Discharge CC: 1D
		Repeat until end of life criteria is met

**Table 6**

*Protocols for conducting formation cycles and regular cycling in the BIG-MAP project.*

The regular cycling consists in charge at constant current - constant voltage (CCCV) charge at 1C until  $i < C/20$  and discharge CC at 1C. Lower and upper cutoffs voltage are adapted as function of the tested chemistry. Figure 22 demonstrates that incorporating a CV step improves performance reproducibility and enhances discharge capacities. This can be explained as at 1C, high polarization leads to incomplete delithiation of the positive electrode material. Extending the charge step during voltage hold until the current cutoff is lower than a C/20 equivalent current increases subsequent discharge capacity by approximately 10%. Similarly, aging protocol can be carried out in a controlled temperature environment in climate chambers, allowing for studying the effect of temperature on degradation rates.

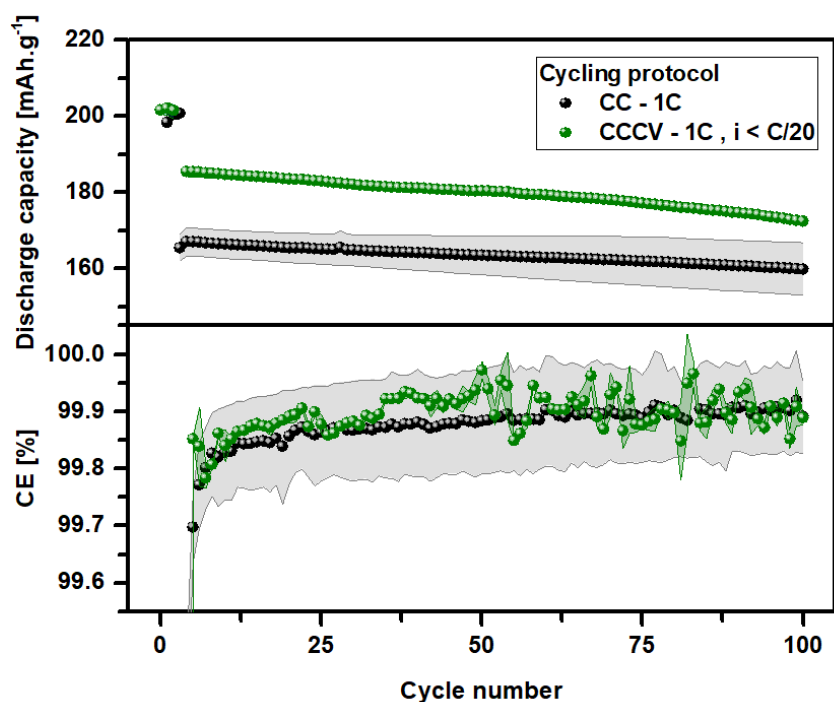


**Figure 22 – Optimizing the aging protocol**

*Incorporating a CV (constant voltage) step at the end of the charge minimizes variability among cells and enhances the subsequent discharge capacity. Tests have been carried out in graphite/NMC811 cells using LP57 between 2.5 and 4.2 V at 1C at a temperature of 25°C, with or without CV steps. Formation cycles consist in three consecutive C/10,  $i < C/50$ . Error bars indicate one standard deviation of error between two samples measured.*

## II.3.2. Second tier testing protocols

### II.3.2.a. Control cycle

When cycling, occasional "control cycles" can be used to assess cell performance throughout regular aging. Control cycles are conducted under specific conditions such as at low current density ( $i \leq C/20$ ) and at constant temperature (in a thermally controlled environment), that allows for performing electrochemical analysis near the thermodynamic equilibrium. Throughout this thesis, control cycles have been extensively utilized as the foundation for conducting comprehensive electrochemical analyses, as discussed in Chapter III.

The aging/control procedure implemented in BIG-MAP consists of two types of cycles: 100 cycles at CCCV 1C,  $i < C/20$  and control cycles composed of  $C/10$ ,  $i < C/20 + C/20$  to evaluate cell performance (Figure 23). Before the control cycle performed at  $C/20$ , a preliminary  $C/10$  cycle is conducted to reset the lithium inventory in the electrodes. This is necessary as the previous discharge at high current (1C) followed by low charge current ( $C/20$ ) can lead to an underestimation of the lithium inventory in the electrodes. It is worth adding that the number of aging cycles can vary depending on the material used. Similarly, the cycling conditions can be modified, including working temperature or voltage cutoffs.

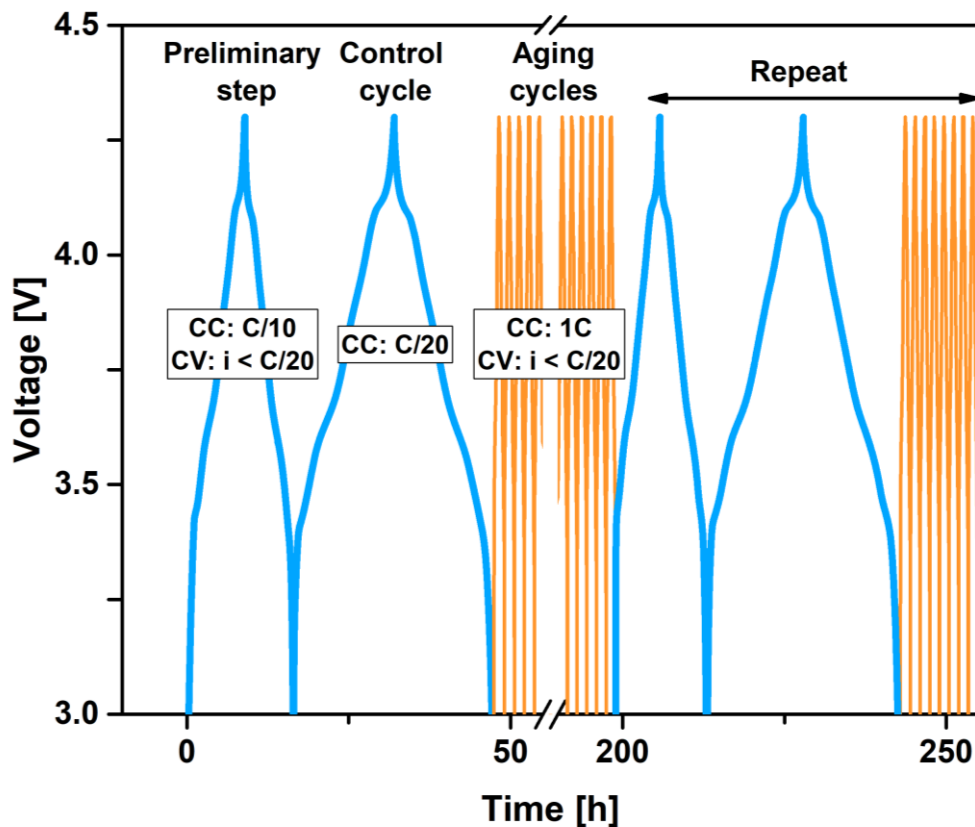


**Figure 23 – Details of control cycle protocols**

*Evolution of cell voltage as a function of time showing the design of control cycles upon cell aging. Graphite/NMC811 cells cycled between 2.5 and 4.3 V using LP57 at a temperature of 25°C.*

### II.3.2.b. Power tests

Power tests are necessary to evaluate the ability of a cell to discharge or charge at different speeds, from 20 hours ( $C/20$ ) to 12 minutes ( $5C$ ). In discharge-focused power tests, the previous charge is performed at a low current rate of  $C/20$  to facilitate complete delithiation

of the positive electrode by minimizing polarization, thus allowing for the maximum amount of removed lithium to possibly be reinserted upon discharge (Table 7). This ensures that the charge step does not restrict the discharge capacity. Conversely, charge-focused power tests involve discharging the cell at a rate of D/20 to achieve maximum relithiation of the positive electrode. The performance is thus solely limited by the subsequent charges. Nevertheless, the high currents of power tests can cause damage to the cell components such as Li plating, which leads to incorrect interpretation of the test results.

### **II.3.2.c. Stability tests**

To evaluate the stability of battery at high voltage, BIG-MAP has developed protocols that highlight possible degradations at a given charged state. After charging, the cell is left at open circuit voltage (OCV) for 50 hours. The expected outcome is for the voltage to decrease solely due to current stop and associated ohmic drop. However, a continuous decrease in voltage can also indicate imperfect passivation of interfaces, where electrolyte decomposes causing lithium to (de-)insert from the electrode and discharge the cell over time. Similar stability test can be performed over a longer period. The cell can be stored at a specific state of charge and left at OCV for days, weeks, or months. This test is known as a calendar aging test. All introduced tests are summarized in Table 7.

2 <sup>nd</sup> tier protocols	Procedure	
Aging/control	<p><b>Formation cycle (3-times)</b>            Charge            CC: C/10            CV: <math>i &lt; C/50</math>            Discharge            D/10</p> <p><b>Aging (e.g. 100-times)</b>            Charge            CC: 1C            CV: <math>i &lt; C/20</math>            Discharge            1D</p> <p><b>Preliminary step of control</b>            Charge            CC: C/10            CV: <math>i &lt; C/20</math>            Discharge            D/10</p> <p><b>Control</b>            Charge            CC: C/20            Discharge            CC: D/20</p>	
	Repeat until end of life criteria is met	
Power test discharge focus	6h rest at OCV CCCV charge (C/20 + D/20) x5 (C/20 + D/10) x5 (C/20 + D/5) x5 (C/20 + D/2) x5 (C/20 + 1D) x5 (C/20 + 2D) x5 (C/20 + 5D) x5 (C/20 + D/20) x5	
Power test charge focus	6h rest at OCV CC charge (C/20 + D/20) x5 (C/10 + D/20) x5 (C/5 + D/20) x5 (C/2 + D/20) x5 (1C + D/20) x5 (2C + D/20) x5 (5C + D/20) x5 (C/20 + D/20) x5	
Stability test	Regular cycling protocol	Charge CC: C/20 50h OCV period at the end of charge
	Repeat until end of life criteria is met	

**Table 7**

Second tier protocols for assessing advanced cell properties as fast (dis-)charging or interface stability in BIG-MAP project.

### II.3.3. Storage of data

After generating the electrochemical data, the final step involves storing efficiently the raw data with the necessary metadata so to comprehend the cell chemistry and cycling conditions in order to share the data with partners. To achieve this, an online laboratory notebook has been implemented to compile raw electrochemical data and sampling conditions, in combination with cell components. The first step to upload data involves filling the metadata fields (Figure 24a), including cell type, used chemistry, and how the cell has been cycled. Afterwards, the user uploads the raw data file in a commonly readable format such as “.txt”, making the data accessible to all partners (Figure 24b). The notebook maintains a certain degree of freedom to upload data that have not followed BIG-MAP standards. As the platform is currently functional, partners have already added over 250 electrochemical data files and continue to expand the collection (Figure 24c). The data may seem low due to the ongoing

**a**

**BATTERY 2030+ BIG-MAP**

**New Entry: Electrochemistry**

[?] Start Date:

[?] End Date:

Permission:

Standard Operating Procedure:

**Section 1: Cell**

General Information

Cell Type:

Cell Dimension:

[?] Electrolyte Volume [cm<sup>3</sup>]:

[?] Reference Electrode (Li, LFP, None, else):

Comments Regarding Specific Cell Format:

Positive Electrode Manufacturing:  Homemade  Supplied

[?] Active Material:

Coating:

[?] Experimental Capacity [mAh/cm<sup>2</sup>]:

[?] Active Material Supplier:

[?] Grain Size [μm]:

[?] Carbon Additive Name:

[?] Carbon Additive Supplier:

**b**

**Section 2-A: Cycline Protocol**

Temperature (K):

Initial Resting Time (h):

Preconditioning

Cycling Steps (2):

Step Number	Number of cycles	C-rate on charge	Cut-off voltage on charge [V]	CV conditions on charge	Resting time after charge (h)	C-rate on discharge	Cut-off voltage on discharge [V]	Temperature applied during step [°C]	Go back to step	Est. % hours
1	<input type="text"/>	<input type="text"/>	<input type="text"/>	<input type="text"/>	<input type="text"/>	<input type="text"/>	<input type="text"/>	<input type="text"/>	<input type="text"/>	<input type="text"/>
2	<input type="text"/>	<input type="text"/>	<input type="text"/>	<input type="text"/>	<input type="text"/>	<input type="text"/>	<input type="text"/>	<input type="text"/>	<input type="text"/>	<input type="text"/>

**Section 2-B: Other Protocols**

Type of Data:  None  CV  GITT  KIR

**c**

**Section 3: Data**

Raw Data

Analyzed Data

**Search: Electrochemistry Entry**

Filter by Institution:

BASF  CEA  CIDETEC  CNR  CNRS  CSC  Chalmers  DTU  EMRI  EPFL  ESRF  FZ Juelich  Fraunhofer ISC  ILL  IT University of Copenhagen  KIT  National Institute of Chemistry  Northvolt  Politecnico di Torino  SOLEIL  Saft  Saftel  Solvay  TU Delft  Unicores  University of Cambridge  University of Liverpool  University of Münster  University of Oxford  University of Jena  University of Vienna  Uppsala University  Wazirio University of Technology

Filter by Surname:

(1) Electrochemistry Entry: [hmd61-20220213-31c5a0ff](#)  
Uploaded by Mathias Leal de Souza [CNRS] on Feb. 13, 2023

(2) Electrochemistry Entry: [hmd61-20220213-301a4e9c](#)  
Uploaded by Mathias Leal de Souza [CNRS] on Feb. 13, 2023

(3) Electrochemistry Entry: [hmd61-20220213-a52c9b62](#)  
Uploaded by Mathias Leal de Souza [CNRS] on Feb. 13, 2023

(4) Electrochemistry Entry: [hmd61-20220213-5cc9c199](#)  
Uploaded by Mathias Leal de Souza [CNRS] on Feb. 13, 2023

(5) Electrochemistry Entry: [hmd61-20220202-199c5a0f](#)   
Uploaded by Valentin Meunier [CNRS] on Feb. 2, 2023

(6) Electrochemistry Entry: [hmd61-20220201-ea40f0f8](#)   
Uploaded by Valentin Meunier [CNRS] on Feb. 1, 2023

(7) Electrochemistry Entry: [hmd61-20220201-act4a19a](#)   
Uploaded by Valentin Meunier [CNRS] on Feb. 1, 2023

Figure 24 – Screenshots of BIG-MAP online notebook

a) Form used to enter metadata of the cell. b) Form dedicated to the description of the used cycling procedure. c) Search tool showing the upload electrochemical data.

efforts to enhance the widespread acceptance of the notebook among partners. Partners are actively working to promote it and increase the number of participants.

Data from this database can then be used to build machine learning models that can anticipate the end-of-life of cells. Some may argue that the data size is too modest and question the veracity of implementing machine learning models with this size of database. Despite their limited scale, small models have already exhibited remarkable results, such as predicting the best charging protocols for fast charging [182] or forecasting battery performance [183].

## CONCLUSION OF CHAPTER II

The process of standardization holds a significant importance for the BIG-MAP initiative as well as the broader battery community. Work package 8 has implemented assembly standards at European scale and has shown in a span of three years the numerous benefits of achieving consistent and dependable data through homogenization efforts. The decision to choose the coin cell format was based on its convenience and the high level of acceptance by partners. In addition, by optimizing the assembly process and controlling the chemistry used by every partner, including electrode homogenization and electrolyte volume, clear improvement of cycling results was observed. Additionally, procedures have been implemented to align with industrial norms, resulting in testing conditions that more closely reflect practical use.

In a second step, cycling protocols have been proposed for BIG-MAP community to ensuring homogeneity in the evaluation of cell performance. These protocols include first-tier methods such as formation step and aging procedure and push further the analysis, with second-tier protocols. These advanced procedures evaluate performance through C-rate performance, stability tests, and control cycles. Finally, the implementation of an online lab notebook enables storage of data, including experimental conditions and output results, on a digital platform. This feature facilitates data retrieval and analysis by individual users or artificial intelligence devices.

Altogether, these efforts undertaken by BIG-MAP partners provide the necessary means to achieve the utmost level of repeatability and data quality throughout the entire cell assembly process, cycling, storage, and data sharing. Ultimately, this chapter emphasizes the significance of the broad implementation of standards within the battery community, which BIG-MAP effort serves as an additional proof of standardization necessity. For instance, battery community may take inspiration from solar cell sector, where individual academic solar cells can undergo standardized testing protocols at the National Renewable Energy Laboratory (NREL) to confirm their performance and receive global accreditation.



# **CHAPTER III: DESIGN OF ANALYSIS WORKFLOWS FOR DETECTING DEGRADATIONS**



## INTRODUCTION OF CHAPTER III

The main goal of the BIG-MAP project is to develop an AI-based environment that can predict the deterioration patterns in batteries and identify the causes of their aging in order to design better electrolytes or coating chemistries and prevent these degradations. While previous attempts have been made to predict the end of a battery's lifespan using discharge capacity and CE, accurately determining the specific cause of battery failure remains challenging using these simple metrics. Indeed, commonly used indicators such as CE and discharge capacity lack knowledge of the underlying chemistry involved in degradation. Therefore, there is a need to expand the set of analysis techniques to gain a more comprehensive understanding of the involved degradation processes.

The battery community has successfully employed adapted electrochemical analyses to identify the type of degradation and electrode at which it occurs. These analyses utilize voltage-capacity curves and monitor the evolution of capacity slippage endpoints, demonstrating high accuracy. However, despite this significant knowledge, these analysis methods, when used independently, have limitations in capturing multiple degradation modes that can simultaneously occur at both electrodes and affect each other. This interdependence, referred to as crosstalk, becomes more pronounced with aging and cycling, gradually accumulating until additional degradations are triggered. Crosstalks have a vast number of potential origins with side reactions that can impact the electrode materials and the interfaces, making their identification challenging [75], as extensively discussed in several reviews [184], [185].

The objective of this chapter is to provide analysis workflows that facilitate a deeper understanding of complex crosstalks in LIBs. These workflows integrate multiple electrochemical techniques that provide essential information for identifying battery failures. Prior to introducing the workflows, the initial section establishes the fundamentals of the analysis by discussing the types of damage batteries are prone to experience and their consequences. Subsequently, the advanced electrochemical analysis techniques on which the workflows rely, will be introduced. This includes a description of derivative curve analysis ( $dV/dQ$  and  $dQ/dV$ ) as well as the methodology of tracking the evolution of charge and discharge capacity endpoints, also known as marching. Lastly, the integration of these techniques into workflows will provide a comprehensive roadmap, revealing the intricate degradation processes at play. Due to the unique nature of BIG-MAP, it is essential for these protocols to be compatible with AI-assisted analysis, as the overarching concept revolves around automating the analysis process.



## III.1. FUNDAMENTALS OF BATTERY ANALYSIS

### III.1.1. Consequences of degradations in LIB

While degradation mechanisms are complex and lead to various evolution of capacity retention curves, degradations are generally categorized into two main groups: loss of lithium inventory (LLI) or loss of active material (LAM) [186], [187]. These can lead to an increase in impedance (IR) and contribute to shifts in voltage or capacity windows (Figure 25). Each of these degradation processes individually contributes to a significant decline in battery capacity over cycling.

**Loss of lithium inventory (LLI)** – LLI corresponds to the decrease in available lithium cations for cycling within a cell due to their consumption in side reactions, such as SEI formation, lithium plating, or electrolyte decomposition. LLI is commonly identified as the primary cause of capacity fading [20], [188]. The concept of LLI can only be validly applied in a full cell configuration, as the utilization of lithium metal in half cells provides a "quasi" infinite source of lithium.

**Loss of active material (LAM)** – LAM refers to the absence of lithium intercalation sites within a material. This phenomenon can result from mechanical events such as the electrical insulation of the material due to cracks, or chemical processes such as an irreversible phase transformation. LAM can manifest at both the negative and positive electrodes and can occur across various lithiation degrees. LAM can be detected in both the positive and negative electrodes, denoted as LAM PE and LAM NE, respectively.

**Impedance raise (IR)** – IR is a consequence of the decrease in lithium kinetics, which typically occurs over time and cycles as a result of various factors, including LAM and LLI. In the subsequent section, we will introduce techniques that allow for the identification of LLI, LAM, and IR from electrochemical curves, specifically indicating the electrodes where these phenomena occur.

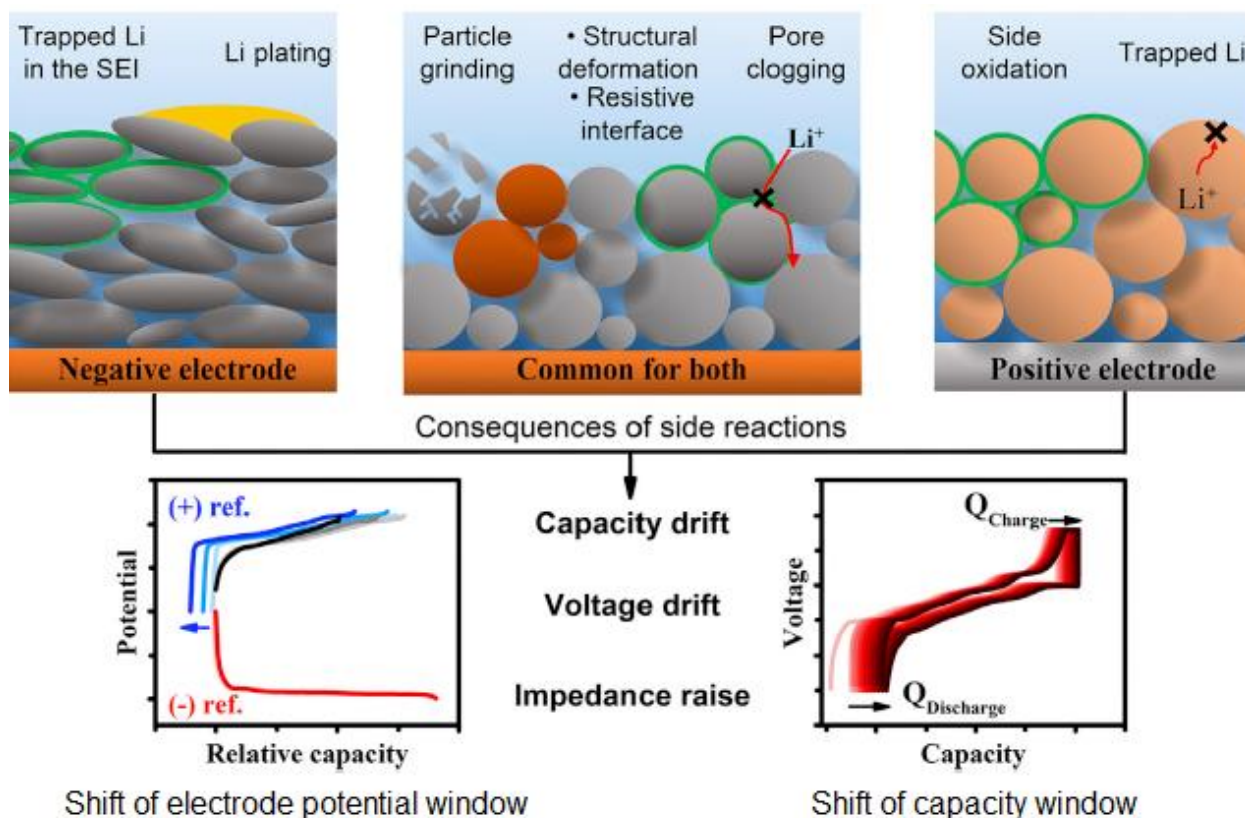


Figure 25 – Overview of cell degradations and consequences

Widespread type of degradation mechanisms occurring at electrode interfaces. The associated loss of lithium inventory (LLI), the loss of active material (LAM), and an increase in impedance (IR) lead to the shift of both capacity and potential windows of electrodes.

### III.1.2. Commonly employed analysis methods

#### III.1.2.a. Marching

The voltage capacity curves of LIBs are often depicted using voltage versus the cumulative capacity, as illustrated in Figure 26a. This graphical representation proves valuable because any mismatch between charge and discharge, attributed to parasitic reactions, causes the curves to shift between cycles. The degree to which the curves shift towards higher cumulative capacity indicates the occurrence of side reactions [189]. For ease of analysis, the cumulative capacity of charge and discharge endpoints can be plotted against cycle number, as demonstrated in Figure 26b. Consequently, the slope value of the capacity endpoints, referred to in the following as marching [190], serves as an indicator of the degradation rate.

When the growth of the SEI dominates, the capacity endpoints for the discharge ( $Q_D$ ) increase at a faster rate compared to the charge ( $Q_C$ ) endpoints (Figure 26b). This occurs because the negative electrode experiences a loss of lithium during each charge cycle, resulting in fewer lithium cations available for intercalation at the positive electrode during

discharge. Consequently, a gradual reduction of the capacity window ( $Q_C \leq Q_D$ ) is observed, with  $Q_D$  increasing at a faster rate than  $Q_C$  [190], [191]. In scenarios involving significant side reactions, both  $Q_C$  and  $Q_D$  endpoints increase rapidly, ultimately leading to an earlier end of life for the cell (Figure 26c). The presence of parasitic oxidation during the charging process can greatly amplify the shift of capacity endpoints, ultimately resulting in a situation similar to the one depicted in Figure 26c.

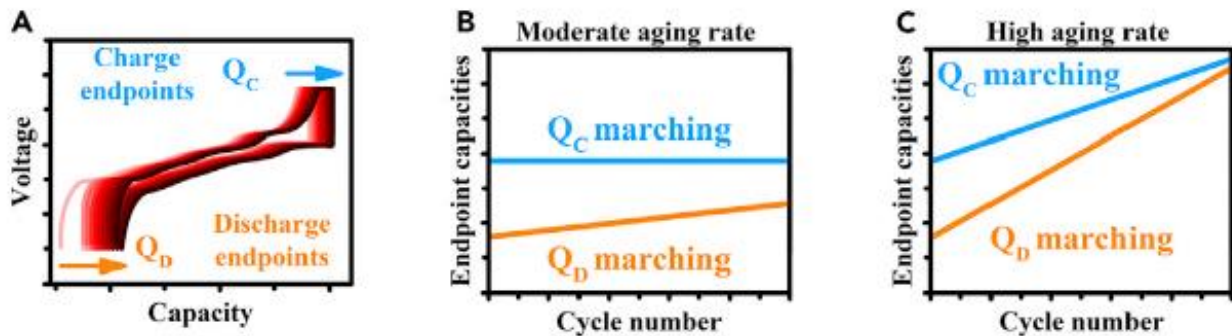


Figure 26 – Description of marching capacities

*Illustration of the consequences associated with common degradation phenomena using the marching analysis. Charge and discharge endpoints (A) are plotted using cumulative capacity to distinguish between moderate (B) and high (C) aging rates.*

### III.1.2.b. Derivative voltage analysis

The derivative voltage analysis (DVA) is a commonly used technique that involves examining the  $dV/dQ$  curves in relation to the capacity. Peaks observed in the derivative curves correspond to the slopes of the  $V(Q)$  curves and indicate single phase regions in the lithiated state of the electrode material [192] (Figure 27). Equation (11) is used to calculate the derivative curves, with  $V$  standing for voltage,  $Q$  the capacity and  $n$  the recorded point number. An example of  $V(Q)$  of  $\text{LiNiO}_2$  vs  $\text{Li}^+/\text{Li}$  and associated  $dV/dQ$  curve is depicted in Figure 27.

$$\frac{dV}{dQ}(n) = \frac{dV_{n+1}}{dQ_{n+1}} - \frac{dV_{n-1}}{dQ_{n-1}} \quad (11)$$

Overall, the analysis of  $dV/dQ$  curves is a less intrusive method to determine the contribution of electrode compared to the insertion of a reference electrode. Adding a third electrode is not a trivial task as it may interfere with cell functioning and has been reported to provide misleading information [193].

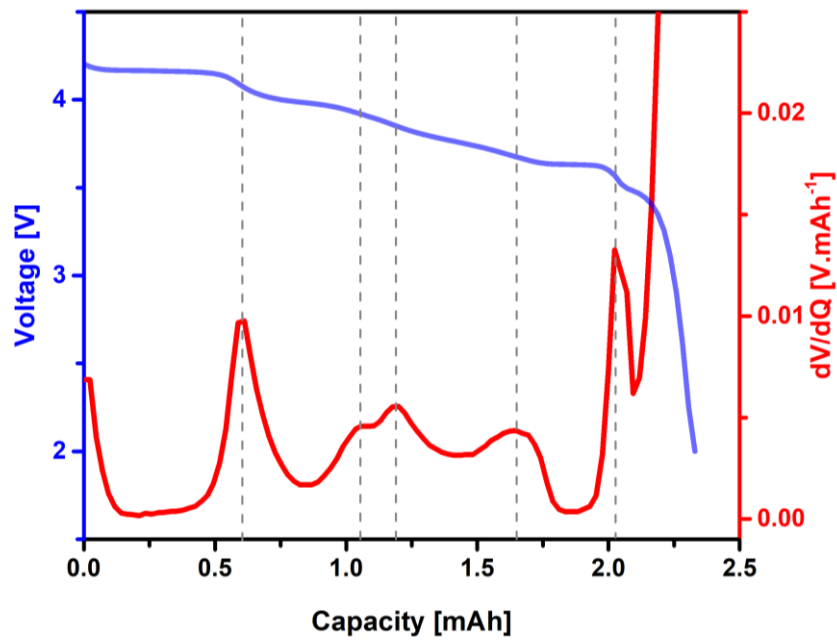


**Figure 27 – Introduction to DVA**

The blue curve represents the Voltage – Capacity discharge curve  $V(Q)$  of the LNO half-cell, while the red curve depicts the corresponding  $dV/dQ$  curve. The derivative curve emphasizes the slopes of the blue curves associated to single phase regions of LNO material.

The significance of the differential curves lies in their sensitivity to highlight features present in the  $V(Q)$  curves, which evolution can provide insights into the degradation of the battery (Figure 28). *Bloom et al.* have first demonstrated that by analyzing the peak intensity and position shift [188], it is possible to identify the contribution of different electrodes to battery degradation. Typically, the presence of LLI is detected through a displacement in the  $dV/dQ$  curve of the full cell. This displacement occurs due to a misalignment in the capacity of the electrodes, as illustrated in Figure 28a. Conversely, the shrinkage of the derivative curves indicates that the active material experiences lower de-lithiation caused by LAM (Figure 28b).

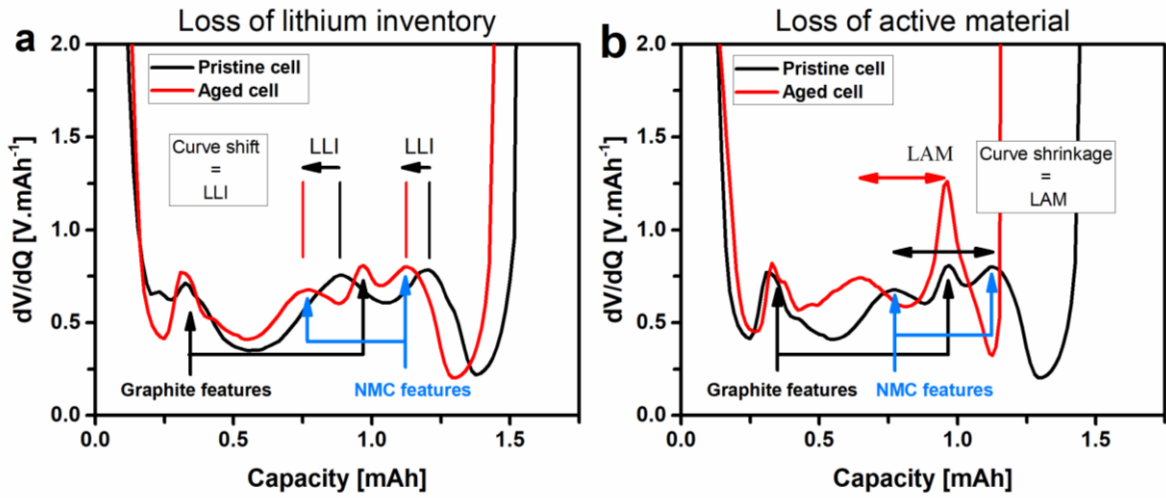


**Figure 28 – Benchmark of  $dV/dQ$  curve before and after aging showing the degradations**

a) The  $dV/dQ$  curves of graphite/NMC811 cell demonstrate a shift in the NMC features due to LLI upon aging. In another cell b), the  $dV/dQ$  curve undergoes a shrinkage of NMC features due to aging, which is attributed to LAM effects. While LAM is prevalent, it is worth noting that the shift of NMC features is visibly associated with LLI.

Moreover, the method initially introduced by Bloom *et al.* involves displaying the derivative curves of the full cell ( $dV_F/dQ_F$ ), which are derived from the positive ( $dV_P/dQ_P$ ) and negative ( $dV_N/dQ_N$ ) half-cells [188] following Equation 12.

$$\frac{dV_F}{dQ_F} = \frac{dV_P}{dQ_P} - \frac{dV_N}{dQ_N} \quad (12)$$

Dahn *et al.* further improved the proposed model by developing automated software [194] that allows fitting of measured  $dV/dQ$  curves using a reconstructed model based on references (Equation 13). The fitting process follows the model described below:

$$\frac{dV^{model}}{dQ_F} = \left( mass_P * \frac{dV}{dQ_P} + S_P \right) - \left( mass_N * \frac{dV}{dQ_N} + S_N \right) \quad (13)$$

with  $mass_P$  &  $mass_N$  (g) the masses of active material for the positive and the negative electrodes, respectively.  $S_P$  &  $S_N$  (mAh) are the relative capacity slippages of the positive and the negative electrodes, respectively. The analyzed curves are recorded during a so-called control cycle carried out under specific conditions, i.e., at low current density (commonly  $i \leq C/20$ ) and at a constant temperature (in a thermally controlled environment) to limit kinetic effect and ensure the analysis is performed close to thermodynamic equilibrium [192], [195].

Illustrated in the schematic panel of Figure 29a, the experimental  $dV/dQ$  versus  $Q$  curve (depicted in black) is subjected to fitting by adjusting the active masses and capacity slippages of the negative (represented in red) and positive (shown in blue) reference curves. Through this fitting process, it becomes possible to plot the potential of the negative and positive electrodes as a function of relative capacity, as demonstrated in Figure 29b and Figure 29c. In the relative capacity plots, the endpoint of the discharge curve for a full cell is established at 0 mAh, allowing for the possibility of referencing a negative capacity. The reconstructed plot enhances the visibility of both LLI and LAM. LLI is mainly responsible for the free space within the positive electrode at the end of discharge, resulting from the growth of SEI and the consumption of  $\text{Li}^+$  ions. On the other hand, LAM is observed as a reduction or shrinkage of the respective electrode, signifying a decrease in the number of available intercalation sites within the active material.

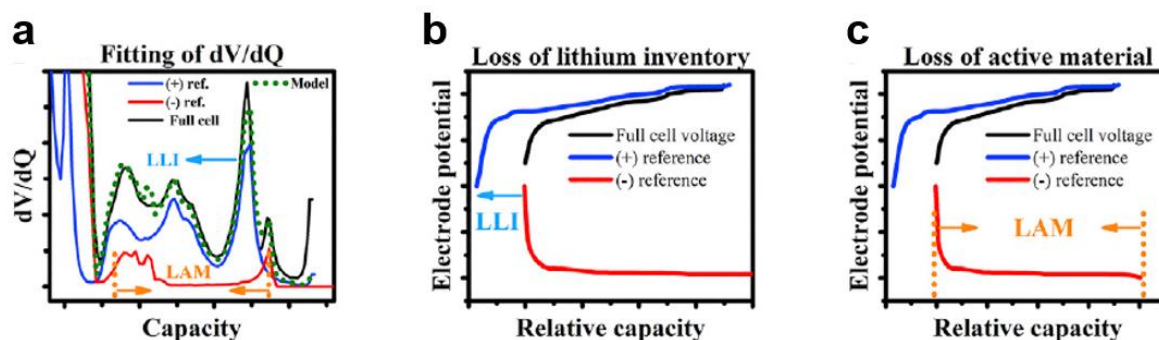


**Figure 29 – Interpretation of  $dV/dQ$  fitting curves**

*The fitting of the  $dV/dQ$  versus  $Q$  curve during DVA (a) reveals any LLI by the shift of one electrode capacity versus the other (b) and any LAM by the shrinkage of the capacity associated with an electrode (c).*

### III.1.2.c. Incremental capacity analysis

The incremental capacity analysis (ICA) involves examining the  $dQ/dV$  derivatives in relation to voltage. By analyzing these derivatives, ICA identifies horizontal segments in the potential versus capacity curve through the presence of peaks in the derivative curves, as shown for  $\text{LiNiO}_2$  vs  $\text{Li}^+/\text{Li}$  in Figure 30. In half cells, these peaks correspond to phase transitions occurring within the electrode materials [196]. However, associating a peak with a specific phenomenon in full cells is less straightforward, as it arises from the cumulative capacity cycling of both the negative and positive electrode materials.

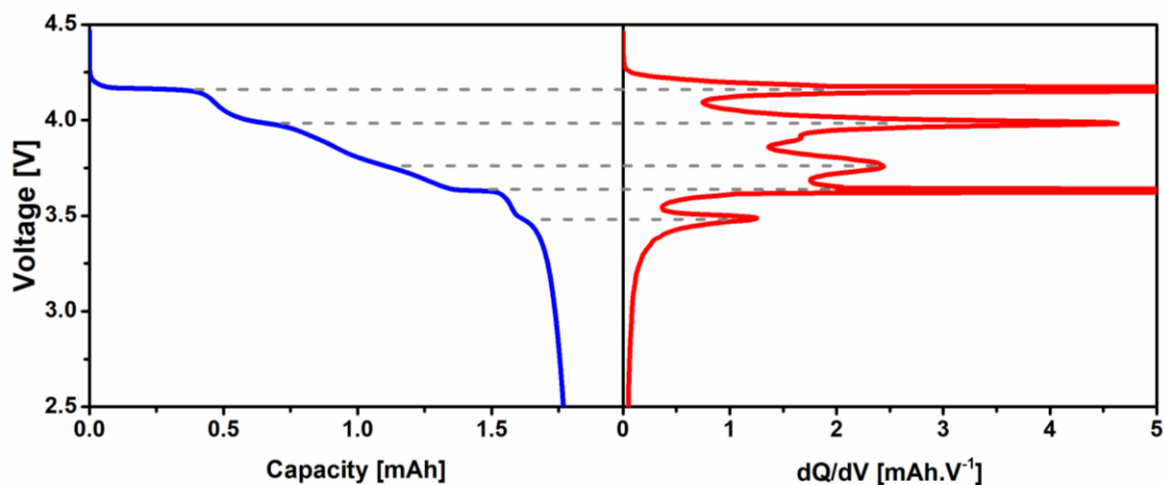


**Figure 30 – Introduction to ICA**

*The blue curve represents the Voltage-Capacity discharge curve  $V(Q)$  of the LNO half-cell, while the red curve depicts the corresponding  $dQ/dV$  curve. The derivative curve emphasizes the plateaus of LNO material associated to phase transitions.*

By examining the position, height, and shape of the peaks, ICA provides direct insights into the evolution of impedance, mass loss [197], and changes in the chemistry of a specific electrode [192], [196]. LAM is characterized by a decrease in intensity for each peak, as depicted Figure 31a. An increase in polarization results in a shift towards higher voltage during charging and lower voltage during discharging for these peaks, as shown in panel (b). The loss or appearance of a  $dQ/dV$  peak during the aging process indicates that the electrochemical processes occurring at the electrodes have been altered, as illustrated in panel (c). The loss of a  $dQ/dV$  peak can be attributed to an irreversible phase transition or an impediment to Li intercalation at a specific phase transition due to high internal resistance. Conversely, the appearance of a new peak at the end of the charge can be associated with lithium plating [196].

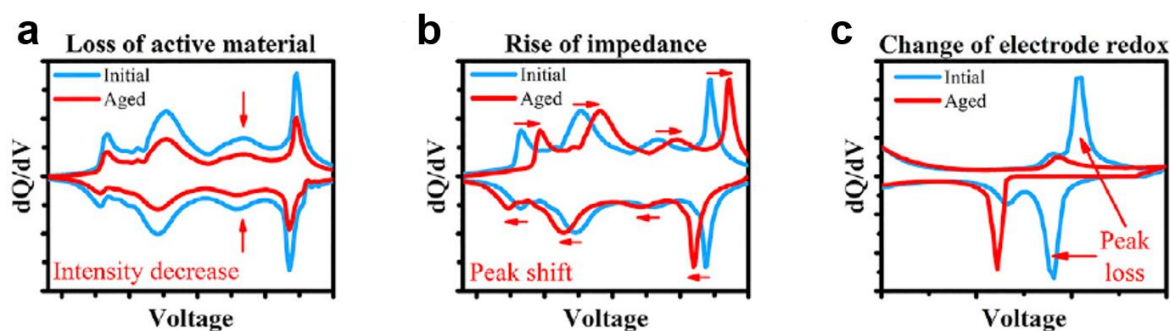


**Figure 31 – Interpretation of dQ/dV curves**

*The ICA reveals the LAM by the drop in intensity of every redox peak a); it reveals the rise of the impedance of the cell by the shift of all the redox peaks toward greater voltage in charge or lower voltage in discharge b) and reveals a change in redox at a given electrode by the dis/appearance of a redox peak c).*

## III.2. THE COMPLEXITY OF KNEE POINT

### III.2.1. Knee points: definition and types

Lithium-ion batteries exhibit diverse behaviors when plotting the discharge capacity against cycle number. These aging trajectories follow a linear aging behavior or present “knee point”, i.e. a discontinuity in capacity retention curves (Figure 32). Knee point can display a sublinear aging behavior (blue curve) that is often associated with side reactions such as the growth of the SEI increasing approximately as the square root of time or cycle number due to its self-passivating nature [20]. While this type of degradation is largely unavoidable, the decreasing rate of degradation is advantageous for applications requiring long battery lifetimes. On the other hand, knee point can also follow superlinear aging behavior (red curve) that corresponds to an acceleration of cell capacity loss [198]. Overall, a knee refers to any change in the aging rate of a battery, and predicting the occurrence of knees remains challenging because they tend to appear suddenly and can result in sharp capacity drops in just a few cycles [97], [199]. As battery scientists strive to achieve longer lifespans, comprehending the origins of knee points becomes increasingly crucial. However, as elucidated in the subsequent section, pinpointing the precise cause of knee points is a challenging endeavor as these fatal outcomes often come from crosstalking events.

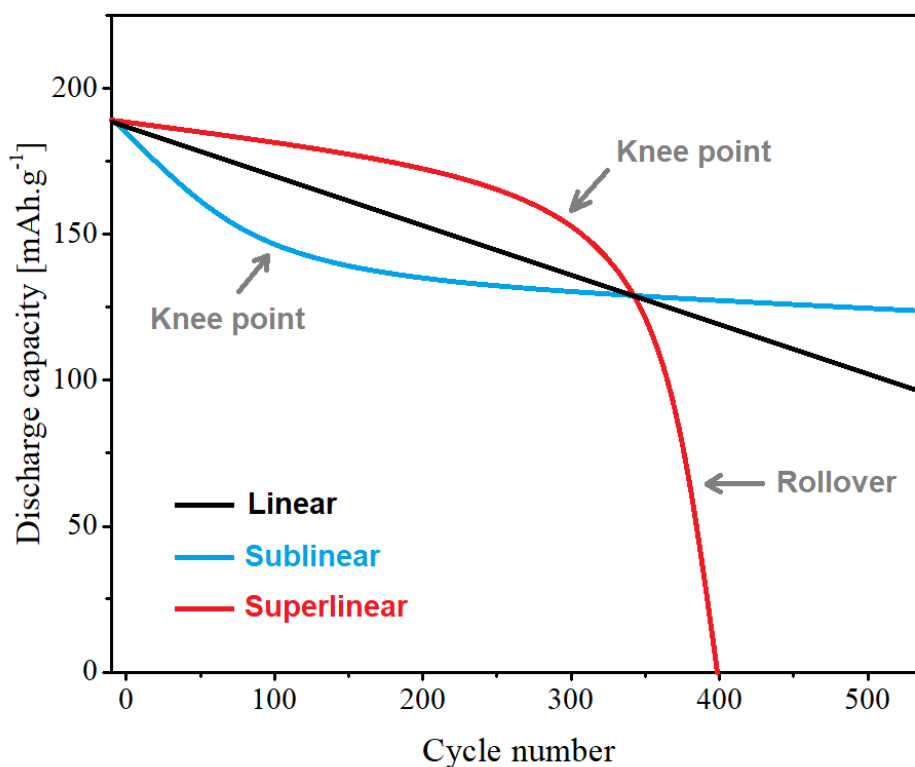


**Figure 32 – Different type of knee points**

*Schematics illustrating aging patterns in lithium-ion batteries (LIBs) and the characteristic curves of capacity retention, including linear, sublinear, and superlinear. Among these aging types, the knee point is an inflection point that can be observed in both sublinear and superlinear aging, often occurring before a capacity rollover.*

### III.2.2. Origins of knee points

The occurrence of a knee point can be attributed to various phenomena [198]. These phenomena can be categorized as either resulting from a sudden change in the dominant degradation mechanism, known as the "threshold effect," or from an accelerated degradation rate, referred to as the "snowballing effect" (Figure 33). In the threshold effect, a single event causes a sudden modification in the rate of capacity fading. Examples include the depletion of electrolyte [164] or a rapid increase in impedance due to lithium plating. The snowballing effect arises from the accumulation of side reactions, such as an increase in transition metal content in the SEI leading to increased lithium loss or loss of electrical contact due to mechanical deformations and particle cracking. Knee points, therefore, emerge as a result of physical and/or chemical events that differ from classical aging phenomena like continuous SEI growth.

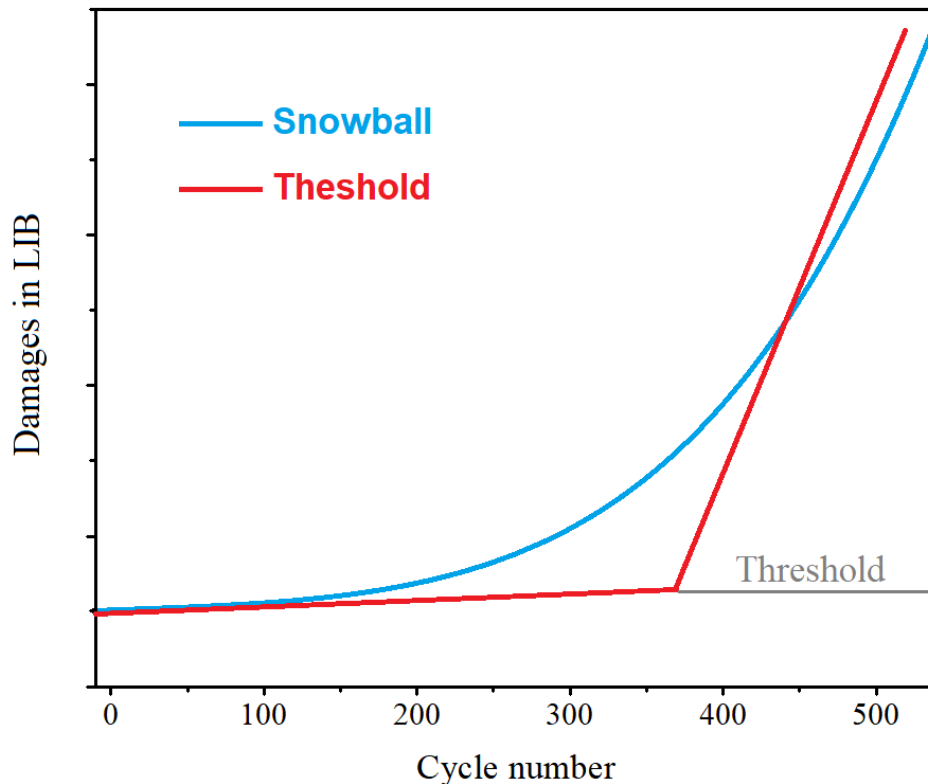


**Figure 33 – Origins of knee points**

*Illustrations depicting the levels of degradation that result in a knee point on capacity retention curves. In the snowball mechanism, degradations build-up gradually over time, while in the threshold effect, degradation experiences a sudden and rapid acceleration once the cell has reached the resilience threshold.*

### III.2.3. Motivations for constructing analysis workflows

Despite the extensive knowledge available, when utilized individually, conventional analysis methods such as CE and capacity fading struggle to capture the simultaneous occurrence of multiple degradation modes that affect both electrodes. This interdependence, known as crosstalk, intensifies over the aging or cycling and accumulates until it triggers additional degradations, leading to a snowball effect or a threshold phenomenon. At this stage, the battery is likely to experience a rollover failure in subsequent cycles. As a result, it is crucial to detect the underlying mechanisms responsible for these rollovers. Three workflows are thus introduced in part III of this chapter to investigate the origins of knee points or rollovers and to detect early indicators of crosstalk. While intuitively carried out by researchers under given circumstances, such workflows are proposed for the first time in the field.

### III.3. WORKFLOWS

The initial step of the analysis involves examining the presence of a knee point in the capacity retention curve. The presence or absence of a knee point (case a in Figure 34) does not necessarily indicate the absence or presence of crosstalks within the system. Therefore, it is important to monitor its occurrence throughout the battery's lifespan using **workflow I**. This initial workflow aims to identify abnormal aging rates, excluding SEI growth, and is particularly effective in uncovering side oxidation and shuttling events (case b in Figure 34). **Workflow I** does not require extensive data processing and involves plotting the capacity marching of the cell. This analysis serves as a preferred method to regularly examine any early signs of knee point emergence (indicated by arrow c). Once a knee point is observed in the capacity retention curve (case d in Figure 34), **workflow II** can be employed to uncover the potential chemical events occurring. This second workflow utilizes DVA to identify the nature of degradations and determine the electrode primarily responsible for the degradations. In cases where there is no chemical crosstalk involved (case e in Figure 34), a third and final workflow, **workflow III**, can be utilized. **Workflow III** focuses on detecting sudden changes in the cell's voltage window, which can lead to a knee point in the capacity retention curve (case f in Figure 34). If, even after utilizing these workflows, the precise origin of a knee point remains unknown (case g in Figure 34), further post-mortem analysis becomes necessary. Numerous characterization

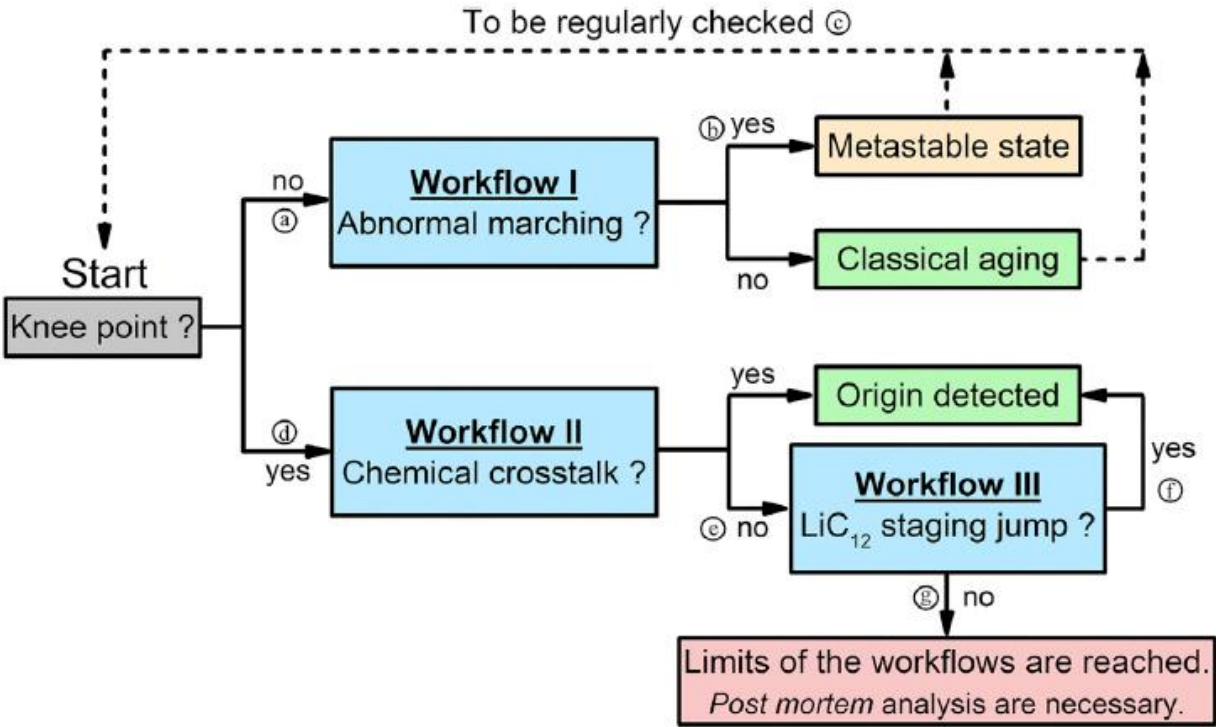


Figure 34 – Overall organization of the workflows

The use of three workflows allows for detecting the origin of knee points or the early sign of their appearance.

techniques can be considered for this purpose, such as imaging techniques, quantification of metals in the SEI, refilling with pristine electrolyte, or assembling symmetric cells, among others, depending on their widespread usage and applicability.

### III.3.1. Detection of shuttling events

#### III.3.1.a. Context

The first workflow is designed to detect abnormal parasitic oxidation and reduction upon aging. This refers to any additional current that is not attributed to the active material's oxidation/reduction. Among the potential interferences, the detection of soluble species transfer is relatively straightforward. This involves chemical substances that undergo repeated reduction and oxidation at the negative and positive electrodes, respectively. Previous studies have reported various types of shuttling in cell chemistries such as graphite/LiNi<sub>x</sub>Mn<sub>y</sub>Co<sub>z</sub>O<sub>2</sub> (NMC, where  $x + y + z = 1$  and  $0 < x, y, z < 1$ ) when employing electrolytes containing dimethyl carbonate [200], [201]. Shuttling has also been observed in Na-ion cells, where the species involved were lithium (or sodium) alkyl carbonate [200], [202] or organophosphate [203], as determined through characterization methods like calorimetry, high-performance liquid chromatography (HPLC) [203], or mass spectrometry (MS) [75]. The first electrochemical indication of shuttling is a decrease in CE [75]. However, a decline in CE can also signify LAM, and relying solely on CE cannot accurately discern cases where different side reactions are competing. To address this, marching capacity tests that monitor the evolution of charge and discharge endpoints, namely  $Q_C$  and  $Q_D$ , respectively, are required.

#### III.3.1.b. Workflow explanations

The initial workflow shown in Figure 35, is designed to identify abnormal parasitic oxidation and reduction during the aging process. In the situation where neither  $Q_C$  nor  $Q_D$  march (as shown in case a in Figure 35), the absence of any side reactions indicates that both interfaces are exceptionally stable and/or fully passivated (as shown by the green case). However, this particular scenario is highly improbable, and  $Q_D$  frequently moves towards higher capacity. In fact,  $Q_D$  advances towards a greater cumulative capacity when the negative electrode has not undergone complete lithiation in the previous charging cycle. This lack of lithium often arises from the lithium loss associated with electrolyte decomposition at the negative electrode and the formation of the SEI. Consequently, there is no significant rise in  $Q_C$  endpoints observed (case b in Figure 35), and the cell ages in a classical manner with  $Q_D$  endpoints, gradually approaching  $Q_C$  endpoints (indicated by the purple case). The rate at which  $Q_C$  and  $Q_D$  progress during this "classical aging" varies depending on battery chemistry and cycling conditions. However, typical values for commercial cells indicate a loss of only

~0.02% of the initial SOC per cycle or less, resulting in the attainment of 80% SOC after 1,000 cycles or more [204]. Unlike  $Q_D$ , an increase in  $Q_C$  endpoints indicates parasitic oxidation, leading to cumulative capacity exceeding the theoretical or experimental limits. By comparing the rates at which  $Q_C$  and  $Q_D$  progress, we can effectively assess degradation at both interfaces, providing valuable information to evaluate the effectiveness of new electrolyte compositions. This approach is exemplified in the work of *Deshpande et al.* [190], where they estimate the advantages of incorporating a 1% vinylene carbonate additive.

The suspicion of shuttling phenomena arises from the observation of similar rates of marching for both  $Q_C$  and  $Q_D$ , as depicted in case c in Figure 35. This occurrence implies the presence of a parasitic oxidation reaction that is precisely counteracted by a reduction reaction at the negative electrode. Consequently, no significant loss in LLI is detected, and the capacity retention remains stable, making it difficult to identify using conventional analysis (depicted as the blue case). Numerous instances of harmless shuttle effects have been documented in the literature [205], and this phenomenon has been utilized to prevent overcharging in graphite/LiFePO<sub>4</sub> cells by introducing benzene-derived substances [206]. Detrimental shuttle phenomena occur when the cell undergoes rapid marching of both  $Q_C$  and  $Q_D$ , as illustrated in

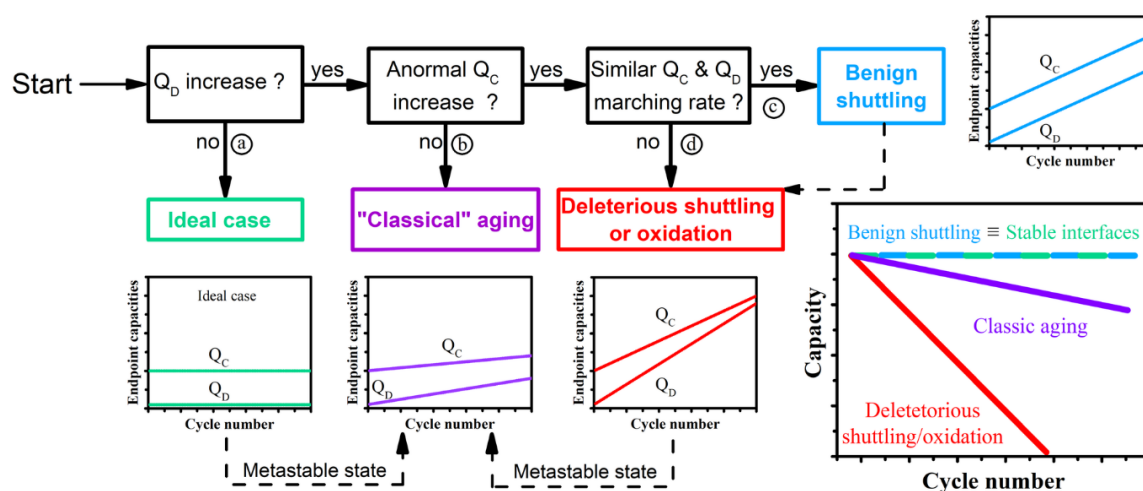


**Figure 35 – Workflow I. Detection of shuttling phenomena**

*The analysis is based on the evaluation of marching capacities. The consequences for the different types of shuttling on the capacity over cycling are schematically shown.*

case d of Figure 35, with  $Q_D$  closing the capacity window rapidly (depicted as the red case). In this scenario, the parasitic oxidation event is not perfectly offset by lithium intercalation at the negative electrode, resulting in an elevated LLI. However, it is important to proceed with caution when attributing the observed electrochemical behaviors solely to shuttle phenomena. It is possible for side reactions at the negative electrode to dominate, and their abundance may mask the presence of a small shuttle current. To complement the analysis based on cycling

data, it is recommended to conduct additional characterizations to determine the nature of the shuttle species and their reactivity. Techniques such as cyclic voltammetry [200] or ultraviolet-visible (UV-vis) spectroscopy [202] can be employed for this purpose.

In conclusion, analyzing the marching rates is a preferred method for closely monitoring cell aging and detecting early indications of shuttle phenomena. This approach is particularly crucial when investigating novel electrolyte compositions or assessing the stability of layered compounds at high potentials. Shuttling events, as described earlier, often go unnoticed in capacity retention curves. However, the accumulation of parasitic reactions can eventually manifest as knee points in the capacity retention curve. These knee points typically signify a shift in the degradation regime or an acceleration of the prevailing aging mechanism. A dedicated workflow, outlined in the following section, can be utilized to study and analyze these phenomena.

### **III.3.2. Detection of chemical crosstalks**

#### **III.3.2.a. Context**

In cell chemistries that employ high potential layered compounds, such as Ni-rich NMC, it is frequently observed that capacity fading slopes exhibit rollovers or knee points. To investigate these phenomena, a tailored workflow is presented in Figure 36. This workflow can be applied in real-time during cell cycling and supplemented with offline analysis once the battery has reached the end of its lifespan.

#### **III.3.2.b. Workflow explanations**

The initial step of the workflow involves conducting DVA prior to the appearance of any knee points. This analysis helps determine whether the capacity fading is attributed to degradation at the positive electrode or the negative electrode. If the graphite electrode exhibits an excess of lithium at the end of discharge, indicated by a leftward shift of the graphite curve (as shown in the inset of Figure 36), it suggests that the primary degradations are associated with the positive electrode. These degradations may include early material fatigue, which can limit the amount of lithium intercalation in layered materials, or the occurrence of parasitic oxidation or crosstalk events discussed earlier. Therefore, it is crucial to verify that the instability does not originate from the material itself. To achieve this, any LAM that coincides with a significant decrease in peak intensities in  $dQ/dV$  during ICA (refer to Figure 31a) would indicate a loss of mechanical properties due to particle grinding, particle disconnection, or loss of contact at the electrode-current collector interface, among other factors. The presence or absence of a single peak in  $dQ/dV$  (refer to Figure 31c) can stem from various factors, such as continuous impedance rise impeding lithium intercalation at a

specific phase transition or the ongoing degradation of the active material itself (case a in Figure 36). The fatigue of the intercalation material can be verified through ex-situ characterizations, including techniques such as X-ray diffraction (XRD) [41], [185], X-ray absorption spectroscopy (XAS) [207], or transmission electron microscopy (TEM) [208], [209]. Electrochemical grinding can be detected using imaging techniques like scanning electron microscopy (SEM) [44], [209], [210] or more advanced tomography techniques [211], [212].

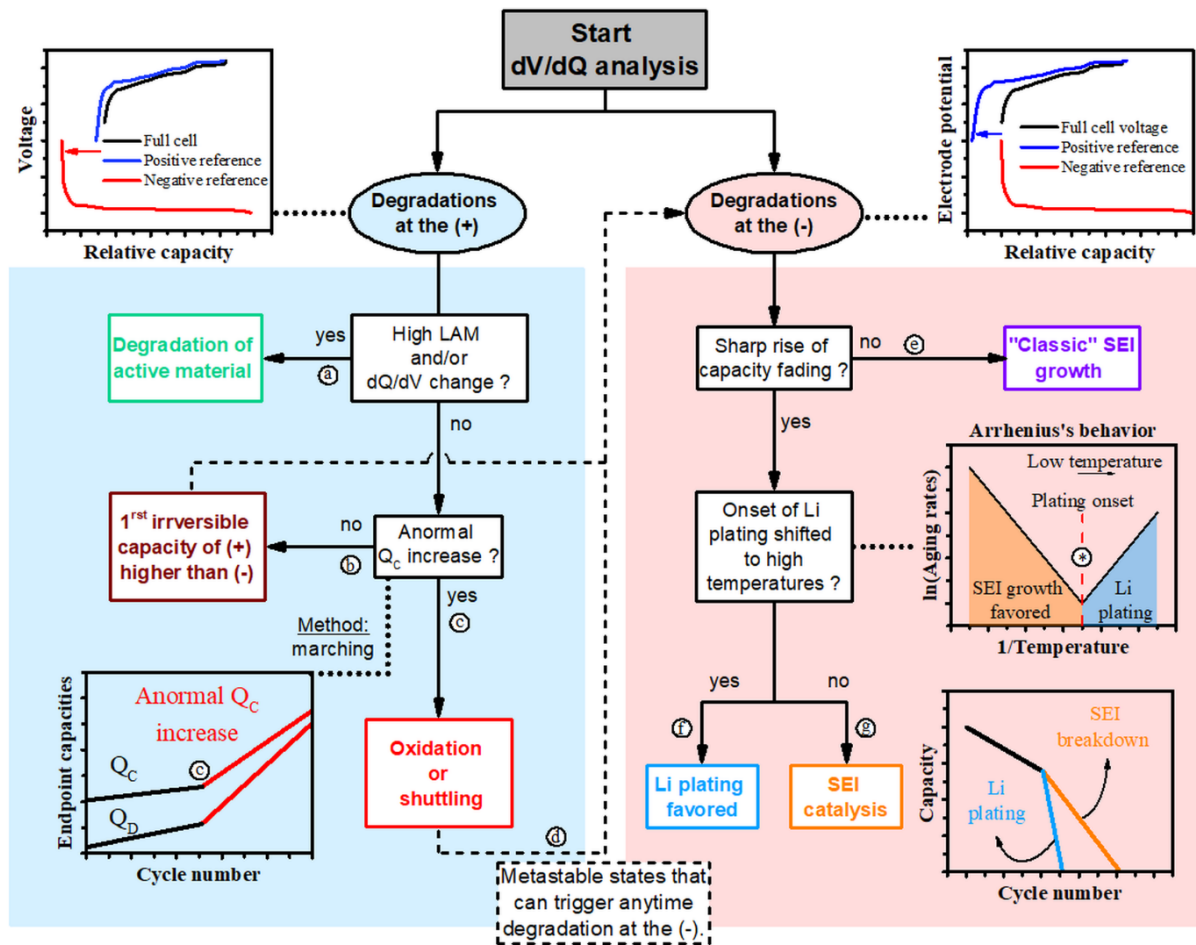


**Figure 36 – Workflow II. Detection of crosstalks from the positive to the negative electrode**  
*The associated effects at the negative electrode interface and the predicted capacity retention curves are schematically represented.*

If the peak intensities in the  $dQ/dV$  curves remain constant with cycling and there is no increase of LAM, it indicates that the degradations are not caused by material-related phenomena. In such cases, another aging mechanism is at play. The subsequent step involves analyzing whether the capacity ( $Q_c$ ) is marching or not. If  $Q_c$  does not increase (case b in Figure 36), it implies that the degradation originates from the initial irreversibility of the positive electrode [199]. Specifically, NMC materials, especially those with high nickel content, tend to

experience a significant capacity loss during the initial cycles, which can surpass the capacity loss associated with the SEI growth at the negative electrode. This phenomenon is expected to be temporary, and the degradation will eventually be dominated by the LLI causing partial delithiation of NMC electrode. On the other hand, when  $Q_C$  is observed to be marching while the positive material does not exhibit fatigue (case c in Figure 36), the instability can be attributed to the oxidation of the electrolyte [49] or the oxidation of species formed upon reduction at the negative electrode, indicating a shuttling event. In this particular situation, the cell is in a metastable state, and the depletion of reductive agents or the accumulation of species formed during oxidation can eventually trigger a sudden acceleration of the LLI. For example, the release of TM cations from the positive electrode can destabilize the SEI and increase the LLI [76], [82], [97]. As previously observed in cases like  $\text{LiMn}_2\text{O}_4$  spinel [80] and lamellar compounds [91], the amount of leached TM depends on the applied voltage [82] and the chemical composition of the electrolyte [143], [145]. Overall, an aging process initially dominated by degradations at the positive electrode can gradually transition to a regime where degradations at the negative electrode become more prominent (case d in Figure 36).

When the degradations at the negative electrode become dominant, which can be attributed to a typical SEI growth, two scenarios are possible. First, the capacity fading remains consistent with what is expected for classical aging (Figure 36, case e, as discussed earlier in relation to classical aging). In this case, the battery is likely undergoing continuous LLI due to the SEI growth. Second, an acceleration of capacity fading is observed, which can be attributed to uncontrolled SEI growth [82], [93], [94]. Additionally, lithium plating may also contribute to this phenomenon, as it occurs when there is an increase in interfacial resistance at the negative electrode, limiting the kinetics of lithium intercalation [96], [97], [213]. To distinguish between these two phenomena without altering the cell's geometry, temperature-dependence studies can be conducted. By examining the Arrhenius behavior of capacity fading at different temperatures, the two mechanisms can be distinguished [101], [102]. At low temperatures, where lithium plating occurs (positive slope on the right side of the Arrhenius plot), the first regime is observed. This is followed by a second regime at high temperatures, which is dominated by interfacial degradations, with SEI growth often being considered the primary factor (negative slope on the left side). *Yang et al.* demonstrated that the temperature at which lithium plating initiates (indicated by \* on the Arrhenius plot in Figure 36) is highly dependent on cycling conditions and internal cell parameters, including capacity balancing [102]. However, by investigating capacity decay at various temperatures, it is possible to determine the sign of the Arrhenius slope, which indicates the prevailing degradation mechanism between lithium plating and SEI growth.

If lithium plating is observed (case f in Figure 36), it is expected to have a detrimental effect on cell performance, leading to a significant increase in IR and the formation of dendrites, which can cause short circuits and ultimately result in a rollover failure [97]. On the other hand, the breakdown or catalysis of the SEI is associated with a break in the slope of the capacity retention curve due to higher rates of LLI (case g in Figure 36, depicted in orange on the capacity retention curve). In both degradation pathways, the cycling capacity windows tend to narrow when plotting the marching capacities, although this phenomenon is expected to occur more abruptly in the case of lithium plating. Therefore, it is recommended to conduct temperature-dependence studies at different stages of cell aging to ensure the early detection of this degradation regime. If the appearance of a knee point is not linked to a shift in degradation mechanism or a chemical crosstalk, it may be attributed to a change in the working potentials of one of the electrodes. This event, which is part of a broader phenomenon often referred to as a shift in voltage windows, necessitates the use of a dedicated workflow based on the ICA, which will be described in the following section.

### III.3.3. Detection of crosstalk associated to voltage window shift

#### III.3.3.a. Context

Recent study has highlighted the significant influence of any alteration in the operating voltage of graphite on the reversibility of lithium intercalation in Ni-rich NMC materials [214]. It is important to note that interfaces within the battery are interconnected not only through chemical crosstalk, as mentioned earlier, but also through modifications in the working potential of one electrode. This phenomenon, commonly known as a voltage window shift, further contributes to the interdependence of battery interfaces. A sudden change in voltage can have different effects: it can either stabilize the capacity retention by preventing lithium plating through an increase in the intercalation potential at the anode [215], or it can accelerate the capacity fading by triggering electrolyte oxidation [76] and/or excessive material fatigue [214]. In either case, a voltage window shift is often caused by an increase in the intercalation potential at the graphite electrode. As a result of the non-reversible lithium intercalation processes discussed earlier, the graphite electrode gradually shifts to lower state of charge (SOC) values at the end of the charge cycle. This continuous shift can cause the potential reached by the graphite electrode at the end of charge to transition from stage I (at 80 mV versus  $\text{Li}^+/\text{Li}$ ) to stage II of intercalation (at 110 mV versus  $\text{Li}^+/\text{Li}$ ). This event is referred as “graphite staging jump” (GSJ).

### III.3.3.b. Workflow explanations

The occurrence of a graphite staging jump is identified through  $dQ/dV$  analysis, where the peak corresponding to the low potential stage I of graphite disappears (case a in Figure 37). This jump can also be confirmed using the DVA, where the lithium intercalation progressively shifts the positive electrode to the left until the charge ends before the  $LiC_{12}$  feature (case b in Figure 37). The primary consequence of the graphite staging jump is the shift of the charge endpoint of the positive electrode to a higher potential when cycling at a fixed cutoff potential (case b in Figure 37). The aging behavior induced by this phenomenon depends on the nature of the positive electrode. For materials with a fixed intercalation potential (case c in Figure 37), such as  $LiFePO_4$ , no significant modification of the aging behavior is expected, and the graphite staging jump is not evident in the capacity retention plot (represented by the green case). However, for layered oxides like NMC materials, cycling at high potential often leads to irreversible structural transitions. Therefore, an increase of 30 mV in the endpoint potential can cause structural damage and accelerate capacity fading (case d in Figure 37), as observed in the cycling of Ni-rich [44], [210], [214] or Li-rich NMC materials [216] at high potential (represented by the red case). The detrimental effects of this jump may include damaging structural changes, as well as side effects such as electrolyte oxidation, particle grinding, or increased internal resistance (case e in Figure 37).

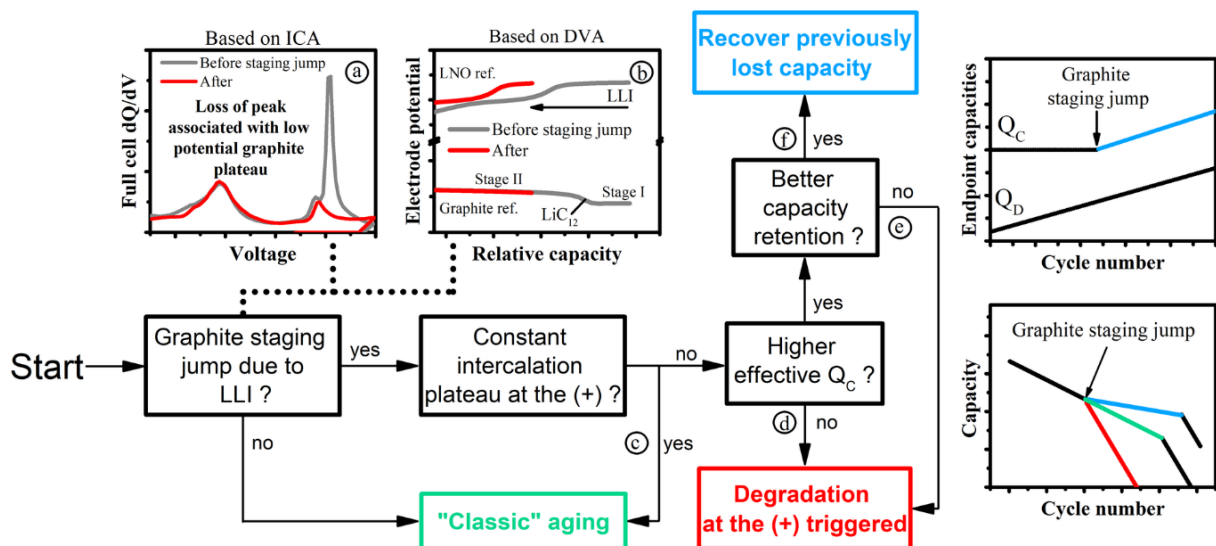


Figure 37 – Workflow III. Detection of graphite staging jump upon aging

*The associated effects on capacity fading are shown depending on the nature of the positive material and its stability at high potential.*

In certain specific cases, GSJ may be temporarily accompanied by beneficial effects on cell capacity (case f in Figure 37). This occurs when a higher SOC achieved by the positive electrode compensates for the aforementioned side effects (represented by the blue case).

The higher effective SOC is evident by the marching of  $Q_C$ , as depicted in Figure 37. Ultimately, the stabilization effect cannot solely be attributed to an increase in negative potential and likely involves other mechanisms, such as the gradual stabilization of the solid electrolyte interface (SEI). Currently, this situation is purely hypothetical, but it can potentially happen with high voltage electrode materials that offer a large capacity within narrow voltage ranges. A specific example of this would be the capacity plateau exhibited by  $\text{LiNiO}_2$  at 4.2 V versus  $\text{Li}^+/\text{Li}$ .

In summary, the consequences of the graphite staging jump on the capacity retention plot can vary depending on the stability of the positive material and/or the electrolyte at high potential. Only by implementing a comprehensive analysis workflow can misinterpretations of knee points in capacity fading curves be avoided. It is crucial to note that a sole electrochemical analysis may only reveal one prevailing degradation mechanism while overlooking the underlying cause of the capacity rollover, as demonstrated in this chapter.



## CONCUSION OF CHAPTER III

In this chapter, we have demonstrated the diversity of chemical and physical events that can cause knee points and capacity rollover in graphite/layered oxide cell chemistries by providing three examples of crosstalking mechanisms previously reported. It is important to note that when cycling cells in laboratory conditions, relying solely on observations of improved capacity retention and/or CE over several hundred cycles can lead to erroneous conclusions. Beneath these positive indicators of cell lifetime, there may be complex crosstalking mechanisms at work, significantly reducing the overall lifespan of the cell. To address this issue, we have proposed several analysis workflows that can be readily implemented to avoid misleading interpretations of the benefits offered by new electrolyte compositions, coatings, separators, and other advancements. Given the objective of machine learning algorithms and AI-driven predictions for cell lifetime in BIG-MAP, the need to obtain clear electrochemical analysis workflow for intricate phenomena like crosstalk was an objective of the project. Furthermore, these workflows can also be applied to other metal-ion chemistries, such as sodium-ion chemistries. However, it is crucial to develop dedicated workflows for metal-based technologies like lithium-metal or all solid-state batteries, as the understanding of LLI and the interpretation of electrochemical signatures at the metallic negative electrode are more challenging compared to graphite.

Overall, the introduced analysis workflows establish a foundation for a better understanding of the degradation processes in battery technologies. These workflows are crucial in facilitating the exploration of methods to stabilize the nickel-rich interface at high voltages, which continues to pose a major challenge in the context of BIG-MAP and, more broadly, in addressing ongoing challenges in the short term. Subsequently, the upcoming chapters will address advanced approaches to stabilize high voltage batteries, focusing on the utilization of LNO and NMC811 materials.

Finally, it is quite probable that comparable approaches for identifying intricate deteriorations have been suggested internally within the industry, such as through Design and Failure Modes Analysis (D-FMEA). However, this intellectual process and rationale for detecting complex failure modes are not commonly found in academia. Hence, we underscore the novelty of the concept and the valuable contribution it brings. In the context of BIG-MAP, the analysis protocols were not mandated; rather, we promoted them and took measures to make them readily available to the majority of researchers.



**CHAPTER IV: ASSESSING THE  
EFFECTS OF DISSOLVED  
TRANSITION METALS IN  
GRAPHITE/LiNiO<sub>2</sub> CELLS  
PERFORMANCE**



## INTRODUCTION OF CHAPTER IV

The lack of stability in Ni-rich positive electrodes poses a barrier to their widespread acceptance within the battery community. This instability stems from various physical factors, such as particle cracking and phase transformation, as well as chemical factors like electrolyte oxidation and the dissolution of transition metals (TM). Further details are available in the introduction chapter. Among the various degradation processes, the presence of TMs at the negative electrode is as a significant contributor to capacity fading in Ni-rich cells, despite their overall weight accounting for less than 1% of the TM's total weight [217]. Hence, TM dissolution is a pertinent illustration of the complex interplay involved in crosstalk, where solvated transition metals (TM) migrate to the negative electrode and initiate unclear side reactions.

When investigating TM-induced deteriorations at the negative electrodes, two scenarios are discussed as the primary causes of knee points or capacity rollover: the acceleration of SEI growth (i) [82], [94] and the initiation of lithium plating (ii) [96], [218]. First, TMs are proposed to activate the decomposition of components derived from solvents or salts, resulting in a more reduced state. Nickel, cobalt, and manganese, known for their catalytic properties in chemistry, have been shown to induce the decomposition of the electrolyte and SEI through density functional theory (DFT) calculations [93]. In the second case, the deposition of transition metals at the anode facilitates the plating of lithium, which leads to further side reactions with the electrolyte, ultimately causing the observed capacity rollover. In more severe instances, this plating process results in the formation of dendrites, leading to localized short-circuits [96]. The previously developed workflows are therefore perfectly suited to address the complexities of crosstalk degradations and provide a new understanding.

In Chapter IV, the goal is to provide insights into the impact of transition metal dissolution complexity. To achieve this, graphite/LiNiO<sub>2</sub> cells will be employed to evaluate the effect of nickel alone, before progressing to more intricate designs. The initial part focuses on assessing cell performance and comprehending the influence of cell voltages on nickel dissolution. Specifically, investigations into the incorporation mechanisms of nickel within the SEI will be conducted. Subsequently, the study expands to encompass the effects of transition metals, namely manganese and cobalt, by introducing additional salts. As a result of degradation, the cells experience changes in aging rates due to the misalignment of electrode capacity windows. Finally, the last part of the study aims to differentiate between the effects of SEI growth and lithium plating.

## IV.1. NICKEL CROSSTALK AND RESULTING CELL PERFORMANCE

### IV.1.1. Graphite LiNiO<sub>2</sub> cell performance

The initial step involves assessing the voltage-dependency of degradations in graphite/LNO cells. To achieve this, the cells were subjected to cycling at 4.2, 4.5, and 4.8 V at C/2 for 100 cycles at CCCV C/2,  $i < C/20$ . Further information on the experimental cycling process are available in Annex 3. To analyze the deteriorations throughout the entire lifespan of the battery, additional control cycles were implemented at regular intervals of 10 cycles, using C/20 cycles (Figure 38). The frequency of these control cycles may appear to be high initially; however, LNO is a highly sensitive material above 4.2 V and can experience degradation within a dozen of cycles. The high frequency of the control cycles aims to capture this evolution.

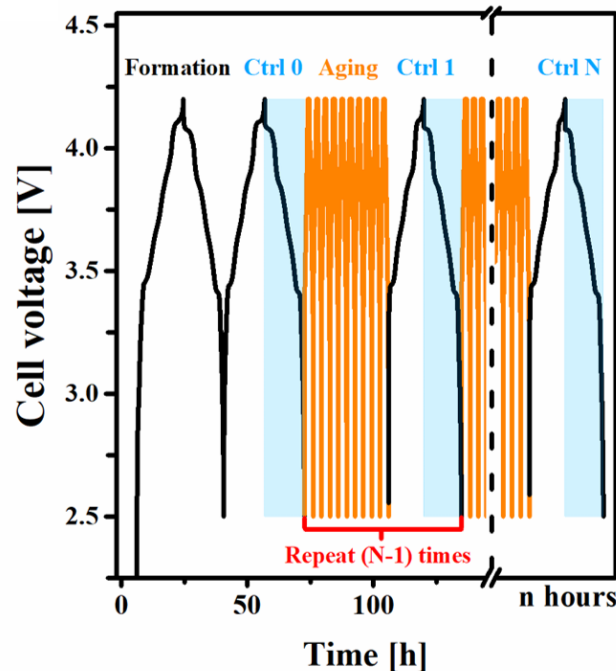


**Figure 38 – Cycling protocol used in graphite/LNO cells**

*Cycling protocol employed to periodically diagnose cell performance of graphite/LNO cells. Aging consists in ten consecutive C/2 – D/2 cycles with a constant voltage (CV) step at the end of each charge until current is lower than C/20. Afterwards, control cycle is performed at C/20 – D/20 to assess cell performance and perform dV/dQ analysis on discharge (shaded blue part).*

Cycling results are shown in Figure 39. Given that the high voltage intercalation plateau for LNO occurs at 4.15 V in the graphite/LNO full cell, equivalent to 4.2 V vs Li<sup>+</sup>/Li, comparable capacities were observed for cutoff voltages of 4.2, 4.5, and 4.8 V (Figure 39a). However, an

additional capacity was initially detected up to the 30<sup>th</sup> cycle specifically for the 4.8 V cutoff voltage, which is further discussed in part IV.1.2.a. Furthermore, the increase of the cutoff voltage beyond 4.5 V has a significant impact on cell performance, resulting in capacity losses of 25% (4.5 V) and 55% (4.8 V) after the 6<sup>th</sup> control cycle, compared to 21% at 4.2 V. These performance degradations corroborate the lower CEs recorded at higher cutoff potentials (Figure 39b).

In addition, it is essential to examine whether the degradation is influenced by the experimental protocols employed, specifically the inclusion of a slow control cycle every 10 cycles, with regard to cell performance. When utilizing cutoff potentials of 4.2 and 4.5 V, CEs

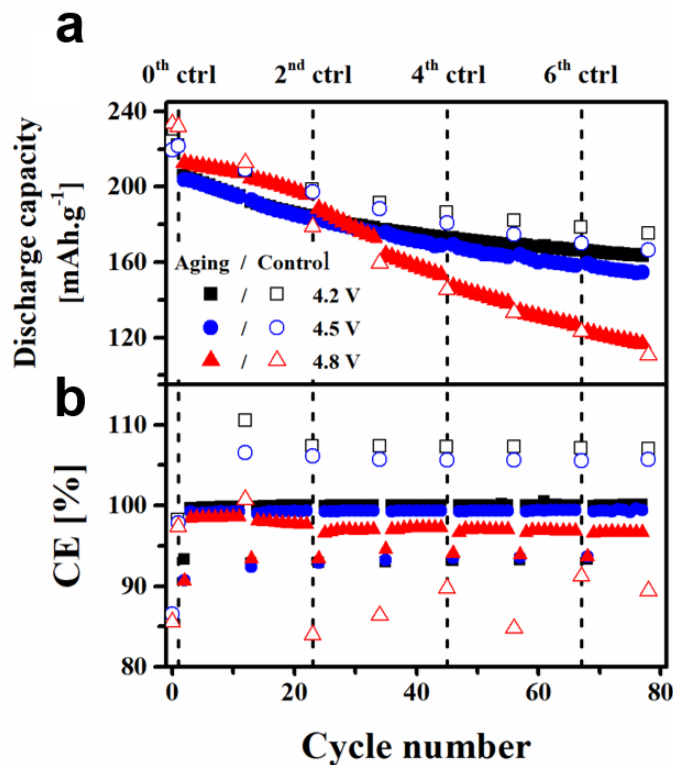


**Figure 39 – Voltage effect on graphite/LNO cells**

*Evaluation of graphite/LNO performance using aging protocols. Capacity retention a) and coulombic efficiency plot b) for cells measured at different voltage cutoffs (4.2, 4.5 and 4.8 V).*

greater than 100% were recorded for each control cycle throughout the cycling process, indicating an artifact related to the testing protocol when changing the current density (Figure 39b). This artifact arises from the incomplete re-lithiation of LNO during the last discharge of the discharge step conducted at C/2, resulting in an artificially lower charge capacity during the subsequent charge at C/20. During the subsequent aging cycle at C/2, CEs close to 90% were observed. This effect stems from the previous discharge at C/20, during which more lithium was intercalated into the LNO electrode, thereby enabling the recovery of additional capacity during the subsequent C/2 charge. Ultimately, this artifact is caused by varying

degrees of intercalation achieved at different C-rates and does not stem from degradations such as electrolyte oxidation.

Another artifact was observed with this protocol: a lower capacity retention compared to aging cycles performed without control cycles at low C-rates (Annex 4, grey, light blue, and orange dots). This capacity loss was observed at high voltage, specifically when employing a cutoff voltage of 4.8 V, indicating that low current densities promote parasitic reactions associated with electrolyte oxidation above 4.5 V, thereby degrading the overall performance of the full cell over time. Additionally, at 4.8 V, a slight initial capacity drop was observed at the beginning of the 10 aging cycle period following the control cycle. This capacity drop was more pronounced at high voltage, resulting in a stair-shaped capacity retention curve (Annex 4). In definitive, although the cycling procedure adopted in this study is not neutral regarding cell performances, degradation mainly occur from the use of high cutoff voltages (i.e. 4.8 V), reinforcing our will to understand the associated side effects. While the capacity retentions of cells at 4.2 V and 4.5 V exhibit a sublinear trend, the cell cycled at 4.8 V encounters a knee point, thus advocating for the utilization of **workflow I** as mentioned earlier in chapter III.

### IV.1.2. In-depth analysis of degradations

#### IV.1.2.a. Marching

The degradations are further evaluated using marching analysis (Figure 40). The three cells experience marching of capacity endpoints, which rate increase with the voltage cutoffs. From one cycle to the next, the cells experience a shift of discharge capacity endpoints ( $Q_D$ ) towards greater capacities, this event being accentuated with increased cutoff voltage. Lithium loss during the SEI build-up or loss of active mass from the electrodes can both explain this shift, but these two effects cannot be distinguished without further analysis. For a cutoff voltage set at 4.8 V, not only  $Q_D$  but also the charge capacity endpoint ( $Q_C$ ) shift, following an extra oxidation reaction occurring at the positive electrode. Since the high voltage (de)intercalation plateau of LNO occurs at 4.15 V vs graphite, oxidation thus originates from parasitic reactions such as electrolyte oxidation, inducing additional lithium intercalation at the negative electrode [189]. The greater lithiation degree of graphite thus compensates in part the lithium losses associated to the SEI formation, explaining the initial greater discharge capacities observed in Figure 39a when using a 4.8 V cutoff potential. Despite this effect, the shift of discharge endpoints remains greater for 4.8 V cutoff potential (Figure 40), inducing a continuous shrinkage of cell capacity window (defined as  $Q_C - Q_D$ ), i.e. a loss of cell capacity. In other words, the oxidation process at 4.8 V does not provide sufficient extra capacity to avoid capacity decrease, leading to a continuous loss of capacity. Ultimately, the shift in endpoint capacities is due to cell degradations from both electrodes, either in the form LLI through various side reactions or as LAM through particle cracks or loss of electronic contacts.

However, from the raw electrochemical curves  $V = f(Q)$  or marching analysis, effects related to LLI and LAM cannot be distinguished that advocates the utilization of **Workflow II** introduced in chapter III.

#### IV.1.2.b. DVA

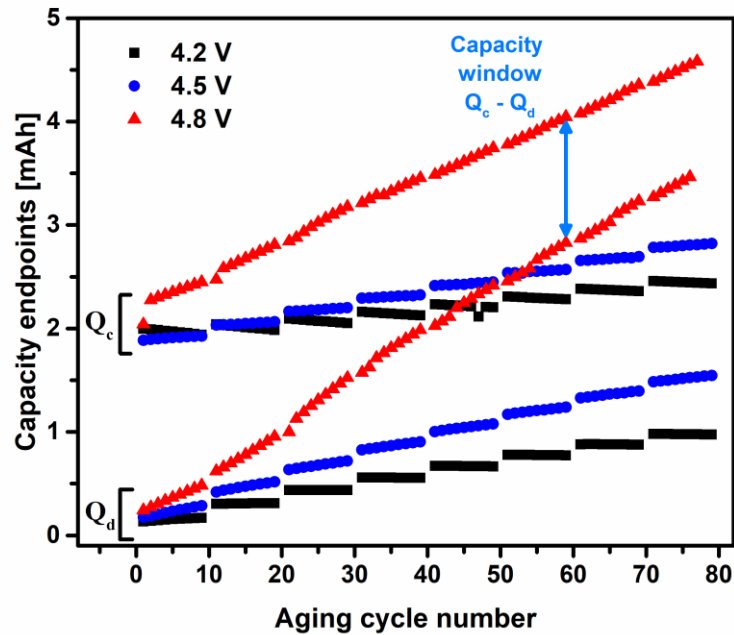


**Figure 40 – Capacity marching of graphite /LNO curves**

*Charge and discharge capacity endpoints of graphite/LNO full cells. Only aging cycles are shown for sake of clarity, i.e. the ten consecutive CCCV ( $C/2$ ;  $i < C/20$ ) followed by  $C/2$  discharge). A clear increase of charge end point capacity ( $Q_c$ ) is observed at 4.8 V associated to parasitic oxidation which compensates lithium losses occurring at the negative electrode (referred as  $Q_D$  increase).*

The DVA provides further information on cell degradations and their associated origins. Using references curves for  $\text{LiNiO}_2$  & graphite vs  $\text{Li}^+/\text{Li}$ , the derivative  $dV/dQ$  vs  $Q$  curves obtained from discharge curves recorded during the control cycles are fitted and results shown in Figure 41. The reconstructed model (green) accurately aligns with the measured full cell curve (black) for the four displayed control cycles throughout the battery's lifespan, indicating the continued validity of the fit. Additional fits can be found in Annex 5 for the control 0 of 4.5 V and 4.8 V cells.

## LP57 - 4.2 V

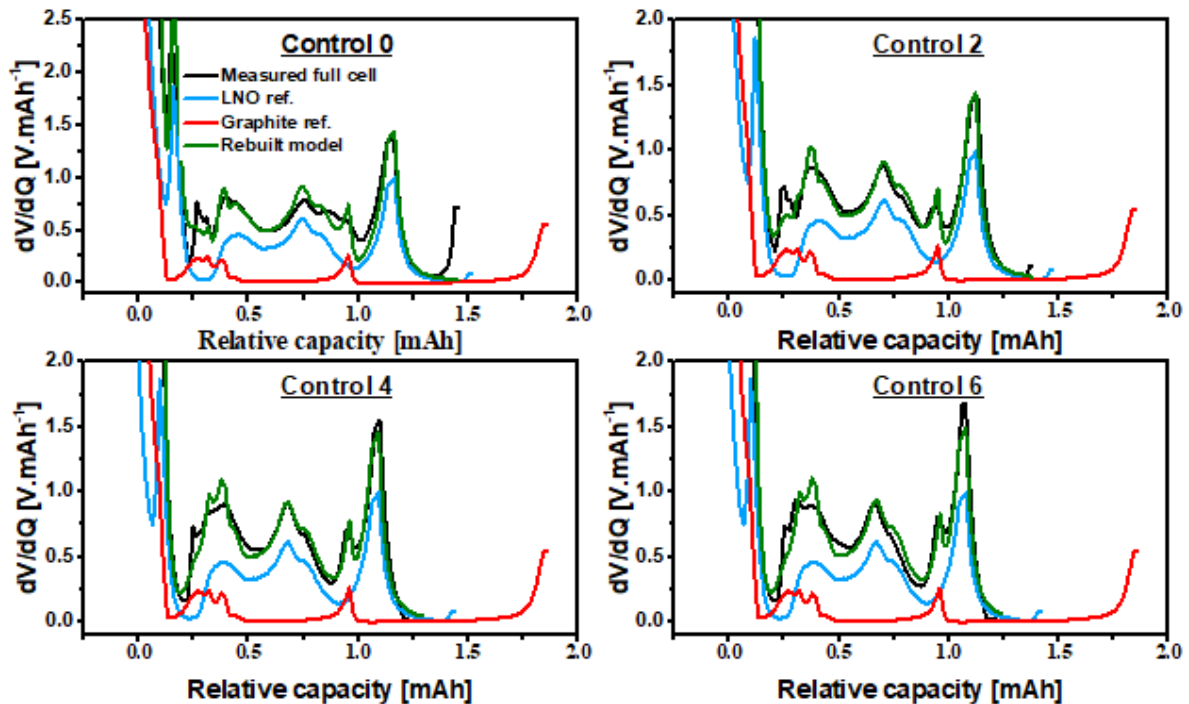


Figure 41 – dV/dQ fitting of graphite/LNO cells

*dV/dQ fittings of graphite/LNO cells at 4.2 V upon aging. LNO and graphite references are recorded at C/20 as well as full cells during control cycles. Fittings remain valid up to 6<sup>th</sup> control.*

Using a relative capacity scale (Figure 42), degradation associated with the negative electrode are visible from a left-shift of the  $\text{LiNiO}_2$  capacity curve (referred to as negative slippage). Indeed, following degradations at the anode such as LLI occurring during the SEI formation, the positive material is not fully relithiated at the end of discharge. In a similar manner, degradations at the positive electrode can be seen by a left-shift of the graphite capacity curve (referred to as positive slippage), revealing that some amount of lithium remains in graphite at the end of discharge following an extra lithiation resulting from solvent oxidation, as discussed above. Ultimately, oxidation and reduction parasitic events lead to continuous modification of lithiation degrees of respective electrodes over cycling. However, the associated capacity slippages are only visible if degradations occurring at one electrode prevail over the other. In other words, if both positive and negative parasitic capacities compensate each other, SEI can grow and the solvent oxidize without recording any capacity slippage. Evidently, this holds true if the mass of active materials remains unchanged.

In Figure 42, the increase of negative slippage over cycling is observed, regardless of the cutoff voltage (ranging from light to dark blue). This negative slippage is linked to the LLI during the initial growth of the SEI and its evolution over cycling, which represents the repairing/ongoing stabilization process. The negative slippage exhibits a similar trend for cutoff voltages of 4.2 V and 4.5 V. In addition, after the 4<sup>th</sup> control cycle, the slippage direction changes to the right (see insets in Figure 42), and a simultaneous increase in positive slippage is observed. This phenomenon indicates a switch in the degradation regime, where the rate of lithium loss at the negative electrode slows down compared to any degradation phenomena occurring at the positive electrode. In other words, starting from the 40<sup>th</sup> aging cycle, the amount of lithium trapped in the SEI decreases gradually from one cycle to the next, suggesting its stabilization. The reversal phenomenon is further intensified by LAMPE, as particle cracking reduces the number of intercalation sites in LNO while the lithium inventory remains relatively constant. No significant modification of the dQ/dV curves is evident in Annex 6, indicating that

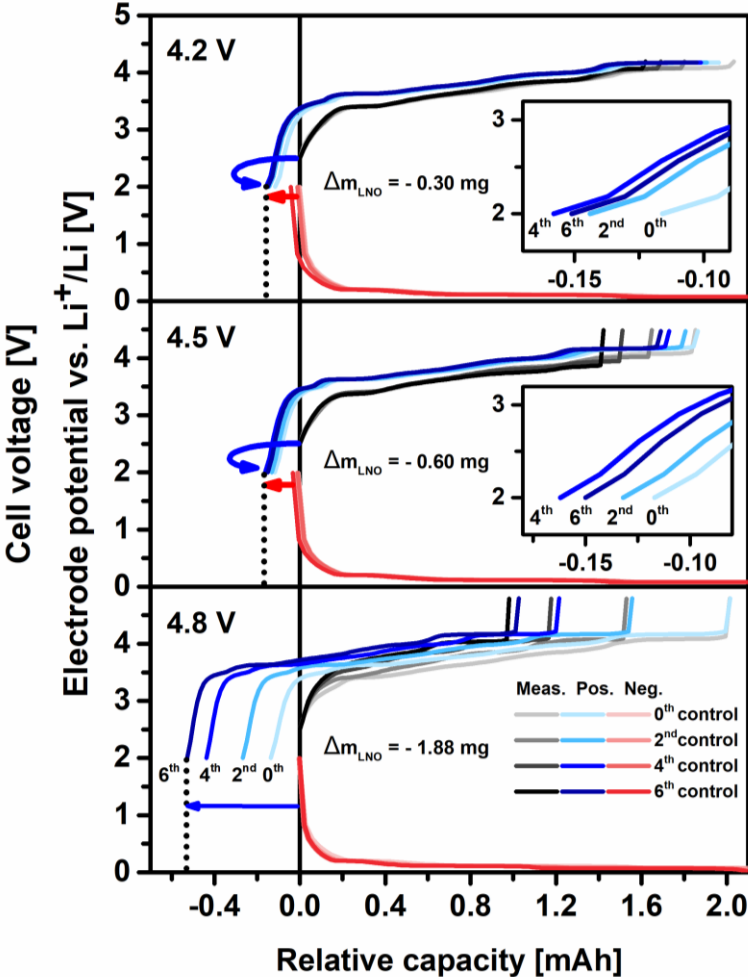


Figure 42 – DVA of graphite/LNO cells

Associated dV/dQ analysis showing capacity degradations mainly originating from lithium loss inventory, as indicated by the negative shift of positive electrode curve.

nickel migration towards interlayers is not the primary contributor to this phenomenon. As a result, the apparent lithiation degree of LNO increases. However, the negative slippage remains significantly larger, indicating the occurrence of massive parasitic reactions, which is consistent with the poorer capacity retention and coulombic efficiency observed in Figure 39.

Moreover, the switch in degradation regime is not observed at 4.8 V, where the negative slippage continues to shift to the left, indicating that the growth of the SEI and its repair process prevail for a longer duration. Since no positive slippage is observed, parasitic oxidation events upon charge at the positive electrode result in additional lithium cations being inserted into the negative electrode, which are subsequently utilized during the subsequent discharge when the graphite electrode becomes fully delithiated. Thus, as the anodic parasitic reactions almost perfectly compensate for the lithium losses at the negative electrode, the detrimental electrolyte oxidation artificially extends cell performance in the early cycles. However, caution must be exercised when performing dV/dQ analysis using large cutoff potentials such as 4.8 V or 4.5 V, as they can induce gradual changes in the potential curves associated with bulk degradations during the H<sub>2</sub>→H<sub>3</sub> phase transition [41]. At 4.2 V, LNO still experiences the deleterious phase transition, but structural degradations do not significantly affect the dV/dQ fitting up to the 6<sup>th</sup> control cycle, as shown in Figure 41. Degradations related to the loss of lithium associated with SEI growth or other parasitic reactions can thus be identified by employing differential voltage analysis.

At last, LAM PE can also be extracted from this analysis. Using 4.2 V cutoff voltage, LAM was found to account for 3.3% of the initial LNO mass at the 6<sup>th</sup> control cycle, while as much as 27.8% LAM was measured at 4.8 V, demonstrating a strong voltage dependency. Further details on calculations can be found in Annex 3. Particles crack, loss of electric contacts or nickel dissolution can all participate to LAM, but their relative extent cannot be assessed using the dV/dQ analysis. Furthermore, as previously discussed in the literature, dissolved transition metal such as nickel are known to precipitate the cell failure.

#### **IV.1.3. Mechanism of Ni incorporation in the SEI**

To distinguish between the dissolution of nickel and the inherent LAM PE by electrochemical grinding or irreversible structural modifications, the amount of leached nickel on graphite electrodes was measured after aging. The cells underwent the following cycling procedure: one formation cycle (C/20), 10 aging cycles (CCCV: C/2;  $i < C/20$ ), and one and a half cycle (C/20) to end cycling in charged state. Subsequently, the cells were opened to recover the negative electrode and the graphite surface was rinsed with EMC. The amount of nickel was quantified using inductively coupled plasma-mass spectrometry (ICP-MS). Further

details about sample preparation and measurement are available in Annex 3. As shown in Figure 43a, the amount of nickel found on the surface of the graphite electrodes increases almost exponentially with the cutoff voltage. At 4.8 V, 0.5% by weight of the nickel contained in the LNO positive electrode, which corresponds to 665 parts per million (ppm) in the electrolyte (30  $\mu$ L), was measured, consistent with previous observations [82]. It is important to note that this quantification only considers the nickel cations deposited onto the negative electrode, and therefore the values are likely underestimated. Nonetheless, the measured quantities account for 0.98% (at 4.5 V) and 1.90% (at 4.8 V) of the previously determined LAM PE after fitting for equivalent cycling times. The amount of dissolved nickel at 4.2 V was insignificant, rendering such a comparison irrelevant. Ultimately, nickel dissolution is an essential aspect of the LAM process, although electrochemical grinding and the loss of electronic conductivity resulting from particle cracking remain the primary contributing factors.

The ICP results further confirm the occurrence of crosstalk phenomena as extensively reported in the literature, drawing our attention to the interaction between TMs and the SEI at the negative electrode. Cyclic voltammograms (CVs) were conducted using electrolytes containing nickel, where the concentration of nickel was set at 665 ppm based on prior ICP-MS measurements. CVs shown in Figure 43b, revealed a reduction peak at 2.3 V vs  $\text{Li}^+/\text{Li}$  associated with nickel reduction on the copper surface before the electrolyte reduction (ethylene carbonate—EC) starting at 0.8 V vs  $\text{Li}^+/\text{Li}$ . Additionally, during the formation of the SEI, the intensity of the nickel reduction peak remains unchanged, unlike the peak associated with EC reduction, indicating that the SEI does not inhibit nickel reduction.

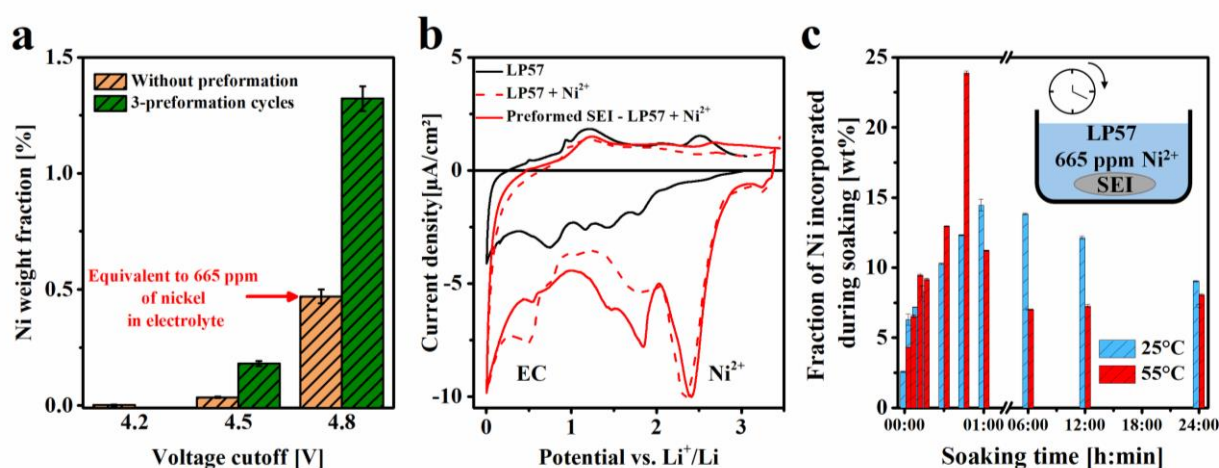


**Figure 43 – Study of TM dissolution and incorporation in the SEI**

*Interaction between leached nickel cations and the SEI. (a) Amounts of nickel detected in graphite electrodes SEI (orange) and with longer formed SEI (green, two additional C/20 cycles beforehand) as a function of cutoff voltage. (b) Cyclic voltammograms showing reduction of nickel cations on copper foil for LP57 electrolyte (black), LP57 + 665 ppm  $\text{Ni}^{2+}$  (red dotted line) and LP57 + 665 ppm  $\text{Ni}^{2+}$  after pre-forming the SEI in LP57 (red). (c) Amounts of nickel detected after soaking a graphite electrode with SEI formed either at 25°C (blue) or 55°C (red) for different immersion times in nickel-contaminated electrolyte (665 ppm).*

The interaction between the SEI and dissolved nickel cations was further examined by immersing pre-cycled graphite electrodes (3 cycles at C/20) in nickel-contaminated electrolyte (665 ppm in 200  $\mu$ L) for different durations. As depicted in Figure 43c, the amount of nickel was observed to increase during the initial hour of immersion. Consequently, the SEI spontaneously absorbs nickel cations even at open circuit potential (OCP), supporting the previously proposed ion-exchange mechanism by *Amine et al.* [89], [219], [220]. To investigate the influence of SEI morphological properties on the ion-exchange process, a thicker SEI was formed on the graphite surface by cycling at 55  $^{\circ}$ C. The results revealed that the amount of nickel increased to approximately twice the amount measured for the SEI formed at 25  $^{\circ}$ C, indicating that a thicker SEI, which contains more lithium cations, absorbs a higher quantity of nickel cations from the electrolyte, as discussed earlier. To illustrate this effect, full cells were first cycled at 4.2 V to form the SEI on the graphite surface (three C/20 cycles at 4.2 V) before being cycled at different cutoff voltages. Consequently, three to four times more nickel was detected at the anode (Figure 43a, green bars).

However, our soaking experiments also demonstrated that after one hour, the nickel content decreased for both SEIs formed at 25 or 55  $^{\circ}$ C, suggesting that the SEI dissolves over time and releases nickel cations (Figure 43c). In conclusion, the ICP results confirmed that nickel is released from cycling LNO at high voltages, and this phenomenon contributes to a portion of the LAM PE. The dissolved nickel cations subsequently incorporate into the SEI through electrochemical reduction at approximately 2.3 V vs Li<sup>+</sup>/Li (Fig. 7b) and an ion-exchange mechanism at open circuit potential (Figure 43c).

In general, while the CVs and ICP quantifications are not included in the developed workflows, they significantly contribute to the understanding of the dynamics of nickel ions at the negative interface. Overall, any additional complementary analyses to the workflows are beneficial for the comprehension of degradation processes.

## IV.2. BENCHMARK OF TRANSITION METAL EFFECTS

### IV.2.1. Effect of TM on cell performance

The DVA and post-mortem ICP-MS analysis cannot conclude that nickel cations released into the electrolyte are responsible for the observed LLI in Figure 42. Therefore, the effect of nickel on cell performance was separately evaluated by adding Ni(TFSI)<sub>2</sub> salt to the LP57 electrolyte. The nickel concentration was set at 665 ppm (12 mM), which corresponds to an amount of nickel equivalent to 0.5wt%, as determined by ICP-MS quantifications at 4.8 V.

Graphite/LNO cells were cycled to 4.2 V using the aging/control protocol (Figure 44), where nickel dissolution can be ignored, as evidenced by the minimal nickel levels observed in Figure 43a. This allowed for a focused analysis of the additional nickel's side effects. As depicted in

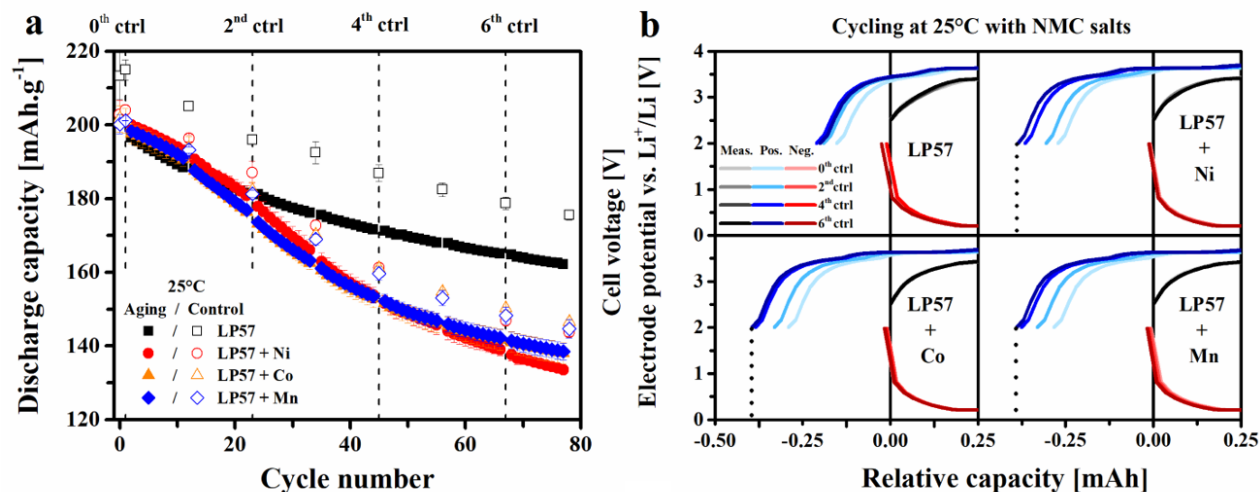


**Figure 44 – Effect of TM on cell performance**

*Performance degradations for TM-contaminated cells upon cycling. (a) Capacity retention measured for LP57 (black) or LP57 contaminated with 665 ppm nickel (red), cobalt (orange) or manganese (blue). Capacity is normalized by the mass of LNO active material. (b) Corresponding slippage analysis showing an increase of lithium loss inventory when TMs are added in the electrolyte.*

Figure 44a, the addition of nickel significantly impacts cell performance right from the beginning of cycling, with an average discharge capacity of 201  $\text{mAh.g}^{-1}$  ( $0^{\text{th}}$  control) compared to 214  $\text{mAh.g}^{-1}$  measured in LP57. The limited concentration of added TFSI<sup>-</sup> anions in the electrolyte does not disturb the favorable passivation of aluminum by PF<sub>6</sub><sup>-</sup> anions, implying that dissolved Ni<sup>2+</sup> cations solely influence the initial cell chemistry, specifically the formation of the SEI. The capacity gap further widens starting from the 13<sup>th</sup> cycle in electrolytes containing dissolved nickel, with a sharp capacity drop observed between the 2<sup>nd</sup> and 4<sup>th</sup> control cycles, before stabilizing and returning to the same degradation rate observed for LP57. To determine if this conclusion is unique to nickel cations, cobalt and manganese salts were also tested by adding Co(TFSI)<sub>2</sub> and Mn(TFSI)<sub>2</sub> (665 ppm) (Figure 44a). Similar findings can be inferred, thus establishing the generality of this conclusion to any TM dissolution relevant to NMC compounds.

The analysis primarily focused on the slippages associated with the introduced transition metals, and the corresponding fits can be found in Annex 7. In all four electrolytes, a negative slippage is observed (indicated by the blue curves), which progressively shifts to the left during cycling. This slippage is primarily associated with LLI occurring at the graphite electrode (Figure 44b). The LAM PE also contributes to the decrease in capacity, but to a

lesser extent, particularly at low cutoff potentials as previously shown in Figure 42. For nickel, cobalt, and manganese, the initial slippage values are approximately double those observed for LP57 (0.27 to 0.29 compared to 0.15 mAh). Additionally, when TMs are present in the electrolyte, the subsequent LLI increases at a rate 1.5 times faster after the 0<sup>th</sup> control, specifically between the 2<sup>nd</sup> and 4<sup>th</sup> control cycles, until reaching a value of approximately 0.4 mAh. This behavior aligns with the capacity fading observed in Figure 44a.

The reduction reaction  $TM^{2+} + 2e^- \rightarrow TM^0$ , considering an initial concentration of 665 ppm (in 30  $\mu$ L of electrolyte), would only account for approximately 0.02 mAh of the observed negative slippage, which is much lower than the actual values recorded. Therefore, the deposition of TMs on graphite electrodes leads to an increase in LLI during the formation of the SEI in the initial cycles, and it triggers additional lithium losses during subsequent cycles, thereby destabilizing the SEI during cycling. The higher LLI associated with dissolved TMs has been discussed in previous studies and has been attributed to catalytic loops [93], decomposition of SEI species [95], or thickening of the SEI [82]. The results conclude on the deleterious role of the TM crosstalk on cell performances. Nevertheless, the ongoing LLI caused by the presence of TMs fails to account for the observed stabilization of discharge capacity beyond the 4<sup>th</sup> control cycle with nickel, manganese, and cobalt. There is another phenomenon at work that demands additional investigation.

#### IV.2.2. Graphite staging jump

To provide an explanation for the observed stabilization of capacity loss with TM in the electrolyte after the 4<sup>th</sup> control cycle, an analysis of raw dV/dQ and dQ/dV curves is conducted, following the **workflow III** introduced in Chapter III. The stabilization corresponds to the disappearance of the LiC<sub>12</sub> feature of graphite in the dV/dQ curves (Figure 45a). The continuous LLI resulting from TM activity at the negative electrode causes GSJ, i.e. a decrease in the SOC of graphite electrode, preventing the lithiation of the graphite lithiation plateau at 80 mV vs Li<sup>+</sup>/Li. The charge endpoint thus occurs on the upper lithiation plateau, approximately 30 mV higher, at around 110 mV vs Li<sup>+</sup>/Li. As a result, the voltage for the last LNO intercalation plateau progressively decreases to 4.08 V during charge in full cells with contaminated electrolytes (Figure 45b), compared to 4.11 V with LP57 electrolyte. While the gradual increase in cell impedance hampers the final oxidation plateau of LNO in the LP57 electrolyte, as observed in the dQ/dV analysis (lower panel, Figure 45b), the lower reaction voltage achieved when introducing TM enables a higher state of charge to be reached by LNO before reaching the 4.2 V cutoff voltage. As a result, the apparent stabilization of capacity retention during cycling arises from the prolonged delithiation stage experienced by LNO during the charging

process. However, this phenomenon cannot be solely attributed to a higher negative potential and likely involves other mechanisms, such as the gradual stabilization of the SEI.

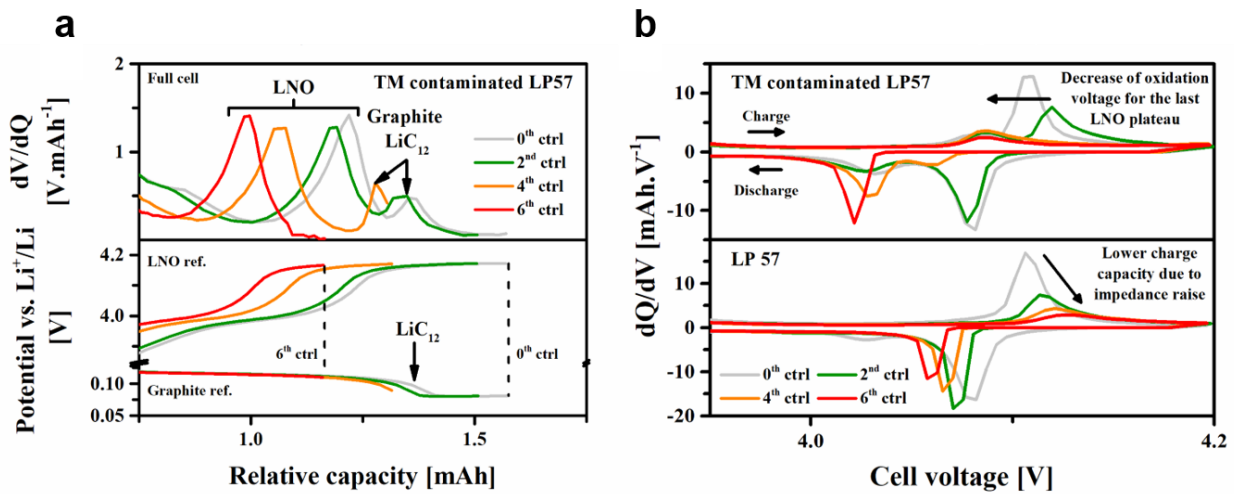


**Figure 45 – Detection of graphite staging jump**

Example of  $dV/dQ$  vs  $V$  curves recorded for TM-contaminated electrolyte (upper panel, Ni-containing LP57) and respective lithiation degree reached at the end of charge for both electrodes (lower panel). (d) Associated  $dQ/dV$  vs  $Q$  curves showing decrease of oxidation voltage for the last LNO plateau with Ni-contaminated electrolyte (upper panel) compared to LP57 where it is absent (lower panel).

### IV.2.3. Short-lived benefits

By enabling re access to the LNO plateau at 4.2 V and allowing for a capacity of 40 mAh.g<sup>-1</sup>, the GSJ facilitates a temporary deceleration of capacity fading. However, over prolonged cycling, the detrimental H2→H3 phase transition at 4.2 V prematurely fatigues the bulk LNO and exacerbates capacity degradation. Dose *et al.* demonstrated comparable aging behavior in graphite/NMC811 cells, in which the graphite anode exhibited a potential jump upon LLI [214]. Subsequently, the increased potential of NMC811 at the end of the charging process led to more significant structural damage, ultimately accelerating capacity losses. Therefore, despite a similar origin rooted in a change in staging at the graphite electrode associated with substantial LLI, cell performance is directly influenced by the nature of the positive electrode material and its working potential. However, the exact cause of the increased LLI in electrolytes contaminated with TMs has not been elucidated at this stage.

## IV.3. EFFECTS OF METALS AT THE GRAPHITE ELECTRODE

### IV.3.1. Method introduction

#### IV.3.1.a. Theory

To determine whether the addition of TMs to the SEI leads to rollover failure caused by lithium plating on the graphite surface, as previously suggested in studies [96], [198], a specific procedure was employed. While our study observed that lithium plating can indeed result in LLI, establishing a clear cause-and-effect relationship between TMs and plating is challenging due to various factors like voltage, current, and temperature [48–52]. Furthermore, identifying the plating phenomenon through post-mortem characterizations is not straightforward, as metallic lithium can reintegrate into graphite during relaxation periods, concealing its presence [96], [198]. Instead of relying on post-mortem techniques, we drew inspiration from recent research that extracted activation energies (AE) for cell capacity loss [221] through temperature-dependent measurements. This method was introduced in **workflow II**, chapter III, and helps in distinguishing between two degradation regimes: one that is primarily dominated by SEI growth and the other by lithium plating.

In previous studies, researchers utilized commercial cells and defined the degradation rate based on cycle number [221] or the time [101] required to reach 80% state of health (i.e., 80% of the initial experimental capacity). However, averaging degradation rates over extended periods may result in the loss of significant information, especially obscuring knee points in the capacity retention plot, such as the ones observed at cycle 30 in Figure 44a. Therefore, in the subsequent study, we assessed degradation rates within specific cycle ranges, specifically from a starting cycle number  $N$  to either  $N + 1$  or  $N + 2$ . The rate was defined as the capacity loss (mAh) normalized by time (h), active material mass (g), and surface area ( $\text{cm}^2$ ). This normalization allows for future comparisons with studies conducted using similar coin cell configurations.

#### IV.3.1.b. C-rate dependent aging

Graphite/LNO cells were initially subjected to cycling at a low C-rate ( $C/2$ ) to promote SEI-dominated degradation. The obtained results were then compared with those obtained at a high C-rate ( $3C$ ), where plating is favored (Figure 46a). When plotting the degradation rates measured at  $3C$  (represented by orange dots) as a function of reciprocal temperature ranging from  $15\text{ }^\circ\text{C}$  to  $55\text{ }^\circ\text{C}$  (forming an Arrhenius plot), two distinct slopes were observed, indicating two different degradation mechanisms. In simpler terms, as the temperature increases, chemical reactions, including SEI formation, are accelerated, resulting in greater lithium

consumption. Conversely, at low temperatures, these reactions become sluggish, combined with slow intercalation reactions, leading to the prevalence of lithium plating on the graphite surface.

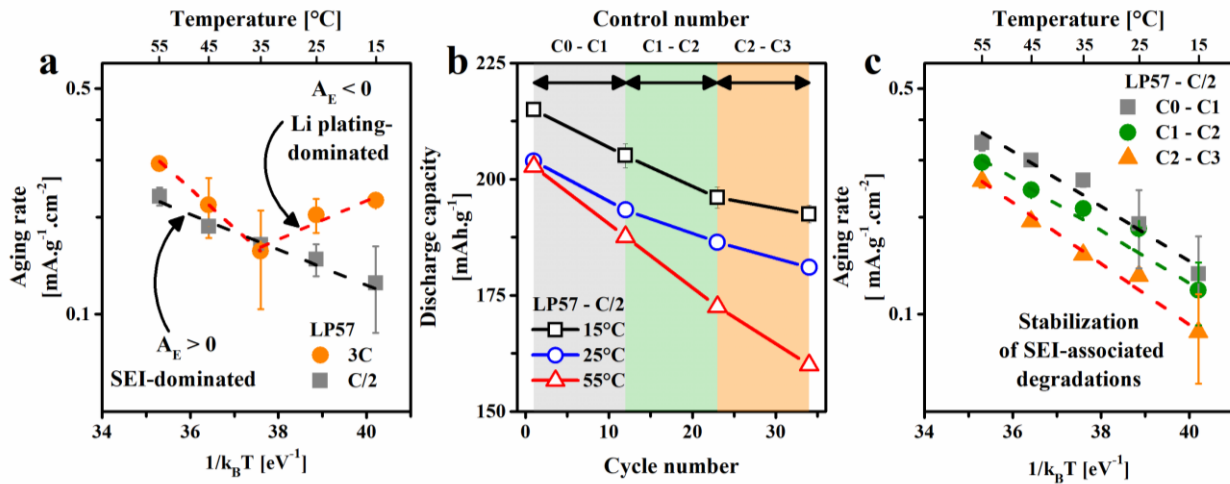


**Figure 46 – Deciphering between SEI growth and Li plating**

The effect of current density and cycle number on degradation rates was investigated. (a) An Arrhenius plot illustrates the degradation rates of graphite/LNO cells at 3C (orange) and C/2 (grey) currents from control 0 to 2. (b) Discharge capacities were measured during the initial control cycles in LP57 at C/2 and various temperatures. The lines serve as visual aids. (c) Arrhenius plots were generated for the degradation rates between the 0th and 1<sup>st</sup> control cycles (grey), 1<sup>st</sup> and 2<sup>nd</sup> cycles (green), and 2<sup>nd</sup> and 3<sup>rd</sup> cycles (orange).

For the low C-rate (C/2, represented by grey squares), degradations consistently followed a SEI growth regime ( $A_E > 0$ ) across the entire temperature range, indicating the absence or limited occurrence of lithium plating. This observation remained consistent throughout cycling, including between control 0 and 1 (C0-C1), control 1 and 2 (C1-C2), or control 2 and 3 (C2-C3) (Figures 46b and c). Furthermore, the observed decrease in degradation rates over cycling aligned with the stabilization of the SEI, as evidenced by the reduction in LLI (Figure 44b). Ultimately, the C-rate played a decisive role in determining the occurrence of plating, providing an opportunity to investigate the influence of dissolved TMs on aging mechanisms.

## IV.3.2. Influence of TM in the SEI

### IV.3.2.a. Origins of the LLI

The temperature dependence of aging was further examined for cells utilizing 12 mM of TM in the LP57 electrolyte. These cells were cycled at a similar C-rate (C/2) as depicted in Figure 44a, and the results were plotted in Figure 47. Regardless of the presence of nickel or manganese in the electrolyte, the activation energies for LP57, LP57 + Ni, and LP57 + Mn were found to be positive, indicating that aging is predominantly influenced by degradations associated to unstable SEI. When TM is present in the electrolyte, the cells experience increased degradation at higher temperatures, suggesting an activation of catalytic degradation processes associated with metals in the SEI. In conclusion, the LLI observed in Figure 44b is caused by uncontrolled SEI growth resulting from the reactivity of TM within the SEI. While plating may occur, it does not represent the primary mechanism of cell degradation. The influence of TM on Li plating is further explored in the subsequent section.

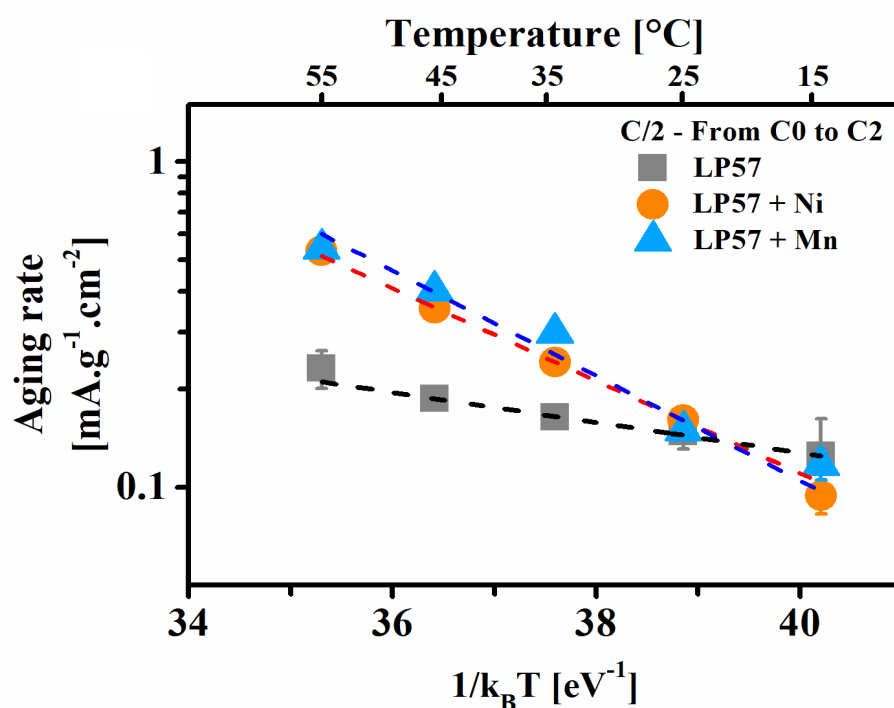


Figure 47 – Effect of TM on SEI growth

Effect of dissolved TMs on lithium plating and SEI growth. Arrhenius plots recorded for nickel- (orange) and manganese-containing (blue) LP57 (grey) at C/2.

### IV.3.2.b. Influence of TM on Li plating

To investigate the impact of TMs in plating scenarios, initial tests were conducted using LP57 at 3C as a reference point (Figure 48). These tests revealed a transition from positive to negative activation energies at 35 °C, indicating that lithium plating becomes more favorable below this temperature. This finding aligns with a previous study by *Yang et al.* [221], where plating was observed to commence at 40 °C under 3C conditions (with a balancing N/P = 1.2). Subsequently, cells were subjected to cycling with electrolytes containing dissolved TMs, and degradation rates exhibited a single slope (AE > 0), unlike the bare LP57 scenario (Figure 48). This observation suggests that the SEI growth regime remains dominant in the presence of nickel and manganese-contaminated electrolytes across the entire temperature range, effectively concealing any influence related to lithium dendrite formation, even under high C-rates such as 3C. Importantly, this result is not attributed to an increase in graphite potential at the end of the charging process, as discussed previously in Figure 45, which could have masked the occurrence of plating [215]. Ultimately, it should be noted that these conclusions are specific to the experimental conditions employed, and under different circumstances, plating may emerge as the primary degradation mechanism at lower temperatures when further reducing the balancing factor.

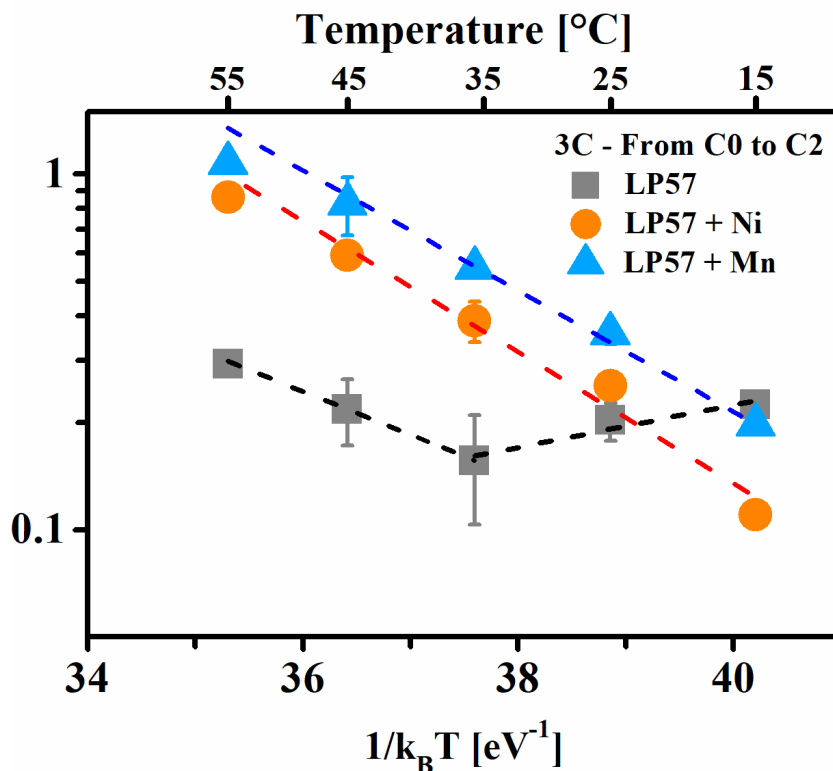


Figure 48 – Effect of TM on Li plating

Arrhenius plots recorded for nickel- (orange) and manganese-containing (blue) LP57 electrolytes compared to LP57 (grey) at 3C.



## CONCLUSION OF CHAPTER IV

In this chapter, the electrochemical workflows were employed to investigate the degradation mechanisms associated with TM dissolution in graphite/LNO cells. Initially, we quantified the amount of dissolved nickel using ICP-MS and found that it accounted for less than 1% of the total nickel content in the active material. However, TM cations were confirmed to be incorporated into the SEI through either electrochemical processes or spontaneous absorption pathways. Subsequently, the DVA revealed that all TMs (nickel, cobalt, and manganese) had a similar disruptive effect on cell performance, particularly leading to increased LLI during the initial cycles. In other words, TMs present in the SEI acted as detrimental agents that promoted parasitic reactions, resulting in lithium losses. Interestingly, we observed that the capacity losses caused by TMs tended to slow down after approximately 50 cycles, coinciding with an increase in the graphite potential charge endpoint. This observation does not question the damaging effect of TMs, but rather highlights a characteristic of the graphite/LNO system where an increase in the negative potential charge endpoint temporarily slows down the capacity loss during the high-voltage LNO plateau. However, prolonged cycling eventually leads to LNO fatigue at high potential, ultimately causing the demise of the cell. Consequently, we emphasize the importance of exercising caution when attributing capacity loss during cycling to a specific factor, and we emphasize the necessity for proper electrochemical protocols. To further investigate the origins of the observed LLI in the presence of TMs, we conducted temperature aging measurements using a dedicated protocol. Our findings indicated that TM deposition at the anode primarily promotes degradation mechanisms associated with SEI growth, which is more dominant than any effects related to lithium plating, contrary to previous proposals in the literature. Finally, we demonstrated that TM reactivity is activated at elevated temperatures, resulting in significant LLI. Overall, we show that implementing appropriate electrochemical methodologies can extend beyond simple evaluation of cell performance, enabling the assessment of complex interfacial effects and the identification of cell degradation origins in a non-invasive manner.



**CHAPTER V: HIGHLY  
CONCENTRATED ELECTROLYTES  
AND CASCADING SIDE REACTIONS  
IN GRAPHITE/NMC811 CELLS**



## INTRODUCTION OF CHAPTER V

Recent years have seen an increase in efforts dedicated to the design and stabilization of Ni-rich NMC materials. Various approaches have been employed, including doping of active materials [51], [58], [59], the design of surface coatings [52], [67], [69], and the use of additives for high voltage [222]–[224]. One strategy recently proposed to tackle instabilities at high potential is the utilization of highly concentrated electrolytes (HCE) [144]. HCE, thanks to their solvation structure, have been suggested to overcome recurring issues associated with high-voltage Ni-rich NMC materials, such as aluminum corrosion [140], [225], dissolution of transition metals (TM) [145], and solvent oxidation [161]. Additionally, HCE has been proposed to form a robust cathode electrolyte interphase (CEI) [145]. These positive attributes have led to reports of improved capacity retention and cycling rates with Ni-rich materials, although these studies have employed a semi-infinite metallic lithium reservoir as the negative electrode [115].

While promising breakthroughs have been achieved in half-cell configurations [31], studies focusing on the long-term aging of full cells under practical conditions, including self-discharge and stability tests at high temperatures, are relatively limited. Furthermore, even when these studies have been conducted, there has been a lack of in-depth analysis of lithium inventory, capacity slippages, and cycling protocols necessary to reveal complex phenomena such as shuttling or lithium plating. In other words, although there is remarkable potential in utilizing HCE to stabilize Ni-rich NMC materials, a significant knowledge gap exists regarding their stability, which hinders the ability to design and optimize HCE composition for high-voltage applications.

In this study, we investigated the effectiveness of various HCE in stabilizing graphite/NMC811 cells at high voltage. To evaluate their performance, we employed the analysis workflow proposed in Chapter III.



## V.1. CASCADING DEGRADATIONS

### V.1.1. Cell performance with HCE

#### V.1.1.a. Capacity retention

To investigate the stability of Ni-rich materials, graphite/NMC811 cells were cycled at 25°C with a voltage range of 2.5 – 4.3 V using three different electrolytes: conventional LP57 (ethylene carbonate EC: dimethyl ethyl carbonate EMC 3:7 with 1M LiPF<sub>6</sub>), LP57 VC (LP57 + 2w% vinylene carbonate), and HCE DMC (5M LiFSI in DMC). The cycling procedure involved 100 cycles at 1C (constant current, CV until current lower than C/20) followed by control cycles at C/20, during which in-depth electrochemical analysis was conducted. The control cycles were designated as follows: control N corresponds to the cycle at C/20 recorded after N-times 100 aging cycles at 1C. For example, control 0 refers to the first C/20 cycle carried out before the initial 100 aging cycles at 1C, while control 2 corresponds to the C/20 cycle performed after 200 aging cycles at 1C. Further details about experiments are available in Annex 8. The resulting capacity retentions are presented in Figure 49.

The LP57 cell exhibited a capacity retention of 80% of the initial state of charge (SOC) after the 65<sup>th</sup> cycle (depicted in grey), while LP57 VC (in green) achieved a similar end-of-life criterion after 130 cycles, confirming that the addition of VC is beneficial for stabilizing the cell at 4.3 V. Throughout the rest of the study, LP57 VC was used as the reference electrolyte. The relative discharge capacity are available in Annex 9. When using HCE DMC (depicted in orange), the cell showed a capacity retention of 70% after 500 cycles, which represented the best performance among the tested electrolytes. However, when examining the coulombic efficiency (CE), the HCE DMC cell exhibited an interesting pattern: initially, there was a sharp increase in CE until the 90<sup>th</sup> cycle, followed by a drastic drop starting at cycle 250. This observation suggests that despite the favorable capacity retention, the use of HCE DMC electrolyte does not completely eliminate all parasitic reactions. Before exploring side reactions, the upcoming sections will assess the structural integrity of bulk NMC811 and the dissolution of TM during aging.

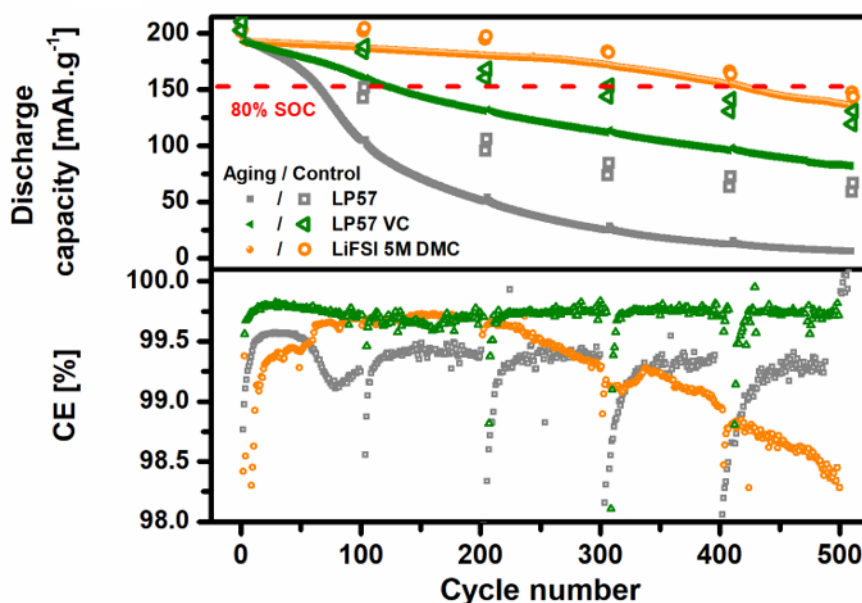


**Figure 49 – Performance of graphite/NMC811 cells at 4.3 V**

Cell performance recorded for graphite/NMC811 cells at 4.3 V - 25°C using LP57, LP57 VC and LiFSI 5M DMC. The control cycles are designated as follows: Control N corresponds to the cycle at C/20 that is measured after subjecting the battery to Nx100 aging cycles at 1C.

### V.1.1.b. Checking potential crosstalks

#### *Solvation of TM in HCE*

To understand the reasons behind the enhanced capacity retention but diminished CE in HCE DMC, we conducted quantifications of dissolved TMs. The influence of varying LiFSI concentrations on TM dissolution was tested by measuring the solubility of nickel, manganese, or cobalt chloride salts ( $\text{TMCl}_2$  -  $\text{TM} = \text{Ni}^{2+}$ ,  $\text{Mn}^{2+}$ , or  $\text{Co}^{2+}$ ) in DMC-based electrolytes. Solutions with different LiFSI concentrations ranging from 0 to 5 M were saturated with  $\text{TMCl}_2$  salts and vigorously stirred for 48 hours under an inert atmosphere (Argon). After achieving thermodynamic equilibrium at ambient temperature, the solutions were centrifuged, filtered, and the TM concentrations were quantified using inductively coupled plasma mass spectrometry (ICP-MS) (Figure 50). The resulting solubility exhibited a bell-shaped curve as a function of the salt concentration, with a maximum at 1 M LiFSI. Among the tested TMs, manganese displayed the highest solubility, followed by cobalt and nickel. This trend remained relatively consistent across the entire range of LiFSI concentrations. In the diluted regime ( $< 1$  M), increasing the concentration of  $\text{FSI}^-$  enhanced the solubility of TMs through the formation of  $[\text{TMFSI}_y]$  complexes, as recently demonstrated [143]. However, above 1 M, the weak dissociation of LiFSI salt and the increased activity coefficient of soluble species resulted in a decrease in the solubility of  $[\text{TMFSI}_y]$  complexes [143]. Consequently, the solubility of metal salts abruptly decreased above 1 M LiFSI and was measured to be five times lower at 5 M

compared to that at 1 M [226]. However, even at high concentrations, the dissolution of transition metals was not completely eliminated, indicating that the positive attributes of HCE DMC regarding capacity retention do not arise solely from a reduced dissolution of TMs.

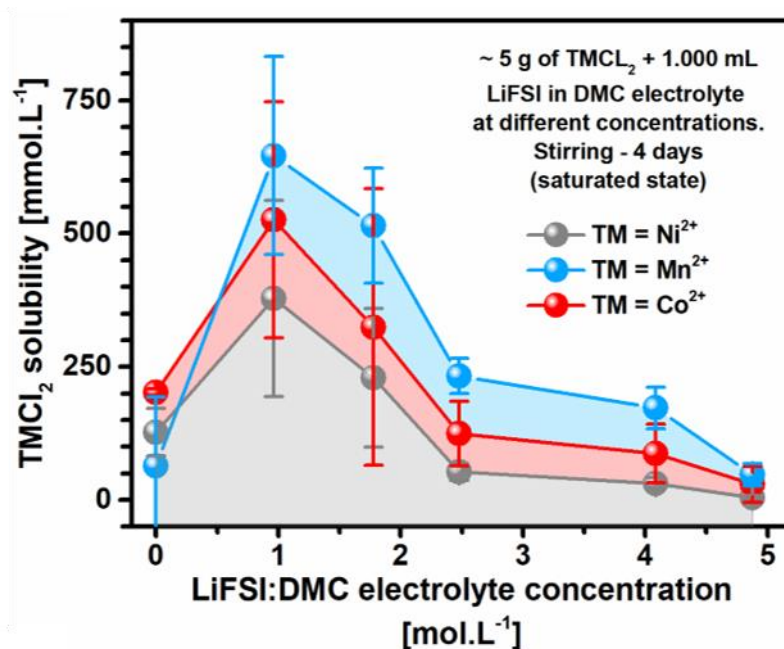


**Figure 50 – Evolution of TM solubility as a function salt concentration**

*Evolution of nickel, manganese and cobalt chloride salt solubilities in LiFSI:DMC electrolytes as a function of LiFSI concentration.*

### *Assessing the crosstalk of TM*

To confirm that the metal dissolution from NMC811 is not at the origin for the better capacity retention, TMs deposited at the graphite negative electrode were quantified after 500 cycles. Graphite electrodes were retrieved after cycling, rinsed with DMC (few drops) and digested into 2wt% nitric acid solutions before TMs to be quantified by ICP-MS (Figure 51). About 75  $\mu\text{g}$  of metals per  $\text{cm}^2$  of graphite were measured for both LP57 VC and HCE DMC electrolytes, confirming that metals dissolve from NMC811 and incorporate into the SEI upon cycling. To no surprise, nickel is found in large quantity at the anode, followed by manganese and cobalt. However, the amount of Mn is found much greater than the initial stoichiometry, consistent with the higher solubility recorded for manganese salt in Figure 50 and previously observed in the literature [86]. More importantly, the quantity of TMs does not drastically differ between HCE DMC and LP57 VC electrolytes, indicating that the different TMs lead to the same level of graphite poisoning. This observation suggests that the dissolution and incorporation follow the applied voltage rather than the solubility limit of NMC materials.

Furthermore, our results indicate that the solvation structure of HCE does not inhibit the crossover of TMs.

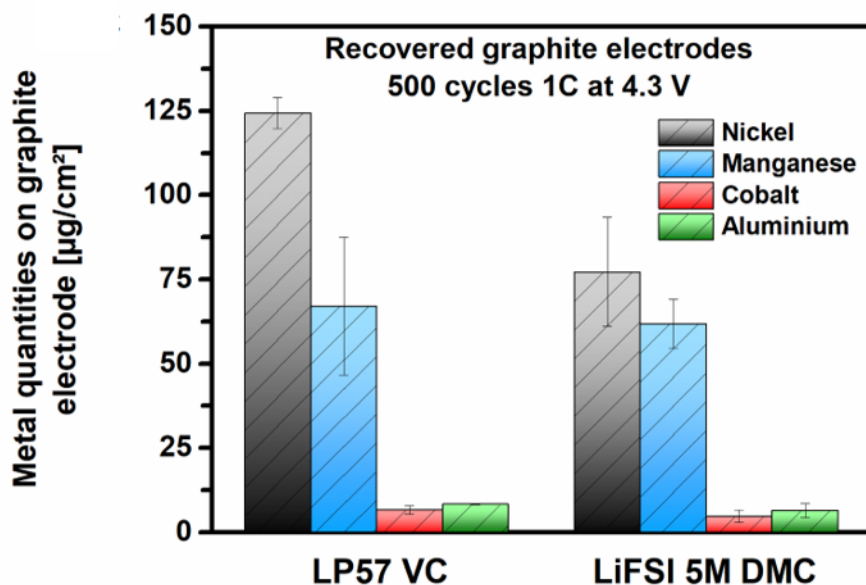


**Figure 51 – Quantification of TM at the negative electrode**

*Transition metal quantities measured on graphite electrodes retrieved after 500 cycles at 4.3 V using LP57 VC and LiFSI 5M DMC. Error bars are obtained from duplicated measurement.*

### V.1.2.c. Looking for bulk degradations

To evaluate the impact of bulk degradation on capacity fading, X-ray diffraction measurements were conducted on NMC811 electrodes in a discharged state after 500 cycles (Figure 52). No additional peaks associated with the formation of secondary phases were observed, nor was there a decrease in peak intensities that would indicate early fatigue of the bulk material. Additionally, the NMC811 electrode recovered in a discharged state after cycling in HCE DMC electrolyte exhibited similar peak positions for the (003) diffraction peak at low angles, indicating a complete degree of lithiation at the end of discharge. In contrast, a decrease in the angle for the (003) peak was observed for NMC811 after discharge in LP57 VC electrolyte, suggesting a lower lithiation content compared to its pristine state. This discrepancy in the lithiation state can be attributed to the low polarization observed during cycling in HCE DMC compared to LP57 VC (Annex 10), as well as the particle fracture of NMC811, which hinders the full reintercalation of lithium during discharge.

Overall, there is no conclusive evidence of structural/chemical degradation in the bulk material or differential poisoning of the solid electrolyte interphase (SEI) due to transition metal dissolution in HCE DMC that could account for the observed improved capacity retention or

lower CE depicted in Figure 49. Instead, the observed differences may be explained by interfacial instability, which will be further investigated below.

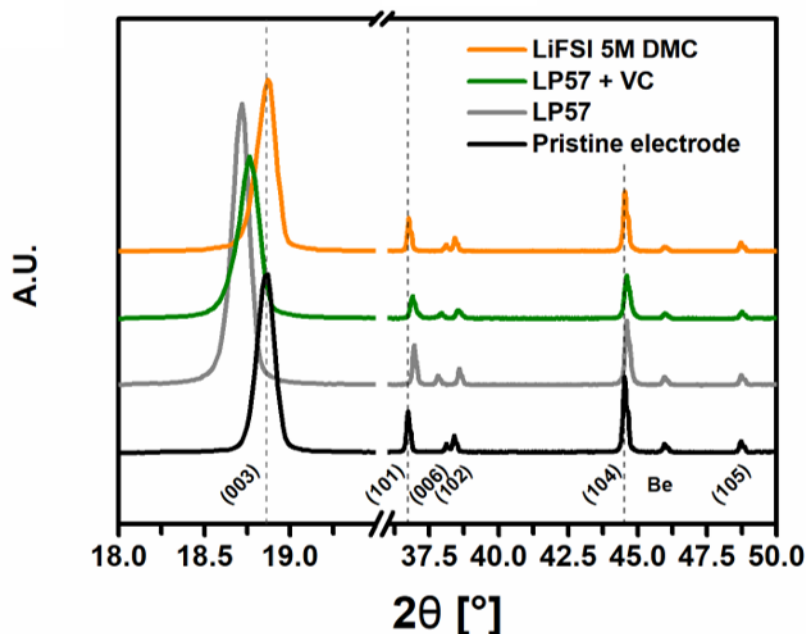


Figure 52 – XRD of NMC811 electrode after 500 cycles at 4.3 V

*Post mortem X-ray diffractograms of NMC811 electrodes showing no early material fatigue after 500 cycles.*

## V.1.2. Determining the cause of instability

### V.1.2.a. From prevailing degradation at the positive to negative electrode

The use of DVA (Figure 53) enables the determination of relative slippages in capacity caused by parasitic reactions at the positive and negative electrodes [195]. The fit for control 0 and 5 for HCE DMC and LP57 VC is provided in Annex 11 and demonstrates accurate results. When employing the LP57 VC electrolyte (lower panel of Figure 53), the graphite curve shifts to the left (indicated by the black arrow), indicating the presence of remaining lithium in the negative electrode at the discharge [227]. This occurrence can be attributed to degradations taking place at the positive electrode, where parasitic oxidation leads to an additional lithiation of the graphite during charging. The increased cell polarization observed with the LP57 VC electrolyte (Annex 10) also contributes to this phenomenon, impeding the re-insertion of lithium into NMC811 during discharge and resulting in residual lithium in the graphite electrode. Similar degradations are observed when comparing HCE DMC with LP57 VC until the 2<sup>nd</sup> control cycle (205<sup>th</sup> cycle, upper panel, 1<sup>st</sup> step indicated by the blue arrow). However, after the second control cycle, there is a sudden rightward shift in the graphite curve and a leftward shift in the NMC811 curve (indicated by the grey arrow, 2<sup>nd</sup> step), leading to a

decrease in CE as shown in Figure 49. This observation suggests that the NMC811 electrode gradually becomes more deficient in lithium at the end of each discharge when using HCE DMC. Furthermore, there is a 33% loss of initial mass in active material at the negative electrode (LAM<sub>NE</sub>), indicating potential issues such as a loss of electrical contact between particles, clogged pores, or electrode delamination [187], [196]. Overall, analysis of the electrochemical cycling data reveals that degradation at the negative electrode increases from the 200<sup>th</sup> cycle onwards and is primarily responsible for the LLI, which significantly contributes to the decline in cell capacity (Annex 9). Thus, cells cycled with HCE DMC electrolyte experience considerable degradations at both interfaces, similar to those observed with LP57 VC electrolyte, albeit with different underlying causes.

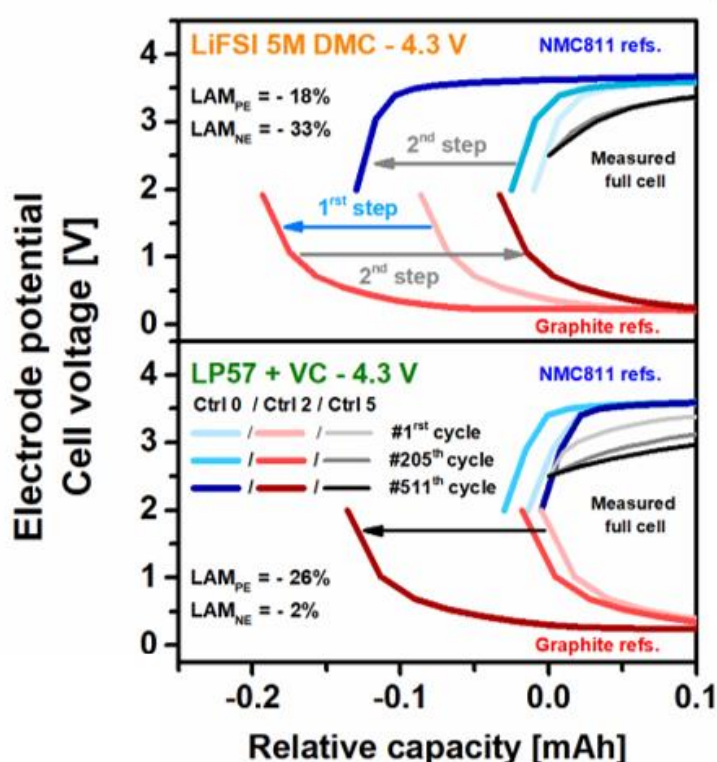


Figure 53 – DVA of graphite/NMC811 cells at 4.3 V

*Derivative voltage analysis (DVA) of graphite/NMC811 cells cycled using LP57 VC and LiFSI 5M DMC. The control cycles are designated as follows: Control N corresponds to the cycle at C/20 that is measured after subjecting the battery to Nx100 aging cycles.*

### V.1.2.b. Marching

To enhance our comprehension of interfacial degradations in HCE, we analyze the cumulative capacity shift of charge ( $Q_C$ ) and discharge ( $Q_D$ ) endpoints as a function of cycle numbers (Figure 54). In the case of LP57 VC electrolyte (green), the  $Q_D$  endpoints exhibit an increase attributed to LLI caused by SEI growth, as previously observed through DVA [191]. Conversely, the relatively stable  $Q_C$  values suggest the absence of electrolyte oxidation.

Therefore, in addition to the rise in cell polarization, the capacity loss can be attributed to side reactions occurring at the negative electrode, which gradually narrows the cycling window (i.e.,  $Q_c - Q_d$ ). For HCE DMC electrolyte (orange),  $Q_c$  experiences a rapid increase, confirming the presence of parasitic oxidation as earlier revealed by DVA (Figure 53). The parasitic oxidation cannot be attributed to inadequate passivation of the aluminum, as linear sweep voltammetry conducted on the aluminum current collector shows no significant oxidation (Annex 12), and the amount of aluminum detected at the graphite electrode is comparable between HCE DMC and LP57 VC electrolytes (Figure 51). Instead, it is likely that components of the electrolyte undergo oxidation, leading to an increase in the lithiation level of the graphite electrode beyond the extent corresponding to lithium de-intercalation from NMC811. From the 250<sup>th</sup> cycle onwards (grey part, 2<sup>nd</sup> step), a rollover is observed for  $Q_d$  endpoints, indicating the destabilization of the negative interface.

The conclusion is therefore twofold. First, degradations recorded with LP57 VC electrolyte are mainly caused by the SEI growth and the increased polarization. Second, cells cycled in HCE DMC electrolyte are plagued by a parasitic oxidation that artificially and temporarily sustains high capacity retention; beyond the 250<sup>th</sup> cycle the negative interface becomes unstable and the performance very rapidly decays.

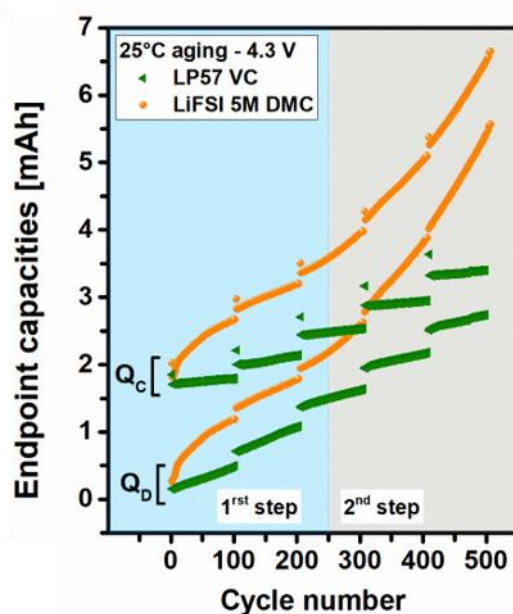


**Figure 54 – Marching capacities highlighting parasitic oxidation in HCE**

*Marching of charge and discharge capacity endpoints of graphite/NMC811 cells cycled using LP57 VC and LiFSI 5M DMC.*

### V.1.2.c. Involved species

The investigation of parasitic oxidation in HCE DMC was extended through self-discharge tests (Figure 55a). In LP57 VC electrolyte, a minimal voltage drop (-0.03 V) is

observed after 50 hours at open circuit voltage, whether at 3.8 V or 4.3 V. This suggests good stability of the electrolyte within this potential range or enhanced passivation of the interfaces. While a similar voltage loss is observed at 3.8 V for HCE DMC, a significant drop of -0.13 V is recorded at 4.3 V after 50 hours, indicating spontaneous re-lithiation of NMC811 likely associated with electrolyte oxidation. Although parasitic reactions at the graphite electrode cannot be discarded, the absence of self-discharge at 3.8 V strongly suggests that it is not responsible for the rapid voltage decay observed after charging at 4.3 V. Instead, the self-discharge observed in HCE DMC implies electrochemical oxidation of the electrolyte, although it does not contribute significantly to capacity loss [72], [76]. The rate of voltage loss, -2.6 mV/h (-0.13 V / 50h), measured at 4.3 V corresponds to a capacity loss of only -0.3 mAh or a parasitic current of approximately 6  $\mu$ A (300  $\mu$ Ah / 50 h).

Similar parasitic anodic currents have been observed, particularly in DMC-based electrolytes, and have been found to cause coloration of the electrolyte [202]. Therefore, in-situ UV-visible measurements were conducted (Figure 55b). During cycling, colored species appeared at the NMC811 electrode (brown) within a few hours, which migration was slow due to the high viscosity of the electrolyte (see inset in Figure 55b). The recorded UV spectrum exhibited three absorption bands at 223, 272, and 363 nm, matching those previously reported in 1.5 M NaPF<sub>6</sub> DMC electrolyte [202].

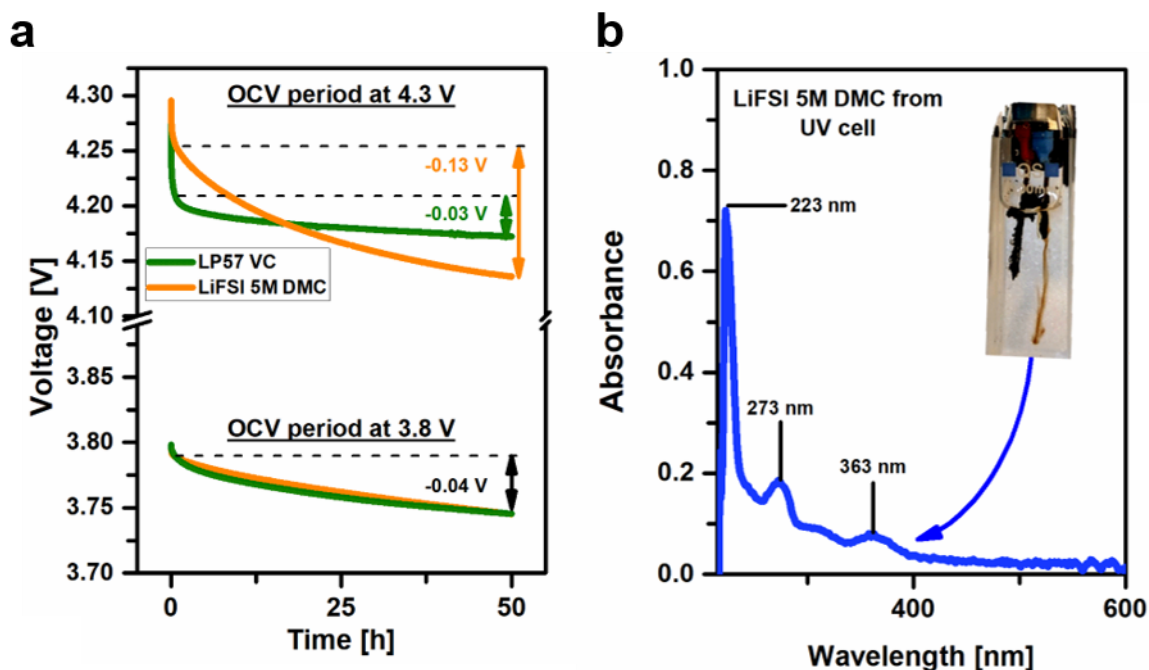


**Figure 55 – Further clues of parasitic oxidation**

Self-discharge tests at 3.8 V and 4.3 V of graphite/NMC811 cells. d) UV-visible spectrum of the species released at the positive electrode when using LiFSI 5M DMC electrolyte.

Furthermore, a similar UV-visible spectrum was obtained when stainless steel and lithium electrodes were used in HCE DMC (Annex 13), indicating that the coloration does not result from the complexation of any released TM from the NMC electrode. Based on these measurements, we conclude that DMC is most likely oxidized. However, this does not explain the abrupt shift in the degradation mechanism from initial dominance by the positive electrode to degradations at the negative electrode after 200 cycles.

### V.1.3. Li plating as a consequence of side oxidation

To uncover the underlying causes of the degradation regime shift observed in HCE DMC, ICA is conducted. When LP57 VC is used (Figure 56a), the intensity of the peak at 4.11 V, associated with NMC811, decreases with cycling, confirming the presence of positive electrode loss of active material (LAM PE) initially observed by DVA (Figure 53). Additionally, the increased peak splitting observed during cycling indicates an increase in cell impedance [82]. Similar conclusions can be drawn for HCE DMC (Figure 56b), but an additional feature appears at 4.21 V during charging (and at 4.16 V during discharging), likely associated with lithium plating (and stripping) on the graphite surface [196]. The occurrence of lithium plating aligns with the estimated onset cycle obtained through capacity marching during charging. Specifically, considering an N/P balancing ratio of 1.27 and specific capacities of Q positive and Q negative of 1.54 mAh and 1.95 mAh, respectively, a safety capacity margin of 0.41 mAh is calculated. Furthermore, the progression of the charge capacity endpoint ( $Q_c$ ) primarily stems from parasitic oxidation at the positive electrode (as observed in DVA), which exhibits an average slope of +0.008 mAh per cycle between the 1<sup>st</sup> and 100<sup>th</sup> cycle. As a result, after 51 cycles ( $0.41 \text{ mAh} / 0.008 \text{ mAh.cycle}^{-1}$ ), the parasitic oxidation surpasses the safety margin, leading to lithium plating as the graphite electrode reaches its maximum capacity, as observed in control 1 (Figure 56b). Additionally, this interpretation aligns with the high LAM observed at the negative electrode (Figure 53), as lithium plating has been previously shown to cause pore clogging, electrical insulation of graphite particles, or electrode delamination [187], [196]. The presence of plating was ultimately confirmed through the observation of grey spots on the graphite electrode after disassembling the cell (Annex 14).

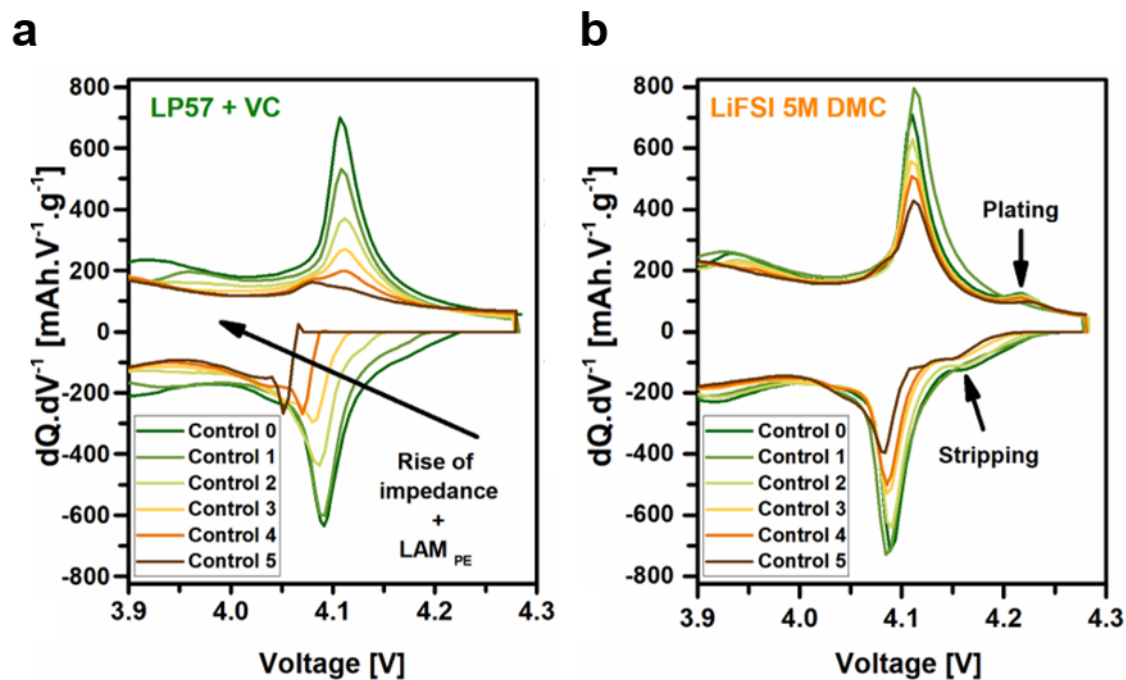


**Figure 56 – ICA highlighting Li plating**

*Incremental capacity analysis (ICA) performed on C/20 control cycle for LP57 VC a) and HCE-DMC b).*

Despite the early-stage observation of lithium plating, cell performance is sustained up to the 250<sup>th</sup> cycle due to the reported ability of HCEs to plate and strip lithium with high CE [31], [135], [228]. This finding is consistent with the low LLI and limited capacity fading observed in Figure 49. Due to the relatively good CE, it takes 250 cycles for the LLI associated with lithium plating to reach a level sufficient to trigger the capacity rollover. It is worth noting that the quantity of lithium present in the HCE electrolyte is twice as high as in NMC811 and five times greater than that in LP57 VC electrolyte. This factor potentially delays the onset of detrimental effects resulting from lithium plating during aging. Lastly, it is important to highlight that no lithium plating is observed for LP57 VC electrolyte, which would lead to a rapid decline in capacity, as previously observed [96], [101], [198].

In conclusion, the degradations observed at the positive and the negative interfaces in cells using HCE DMC are interconnected. Indeed, DMC solvent is anodically decomposed upon charge, the additional capacity associated with this oxidation cannot be completely compensated by the sole intercalation of Li cation in graphite resulting in Li plating. Up until the 250<sup>th</sup> cycle, lithium plating cannot be detected by the use of metrics such as capacity retention of CE, and only once the effects have sufficiently accumulate to destabilize the negative electrode a drop in CE and a knee point in the capacity retention curve are observed

[198]. To tackle this cascading effect, two strategies are proposed: formation of interphase at higher temperature and solvent optimization.

## V.2. MITIGATING THE SIDE REACTIONS

### V.2.1. Outcome of higher cycling temperatures

First, to alleviate the Li plating issues, cells were cycled at 55°C, a temperature at which the Li plating reaction is disfavored [101], [221]. The capacity retention recorded at 55°C for HCE DMC is relatively similar to that recorded at 25°C, although the initial capacity is greater due to enhanced kinetics for intercalation at high temperature ((Figure 57a). On the other hand, the CE remains steady at 99.7% at 55°C, unlike at 25°C where a rollover was observed after 200 cycles. The DVA (Figure 57b) and the evolution of capacity endpoints (Figure 57c) both indicate that cycling at elevated temperature is beneficial for reducing the rates of side reactions. Specifically, there is no sign of lithium plating detected (see the ICA in the inset of Figure 57c), which reduces the LLI associated with parasitic reactions at the negative electrode (Figure 57b). It is worth noting that the peak associated with the NMC811 plateau at 4.2 V is lost after the 5<sup>th</sup> control, which we attribute to an increase in cell impedance (Annex 10). However, at this stage, it remains unclear whether the positive effect of temperature is solely associated with the enhanced kinetics of lithium intercalation, reducing plating risks, and/or the stabilization of the interphases.

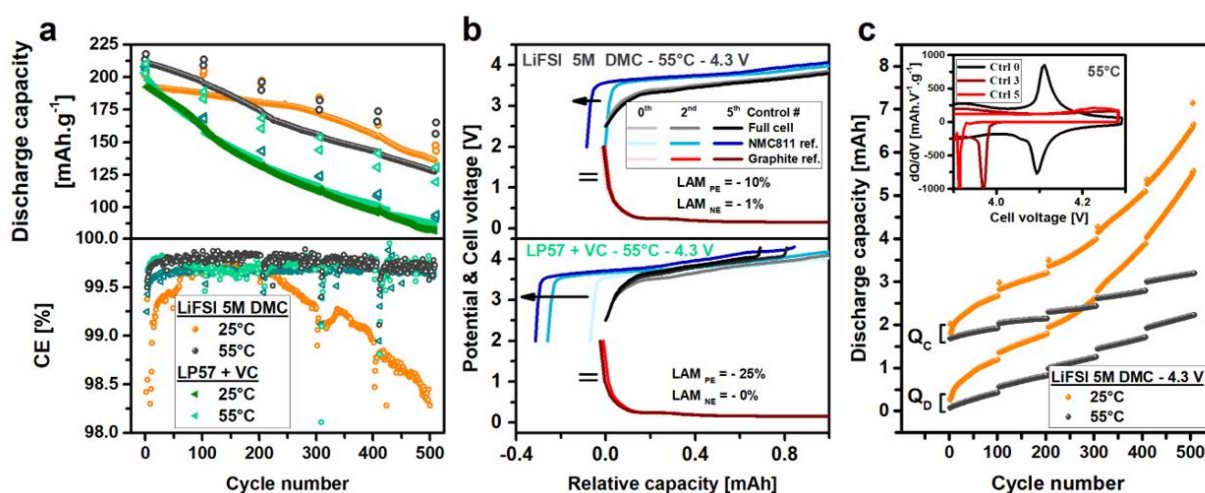


Figure 57 – Advantage of high temperature in mitigating Li plating

a) Graphite/NMC811 performance at 55°C – 4.3 V for cells cycled using LP57 VC and LiFSI 5M DMC electrolyte. b) Associated derivative voltage analysis. c) Capacity endpoints of LiFSI 5M DMC at 25°C and 55°C. Incremental capacity analysis for cell cycled in LiFSI 5M DMC at 55°C is given in insert. The control cycles are designated as follows: Control N corresponds to the cycle at C/20 that is measured after subjecting the battery to Nx100 aging cycles at 1C.

## V.2.2. Formation of SEI and CEI

### V.2.2.a. Electrochemical considerations

To investigate the impact of interphases on the improved performance, the effect of pre-forming each interphase at 55°C was independently tested. For this purpose, the SEI and the CEI were pre-formed at 55°C by cycling cells in HCE DMC electrolyte at C/20 before being re-assembled with complementary electrodes. Specifically, the aged NMC811 and its CEI were paired with a pristine graphite electrode, while the aged graphite and its SEI were paired with a pristine NMC811 electrode. Additionally, a third cell was prepared in which both the SEI and the CEI were pre-formed at 55°C. The process is summarized in Figure 58a, and the results obtained at 25°C with the newly assembled full cells are presented in Figure 58b and 58c.

While the capacity retention was found to be similar for all three cases (Figure 58b), the degradation rates clearly differed (Figure 58c). When the CEI was pre-formed (black cell), the shift of capacity endpoints was similar to that observed without pre-formation, i.e., +0.045 mAh/cycle (Figure 58c) versus +0.038 mAh/cycle (Figure 54), indicating that the sole passivation of the CEI is insufficient to eliminate parasitic oxidation. Moreover, the ICA (Figure 58d) once again exhibited features previously attributed to Li plating, similar to the cell cycled at 25°C. This observation confirms that the instability caused by Li plating is responsible for the capacity rollover from the 250<sup>th</sup> cycle onwards (Figure 58b). When the SEI was pre-formed at 55°C (red cell), the rapid shift of capacity endpoints (Figure 58c) was similar to that observed for the cell cycled at 25°C without SEI formation, consistent with extensive electrolyte (DMC) oxidation. However, lithium plating was no longer observed (Figure 58e), suggesting that preformation of the negative interphase can effectively reduce plating and prevent capacity rollover. Only when both the SEI and the CEI were pre-formed at 55°C did a significant decrease in the capacity shifting rate occur, i.e., 0.02 mAh/cycle, along with an improved CE (blue cell). The ICA (Figure 58f) revealed a doubling of the peak at 4.11 V with the progressive appearance of a peak at 4.08 V upon successive charges (and 4.08 to 4.05 V for discharge). This peak doubling is attributed to GSJ as previously observed in Chapter III, part III.3.3. [214], [215]. The copious LLI resulting from the SEI and the CEI formation at 55°C lowers the lithiation degree of the negative electrode at the end of charge. Graphite completes the charge in stage II of intercalation, at 110 mV, instead of stage I at 80 mV. Ultimately, this 30 mV upshift of the graphite operating potential significantly reduces the risk of lithium plating. In summary, our findings suggest that pre-forming the interphases at 55°C influences their chemical nature and stability, conditioning the capacity window at which the electrodes operate, including the GSJ.

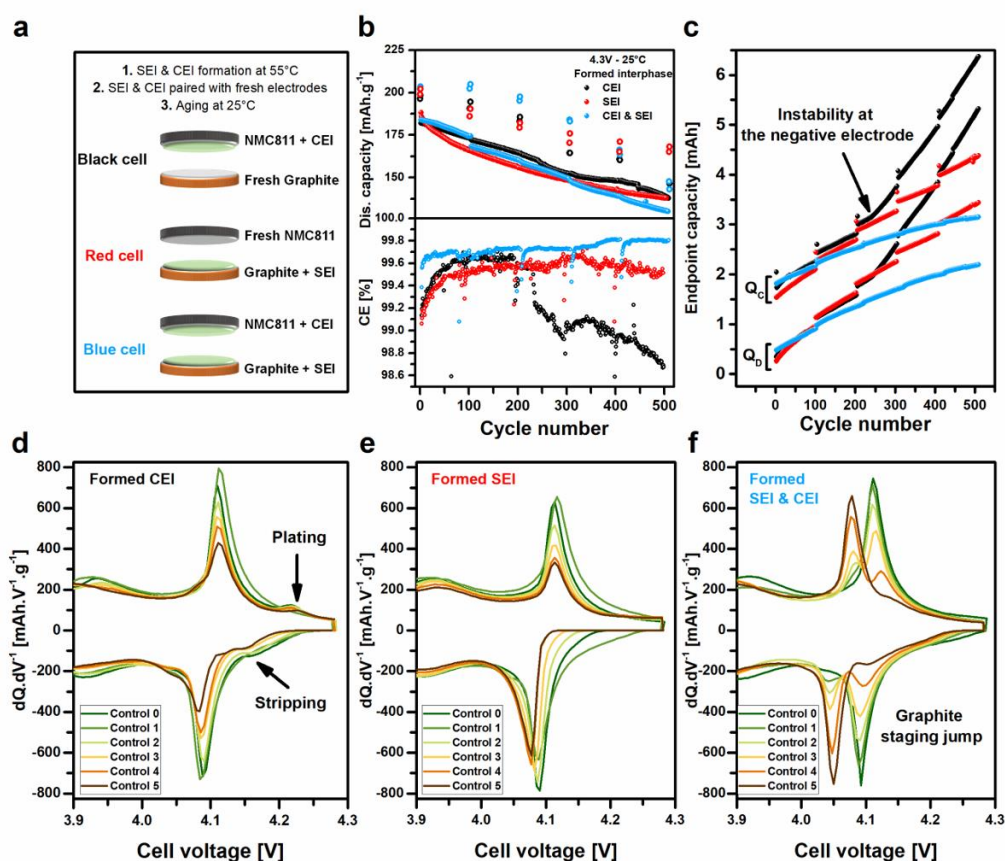


**Figure 58 – Effect of interphase formation at high temperatures**

*Schematic view of the interphases pre-formation steps performed at 55°C and tested conditions. b) Cycling performance of reassembled cells with the interphases pre-formed at 55°C. c) Shift of capacity endpoints recorded for cells using pre-formed interphases. Incremental capacity analysis of cells which CEI d), SEI e) and both CEI and SEI are pre-formed at 55°C. The control cycles are designated as follows: Control N corresponds to the cycle at C/20 that is measured after subjecting the battery to Nx100. aaina cycles at 1C.*

### V.2.2.b. SEI characterization

To gain further insight into the chemical composition of the SEI, XPS (X-ray photoelectron spectroscopy) experiments were conducted on graphite electrodes retrieved after 100 cycles at both 25 and 55°C from graphite/NMC811 cells cycled using LP57 VC and HCE DMC electrolytes. Two different photon energies, namely 3.0 and 6.9 keV (in the hard X-ray range), provided by synchrotron radiation, were employed to examine the SEI composition as a function of depth. These photon energies correspond to probing depths estimated at 20-25 nm and 40-50 nm, respectively (see experimental details in Annex 8). Notably, the use of Hard X-ray photoemission spectroscopy (HAXPES) enabled reaching a greater probing depth compared to the SEI thickness, thereby facilitating the detection of the C 1s signal of graphite.

The results for 3.0 keV photon energy are depicted in Figure 59, while Annex 15 displays the results for 6.9 keV.

The C 1s spectra of all samples (Figure 59a) exhibit the same components. These include a thin and asymmetric component at low binding energy ( $\sim 283$  eV) assigned to graphite, and four components at 285 eV, 286.5-287 eV,  $\sim 288$  eV, and 289.5-290 eV, attributed to hydrocarbon ( $\text{CH}_x$ ), one-oxygen, two-oxygen, and three-oxygen (carbonate) environments of carbon, respectively. It is worth noting that the observed binding energy of graphite ( $\sim 283$  eV) is approximately 1 eV weaker than that observed for pure graphite material. This difference cannot be attributed to the lithiation of graphite but rather to the differential charging effect between the SEI and the graphite substrate during the ejection of photoelectrons due to their significantly different electronic conductivities. The four other components align with what is conventionally observed for the SEI formed with carbonate-based electrolytes, indicating the presence of carbonaceous species resulting from the reduction of solvents [229]. Additionally, a weak additional component at  $\sim 291$  eV is observed, which could originate from the polymerization of VC (vinylene carbonate) on the graphite surface, resulting in poly(VC) in the case of LP57 electrolyte [229], or it may correspond to the  $\pi\text{-}\pi^*$  shake-up satellite of the graphite peak.

The F 1s spectra (Figure 59b) consist of two components. The first one, at high binding energy, is assigned to the salt used ( $\text{PF}_6^-$  in the case of LP57 VC and  $\text{FSI}^-$  in the case of HCE DMC), while the second one, at lower binding energy ( $\sim 685$  eV), is attributed to LiF, which is a common degradation compound observed for fluorinated salts. The degradation compounds of the salts are also detected in the P 2p spectra (for  $\text{LiPF}_6$ ) by the presence of a P 2p doublet at low binding energy ( $\sim 134$  eV) corresponding to phosphates, and in the N 1s spectra (for LiFSI) by the presence of a component at low binding energy ( $\sim 398.5$  eV) resulting from the breakage of S-F bonds and subsequent formation of LiF [230].

The O 1s spectra (Figure 59c) exhibit notable differences for the two different electrolytes. In the case of LP57 VC, they consist of two components at  $\sim 532$  and  $\sim 533.5$  eV, which are consistent with oxygenated carbonaceous species such as  $\text{Li}_2\text{CO}_3$  and lithium alkylcarbonates, commonly described as the main species of the SEI [231]. For HCE DMC, the O 1s spectra are modified by the presence of the oxygenated salt  $\text{LiN}(\text{SO}_2\text{F})_2$ . Additionally, most O 1s spectra display a very weak component at low binding energy ( $\sim 528$  eV), corresponding to  $\text{Li}_2\text{O}$ . This component is easily distinguishable from the others but represents a minimal amount within the SEI.

Examining the differences between these samples, an important characteristic is the relative intensity of the C 1s component of graphite compared to other carbonaceous species. This ratio provides a qualitative indication of the SEI thickness. For the LP57 VC electrolyte, the SEI thickness is significantly greater after cycling at  $55^\circ\text{C}$  than at  $25^\circ\text{C}$  (the relative area of

C 1s components corresponding to the SEI is approximately doubled compared to graphite). Nevertheless, the SEI thickness still remains below the probing depth (20-25 nm at 3 keV) as the graphite signal is clearly detected. Unfortunately, due to the lack of a reliable photoionization cross-section database and information on the analyzer transmission function at each possible photon energy of the beamline, a detailed quantification of species is not possible. However, quantitative comparisons between samples can be made. For instance, for the LP57 VC electrolyte, the F 1s / C 1s area ratio only decreases by a negligible 7% from 25°C to 55°C. This indicates that the overall amount of fluorinated species is similar at both temperatures. However, the relative amount of LiF compared to  $\text{PF}_6^-$  is much higher at 55°C than at 25°C, which aligns with an increased degradation of the salt at higher temperature. This enhanced salt degradation is also evident in the P 2p spectra, which show more phosphates compared to  $\text{PF}_6^-$  at 55°C. Consequently, it can be concluded that the SEI is thicker and contains more inorganic species resulting from salt degradation at 55°C. This observation should be considered in relation to the electrochemical results. Although the SEI is thicker at 55°C, which should lead to an increase in interfacial impedance, this effect is counterbalanced by a faster kinetic for lithium exchange. Similar observations can be made for the HAXPES spectra obtained with the higher photon energy (6.9 keV, see Annex 15), which corresponds to a doubling of the probing depth. The relative area of the C 1s components corresponding to the SEI is indeed doubled compared to graphite, confirming the thickening of the SEI.

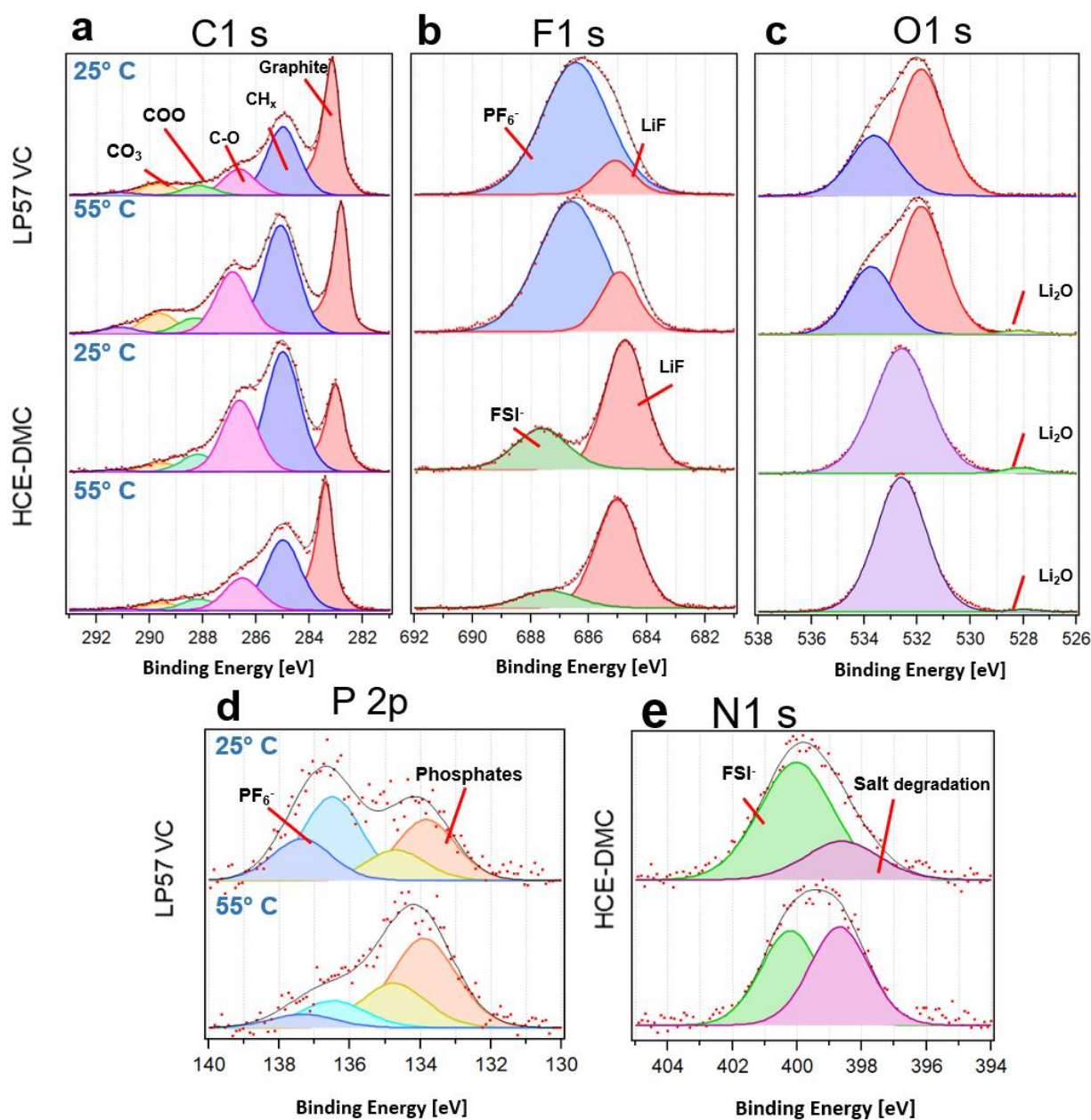


**Figure 59 – XPS of graphite electrode**

a), C 1s, b) F 1s and c) O 1s HAXPES spectra of graphite electrodes recovered from graphite/NMC811 cells after 100 cycles performed at 25 and 55°C, using LP57 VC and LiFSI 5M DMC electrolytes. d) P 2p spectra in the case of LP57 VC (LiPF<sub>6</sub> salt), and e) N 1s spectra in the case of LiFSI 5M DMC. The HAXPES spectra were recorded with 3 keV photon energy.

Shifting focus to the HCE DMC electrolyte, the effect of temperature on the SEI thickness is opposite: the SEI is thinner at 55°C than at 25°C. As seen from the C 1s signal of graphite in Figure 59a, the relative area of C 1s components corresponding to the SEI is reduced by a factor of 2.4 compared to graphite. The SEI thickness for HCE DMC at 25°C is the largest among the two sets of samples. Additionally, the F 1s / C 1s area ratio decreases by 32% at 55°C, indicating that the SEI has experienced significant depletion of fluorinated

species compared to 25°C. These observations align well with the electrochemical results. At 25°C, lithium plating was observed during over-lithiation of the graphite electrode, which is consistent with a thick and resistive SEI hindering intercalation into graphite. Conversely, at 55°C, the SEI is not only thinner but also contains fewer inorganic (and presumably more resistive) species compared to 25°C, resulting in a positive effect on electrochemical performance. The results suggest that lithium plating observed at 25°C with HCE DMC leads to more electrolyte decomposition at the negative electrode, which is consistent with the increased LLI during DVA (Figure 53) and the rollover of marching capacity (Figure 49).

### V.2.3. Electrolyte optimization

#### V.2.3.a. Addition of VC

Our results demonstrate that at 55°C, the formation of the SEI effectively prevents lithium plating in HCE DMC, thus averting destabilization of the negative interface. Another approach to stabilize the negative electrode involves the use of additives. Taking inspiration from LP57 VC, which proved efficient in stabilizing the negative electrode as shown in Figure 49, VC was added at a weight proportion of 2wt% in the HCE DMC electrolyte. The results are presented in Figure 60, with the HCE results (red) serving as the benchmark reference. The cell using HCE VC (blue) exhibited a linear decrease in capacity over cycles without any change in slope, suggesting no clear change in the degradation mechanism (Figure 60a). Furthermore, CE remained consistently high even beyond the 250<sup>th</sup> cycle, suggesting that the cell did not experience any further destabilization at the negative electrode. However, during the initial ten cycles, a low CE is recorded, associated with an increase in capacity endpoints at a similar rate to that of pristine HCE (Figure 60b). This strongly indicates, to no surprise as VC is known for its beneficial effects at the negative electrode, that the undesired oxidation of DMC was not suppressed. Additionally, the mean polarization reached 0.16 V with HCE VC in the last and 5<sup>th</sup> control cycles, compared to 0.09 V with pristine HCE (Figure 60c), suggesting the decomposition of VC at the negative electrode leads to more resistive interface.

The degradation of HCE VC electrolyte is further supported by the DVA results (Figure 60d), which demonstrate that the primary capacity slippage is associated with degradation at the positive electrode most likely parasitic oxidation of DMC. Importantly, the ICA reveals the appearance of peaks at the end of charge (Figure 60e), which are associated with lithium plating alike observed for HCE (Figure 56). The findings confirm that the initiation of lithium plating is linked to an imbalance between the capacities of the electrodes during aging, rather than the deposition of an oxidation product on the graphite surface that hinders Li<sup>+</sup> intercalation [104]. In ref [104], the addition of VC additives was shown to successfully mitigate the increase in cell impedance, which is not observed in our work. The disparity in results can be attributed to two factors. Firstly, the difference in cell format may play a significant role. Dahn's group

cycled 18650 cells, which have distinct characteristics compared to the ones used in the study, such as differences in balancing and electrolyte volume. Secondly, the better  $\text{Li}^+$  intercalation kinetic observed could be due to a lower additive amount of 1.5wt% compared to 2wt% and the higher cycling temperature of 30°C. However, the inclusion of VC additives has a positive impact on cell performance by reducing the LLI caused by the highly reactive lithium metal at the graphite surface. VC thus aids in stabilizing the negative electrode, sustaining a good CE during cycling and thereby preventing capacity rollover beyond the 250<sup>th</sup> cycle.

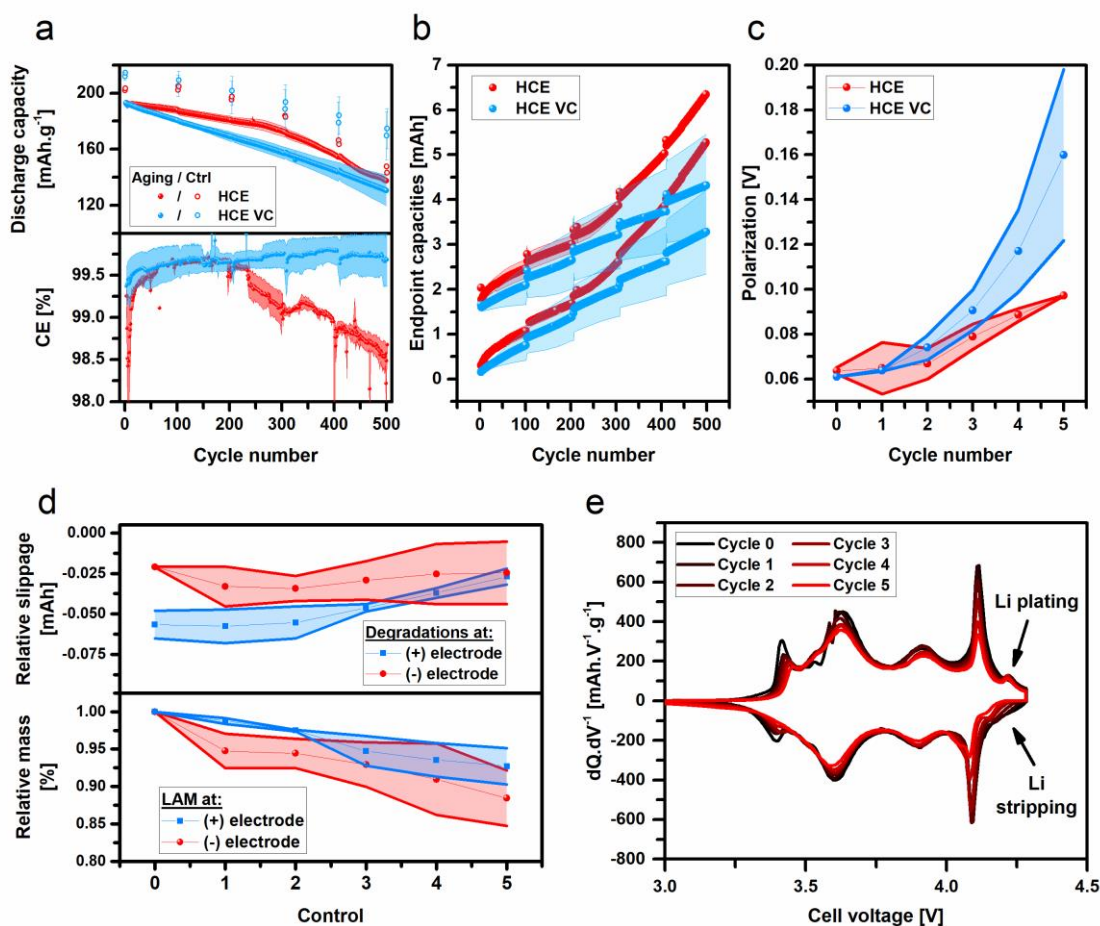


**Figure 60 – Advantages of using VC in HCE on cell performance**

*Effect of 2wt% VC additive in HCE on the performance of graphite/NMC811 cell at 4.3 V. Control N corresponds to the cycle at C/20 that is measured after subjecting the battery to Nx100 aging cycles at 1C b) Comparison of marching capacities between HCE and HCE VC. c) Associated cell polarization recorded for control cycles. d) DVA of the cells using HCE showing relative slippages (higher panel) and LAM (lower panel). e) ICA performed at 25° for HCE VC. Error bars in the data are obtained by duplicating the cell conditions.*

### V.2.3.b. Use of EC instead of DMC

While we demonstrated that VC additive can prevent uncontrolled destabilization of the SEI upon lithium plating, it does not eliminate the chemical cause of this reaction, which originates from the parasitic oxidation of DMC. To address this issue, DMC was replaced with EC to form a LiFSI 5M in EC (HCE EC) electrolyte, which was tested at both 25°C and 55°C (Figure 61a). At 25°C, the capacity retention curve exhibits a gradual degradation with a significantly improved CE averaging at 99.4%. The endpoints of the capacity marching (Figure 61b) and the DVA (Figure 61c) demonstrate no notable signs of parasitic oxidation when compared to HCE DMC. Consequently, the primary cause of capacity loss can be attributed to the LLI associated with the SEI growth, which is evident by the shift towards the left of the positive electrode. This LLI cannot be attributed to higher amounts of transition metals, as suggested by the ICP-MS quantification in Annex 16. At 55°C, no parasitic oxidation is

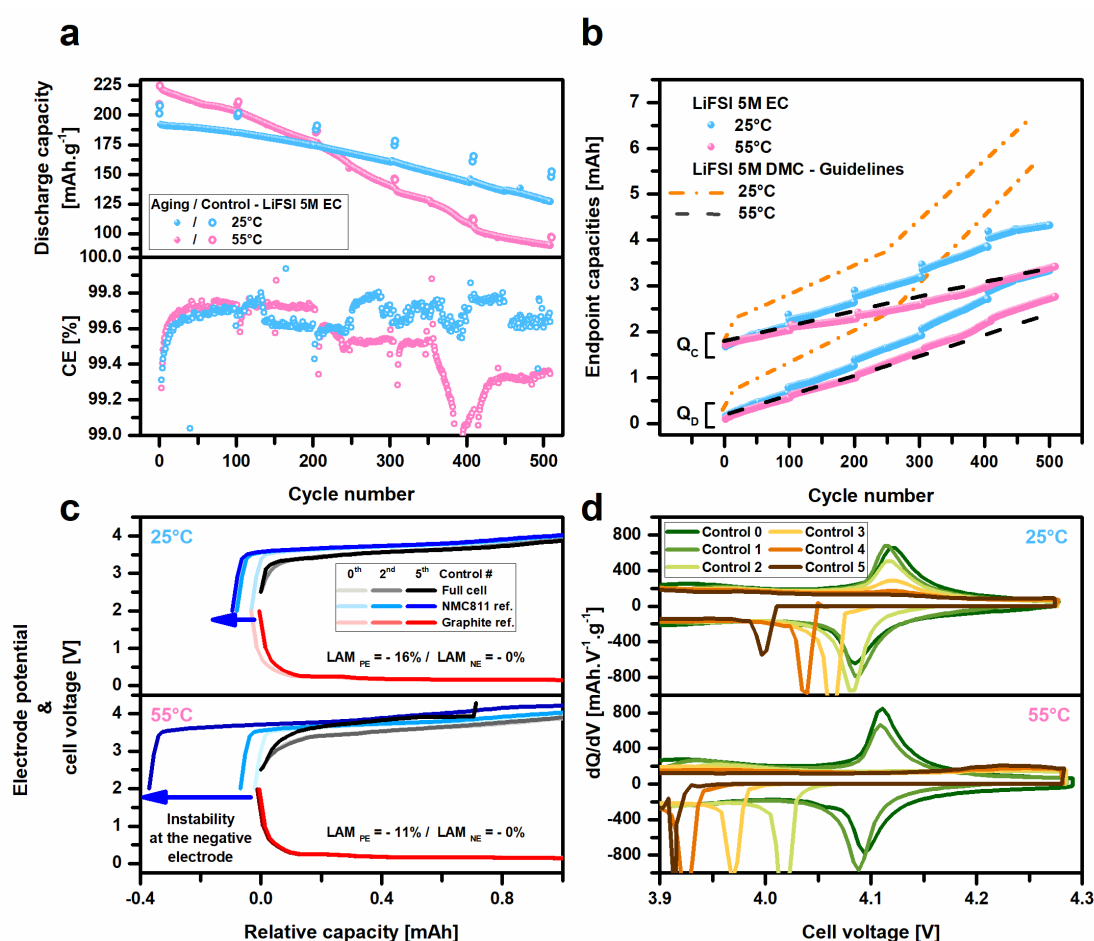


**Figure 61 – Outcomes of using EC-based HCE on cell performance**

a) Cycling performance measured using LiFSI 5M EC at 25 and 55°C. The control cycles are designated as follows: Control N corresponds to the cycle at C/20 that is measured after subjecting the battery to Nx100 aging cycles at 1C. b) Comparison of marching capacities between LiFSI 5M DMC and LiFSI 5M EC as a function of cycling temperature. c) DVA of the cells using HCE-EC at 25°C (higher panel) and 55°C (lower panel). d) ICA performed at 25°C (upper panel) and 55°C (low panel) for HCE-EC.

detected, and the accelerated capacity fading, when compared to 25°C, is once again attributed to the LLI being more favorable at higher temperatures.

Furthermore, no lithium plating/stripping is observed during ICA (Figure 61d), and as a result, no rollover in the capacity marching plots is observed at either 25°C or 55°C. Considering that lithium plating was previously shown to be directly caused by the additional capacity resulting from DMC oxidation, our findings indicate that the key advantage of HCE EC lies in its stability and absence of parasitic oxidation at high potentials. However, the DVA reveals that HCE EC experiences a severe LLI at the negative electrode and uncontrolled SEI growth when cycled at 55°C.

## V.3. LOCALIZED HIGH CONCENTRATION ELECTROLYTE

### V.3.1. Finding the ideal composition

#### V.3.1.a. Stabilization of the negative electrode interface

Although HCE EC or VC additive show improvements in stabilizing graphite/NMC811, parasitic reactions still exist and capacity fading limits the performance to less than few hundreds of cycles before reaching 80% SOC. Another recently designed HCE variant has also shown promising properties in stabilizing high voltage materials by incorporating a highly fluorinated ether called TTE as co-solvent (C.f. introduction chapter). These so-called localized high concentration electrolytes (LHCE) have not been subjected to comprehensive cell degradation studies until now. In this section, our goal is to assess the performance of LHCE with a LiFSI:DMC:TTE composition having a molar ratio of 1:2:3 in graphite/NMC811 cells at 4.3 V. The cycling conditions are similar to those used in section V.1.1. Two additives at 2wt% of the total electrolyte amount, VC and FEC, were also tested to stabilize the negative interface. The resulting performances are depicted in Figure 62.

When using pristine LHCE, the cells retain an average of 83% of their initial capacity after 500 cycles at 1C, with a steady CE averaging 99.6% (Figure 62a). Moreover, the marching rates, shown in Figure 62b, exhibit an average of  $3 \mu\text{Ah}\cdot\text{cycle}^{-1}$ , which is three times lower than that observed with HCE and equivalent to LP57 VC under similar cycling conditions. This suggests the absence of parasitic oxidation or unexpected interface destabilization. Additionally, the low polarization shown in Figure 62c confirms the absence of resistive interphase formation or uncontrolled degradation of the electrolyte upon lithium plating.

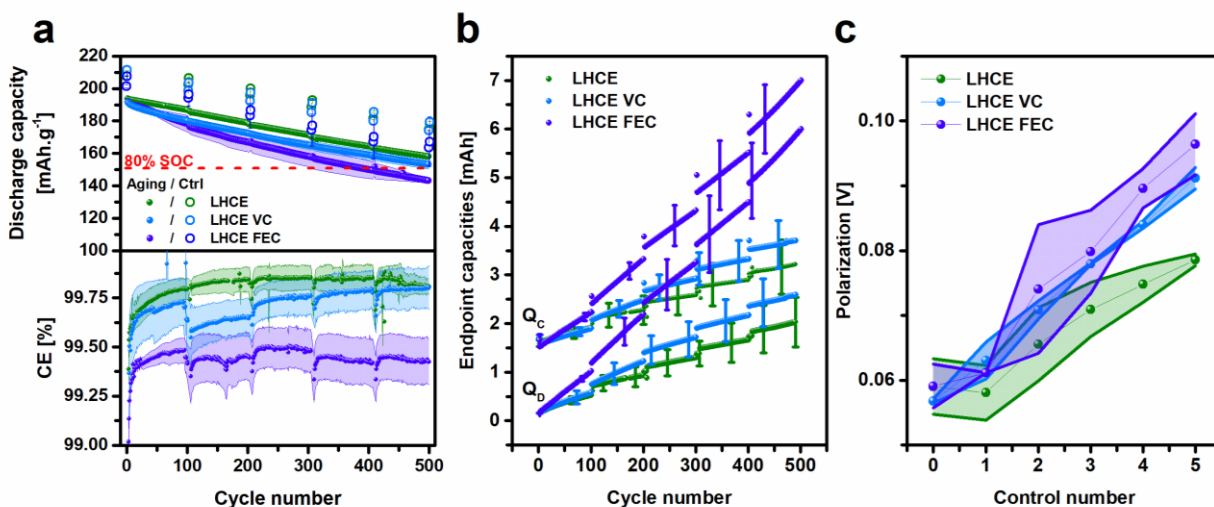


**Figure 62 – Performance using LHCE and SEI additives**

a) Capacity retention for graphite/NMC811 cells at 4.3 V using LHCE (green), LHCE VC (light blue), and LHCE FEC (purple). Associated CE depicting more degradation when VC and FEC are added. b) Marching of charge and discharge capacity endpoints. c) Polarization of control cycles that confirms that the addition of VC and FEC leads to resistive interphases. Error bars in the data are obtained by duplicating the cell conditions.

When VC and FEC are added, capacity retention are surprisingly lower than with bare LHCE, reaching 80% and 75% in average after 500 cycles, respectively (Figure 62a). The progressive cycling capacity window by Q<sub>D</sub> in marching curves (Figure 62b) as well as the increase of cell polarization (Figure 62c) suggest that decomposition of the additives induces higher lithium losses and the formation of more resistive interphases. The addition of 2wt% VC or FEC, is therefore not ideal for stabilizing the cell. However, capacity losses are slowing down from cycle 400 when VC is present, which suggests that better performance could possibly be achieved over the next 500 cycles. Further analysis are provided in the following sections.

The DVA of LHCEs is illustrated in Figure 63, with the upper panel showing the relative slippage between electrodes in mAh, and the lower panel demonstrating the evolution of the active mass material, initial mass being equal to unity. Using pristine LHCE (Figure 63a), the relative slippage associated with degradation is minimal at both the positive and negative electrodes, confirming the absence of significant degradation. It is worth noting that the absence of relative slippages does not arise from an equal increase in absolute slippage (see low marching in Figure 62b), which would suggest degradation occurring at the same rate at both the positive and negative electrodes. Indeed, relative slippage only becomes evident when one slippage is greater than the other. If both slippages are equal, even if they are not

null, the relative slippage will be zero. In results, LHCE show very high stability at interfaces and the excellent performance of LHCE is not artificially induced, as was previously observed with HCE. When VC or FEC are added (resp. Figure 63b and 63c), the degradations are prevalingly localized at the negative electrode. This suggests that the additives promote the formation of SEI which triggers higher consumption of lithium ions and eventually leads to LLI. Furthermore, the stabilization of LLI with VC prompts the examination of cell performance for extended cycles exceeding 500 cycles. It is important to note that the amounts of additives used in this study are not optimized, and it is possible that 2wt% is already too high. Further optimization work can be considered, but due to time constraints, it has not been conducted in this thesis work. The conclusion regarding additives is thus specific to the tested cell configuration and electrolyte composition.

When FEC is used, the LLI do not stabilize throughout the cycling indicting the poor passivating properties of FEC-derived SEI. Finally, the LAM remain similar independently of electrolyte used, ranging between -5% and -15% of the initial active material masses, that is the usual value recorded for NMC811 at 4.3 V as shown in Figure 53. Moreover, there is no observation of lithium plating/stripping during incremental capacity analysis (ICA, see Annex 17), nor any notable changes in the electrochemical behavior. Altogether the results indicate that the addition of common additives for the SEI at 2wt% does not lead to higher performance in the first 500 cycles. The inertness of pristine LHCE is its best outcome and over-optimizing the composition with VC or FEC is not ideal before 500 cycles. However, the actual outcomes of VC may become apparent in subsequent cycles.

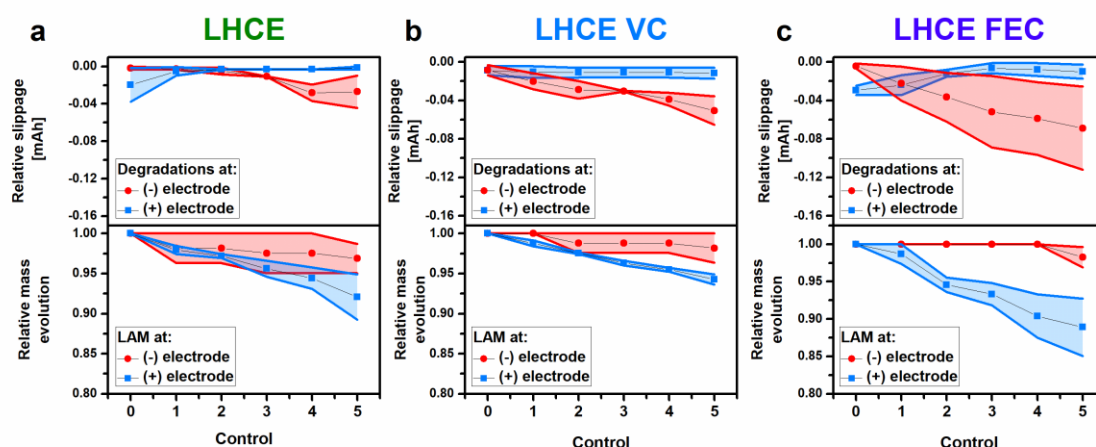


**Figure 63 – DVA with LHCE and SEI additives**

*DVA showing the evolution of relative slippage [mAh] in upper panel and relative active material mass for cell using LHCE a), LHCE VC b) and LHCE FEC c). When VC and FEC are added, relative slippage evolution show continuous degradation at the negative electrode associated to the SEI growth. Error bars in the data are obtained by duplicating the cell conditions.*

### V.3.1.b. Stabilizing the positive electrode interface

Our attention then turns to the use of additives to stabilize the positive electrode, following past reports in which additives have been described as beneficial in the formation of a more passivating CEI. Although not extensively studied or fully understood, past reports have shown positive results with trimethylphosphite (TMP) [232], [233] and fluorobenzene (FB) [234], encouraging us to further test and investigate these additives. TMP and FB were added at a concentration of 2wt% in LHCE and tested using a similar cell configuration and testing protocols. The results are benchmarked against bare LHCE (shown in green, in Figure 64). The results of LHCE with CEI additives exhibit poor performance. LHCE FB falls below 80% SOC in average at cycle 365, while LHCE TMP falls below 80% SOC at cycle 255. Furthermore, pristine LHCE recorded a CE of 99.7% while LHCE FB and LHCE TMP recorded 99.6% and 99.3% SOC, respectively, indicating higher degradations for LHCE with CEI additives.

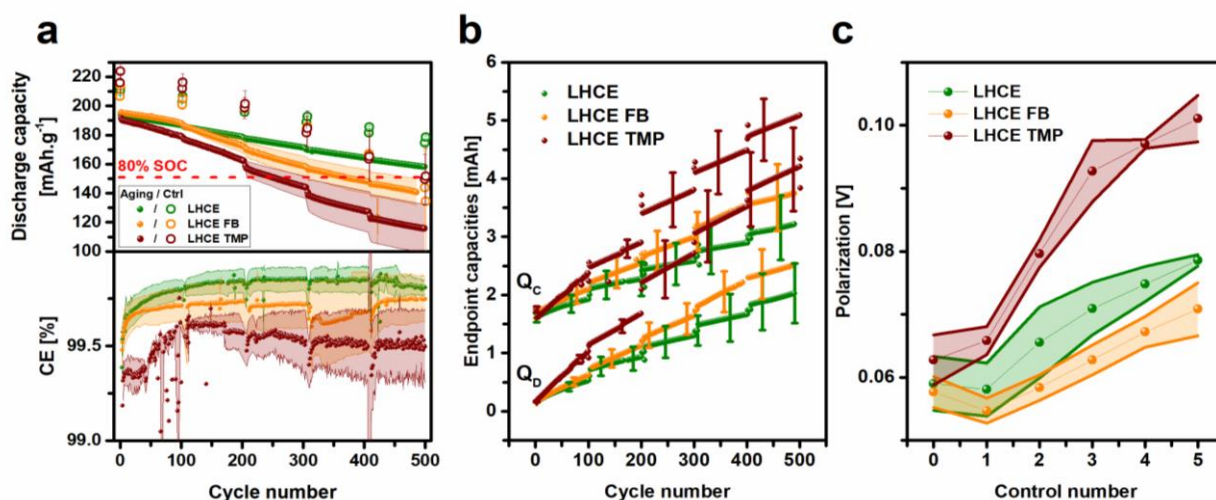


**Figure 64 – Performance of LHCE with CEI additives**

a) Capacity retention for graphite/NMC811 cells at 4.3 V using LHCE (green), LHCE FB (orange), and LHCE TMP (brown). Associated CE depicting more degradation when FB and TMP are added. b) Marching of charge and discharge capacity endpoints. c) Polarization of control cycles that confirms the addition of VC and FEC lead to resistive interphases. Error bars in the data are obtained by duplicating the cell conditions.

The evolution of capacity endpoints confirms the results primarily observed, with higher degradation rates in the presence of FB and TMP additives (Figure 64b). Specifically, when TMP is added, the increase in  $Q_C$  endpoints drives the progressive marching up to the 200<sup>th</sup> cycle before the capacity window closes, i.e. when  $Q_D$  increases faster than  $Q_C$ . This observation indicates that parasitic oxidation is the main degradation mechanism initially, before transitioning to predominant degradation at the negative electrode, likely due to intense SEI growth. The significant rise in polarization when using TMP validates the formation of

resistive interphase during TMP decomposition (Figure 64c). This phenomenon can be associated to the formation of  $\text{Li}_x\text{PO}_y$  species, as observed in previous studies on  $\text{LiCoO}_2$  surface when 5wt% TMP was used [233]. When FB is added, degradation rates are slightly higher compared to pristine LHCE (Figure 64b), although the average polarization is in average 9% lower (Figure 64c). This result can be rationalized by the use of FB as a co-solvent for LHCE, where a slight additional dilution may enhance interfacial kinetics and lead to faster reactions [152].

The effect of additives was further investigated using DVA, and the results are presented in Figure 65. When FB is added in LHCE, degradation at the negative interface (panel a) initially increases, as a result of LLI, before stabilizing at -0.03 mAh, which is a similar value to that observed in DVA for LHCE (Figure 63a). This observation suggests that FB is relatively inert, confirming its ideal use as a co-solvent for LHCE [152], [234], rather than as an additive. When TMP is added (panel b), the initial degradation occurs predominantly at the positive electrode, which is consistent with the high  $Q_c$  marching observed in Figure 64b. However, starting from the second control (approximately at the 200<sup>th</sup> cycle), the relative slippage of the negative electrode is likely associated to LLI due to the SEI formation. In other words, the TMP is oxidized at the positive electrode, leading to the formation of a thick and resistive CEI, which adversely affects the performance of the cell. The information provided in the ICA in the Annex 18 confirms that the destabilization of the negative electrode is not caused by lithium plating, but rather is assumed to be due to a significant SEI growth.

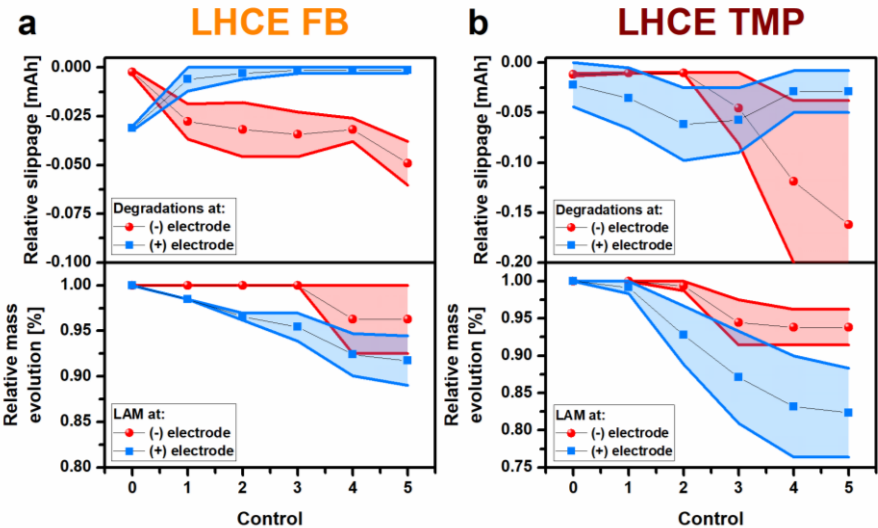


Figure 65 – DVA for LHCE with CEI additives

DVA showing the evolution of relative slippage [mAh] in upper panel and relative active material mass for cell using LHCE a), LHCE VC b) and LHCE FEC c). Error bars in the data are obtained by duplicating the cell conditions.

In results, the utilization of 2wt% additives for SEI and CEI in the state-of-the-art LHCE is not conclusive in enhancing the long-term performance of graphite/NCM811 cells. Instead, their usage leads to accelerated cell degradation by initiating SEI growth and/or formation of an interphase too resistive, thereby limiting their overall effectiveness before the 500<sup>th</sup> cycle. Therefore, after this study, bare LHCE was considered as state of the art for the remaining part of the study.

### V.3.2. Stability limits at high voltages

We have established that bare LHCE, i.e. without additives, was the most effective at stabilizing graphite/NCM811 cells at 4.3 V. This notable outcome serves as motivation to investigate the extent to which upper voltage can be extended, as NMC811 does not reach a fully delithiated state at 4.3 V in full cell. An additional 9 mAh.g<sup>-1</sup> can be obtained by cycling the cell to 4.5 V vs Li<sup>+</sup>/Li (i.e. 4.42 V in full cell), as illustrated in Figure 8 of the Introduction chapter. To study the effect of upper cutoff voltage, a set of graphite/NCM811 cells was cycled at different cutoff voltages using a similar procedure explained in part V.1.1. Their performance is shown in Figure 66a. As expected from the half-cell curves, increasing the cutoff voltage from 4.3 to 4.4 V results in an increase in discharge capacity of up to 7 mAh.g<sup>-1</sup>, while cell maintains 82% SOC after 500 cycle. When the upper voltage is set to 4.5 V, the capacity fading accelerates, and the cell fails below 80% state of charge (SOC) by the 410<sup>th</sup> cycle. Furthermore, the decrease in CE to 98% starting from the 400<sup>th</sup> cycle indicates an impending capacity rollover in subsequent cycles. Additionally, the cell operating at 4.6 V fails before the 80<sup>th</sup> cycle, indicating a profound destabilization of materials and interfaces at this voltage. The observation is corroborated by the significant increase in cell polarization shown in Figure 66b for control 2, suggesting that the cell experiences degradations that hinder Li intercalation, such as bulk fatigue or resistive interphase growth.

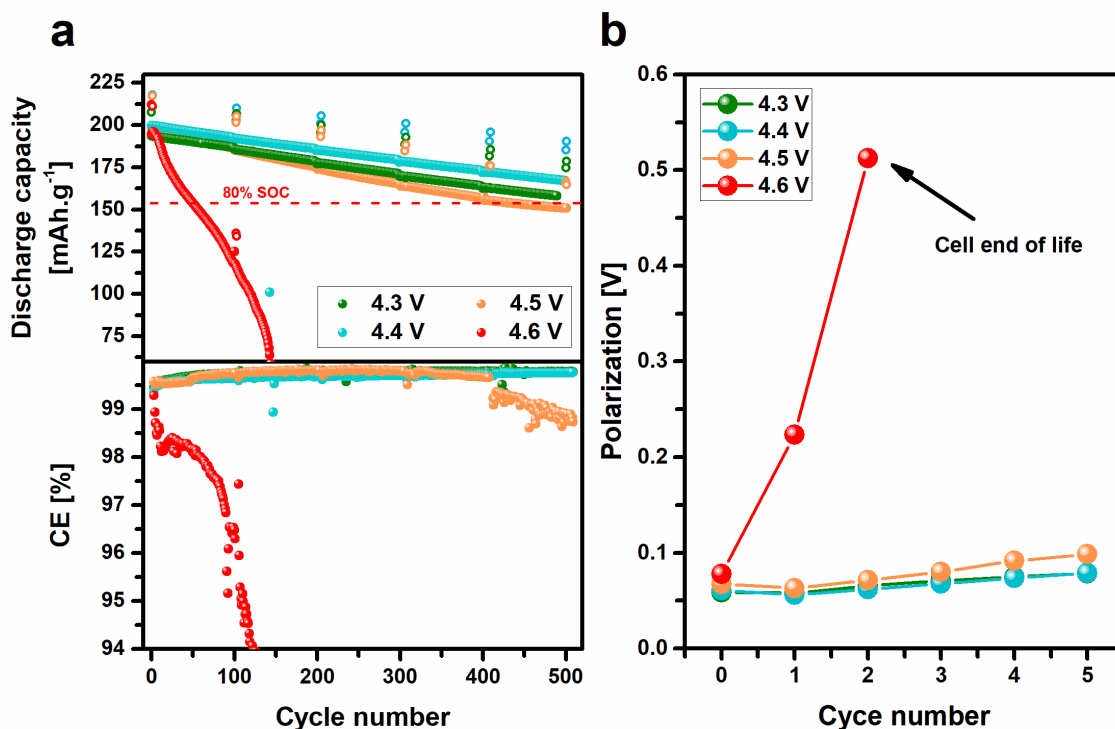


**Figure 66 – Stabilization of cells at high voltage using LHCE**

a) Performances of graphite/NMC811 cells using LHCE at different upper voltage cutoffs from 4.3 to 4.6 V. Cell cycled at 4.6 V fails at cycle 200. b) Associated polarization of cell showing the large increase in 4.6 V cell.

Cycling behaviors observed at 4.4 V and 4.5 V are further investigated using DVA (Figure 67, panels a and b, respectively). The analysis of relative slippage (upper panel) reveals low values for both cells, indicating that degradation is primarily occurring at the negative electrode. Unlike the HCE case shown in Figure 53, there is no clear evidence of initial side oxidation. Instead, the growth and repair of the SEI layer become the dominant degradation mechanism in these cells. At 4.5 V (Figure 67b), a similar behavior is observed, but starting from control 4, the dominant degradation shifts to the positive electrode. This suggests that lithium is unable to effectively reinsert into the NMC material at the end of discharge. This finding is consistent with the high LAM PE of -23% after 500 cycles compared to -9% at 4.3 V. Lastly, it is important to note that the dV/dQ data at 4.6 V do not allow for a proper DVA analysis and slippage analysis.

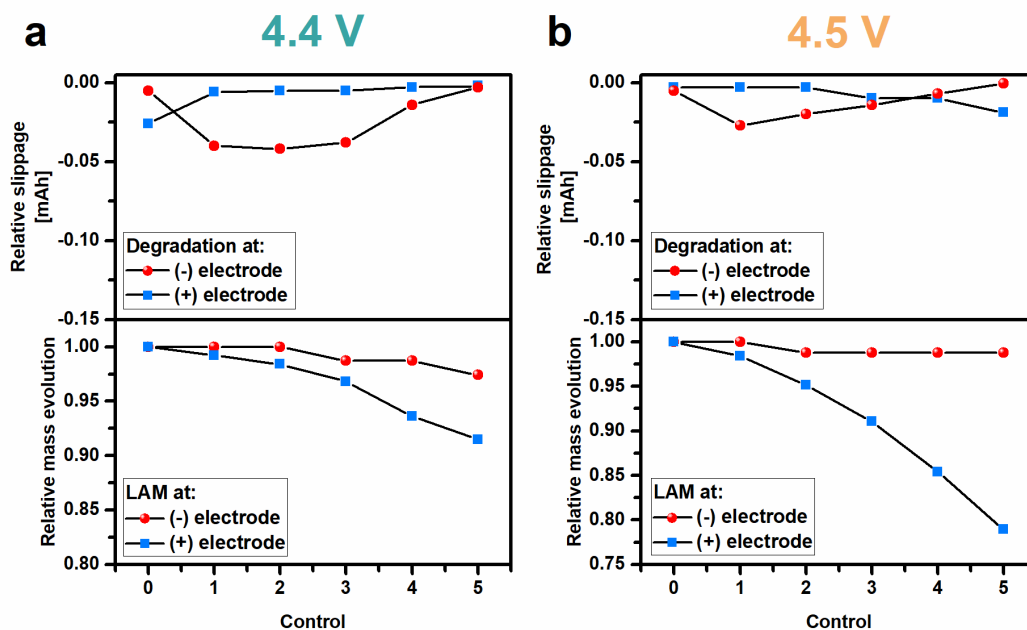


**Figure 67 – DVA of high voltage cells using LHCE**

*DVA of graphite/NMC811 cells using pristine LHCE at 4.3 V a) and 4.4 V b). The LAM PE increases with cutoff increase from 4.4 to 4.5 V.*

The ICA provides further confirmation of the high performance of LHCE in graphite/NMC811 cells up to 4.5 V, as the  $dQ/dV$  curves show nearly perfect overlapping even after aging (Figure 68a and b). Furthermore, there are no indications of lithium plating occurring up to 4.5 V. However, for the 4.6 V cell (Figure 68c), the ICA reveals significant drops in peaks

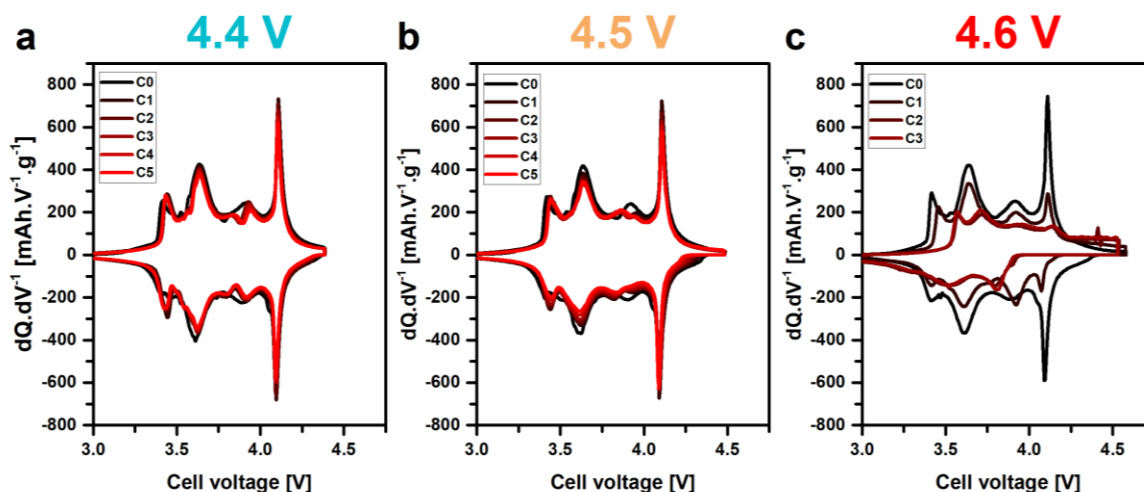


**Figure 68 – ICA of high voltage cells using LHCE**

*ICA of graphite/NMC811 cells performed at different voltage cutoff 4.4 V a), 4.5 V b) and 4.6 V c). The electrochemical performance are maintained up to 4.5 V.*

associated with high LAM. Additionally, there is a loss of peak intensity at 4.15 V during charging, indicating an increase in cell impedance, which aligns with the observed high polarization.

In summary, LHCE effectively stabilizes the interfaces of graphite/NMC811 cells up to 4.5 V, allowing for the full utilization of the NMC811 capacity. The degradations observed are associated with minor LLI related to SEI growth and LAM of the positive electrode material, which is expected at high working potentials. It is worth noting that the use of a cutoff voltage of 4.5 V is unnecessary since the cell operated at 4.4 V exhibits the same discharge capacity and experiences less capacity fading during cycling.

### V.3.3. Overview of electrolyte degradations

In Chapter V, we conducted tests at 4.3 V using three different types of electrolytes. The first one was the conventional electrolyte, 1 M LiPF<sub>6</sub> in EC:EMC (3:7) + 2%VC (LP57 VC). The second was a highly concentrated electrolyte (HCE) consisting of LiFSI:DMC in a 1:1.6 mol ratio. The third was a localized high concentrated electrolyte (LHCE) containing LiFSI, DMC, and TTE in a 1:2:3 mol ratio. Throughout the experiments, we observed various aging phenomena, including lithium plating and SEI growth, which can be summarized using an Arrhenius plot. To analyze these phenomena, the logarithm of capacity losses is plotted after 200 cycles at 2C (normalized by time and electrode surface area) against the inverse of aging temperature (Figure 69). Further details regarding this analysis can be found in Annex 3.

All three electrolytes experience an evolution of aging rates that follow a "V" shape as a function of temperature, indicating two distinct regimes. In the high-temperature regime ( $T > 20^{\circ}\text{C}$ , represented by full lines), degradation increases, suggesting that the mechanisms associated with solid electrolyte interface (SEI) growth and repair prevail. Conversely, in the low-temperature regime ( $T < 20^{\circ}\text{C}$ , represented by dashed lines), degradation primarily occurs due to lithium plating. At low temperatures, the slower kinetics of Li intercalation can lead to the formation of lithium metal deposits on the electrode surface. The electrolytes tested in this study demonstrate distinctive aging behaviors, which can be seen as an electrochemical signature linked to their specific compositions. Factors such as the onset temperature of lithium plating, degradation rates, and activation energies are specifically associated with each electrolyte. By analyzing the aging rates and temperature dependence, researchers can gain insights into the mechanisms of degradation and identify critical temperature thresholds for specific degradation processes such as SEI growth and repair as well as lithium plating.

When LP57 VC electrolyte is used, the degradation rates are the highest among the tested electrolytes, consistent with the early failure observed in Figure 49. Additionally, the cell exhibits increased sensitivity to lithium plating, with an onset of degradation occurring at approximately 35°C under 2C and 4.3V conditions. In the case of LHCE electrolyte, the lowest aging rate is observed at temperatures close to ambient temperature, around 25°C. The lower capacity loss observed with LHCE electrolyte corroborates the findings depicted in Figure 62 and 63. Lastly, when HCE electrolyte is used, the degradation regimes closely resemble those observed with LHCE. However, the capacity loss remains the lowest among the tested electrolytes. This can be explained by the phenomenon of parasitic oxidation being balanced by lithium plating, resulting in an artificially sustained capacity retention. It is important to note that for all three electrolytes, the activation energy for the SEI growth regime is similar, ranging from 0.47 to 0.52 eV. *Waldman et al.* and *Yang et al.* reported lower values of 0.38 eV [101] and 0.28 eV [221], respectively. These lower values can be attributed to the use of optimized commercial cells, e.g. 18650 batteries and batteries for plug-in hybrid electric vehicles (PHEVs), while coin cells are utilized in the current study.

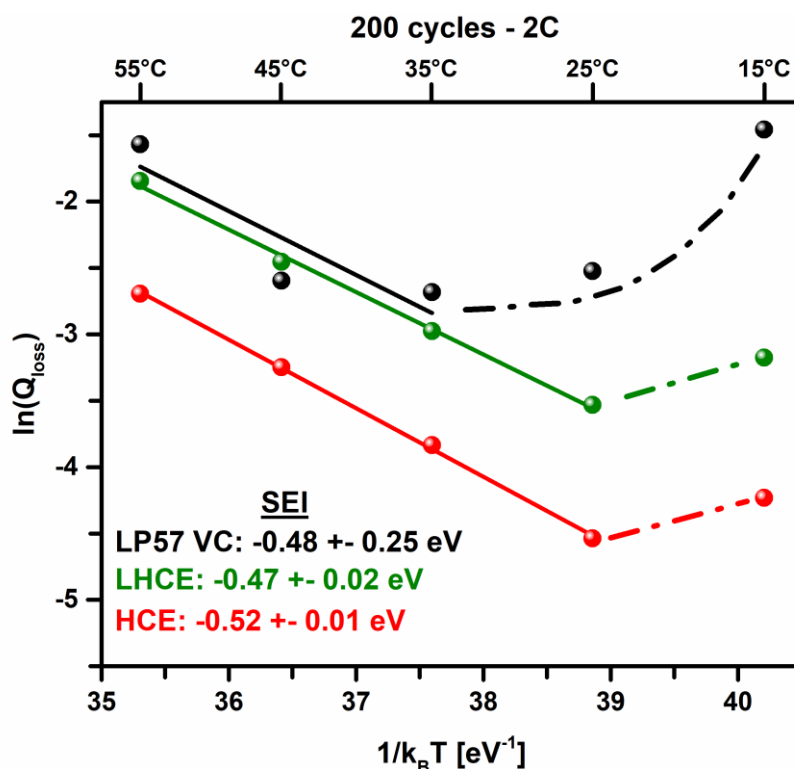


**Figure 69 – Overview of degradation behavior depending on used electrolyte**

Arrhenius plot of degradation rates recorded after 200 cycles at 4.3 V and 2C for graphite/NMC811 cells. The solid line corresponds to the regime characterized by SEI growth, and the activation energy values for this regime were obtained through fitting. The dashed lines represent the regime dominated by lithium plating.



## CONCLUSION OF CHAPTER V

Cycling NMC811 at a high potential of 4.3 V is known to result in rapid capacity decay. Our study confirms that the use of HCE-DMC initially improves the performance of graphite/NMC811 cells. However, a thorough analysis of the electrochemical results using DVA, ICA, and capacity marching exposes a series of side reactions that artificially maintain the seemingly good performance of HCE-DMC. The cascade of side reactions is initiated by the anodic decomposition of DMC at high potential, which, contrary to previous beliefs, is not prevented by the use of highly concentrated electrolyte. The additional capacity arising from DMC oxidation is counteracted by over-lithiation of the graphite electrode, eventually leading to lithium plating. Unlike in diluted carbonate electrolytes where lithium plating often causes a capacity rollover, the high CE associated with lithium plating/stripping in HCE-DMC does not result in a capacity drop. However, after 250 cycles, the accumulation of degradation mechanisms eventually destabilizes the negative electrode and triggers capacity fading.

To address the issue of lithium plating, we propose two strategies in this study: the development of DMC-free HCE and the enhancement of SEI and CEI stability through pre-formation steps at elevated temperatures. Consequently, our research reveals that when cycling at 55°C, the SEI becomes thinner and less resistive, effectively preventing lithium plating on the graphite surface. Higher temperatures also influence the capacity/voltage windows of electrodes, delaying the occurrence of lithium plating through the suppression of the GSJ and an upward shift of the working potential at the negative electrode. Moreover, by comparing the results obtained with HCE-DMC and HCE-EC, we confirm the detrimental role of DMC at high potential, as EC-based HCE exhibits no signs of parasitic oxidation at 4.3 V and no lithium plating at the negative electrode. However, significant LLI is observed when cycling at 55°C, significantly impacting the capacity retention achieved with HCE-EC. Ultimately, our findings suggest that selecting an appropriate solvent as EC or additives VC can mitigate the cascade of side reactions during cell aging, though cell remains not completely free of side reactions.

Lastly, LHCE successfully demonstrated a high level of stabilization for cell interfaces, resulting in 83% capacity retention at 4.3 V, which performance is not attributed to side reactions that artificially extend cell lifetime. Moreover, it is important to note that the inclusion of additives for SEI such as VC and FEC, as well as additives for CEI such as FB and TMP, does not yield to clear improvements before the 500<sup>th</sup> cycle. Instead, the introduction of these additives contributes to the formation of resistive layers and interphases, hastening the end-of-life of the cell. The pristine composition of LHCE alone proves sufficient to achieve the

longest lifetime and successful stabilization of the cell up to 4.4 V, enabling the full recovery of the capacity of NMC811. Finally, it should be emphasized that only through the use of appropriate electrochemical analysis and analysis workflows can such complex phenomena be revealed, where side reactions trigger one another. These practices should be widely adopted in the field to assess the advantages associated with novel electrolytes accurately and prevent any false positive results.

# **CONCLUSION AND PERSPECTIVE**



Achieving the goal of reaching Net Zero Emissions by 2050 is an ambitious challenge, and Li-ion batteries play an important role in this pursuit. Over the past three decades, significant progress has been made in cell chemistry and design, propelling this technology as a valuable solution for reducing carbon emissions, especially in the mobility sector. As the industry trends toward energy-dense batteries utilizing Ni-rich materials, the need for advanced stabilization strategies becomes crucial to effectively cycle these materials at high voltages and recover their full capacity. Although strategies using material doping, electrolyte design, or particle coating have undoubtedly enhanced performance, the evaluation methods used in testing occasionally impede an accurate assessment of the overall advantages obtained from the implemented approach. The conventional benchmark for evaluating battery performance, including discharge capacity and CE, seems to be insufficient, highlighting the need for an update in understanding what can be learned from electrochemical curves.

The goal of this Ph.D. research is to establish advanced battery testing protocols, including cell assembly, data analysis, and the evaluation of performance-enhancing solutions to mitigate degradation at Ni-rich interfaces. In Chapter II, the main focus is to ensure the acquisition of high-quality electrochemical data and implement appropriate electrochemical procedures. As part of the BIG-MAP project, the standardization of testing and cycling procedures plays a critical role in ensuring consistent testing across the 34 partner organizations and enabling direct processing of the resulting data using artificial intelligence (A.I.). To facilitate the testing of new chemistry on a larger scale, the coin cell format is considered ideal, and the assembly procedure is optimized accordingly. The optimized procedure involves filling the material and separator porosity with electrolyte four times to achieve a balance between ionic conductivity and enhanced performance. Additionally, achieving optimal internal pressure is accomplished by using the proper selection of component stack height, ensuring high electronic conductivity. With the incorporation of well-defined cycling conditions, the battery testing results are now reproducible and reliable. It is worth noting that the optimization process has been specifically conducted for the coin cell format and would require adaptation for implementation in industrial settings using 18650 or pouch cells.

The second phase of the research introduces analysis workflows aimed at establishing a solid foundation for better understanding degradation processes in battery technologies. We implement analysis workflows primarily based on capacity marching, DVA, and ICA to identify the exact causes of cell degradation. These workflows are put to the test by studying complex aging phenomena, such as the origin of the knee point in different graphite/Ni-rich chemistries. The knee point often arises from intertwined degradations known as crosstalk, where different

degradation mechanisms interact with each other. The developed analysis workflows successfully distinguish between three main causes of knee points. The first successfully detects the shuttle of redox species, which can have either benign or deleterious consequences. The second workflow focuses on the detection of crosstalk phenomena as the migration of metals to the SEI and determines the consequences metals deposited at the negative electrode have on lithium plating or SEI growth. Lastly, the third workflow aims at highlighting crosstalk that has a physical origin, such as the graphite staging jump (GSJ), and which causes a significant shift in the working potential of both the negative and positive electrodes, by several millivolts. This workflow is developed to reveal the consequences of GSJ and forecasts an acceleration or slowdown of cell degradation depending on the specific positive electrode used. Overall, this chapter focuses on theoretical aspects and outlines the promising strategies to investigate real-life cases involving the stabilization of Ni-rich materials. It is worth noting that these analysis procedures are transferable to any type of batteries, including sodium-ion or anode-less all-solid-state batteries (ALASSB). LLI conception is, however, not conceivable for batteries using metal anodes, which benefits from a semi-infinite alkali-cation reservoir, curbing its meaning.

With the incorporation of these new analysis workflows, our research focus shifts to the examination of Ni-rich materials, specifically LiNiO<sub>2</sub> in Chapter IV and NMC811 in Chapter V. It is crucial to emphasize that the outcomes in Chapters IV and V are exclusively relevant to the specific positive and negative electrode materials with their distinct properties. Variations in electrode and cell design may yield differing results, potentially complicating benchmarking across academic studies. Chapter IV investigates graphite/LiNiO<sub>2</sub> cells at high voltages, ranging from 4.2 to 4.8 V. As the voltage increases, capacity fading becomes more pronounced, and the use of DVA provides additional insights. At 4.2 and 4.5 V, the primary degradation originates from the growth and repair process of the SEI, which traps lithium and leads to LLI degradation. As the SEI growth rate slows down, degradation at the positive electrode progressively increases, accentuated by the LAM PE phenomenon. It is worth noting that despite detecting a parasitic oxidation event at 4.8 V, the relative slippage masks this phenomenon, highlighting the predominant degradation at the negative electrode associated with SEI growth. The results raise a question as to why most degradation recorded in this work occurs at the negative electrode, even though high voltage mainly promotes damages at the positive electrode. Our study reveals that this is attributed to nickel dissolution from LiNiO<sub>2</sub>, which migrates and incorporates into the SEI or reduces on the graphite surface, leading to further electrolyte decomposition and an increase in LLI. A temperature-dependence study revealed that nickel deposition at the graphite favors degradation mechanisms associated with SEI growth, surpassing any effect related to lithium plating, contrary to previous observations

in the literature. Similar conclusions are applicable to cobalt and manganese, both of which were also tested in this study. In addition, any type of metal deposited at the negative electrode was associated with an increase in LLI at high aging temperatures. In the subsequent phase of this research, testing a chelating membrane to capture the metals released from the positive electrode in the electrolyte or exploring additives to promote the formation of a robust CEI to limit metal leaching could be considered. As a final remark of this chapter, one must emphasize that no advantages are obtained when cycling  $\text{LiNiO}_2$  above 4.2 V, as all the capacity is extracted below 4.2 V. However, the primary aim of this study was to serve as a model for understanding the effects of transition metal dissolution, and the most relevant materials will be tested at high voltage in future research.

The final chapter focuses on analyzing the behavior of HCE in graphite/NMC811 cells, known for their ability to enhance performance due to the formation of robust and thin interphases. The electrolyte composition containing 5M LiFSI in DMC (HCE-DMC) demonstrates improved capacity retention during the initial 250 cycles, but afterwards, it experiences significant destabilization. Through high  $Q_c$  marching and DVA analysis, a parasitic oxidation process is identified, which is found to be linked to DMC oxidation, in agreement with UV-visible measurements. The additional capacity resulting from this oxidation is compensated at the negative electrode through excessive lithiation of graphite until plating occurs, as revealed by the appearance of plating features in ICA. Thanks to the efficient lithium plating/stripping in HCE, the consequences of plating are only evident after the 250<sup>th</sup> cycle, at which metallic lithium copiously reacts with the electrolyte, causing LLI, and whose decomposition products were observed by XPS. As a result, the HCE-DMC electrolyte artificially maintains high-performance levels. To address this issue, VC was introduced as an improvement to the HCE-DMC electrolyte, which limited the destabilization of the SEI layer, although some Li plating was still detected. Another approach was to dilute the HCE using TTE, creating a third type of electrolyte coined as LHCE (Locally Diluted HCE). This type of electrolyte exhibits the highest performance levels with low parasitic reactions and an impressive 82% capacity retention achieved at 4.4 V after 500 cycles, effectively recovering the full capacity of NMC811. In the quest to find suitable additives for SEI or CEI, tests with FEC, FB, and TMP did not yield conclusive results. Only VC showed promising stabilization of the negative interface, but only after prolonged cycling, making this additive potentially relevant in long-term cycling, particularly over 500 cycles. However, our results suggest that 2wt% of additive might be excessive for this application, and further optimization in this area is needed. Furthermore, the additives tested for improving the SEI are similar to those commonly used in LP class electrolytes but may not be well-suited for HCE or LHCE that show specific solvation properties; exploration of dedicated additives is therefore needed. Similarly, it is recommended

to test new additives and co-solvents with low fluorine content. Indeed, the main byproduct of electrolyte degradation, i.e., LiF, exhibits poor lithium conductivity and is increasingly seen as a drawback for SEI. Additionally, future regulations foresee a reduction in the commercialization of fluorinated compounds, making it essential to explore alternative options for electrolyte optimization.

More generally, the battery sector presents exceptional opportunities in the coming years to contribute to the decarbonization of our society. It generates enthusiasm in both academic and industry sectors, encouraging tackling the aforementioned challenges in research and innovation. Exploring novel material chemistries and proactively anticipating solutions for solid-state or sodium-ion batteries, along with the establishment of fresh regulations concerning the use of chemicals, are key milestones driving advancements in battery development. Alongside advancements in cell performance, the development of batteries raises concerns regarding material supply, production, and recycling. In 2021, nickel-based chemistries, specifically NMC and NCA, dominated the electric car battery market with a substantial 75% market share. This dominance was attributed to their advantageous characteristics, such as an extended driving range. However, the impending surge in battery production underscores the escalating mineral demand, notably for lithium, nickel, copper, and cobalt. Their finite availability and fluctuating price raise concerns about their adequacy to supply a global EV fleet. When considering both performance and cost aspects, the need for Ni-rich chemistries in all applications becomes questionable. Developing battery chemistries that utilize alternative elements can assist in relieving the pressure on material supply and reducing reliance on specific resources. It is worth noting that there has been a noticeable resurgence of LFP batteries in the market over the past two years. LFP batteries are suitable for mid-range vehicles and urban mobility, enduring frequent charging and intensive usage. Consequently, companies like Tesla and Volkswagen utilize LFP batteries for certain models, reserving the use of Ni-rich chemistries for top-of-the-range models. Moreover, the establishment of European "gigafactories" and mineral mining sites ensures more localized production, promoting greater independence. Finally, as the number of gigafactories for battery production increases, it is crucial to consider the next steps and contemplate the second life of batteries after reaching 80% state of charge (SOC). Planning a usage for second-use application and sizing of recycling units should not be overlooked, as it would be prudent to treat a large amount of used batteries.

In contrast to the general introduction chapter, these closing remarks adopt a resolutely optimistic perspective on the future. While climate change is unquestionably a recognized threat, it also offers the research community, including the battery field, thrilling challenges that

drive us towards a more sustainable world with each step we take. Each individual has the power to make changes in their lives and actively contribute to the solution.







## ANNEX 2 – ELECTROLYTE VOLUME CALCULATION TOOL

	Current collector thickness [μm]	Total electrode thickness Current collector + coating [μm]	Coating porosity (%)	Electrode diameter [mm]
Positive	20	39	32.6	14
Negative	9	39	48	15
	Separator thickness [μm]	Porosity [%]	Separator diameter [mm]	
Separator	25	55	20	
	Volume [μL]			
Total porosity [μL]	7.82			
Advised electrolyte amount to add (=4 times total porosity)	31.3			
Actual added amount [μL]	31.3			
Ratio - Used electrolyte / Total porosity	4.00			
Comment	Target met - Suitable electrolyte amount			

Snapshot of the electrolyte volume calculator design for coin cells. The advised electrolyte volume is to fill four times the total porosity of electrode and separator.

$$\text{Advised electrolyte volume} = 4 * V_{\text{total porosity}}$$

$$V_{\text{total porosity}} = V_{\text{porosity}}^{\text{negative electrode}} + V_{\text{porosity}}^{\text{positive electrode}} + V_{\text{porosity}}^{\text{separator}}$$

$$V_{\text{porosity}}^{\text{electrode}} = \pi * r_{\text{electrode}}^2 * (T_{\text{coating+cc}} - T_{\text{cc}}) * p_{\text{electrode}}$$

$$V_{\text{porosity}}^{\text{separator}} = \pi * r_{\text{separator}}^2 * T_{\text{separator}} * p_{\text{separator}}$$

With  $V$  the volume [μL],  $r$  the radius of electrodes/separator [μm],  $p$  the porosity of electrodes/separator [%],  $T$  the thickness of electrodes/separator [μm].

To ensure sufficient electrolyte volume in the cell before crimping, it is advised that electrolyte volume should be capable of filling at least four times the total porosity of both electrodes and the separator. The additional volume compensates for the inherent dead space within the coin cell, which allows for potential electrolyte flow.

### ANNEX 3 – EXPERIMENTAL SECTION OF CHAPTER III

**Electrode manufacturing** – Graphite electrodes were composed of 93.2wt% of active material (graphite GHDR 10–93, Imerys), 3wt% of carbon black (Super C45, Timcal), and a mixture of 2wt% carboxymethylcellulose (CMC), 1wt% styrene-butadiene rubber (SBR), and 0.8wt% surfactant (TritonX). Osmosed water, produced with a Merck Millipore (MilliQ), was added as a solvent until achieving a final dry mass ratio (total powder mass / (solvent + powder mass)) of 37wt%. Positive electrodes consisted of 92wt% LiNiO<sub>2</sub> (LNO, BASF, Germany), 4wt% polyvinylidene fluoride (PVDF) binder, and 4wt% carbon black (Super C45, Timcal). N-methyl-2-pyrrolidone (NMP, DoDoChem, 99.9%) was added as a solvent until the final dry mass ratio reached 25wt%. The respective inks were cast onto 20 μm thick copper and aluminum current collectors and then calendered to reduce the porosity to approximately 30%. The resulting final active material loadings were 4.2 mg/cm<sup>2</sup> for graphite and 5.6 mg/cm<sup>2</sup> for LNO.

**Coin cell assembly** – All coin cells were assembled in an argon-filled glove box using 2032-type casings, 1.23 mm thick wave springs, and a set of 0.5 and 1 mm 316-stainless steel spacers (AOT Battery, China). The electrodes were punched into circular disks with Ø14 mm (positive) and Ø15 mm (negative) dimensions, and then dried overnight at 80°C under reduced pressure. The negative capacity was oversized by 1.5 times compared to the positive one, resulting in a balancing N/P ratio of 1.5. Experimental capacities were calculated with the understanding that no additional capacity is measured above 4.2 V in graphite/LNO cells. Polypropylene films (Celgard 2500) were punched and dried at 55°C one week before use, and a single layer of separator was added. During assembly, the electrodes and separator were soaked with 30 μL of LP57 electrolyte (1M LiPF<sub>6</sub> in EC:EMC 30:70wt% – E-lyte, Germany), added in two steps: 15 μL on the anode and the remaining 15 μL on the separator.

**Investigation of transition metal effects** – To examine the impact of transition metal ions, salts of nickel bis(trifluoromethylsulfonyl)imide Ni(TFSI)<sub>2</sub>, manganese bis(trifluoromethylsulfonyl)imide Mn(TFSI)<sub>2</sub>, and cobalt bis(trifluoromethylsulfonyl)imide Co(TFSI)<sub>2</sub> (Alfa-Aesar, 97.0 +%) were dissolved in 1.000 mL of LP57 electrolyte. The metal concentrations were adjusted to 665 ppm, which corresponds to approximately 0.5% of the total weight of nickel present in the positive electrode.

**Electrochemical tests** – The cells were cycled at 25°C in a controlled temperature chamber (Memmert, Germany) using a BCS-810 potentiostat (BioLogic, France). Before the initial charge, the cells were allowed to rest for 6 hours to ensure that the electrolyte fills the

electrode/separator pores and reaches thermal equilibrium. The gravimetric capacity based on the LNO active mass was used. Similar currents were applied during charge and discharge, referred to as C-rates. Cycling was conducted from 2.5 V to 4.2, 4.5, or 4.8 V with C-rates defined based on the theoretical capacity of LNO ( $Q_{th} = 275 \text{ mAh.g}^{-1}$ ). After a formation step comprising two C/20 cycles, an "aging" period was carried out at C/2 current with a constant voltage step at the end of each charge until the current dropped below C/20. Every 10 cycles, a "control cycle" was performed to assess cell performance at low current (C/20) and conduct DVA (explained in detail below).

**Aging at different temperatures** – All cells were initially preconditioned with two cycles at C/20 at 25°C in a controlled temperature chamber (Mettler, Germany). Subsequently, independent cells were aged at various temperatures of interest, ranging from 15°C to 55°C. The cycling procedure commenced with a 6-hour open circuit voltage (OCV) rest to achieve thermal equilibrium, followed by an aging control procedure consisting of a repetitive cycle (C/20) alternating with 10 cycles of C/2, with a CV step at the end of charge  $i < C/20$ . Degradation rates were then calculated as the difference in discharge capacity between two control cycles, normalized by cycling time, working electrode surface area, and mass. For the study of lithium plating, the aging current was increased to 3C (instead of C/2), and the capacity balancing was reduced to 1.3 (previously 1.5). For each tested condition, cells were duplicated, resulting in the inclusion of error bars.

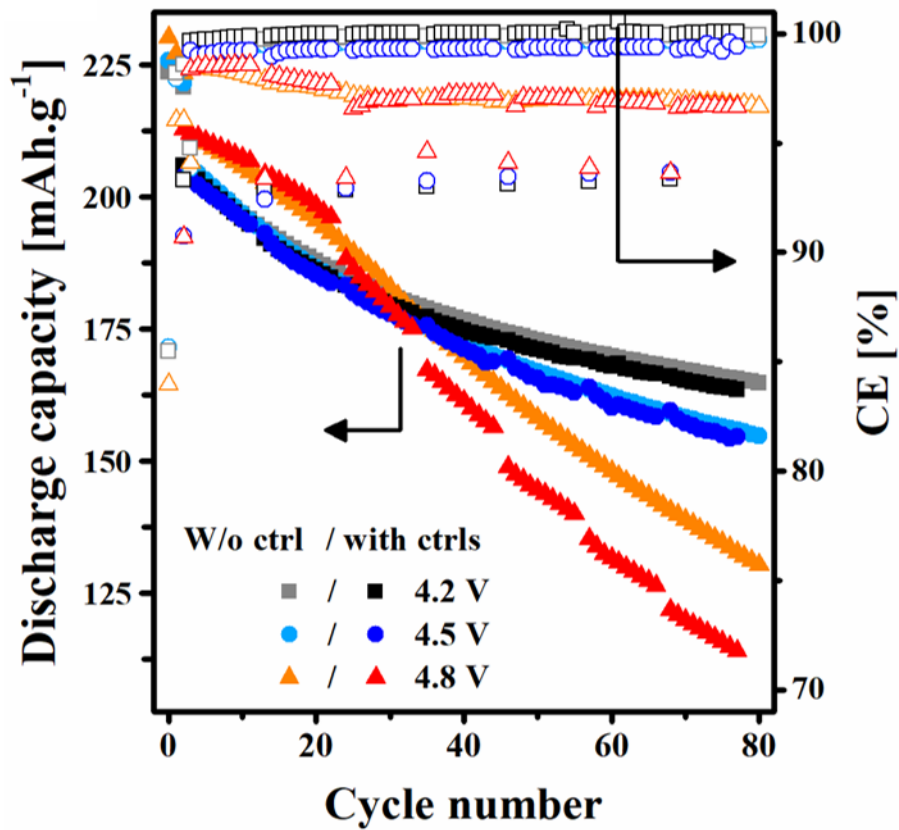
**Cyclic voltammetry (CV)** – Cyclic voltammograms were obtained using 2032-coin cells configured with a two-electrode setup. Half-charged  $\text{LiFePO}_4$  served as the reference/counter electrode, and a polished copper foil was used as the working electrode. The potential was scanned at a rate of  $0.1 \text{ mV.s}^{-1}$  between the open circuit voltage (OCV) (3.45 V vs  $\text{Li}^+/\text{Li}$ ) and 0.005 V vs  $\text{Li}^+/\text{Li}$  with LP57 or LP57 + 665 ppm  $\text{Ni}^{2+}$ . For tests conducted with a separately formed solid electrolyte interface (SEI), LP57 was initially reduced on copper foil through three consecutive scans at  $0.1 \text{ mV.s}^{-1}$  between 3.45 V and 0.005 V vs  $\text{Li}^+/\text{Li}$ . Subsequently, the foil was recovered and reused in a new coin cell setup with nickel-contaminated electrolyte (665 ppm). The same scanning conditions as described above were then applied.

**Inductively coupled plasma mass spectroscopy (ICP-MS)** – Nickel leaching from graphite electrodes was quantified using inductively coupled plasma mass spectroscopy (ICP-MS, Nexion 2000, Perkin Elmer). Prior to analysis, cells underwent the following cycling protocol: one formation cycle (C/20), 10 aging cycles (constant current constant voltage, CCCV, C/2,  $i < C/20$ ), and one and a half cycles (C/20) with cutoff voltages of 4.2, 4.5, or 4.8 V. Cells were stopped in a charged state, i.e.,  $\text{LiNiO}_2$  in a delithiated state and graphite electrodes in a

lithiated state. The cells were then de-crimped in an argon-filled glove box to retrieve the negative electrodes and immediately rinsed with approximately 5 mL of dimethyl carbonate (DMC) on the front and back surfaces to remove nickel-contaminated electrolyte from the graphite. The wash time and solvent volume were minimized to minimize the risk of SEI dissolution and any nickel loss. Graphite electrodes were subsequently dissolved in 10 mL of 2% nitric acid (Suprapur, 65% HNO<sub>3</sub>, Merck), and the solutions were sonicated and left to rest overnight. The solutions were filtered using 0.2 μm polypropylene filters (VWR) and diluted with a 2% nitric acid solution to achieve final nickel concentrations between 1 ppb and 1 ppm. The dilution step was repeated to obtain error bars for experimental measurements, as indicated in the figures. Calibration was performed using nine diluted nickel standard solutions (TraceCERT, 1 mg.L<sup>-1</sup> Ni in nitric acid, Sigma-Aldrich).

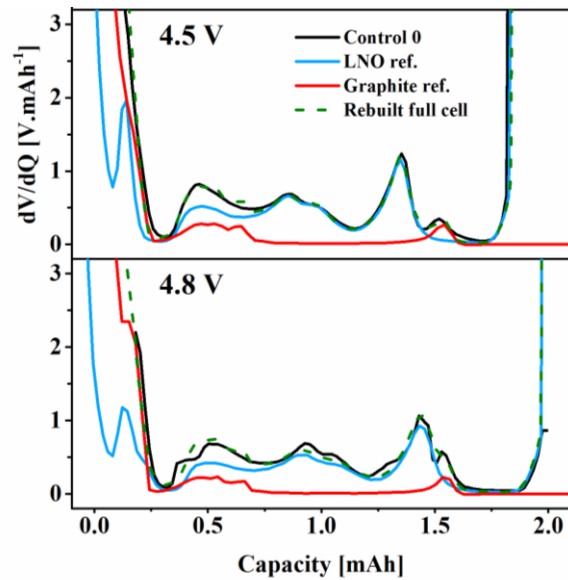
**Differential voltage analysis (DVA)** – Slippage analysis was conducted by fitting the discharge curves' differential voltage (dV/dQ vs Q) obtained during the control cycles (0<sup>th</sup>, 2<sup>nd</sup>, 4<sup>th</sup>, and 6<sup>th</sup> control cycles). This method involves recording cycles at low current to recover accessible capacity and minimize kinetic artifacts during phase transitions of materials, ensuring quasi-equilibrium conditions. To reduce noise in the dV/dQ curves associated with slow discharge rates, the number of data points was reduced to 100 using linear interpolation. Reference curves for graphite and LiNiO<sub>2</sub> half-cells were measured at C/20 under the same temperature as that of the full cell. These reference curves were then used to build a dV/dQ model following equation presented in Equation 13, part III.1.2.b. and the fitting process was performed using the VAWQuum v1.2 freeware. The LAM was estimated between the initial control and subsequent control using the fitting model outlined in Equation 13. Values are presented in relative terms using the initial mass of the active material as a reference.

## ANNEX 4 – EFFECT OF CONTROL CYCLES ON CELL PERFORMANCE



Capacity retention and coulombic efficiencies measured using continuous cycling procedure when compared to adding control cycles at C/20 every ten cycles. All capacities are normalized by LNO active material mass.

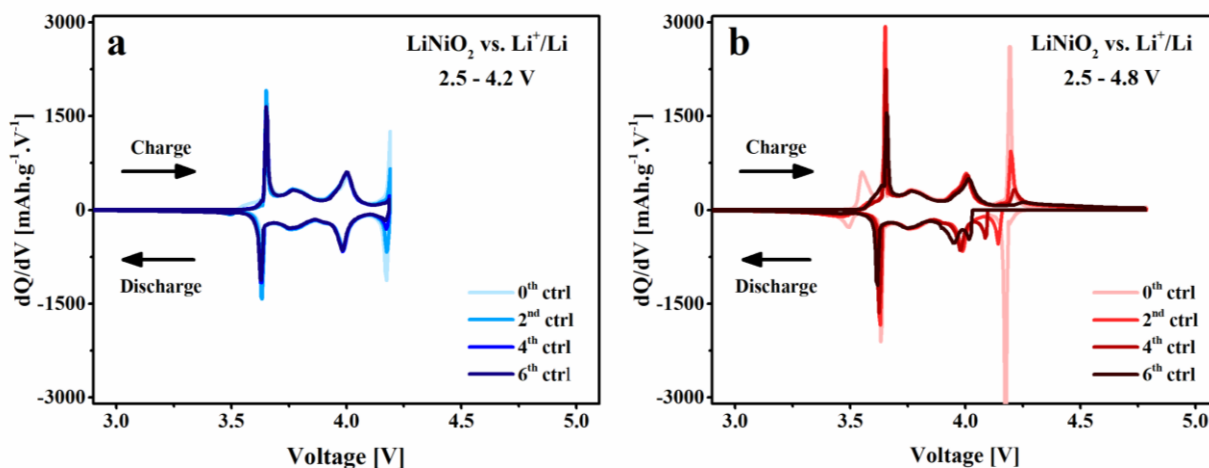
## ANNEX 5 – FITS OF CONTROL 0 FOR 4.5 AND 4.8 V CELLS



### Fits for control 0 at 4.5 and 4.8 V.

Full cell model (dotted green line) originates from the sum of  $\text{LiNiO}_2$  ( $dV/dQ_{\text{pos.}}$ ) and graphite ( $-dV/dQ_{\text{neg.}}$ ) references scaled with respective active mass materials and capacity slippages.

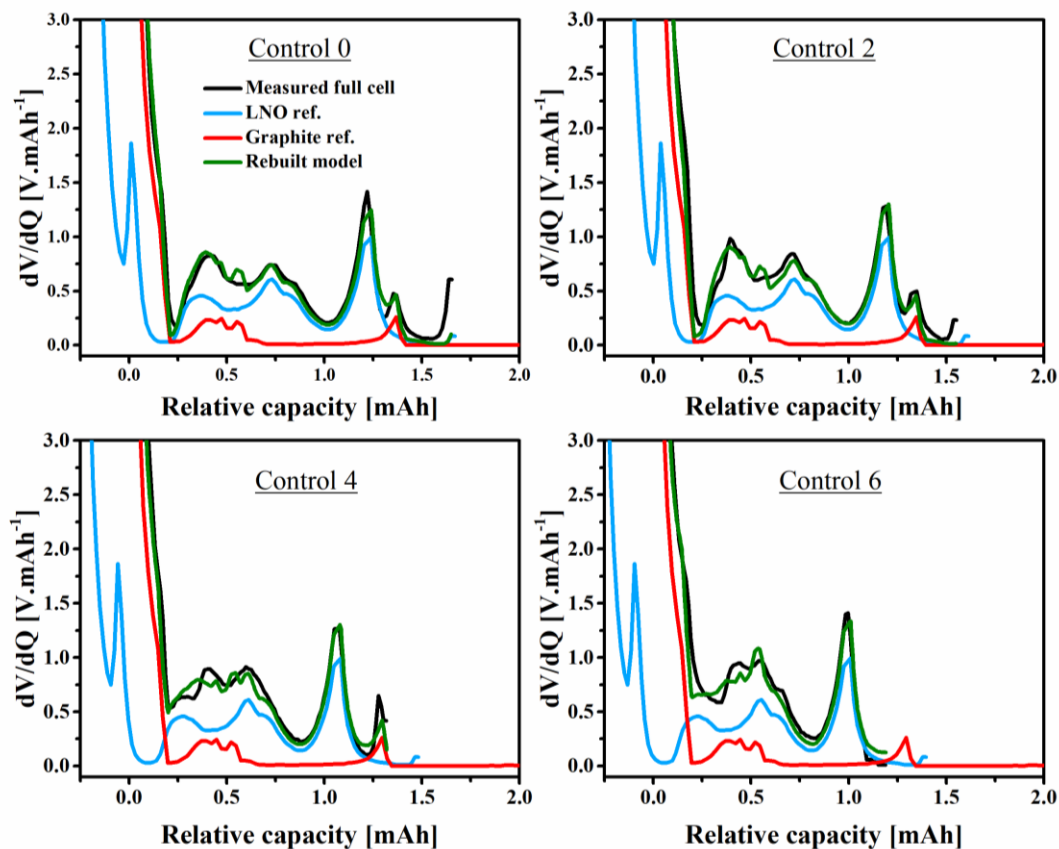
## ANNEX 6 – ICA OF LNO HALF CELLS



### Assessment of $\text{LiNiO}_2$ electrochemical performance upon aging.

$dQ/dV$  curves of  $\text{LiNiO}_2$  vs.  $\text{Li}^+/\text{Li}$  recorded at  $C/20$  in range 2.5 – 4.2 V. a) and 2.5 – 4.8 V b) from 0<sup>th</sup> to 6<sup>th</sup> control. No drastic modification of  $dQ/dV$  profiles is observed at 4.2 and 4.8 V indicating similar electrochemical behavior. Peak shift to higher voltage for 4.8 V cell denotes impedance raise.

## ANNEX 7 – FITS OF 4.2 V CELLS USING LP57 + Ni<sup>2+</sup> ELECTROLYTE



**$dV/dQ$  fittings of graphite/LNO cells using LP57 + Ni<sup>2+</sup> at 4.2 V upon aging.**

*LNO and graphite references are recorded at C/20 as well as full cells during control cycles. Fittings remain valid up to 6<sup>th</sup> control.*

## ANNEX 8 – EXPERIMENTAL SECTION OF CHAPTER IV

**Electrode materials** – Graphite electrodes coated on copper foil with a loading of  $1.1 \text{ mAh}\cdot\text{cm}^{-2}$  were sourced from Cidotec (Spain). NMC811 electrodes coated on aluminum foil with a loading of  $1.0 \text{ mAh}\cdot\text{cm}^{-2}$  were obtained from Umicore (Belgium).

**Composition of Graphite electrodes** – The graphite electrodes comprised 94wt% 15-4 Graphite (Imerys), 2wt% C45 carbon black (Imerys), and a blend of 2wt% styrene butadiene rubber (SBR) BM451B (Zeon) with 2wt% carboxymethylcellulose (CMC) CRT2000 (DOW chemical) as binders.

**Composition of NMC811 electrodes** – The NMC811 electrodes consisted of 95wt% NMC811 (Umicore), 3wt% C65 carbon black, and 2wt% polyvinylidene fluoride (PVDF).

**Electrode preparation** – The electrodes were punched into circular disks with a diameter of  $\text{Ø}14 \text{ mm}$  (positive electrode) and  $\text{Ø}15 \text{ mm}$  (negative electrode), ensuring a capacity balance with  $N/P = 1.27$ . Prior to coin cell assembly, the electrodes underwent overnight drying at  $80^\circ\text{C}$  under reduced pressure.

**Coin cell assembly** – 2032-type coin cells, constructed with 316-stainless steel grade, were assembled using 1.23 mm thick wave springs and a set of 0.5 and 1 mm spacers from AOT Battery (China). The assembly process took place in an argon-filled glovebox. Aluminum foils with a diameter of  $\text{Ø}20 \text{ mm}$  were inserted between the positive electrode and the spacer, as well as between the spacer and the positive cap to prevent stainless steel corrosion. A coated polypropylene separator film (Celgard 3501) was utilized to enhance the wettability of the highly concentrated electrolytes. Disks were punched and dried at  $55^\circ\text{C}$  for approximately 72 hours before use, serving as a single-layer separator. The electrolyte volume was determined to fill four times the total porosity of the separator and both electrodes, amounting to  $31.2 \mu\text{L}$ . It was added in two steps:  $15.6 \mu\text{L}$  on the anode and the remaining  $15.6 \mu\text{L}$  on the separator. LP57 VC (1M LiPF<sub>6</sub> in EC: EMC 30:70wt% + 2wt% VC, E-lyte, Germany) and LiFSI 5M in DMC (Solvionic, France) were the electrolytes used in this study. LiFSI 5M EC was prepared by vigorously stirring the LiFSI salt (99.9% pure, Solvionic, France) into EC (DodoChem, China) at  $55^\circ\text{C}$ .

When LHCE was used, the co-solvents 1,1,2,2-tetrafluoroethyl-2,2,3,3-tetrafluoropropylether (TCI, 95% pure) and dimethyl carbonate (DMC, Elyte) were employed and dried before use. A blend of LiFSI:DMC:TTE using a molar ratio of 1:2:3 was prepared.

**Electrochemical tests** – The cells were subjected to cycling in a controlled temperature chamber (Mettler, Germany) using a BCS-810 potentiostat (BioLogic, France). Before the initial charge, the cells were rested for 12 hours at 55°C to reduce the electrolyte viscosity and ensure proper filling of the electrode/separator pores. This step was especially important due to the higher viscosity of LiFSI 5M DMC (120 mPa.s) compared to LP57 (2.8 mPa.s). The cell was then equilibrated at room temperature before use. The C-rate was defined based on the theoretical capacity of NMC811 ( $C = 275 \text{ mAh.g}^{-1}$ ), and all capacities were normalized by the active mass material of NMC811. The cycling procedure involved 100 cycles at CCCV 1C,  $i < C/20$ , and control cycles composed of C/10,  $i < C/20 + C/20$  to evaluate cell performance. All cells were cycled within a voltage range of 2.5 – 4.3 V. The initial C/10 cycle, preceding the control cycle performed at C/20, served to reset the lithium inventory in the electrodes. This step was necessary to account for potential underestimation of lithium inventory when transitioning from a high discharge current (1C) to a low charge current (C/20), as previously observed. The C/20 cycle provided a more representative evaluation of cell performance.

**Study of transition metal dissolution** – Solubility tests of transition metals were conducted under an argon atmosphere. The tests involved adding approximately 5 g of anhydrous  $\text{NiCl}_2$ ,  $\text{MnCl}_2$ , or  $\text{CoCl}_2$  (Alfa-Aesar, purity of 99+%) to 1.000 mL of LiFSI in DMC electrolyte. Chloride salts were used instead of TFSI salts due to their lower solubility, and the saturation point was achieved with 1.000 mL of solution. The solutions were vigorously stirred for 3 days at room temperature to reach thermodynamic equilibrium. After centrifugation at 6000 rpm for 10 minutes, the supernatant was collected and further diluted with a 2wt%  $\text{HNO}_3$  solution (Suprapur, 65%  $\text{HNO}_3$ , Merck, Ni impurities  $\leq 5.0$  ppb; Mn, Ni impurities  $\leq 0.5$  ppb) for ICP-MS analysis.

**Migration of transition metals from NMC811 electrodes** – The migration of transition metals from the NMC811 electrodes was studied by retrieving the graphite electrodes from graphite/NMC811 coin cells cycled 500 cycles at 4.3 V. Graphite electrodes were rinsed back and forth with a few drops of DMC (~1 mL). The rinsed electrodes were then digested in 10.000 mL of 2wt% nitric acid (Suprapur, 65%  $\text{HNO}_3$ , Merck, Ni & Al impurities  $\leq 5.0$  ppb; Mn, Co, Li impurities  $\leq 0.5$  ppb). The solutions were sonicated and left at rest overnight. The resulting solutions were recovered, followed by centrifugation at 6000 rpm for 10 minutes, and the supernatant was filtered using polypropylene 0.2  $\mu\text{m}$  PP syringe filters. The filtrate was further diluted with a 2wt%  $\text{HNO}_3$  solution to achieve metal concentrations ranging from 1 ppb to 1 ppm (wt ppb & ppm).

**Incremental capacity and derivative voltage analysis** – DVA and ICA were performed on cycles recorded at C/20 in a temperature-controlled chamber to ensure conditions close to

thermodynamic equilibrium. During ICA, capacity was normalized by active mass material of positive electrode, and  $dQ/dV$  curves thus obtained smoothed using binomial filter. For DVA,  $dV/dQ$  discharge curves were plotted and fitted using VAWQuum v1.2 freeware provided by the Department of Physics and Atmospheric Science, Dalhousie University, Canada. The reference curves, i.e. NMC811 vs  $\text{Li}^+/\text{Li}$  and graphite vs  $\text{Li}^+/\text{Li}$ , were recorded at C/20 and at the same working temperature as for full cells. Before fitting, the reference and full cell files were reduced to 100 points using linear interpolation and discharge endpoints set to 0 mAh to meet software requirements. The fitting model is detailed in Equation 13 page 81, Chapter III. The full cell model was fitted with recorded data by varying masses and capacity slippages of reference curves. The potential of the negative and the positive electrodes are plotted as function of capacity after the fitting.

**Inductively coupled plasma mass spectrometry (ICP-MS)** – Lithium, nickel, manganese, and cobalt levels were quantified using the Nexion 2000 ICP-MS instrument (PerkinElmer) after calibration with ten standard points from a multi-element standard solution (Certified reference materials in 2%  $\text{HNO}_3$ , CPA Chem, Bulgaria). Error bars on data plots were obtained from duplicate measurements under the same conditions.

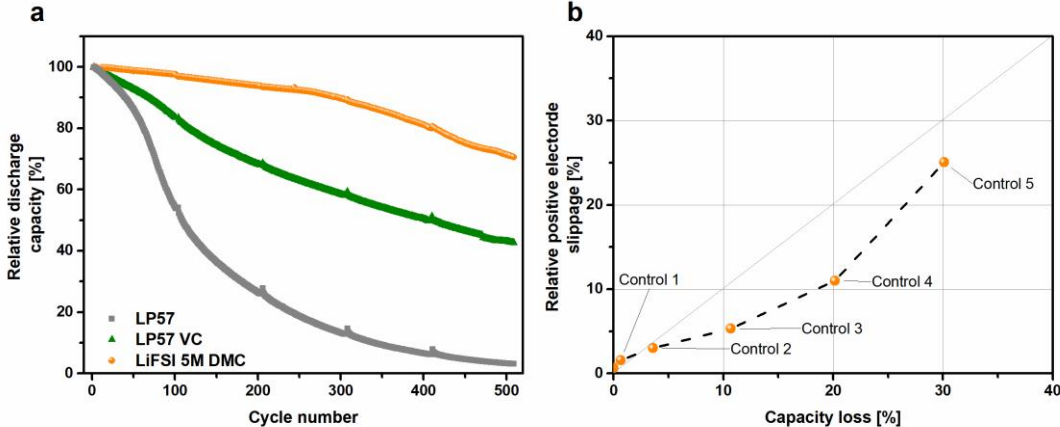
**In situ UV-visible** – Graphite and NMC811 slurries (90% active material) were casted onto 316-stainless grids and dried under vacuum at  $80^\circ\text{C}$  overnight. The obtained electrodes were then cycled using approximately 3 mL of LiFSI 5M DMC in a commercial UV-visible cell (Sphere-energy, France). A voltage scan in the range of 2.5 – 4.3 V was performed at a scan rate of  $0.5 \text{ mV}\cdot\text{s}^{-1}$ . Ex-situ UV-visible spectra were recorded using a UV5 Bio spectrometer (Mettler Toledo). Prior to the measurements, a blank spectrum was obtained using pristine LiFSI 5M in DMC electrolyte.

**X-ray photoemission spectroscopy (XPS)** – XPS data were collected at the GALAXIES beamline of the SOLEIL synchrotron in France, utilizing two different photon energies in the hard X-ray range, a technique known as Hard X-ray photoemission spectroscopy (HAXPES). The electrochemical cells were opened in a glovebox filled with Ar, ensuring  $\text{O}_2$  and  $\text{H}_2\text{O}$  contents below 0.1 ppm. The electrodes were soaked in three successive DMC baths (1 minute each) to remove the electrolyte from the surface and expose the SEI (Solid-Electrolyte Interphase). After drying the electrodes under vacuum, they were placed onto a sample holder. A vacuum chamber was used to transfer the sample holder from the argon glovebox to the HAXPES introduction chamber, avoiding contact with air. Photon energies of  $h\nu = 3.0$  and  $6.9$  keV were obtained from the first and third order reflections of the Si(111) double-crystal monochromator, respectively. The probing depth, defined as three times the photoelectron inelastic mean free path (IMFP), was estimated using the TPP-2M model developed by

Tanuma et al. 40, which takes into account the density and band gap of the probed material. The probing depth of the SEI is challenging to accurately estimate due to its complex chemical composition and morphology. As a rough estimation, it was assumed that the SEI is a mixture of carbonaceous and inorganic species, approximated as a mixture of  $\text{Li}_2\text{CO}_3$  and  $\text{LiF}$ . The density of  $\text{Li}_2\text{CO}_3$  was assumed to be 2.1 and its band gap fixed at 5 eV, while the density of  $\text{LiF}$  was assumed to be 2.6 with a fixed band gap of 14 eV. The photoelectrons were collected and analyzed using a SCIENTA EW4000 spectrometer, with energy resolutions of 0.32 eV for 3.0 keV and 0.14 eV for 6.9 keV obtained from the Au Fermi edge. The analysis chamber pressure was maintained at approximately  $10^{-8}$  mbar throughout the experiment, without the use of a charge neutralizer. The binding energy scale was calibrated using the C 1s contribution of hydrocarbon at 285 eV. Filters were employed to minimize the synchrotron brilliance onto the samples, reducing the potential degradation of the fragile SEI under the X-ray beam: a 95% filter (5% transmittance) at 3.0 keV and a 60% filter (40% transmittance) at 6.9 keV.

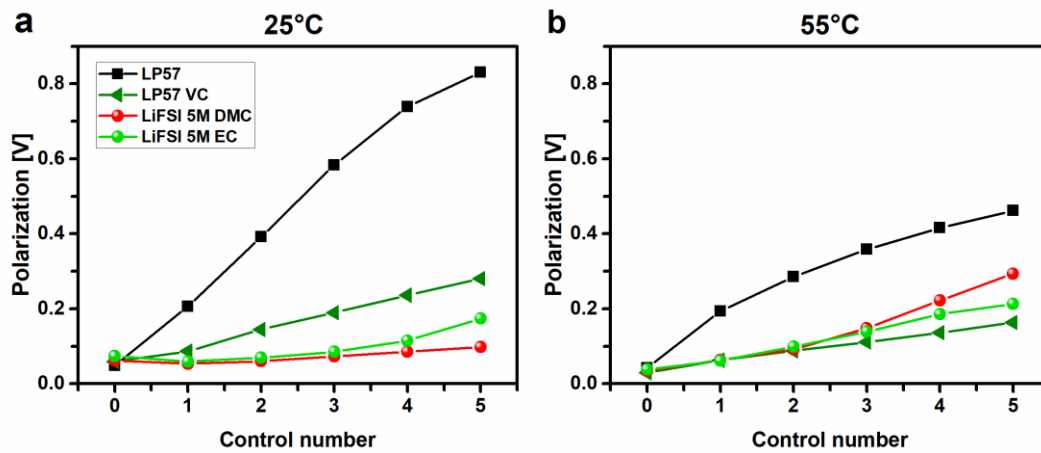
**Aging in temperatures** – To initiate the aging process, all cells underwent an initial preconditioning phase. This involved subjecting the cells to two cycles at a rate of C/20–D/20 at a temperature of 55 °C. This preconditioning was carried out in a controlled temperature chamber by Memmert in Germany. Following the preconditioning phase, individual cells were subjected to aging at various temperatures within the range of 15 °C to 55 °C. The aging process involved a specific cycling procedure. Initially, a 6-hour open circuit voltage (OCV) rest was applied to ensure thermal equilibrium was reached. Subsequently, an aging control procedure was implemented, which consisted of repetitive slow cycles at a rate of C/20–D/20, alternating with 100 cycles at a rate of 2C. At the end of the charge cycle, a constant voltage (CV) step was applied with the current (i) limited to less than C/20. Degradation rates were calculated by comparing the discharge capacity of two control cycles and normalizing the difference by the cycling time, working electrode surface area, and mass.

# ANNEX 9 – RELATIVE DISCHARGE CAPACITIES AND CORRESPONDING LLI



a) The discharge capacity, normalized by the initial discharge capacity of the first cycle recorded at 1C, is evaluated for LP57, LP57 VC, and LiFSI 5M DMC. b) The relative slippage, determined through dV/dQ analysis of the positive electrode, is examined in relation to the loss of cell capacity. The primary reason for the capacity decrease noticed from the 250<sup>th</sup> cycle onwards, specifically between control 2 and 3, can be attributed mainly to LLI associated to positive electrode slippage.

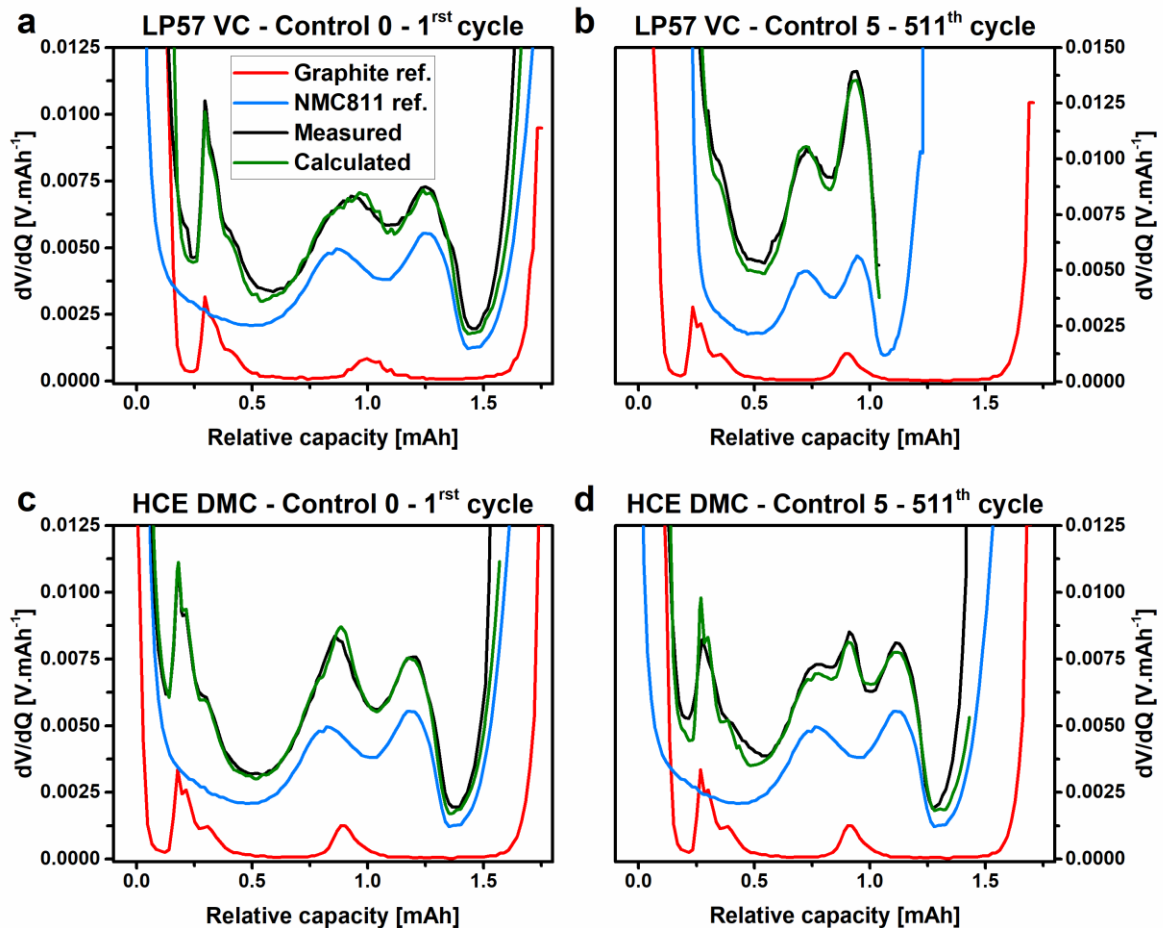
## ANNEX 10 – EVOLUTION OF CELL POLARIZATION AT 25°C AND 55°C



Evolution of the polarization recorded during the control cycles (C/20) upon aging at 25°C a) and 55°C b) using different electrolytes. Polarizations are obtained from the difference between the average voltages of the charge and the discharge curves, following the equation:

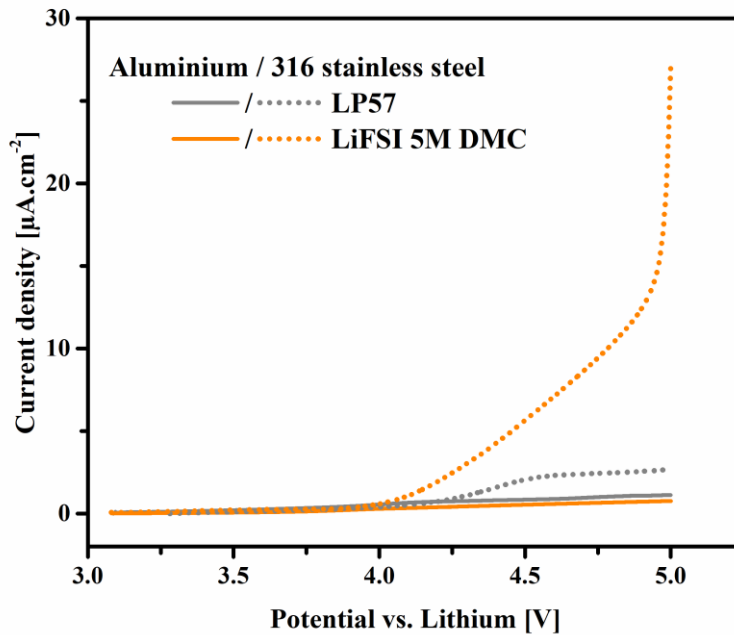
$$\begin{aligned}
 \text{Polarization [V]} &= \text{Voltage}_{\text{Charge}}^{\text{Mean}} - \text{Voltage}_{\text{Discharge}}^{\text{Mean}} \\
 &= \frac{\text{Energy [Wh]}_{\text{Charge}}}{\text{Capacity [A.h]}_{\text{Charge}}} - \frac{\text{Energy [Wh]}_{\text{Discharge}}}{\text{Capacity [A.h]}_{\text{Discharge}}}
 \end{aligned}$$

## ANNEX 11 – FITS OF $dV/dQ$ CURVES WITH CELLS USING LP57 VC AND HCE DMC



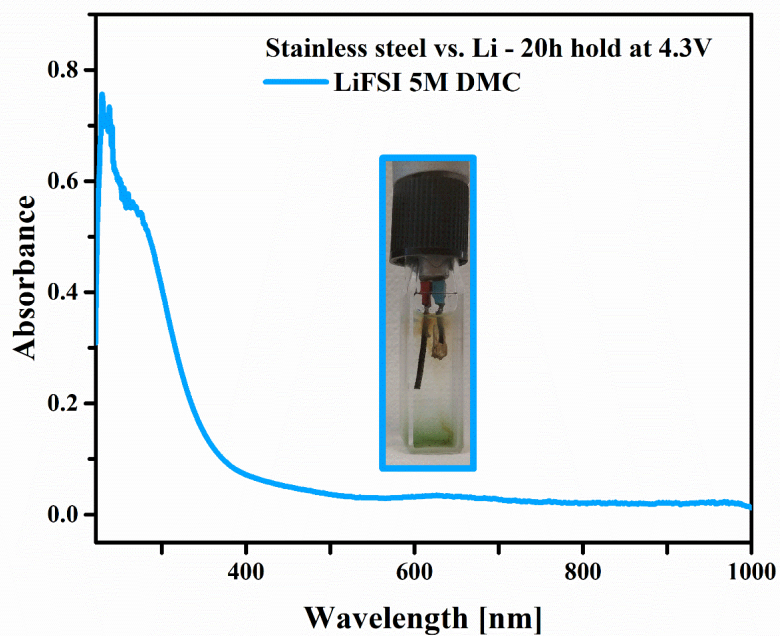
a) The graphite/NMC811 cell's control 0 fitting is carried out at 4.3 V and 25°C using LP57 VC. b) Control 5 fitting shows a consistent increase in negative electrode slippage, causing the obscuring of the graphite reference's 0.1 mAh characteristic. The positive electrode encounters significant LAM at the beginning of the  $dV/dQ$  reference curve shrinkage. c) The graphite/NMC811 cell's control 0 fitting is performed at 4.3 V and 25°C using HCE DMC. The initial capacity decrease is attributed to parasitic oxidation at the negative electrode. d) Control 5 fitting of graphite/NMC811 cells experiences slippage due to LLI at the negative electrode and LAM NE.

## ANNEX 12 – LIMITED OXIDATION OF ALUMINUM USING HCE DMC



Linear sweep voltammograms recorded versus lithium at  $0.1 \text{ mV}\cdot\text{s}^{-1}$  using aluminum or 316-stainless steel as working electrode. The oxidation current decreases when using aluminum foils on top of the stainless steel casing for LP57 and LiFSI 5M DMC.

## ANNEX 13 – OXIDATION PRODUCTS OF HCE DMC USING STAINLESS STEEL FOIL



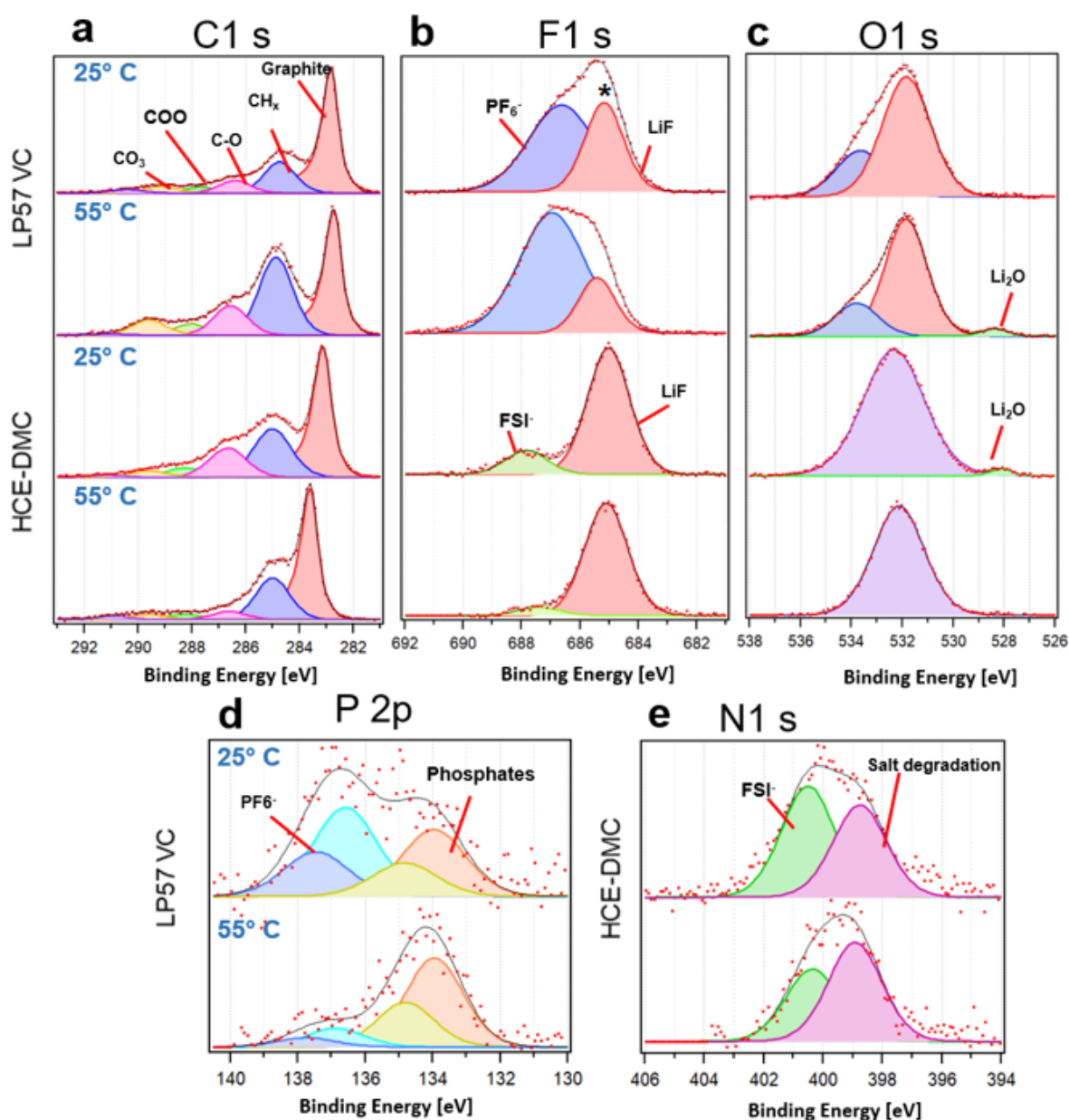
*Ex-situ UV-visible spectra obtained after a potential holding step at 4.3 V vs.  $\text{Li}^+/\text{Li}$  for 20 h using stainless steel foil as working electrode in LiFSI 5M DMC. Inset picture shows the appearance of a colored species which spectrum is similar the one obtained in graphite/NMC811 system, suggesting that the color is not associated with the complexation of transition metal.*

## ANNEX 14 – PHOTOGRAPH OF LI PLATING ON GRAPHITE ELECTRODE USING HCE DMC



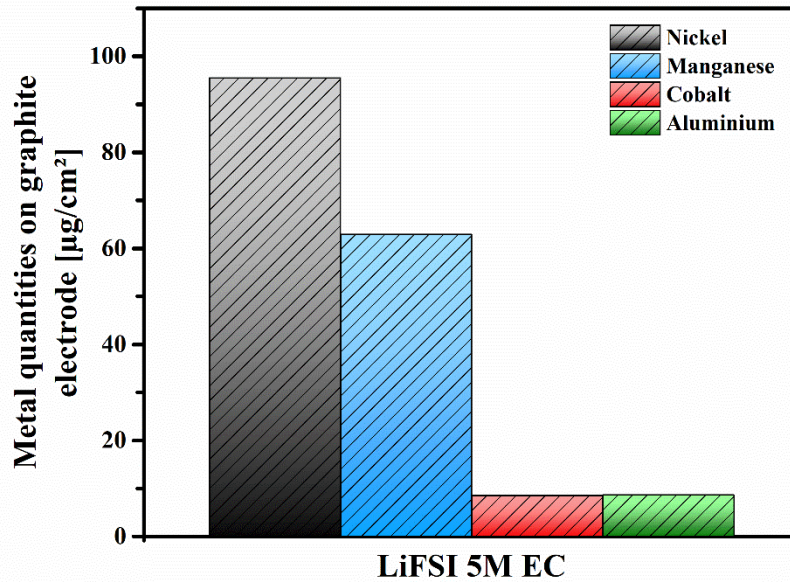
*Image of a graphite electrode in its delithiated state after experiencing 500 cycles in the range of 2.5 to 4.3 V at 1C in graphite/NMC811 cell (25°C). Prior to capturing the photograph, the electrode was rinsed with DMC. The presence of grey and golden spots on the graphite surface advocates for the presence of metallic lithium deposits.*

## ANNEX 15 – HAXPS DATA OF GRAPHITE ELECTRODES RECORDED AT 6.9 KEV



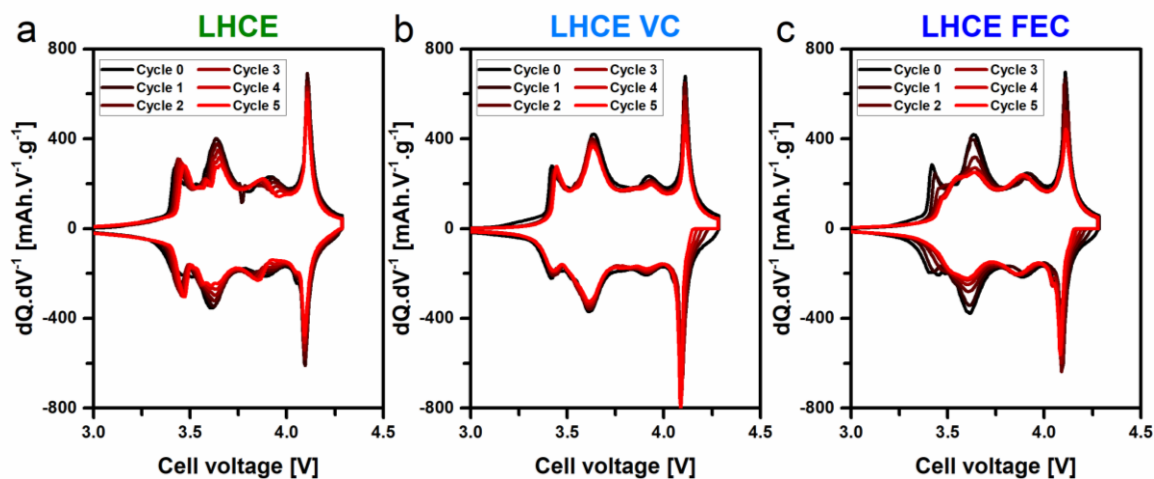
a), b) and c) C 1s, F 1s and O 1s HAXPES spectra of graphite electrodes recovered from graphite/NMC811 cells after 100 cycles at 1C at two different temperatures, 25 and 55°C, using LP57 VC and LiFSI 5M DMC electrolytes. d) P 2p spectra in the case of LP57 VC (LiPF<sub>6</sub> salt), and e) N 1s spectra in the case of LiFSI 5M DMC. The HAXPES spectra were recorded with 6.9 keV photon energy. Note that the F 1s peak of LiF for LP57 VC at 25°C (highlighted with \*) exhibits some inconsistency with the P 2p peak due to degradation caused by the X-ray beam at the end of the experiment. Therefore, the observed amount of LiF appears artificially higher than the actual value.

## ANNEX 16 – TM QUANTIFICATION BY ICP-MS OF GRAPHITE ELECTRODE USING HCE EC



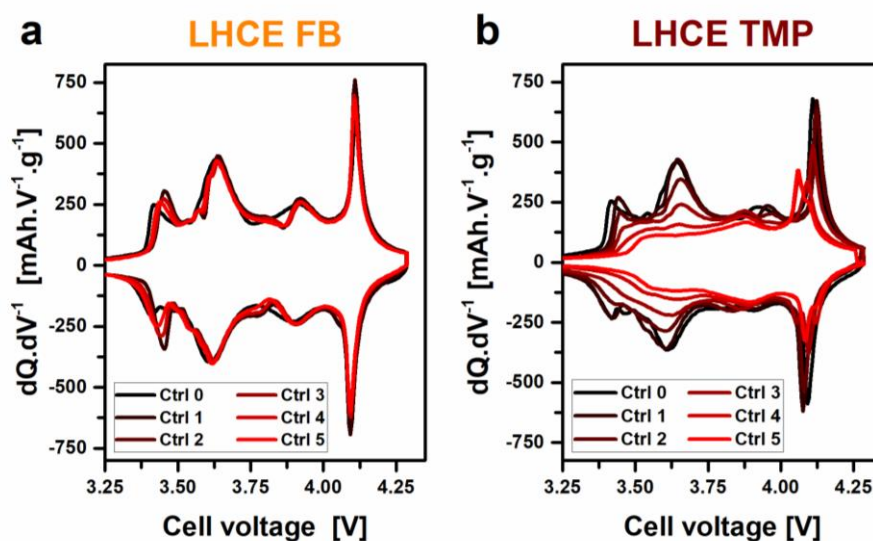
Quantification of metal amounts found on graphite electrode after 500 cycles at 25°C in graphite/NMC811 cell using LiFSI 5M EC. Metal amounts are similar to those measured with LP57 VC and LiFSI 5M DMC in similar conditions.

## ANNEX 17 – ICA OF LHCE WITH ADDITIVES FOR SEI (2%wt VC AND 2wt% FEC)



Incremental Capacity Analysis (ICA) of graphite/NMC811 cells at 4.3 V was conducted using three different electrolytes: LHCE a), LHCE VC b), and LHCE FEC c). No significant alteration in cell chemistry related to Li plating stripping was observed for any of the three electrolytes. However, it is worth mentioning that the ICA performed with LHCE FEC exhibited a decrease in peak intensities below 3.75 V, which can be attributed to capacity slippages in the graphite electrode.

## ANNEX 18 – ICA OF LHCE WITH ADDITIVES FOR CEI (2wt% FB AND 2wt% TMP)



*Incremental Capacity Analysis (ICA) of graphite/NMC811 cells at 4.3 V was conducted using two different electrolytes: LHCE FB a), LHCE TMP b). No significant alteration in cell chemistry related to Li plating stripping was observed for both electrolytes. However, it is worth mentioning that the ICA performed with LHCE TMP exhibited a decrease in peak intensities and a shift of peak position, which can be attributed to LAM of positive electrode and impedance increase.*



## LEXICON

**BIG-MAP** – Big interface genome material acceleration platform  
**CC** – Constant current  
**CE** – Coulombic efficiency  
**CEI** – Cathode electrolyte interphase  
**CMC** – Carboxy methyl cellulose  
**CV** – Constant voltage  
**DEC** – Diethyl carbonate  
**DMC** – Dimethyl carbonate  
**DVA** – Derivative voltage analysis  
**EA** – Ethyl acetate  
**EC** – Ethylene carbonate  
**EMC** – Ethyl methyl carbonate  
**EV** – Electric vehicle  
**FEC** – Fluoro ethyl carbonate  
**FB** – Fluoro benzene  
**HCE** – Highly concentrated electrolyte  
**ICA** – Incremental capacity analysis  
**ICP MS** – Inductively coupled plasma mass spectroscopy  
**IR** – Increase of resistance  
**LAM** – Loss of active material  
**LFP** – Lithium iron phosphate ( $\text{LiFePO}_4$ )  
**LIB** – Li-ion battery  
**LLI** – Lithium loss inventory  
**LNO** – Lithium nickel oxide ( $\text{LiNiO}_2$ )  
**LHCE** – Localized high concentrated electrolyte  
**LP30** – 1M  $\text{LiPF}_6$  in EC/DMC 50:50wt%  
**LP57** – 1M  $\text{LiPF}_6$  in EC/EMC 30:70wt%  
**NCA** – Lithium nickel cobalt aluminum oxide  
**NMC** – Lithium nickel manganese cobalt oxide  
**PC** – Propylene carbonate  
**PHEV** – Plug-in hybrid electric vehicle  
**PVDF** – Polyvinylidene fluoride  
**Q<sub>C</sub>** – Charge capacity  
**Q<sub>D</sub>** – Discharge capacity  
**SEI** – Solid electrolyte interphase  
**TMP** – Trimethylphosphite  
**VC** – Vinylene carbonate  
**XRD** – X-ray diffraction  
**XPS** – X-ray photoelectron spectroscopy



## TABLE OF FIGURES

Figure 1 – Evolution of CO <sub>2</sub> emission over the last twenty years .....	14
Figure 2 – Evolution of EV stocks over the last ten years .....	16
Figure 3 – Schematic of Li-ion battery .....	17
Figure 4 - Overview of common descriptors of cell performance .....	21
Figure 5 – Available commercial cell formats.....	23
Figure 6 – Widespread used academic cell formats .....	24
Figure 7 – Stability of NMC compounds .....	28
Figure 8 – Performance of LiNiO <sub>2</sub> and NMC811 materials.....	30
Figure 9 – Phase transitions of LiNiO <sub>2</sub> .....	31
Figure 10 – Degradation of Ni-rich compounds at high voltage.....	33
Figure 11 – Competition between Li plating and SEI growth depending on temperature .....	37
Figure 12 – Performance and properties of HCE .....	42
Figure 13 – Schematic of solvation structures in HCE and LHCE.....	44
Figure 14 – Outcomes of LHCE with Ni-rich materials.....	45
Figure 15 – Overview of tested HCE compositions and outcomes.....	46
Figure 16 – Effect of electrode loading and composition on cell performance.....	54
Figure 17 – Effect of spacers on coin cell internal pressure.....	58
Figure 18 – Performance of low and high loading electrodes in BIG-MAP .....	61
Figure 19 – Effect of electrolyte volumes in coin cells.....	62
Figure 20 – Outcomes of cell standardization.....	64
Figure 21 – Optimizing formation protocol .....	66
Figure 22 – Optimizing aging protocol .....	68
Figure 23 – Details of control cycle protocols .....	69
Figure 24 – Screenshots of BIG-MAP online notebook.....	72
Figure 25 – Overview of cell degradations and consequences .....	81
Figure 26 – Description of marching capacities .....	82
Figure 27 – Introduction to DVA .....	83
Figure 28 – Benchmark of dV/dQ curve before and after aging showing the degradations ...	84
Figure 29 – Interpretation of dV/dQ fitting curves.....	85
Figure 30 – Introduction to ICA.....	86
Figure 31 – Interpretation of dQ/dV curves.....	87
Figure 32 – Different type of knee points.....	88
Figure 33 – Origins of knee points.....	89
Figure 34 – Overall organization of the workflows .....	90
Figure 35 – Workflow I. Detection of shuttling phenomena .....	92
Figure 36 – Workflow II. Detection of crosstalks from the positive to the negative electrode.	94
Figure 37 – Workflow III. Detection of graphite staging jump upon aging.....	97
Figure 38 – Cycling protocol used in graphite/LNO cells.....	105
Figure 39 – Voltage effect on graphite/LNO cells.....	106
Figure 40 – Capacity marching of graphite /LNO curves.....	108
Figure 41 – dV/dQ fitting of graphite/LNO cells.....	109
Figure 42 – DVA of graphite/LNO cells.....	110
Figure 43 – Study of TM dissolution and incorporation in the SEI.....	112
Figure 44 – Effect of TM on cell performance .....	114
Figure 45 – Detection of graphite staging jump .....	116
Figure 46 – Deciphering between SEI growth and Li plating.....	118
Figure 47 – Effect of TM on SEI growth.....	119
Figure 48 – Effect of TM on Li plating .....	120
Figure 49 – Performance of graphite/NMC811 cells at 4.3 V .....	129
Figure 50 – Evolution of TM solubility as a function salt concentration .....	130
Figure 51 – Quantification of TM at the negative electrode.....	131
Figure 52 – XRD of NMC811 electrode after 500 cycles at 4.3 V .....	132
Figure 53 – DVA of graphite/NMC811 cells at 4.3 V .....	133

Figure 54 – Marching capacities highlighting parasitic oxidation in HCE.....	134
Figure 55 – Further clues of parasitic oxidation .....	135
Figure 56 – ICA highlighting Li plating .....	137
Figure 57 – Advantage of high temperature in mitigating Li plating.....	138
Figure 58 – Effect of interphase formation at high temperatures.....	140
Figure 59 – XPS of graphite electrode.....	143
Figure 60 – Advantages of using VC in HCE on cell performance .....	145
Figure 61 – Outcomes of using EC-based HCE on cell performance.....	146
Figure 62 – Performance using LHCE and SEI additives.....	148
Figure 63 – DVA with LHCE and SEI additives.....	149
Figure 64 – Performance of LHCE with CEI additives .....	150
Figure 65 – DVA for LHCE with CEI additives .....	151
Figure 66 – Stabilization of cells at high voltage using LHCE .....	153
Figure 67 – DVA of high voltage cells using LHCE .....	154
Figure 68 – ICA of high voltage cells using LHCE .....	154
Figure 69 – Overview of degradation behavior depending on used electrolyte .....	156

# REFERENCES



- [1] IEA, 'World Energy Outlook 2021', *IEA Publications*, p. 15, 2021, [Online]. Available: [www.iea.org/weo](http://www.iea.org/weo).
- [2] French ministry of ecological transition, 'Energy outlook', 2021. [Online]. Available: <https://www.statistiques.developpement-durable.gouv.fr/edition-numerique/chiffres-cles-energie-2021/livre>.
- [3] IEA, 'Net Zero by 2050: A Roadmap for the Global Energy Sector', *International Energy Agency*, p. 224, 2021, [Online]. Available: <https://www.iea.org/reports/net-zero-by-2050>.
- [4] M. Jarraud and A. Steiner, *Summary for policymakers*, vol. 9781107025. 2012.
- [5] V. Clement *et al.*, 'Groundswell Part 2: Acting on internal climate migration', *World Bank Group*, pp. 1–362, 2021, [Online]. Available: [www.worldbank.org](http://www.worldbank.org).
- [6] International Energy Agency (IEA), 'Global EV Outlook 2022 - Securing supplies for an electric future', *Global EV Outlook 2022*, p. 221, 2022, [Online]. Available: <https://www.iea.org/reports/global-ev-outlook-2022%0Ahttps://iea.blob.core.windows.net/assets/ad8fb04c-4f75-42fc-973a-6e54c8a4449a/GlobalElectricVehicleOutlook2022.pdf>.
- [7] S. Amant, N. Meunier, and C. de Cossé Brissac, 'Road transportation: what alternative motorisations are suitable for the climate? A comparison of the life cycle emissions, in France and Europe', *Carbone 4*, no. November, pp. 1–52, 2020, [Online]. Available: <http://www.carbone4.com/wp-content/uploads/2021/02/Road-transportation-what-alternative-motorisations-are-suitable-for-the-climate-Carbone-4.pdf>.
- [8] A. Manthiram, 'A reflection on lithium-ion battery cathode chemistry', *Nature Communications*, vol. 11, no. 1, pp. 1–9, 2020, doi: 10.1038/s41467-020-15355-0.
- [9] K. *et al.* (2020)., 'Evolution of Li-ion battery price, 1995-2019'. <https://www.iea.org/data-and-statistics/charts/evolution-of-li-ion-battery-price-1995-2019>.
- [10] W. Li, E. M. Erickson, and A. Manthiram, 'High-nickel layered oxide cathodes for lithium-based automotive batteries', *Nature Energy*, vol. 5, no. 1, pp. 26–34, 2020, doi: 10.1038/s41560-019-0513-0.
- [11] J. B. Quinn, T. Waldmann, K. Richter, M. Kasper, and M. Wohlfahrt-Mehrens, 'Energy Density of Cylindrical Li-Ion Cells: A Comparison of Commercial 18650 to the 21700 Cells', *Journal of The Electrochemical Society*, vol. 165, no. 14, pp. A3284–A3291, 2018, doi: 10.1149/2.0281814jes.
- [12] I. Belharouak *et al.*, *Operation, Manufacturing, and Supply Chain of Lithium-ion Batteries for Electric Vehicles*, no. August. 2020.
- [13] P. Daubinger *et al.*, 'Impact of Bracing on Large Format Prismatic Lithium-Ion Battery Cells during Aging', *Advanced Energy Materials*, vol. 12, no. 10, 2022, doi: 10.1002/aenm.202102448.
- [14] F. Lepoivre, A. Grimaud, D. Larcher, and J.-M. Tarascon, 'Long-Time and Reliable Gas Monitoring in Li-O<sub>2</sub> Batteries via a Swagelok Derived Electrochemical Cell', *Journal of The Electrochemical Society*, vol. 163, no. 6, pp. A923–A929, 2016, doi: 10.1149/2.0421606jes.
- [15] M. Li, C. Wang, Z. Chen, K. Xu, and J. Lu, 'New Concepts in Electrolytes', *Chemical Reviews*, vol. 120, no. 14, pp. 6783–6819, 2020, doi: 10.1021/acs.chemrev.9b00531.
- [16] D. S. Hall, J. Self, and J. R. Dahn, 'Dielectric Constants for Quantum Chemistry and Li-Ion Batteries: Solvent Blends of Ethylene Carbonate and Ethyl Methyl Carbonate', *Journal of Physical Chemistry C*, vol. 119, no. 39, pp. 22322–22330, 2015, doi: 10.1021/acs.jpcc.5b06022.
- [17] M. S. Ding, 'Liquid Phase Boundaries, Dielectric Constant, and Viscosity of PC-DEC and PC-EC Binary Carbonates', *Journal of The Electrochemical Society*, vol. 150, no. 4, p. A455, 2003, doi: 10.1149/1.1557968.
- [18] P. Keil and A. Jossen, 'Aging of lithium-ion batteries in electric vehicles', *Dissertation*, vol. 7, no. 1, pp. 41–51, 2017.
- [19] E. Peled and S. Menkin, 'Review—SEI: Past, Present and Future', *Journal of The Electrochemical Society*, vol. 164, no. 7, pp. A1703–A1719, 2017, doi: 10.1149/2.1441707jes.
- [20] A. J. Smith, J. C. Burns, X. Zhao, D. Xiong, and J. R. Dahn, 'A High Precision Coulometry Study of the SEI Growth in Li/Graphite Cells', *Journal of The Electrochemical Society*, vol. 158, no. 5, p. A447, 2011, doi: 10.1149/1.3557892.
- [21] J. R. Dahn, 'Studies of Lithium Intercalation into Carbons Using Nonaqueous Electrochemical Cells', vol. 137, no. 7, pp. 3–7, 1990.
- [22] E. Peled, 'The Electrochemical Behavior of Alkali and Alkaline Earth Metals in Nonaqueous Battery Systems—The Solid Electrolyte Interphase Model', *Journal of The Electrochemical Society*, vol. 126, no. 12, pp. 2047–2051, 1979, doi: 10.1149/1.2128859.
- [23] D. Y. Wang, N. N. Sinha, J. C. Burns, R. Petibon, and J. R. Dahn, 'A high precision study of the electrolyte additives vinylene carbonate, vinyl ethylene carbonate and lithium bis(oxalate)borate in LiCoO<sub>2</sub>/graphite pouch cells', *Journal of Power Sources*, vol. 270, pp. 68–78, 2014, doi: 10.1016/j.jpowsour.2014.07.053.
- [24] L. Ma, J. Xia, X. Xia, and J. R. Dahn, 'The Impact of Vinylene Carbonate, Fluoroethylene Carbonate and Vinyl Ethylene Carbonate Electrolyte Additives on Electrode/Electrolyte Reactivity Studied Using Accelerating Rate Calorimetry', *Journal of The Electrochemical Society*, vol. 161, no. 10, pp. A1495–A1498, 2014, doi: 10.1149/2.0091410jes.
- [25] S. A. Delp, O. Borodin, M. Olguin, C. G. Eisner, J. L. Allen, and T. R. Jow, 'Importance of Reduction and Oxidation Stability of High Voltage Electrolytes and Additives', *Electrochimica Acta*, vol. 209, pp. 498–510, 2016, doi: 10.1016/j.electacta.2016.05.100.
- [26] Q. Liu *et al.*, 'Kinetically Determined Phase Transition from Stage II (LiC<sub>12</sub>) to Stage I (LiC<sub>6</sub>) in a Graphite Anode for Li-Ion Batteries', *Journal of Physical Chemistry Letters*, vol. 9, no. 18, pp. 5567–5573, 2018, doi: 10.1021/acs.jpcclett.8b02750.

- [27] T. Hou *et al.*, 'The influence of FEC on the solvation structure and reduction reaction of LiPF<sub>6</sub>/EC electrolytes and its implication for solid electrolyte interphase formation', *Nano Energy*, vol. 64, no. July, p. 103881, 2019, doi: 10.1016/j.nanoen.2019.103881.
- [28] R. Narayan, C. Laberty-Robert, J. Pelta, J. M. Tarascon, and R. Dominko, 'Self-Healing: An Emerging Technology for Next-Generation Smart Batteries', *Advanced Energy Materials*, vol. 12, no. 17, 2022, doi: 10.1002/aenm.202102652.
- [29] X. Shen, R. Zhang, X. Chen, X. B. Cheng, X. Li, and Q. Zhang, 'The Failure of Solid Electrolyte Interphase on Li Metal Anode: Structural Uniformity or Mechanical Strength?', *Advanced Energy Materials*, vol. 10, no. 10, pp. 1–8, 2020, doi: 10.1002/aenm.201903645.
- [30] M. J. Zachman, Z. Tu, S. Choudhury, L. A. Archer, and L. F. Kourkoutis, 'Cryo-STEM mapping of solid–liquid interfaces and dendrites in lithium-metal batteries', *Nature*, vol. 560, no. 7718, pp. 345–349, 2018, doi: 10.1038/s41586-018-0397-3.
- [31] G. M. Hobold *et al.*, 'Moving beyond 99.9% Coulombic efficiency for lithium anodes in liquid electrolytes', *Nature Energy*, vol. 6, no. 10, pp. 951–960, 2021, doi: 10.1038/s41560-021-00910-w.
- [32] C. Delmas, D. Carlier, and M. Guignard, 'The Layered Oxides in Lithium and Sodium-Ion Batteries: A Solid-State Chemistry Approach', *Advanced Energy Materials*, vol. 11, no. 2, pp. 1–20, 2021, doi: 10.1002/aenm.202001201.
- [33] J. R. Dahn and C. A. Michal, 'Structure and electrochemistry of Li<sub>1-x</sub>NiO<sub>2</sub> and a new Li<sub>2</sub>NiO<sub>2</sub> phase with the Ni(OH)<sub>2</sub> structure', *Solid State Ion.*, vol. 44, pp. 87–97, 1990.
- [34] J. Li, J. Harlow, N. Stakheiko, N. Zhang, J. Paulsen, and J. Dahn, 'Dependence of Cell Failure on Cut-Off Voltage Ranges and Observation of Kinetic Hindrance in LiNi<sub>0.8</sub>Co<sub>0.15</sub>Al<sub>0.05</sub>O<sub>2</sub>', *Journal of The Electrochemical Society*, vol. 165, no. 11, pp. A2682–A2695, 2018, doi: 10.1149/2.049181jes.
- [35] R. Sharabi *et al.*, 'In situ FTIR spectroscopy study of Li/LiNi<sub>0.8</sub>Co<sub>0.15</sub>Al<sub>0.05</sub>O<sub>2</sub> cells with ionic liquid-based electrolytes in overcharge condition', *Electrochemical and Solid-State Letters*, vol. 13, no. 4, pp. 32–35, 2010, doi: 10.1149/1.3292635.
- [36] Y. Wang *et al.*, 'Preventing Sudden Death of High-Energy Lithium-Ion Batteries at Elevated Temperature Through Interfacial Ion-Flux Rectification', *Advanced Functional Materials*, 2022, doi: 10.1002/adfm.202208329.
- [37] N. Yabuuchi and T. Ohzuku, 'Novel lithium insertion material of LiCo<sub>1/3</sub>Ni<sub>1/3</sub>Mn<sub>1/3</sub>O<sub>2</sub> for advanced lithium-ion batteries', *Journal of Power Sources*, vol. 119–121, pp. 171–174, 2003, doi: 10.1016/S0378-7753(03)00173-3.
- [38] W. M. Dose *et al.*, 'Electrolyte Reactivity at the Charged Ni-Rich Cathode Interface and Degradation in Li-Ion Batteries', *ACS Applied Materials and Interfaces*, vol. 14, no. 11, pp. 13206–13222, 2022, doi: 10.1021/acsami.1c22812.
- [39] J. E. Harlow *et al.*, 'A Wide Range of Testing Results on an Excellent Lithium-Ion Cell Chemistry to be used as Benchmarks for New Battery Technologies', *Journal of The Electrochemical Society*, vol. 166, no. 13, pp. A3031–A3044, 2019, doi: 10.1149/2.0981913jes.
- [40] C. Xu, P. J. Reeves, Q. Jacquet, and C. P. Grey, 'Phase Behavior during Electrochemical Cycling of Ni-Rich Cathode Materials for Li-Ion Batteries', *Advanced Energy Materials*, vol. 11, no. 7, pp. 1–12, 2021, doi: 10.1002/aenm.202003404.
- [41] C. Xu *et al.*, 'Bulk fatigue induced by surface reconstruction in layered Ni-rich cathodes for Li-ion batteries', *Nature Materials*, vol. 20, no. 1, pp. 84–92, 2021, doi: 10.1038/s41563-020-0767-8.
- [42] L. Croguennec, C. Poullierie, A. N. Mansour, and C. Delmas, 'Structural characterisation of the highly deintercalated Li<sub>x</sub>Ni<sub>1.02</sub>O<sub>2</sub> phases (with x ≤ 0.30)', *Journal of Materials Chemistry*, vol. 11, no. 1, pp. 131–141, 2001, doi: 10.1039/b003377o.
- [43] K. Märker, P. J. Reeves, C. Xu, K. J. Griffith, and C. P. Grey, 'Evolution of Structure and Lithium Dynamics in LiNi<sub>0.8</sub>Mn<sub>0.1</sub>Co<sub>0.1</sub>O<sub>2</sub> (NMC811) Cathodes during Electrochemical Cycling', *Chemistry of Materials*, vol. 31, no. 7, pp. 2545–2554, 2019, doi: 10.1021/acs.chemmater.9b00140.
- [44] A. O. Kondrakov *et al.*, 'Anisotropic Lattice Strain and Mechanical Degradation of High- and Low-Nickel NCM Cathode Materials for Li-Ion Batteries', *Journal of Physical Chemistry C*, vol. 121, no. 6, pp. 3286–3294, 2017, doi: 10.1021/acs.jpcc.6b12885.
- [45] W. M. Dose, J. K. Morzy, A. Mahadevegowda, C. Ducati, C. P. Grey, and M. F. L. De Volder, 'The influence of electrochemical cycling protocols on capacity loss in nickel-rich lithium-ion batteries', *Journal of Materials Chemistry A*, vol. 9, no. 41, pp. 23582–23596, 2021, doi: 10.1039/d1ta06324c.
- [46] J. Xu *et al.*, 'Understanding the degradation mechanism of lithium nickel oxide cathodes for Li-ion batteries', *ACS Applied Materials and Interfaces*, vol. 8, no. 46, pp. 31677–31683, 2016, doi: 10.1021/acsami.6b11111.
- [47] C. S. Yoon, D. W. Jun, S. T. Myung, and Y. K. Sun, 'Structural Stability of LiNiO<sub>2</sub> Cycled above 4.2 V', *ACS Energy Letters*, vol. 2, no. 5, pp. 1150–1155, 2017, doi: 10.1021/acsenenergylett.7b00304.
- [48] K. Dokko, M. Nishizawa, S. Horikoshi, T. Itoh, M. Mohamedi, and I. Uchida, 'In situ observation of LiNiO<sub>2</sub> single-particle fracture during Li-ion extraction and insertion', *Electrochemical and Solid-State Letters*, vol. 3, no. 3, pp. 125–127, 2000, doi: 10.1149/1.1390977.
- [49] J. Li, L. E. Downie, L. Ma, W. Qiu, and J. R. Dahn, 'Study of the Failure Mechanisms of LiNi<sub>0.8</sub>Mn<sub>0.1</sub>Co<sub>0.1</sub>O<sub>2</sub> Cathode Material for Lithium Ion Batteries', *Journal of The Electrochemical Society*, vol. 162, no. 7, pp. A1401–A1408, 2015, doi: 10.1149/2.1011507jes.
- [50] F. Lin *et al.*, 'Surface reconstruction and chemical evolution of stoichiometric layered cathode materials for lithium-ion batteries', *Nature communications*, vol. 5, p. 3529, 2014, doi: 10.1038/ncomms4529.
- [51] S. Ober, A. Mesnier, and A. Manthiram, 'Surface Stabilization of Cobalt-Free LiNiO<sub>2</sub> with Niobium for Lithium-Ion Batteries', *ACS Applied Materials and Interfaces*, no. Li, 2023, doi: 10.1021/acsami.2c20268.

- [52] Y. Gao, J. Park, and X. Liang, 'Comprehensive Study of Al- And Zr-Modified LiNi<sub>0.8</sub>Mn<sub>0.1</sub>Co<sub>0.1</sub>O<sub>2</sub> through Synergy of Coating and Doping', *ACS Applied Energy Materials*, vol. 3, no. 9, pp. 8978–8987, 2020, doi: 10.1021/acsaem.0c01420.
- [53] S. Priyono, J. Triwibowo, and B. Prihandoko, 'The effect of 0.025 Al-doped in Li<sub>4</sub>Ti<sub>5</sub>O<sub>12</sub> material on the performance of half cell lithium ion battery', *AIP Conference Proceedings*, vol. 1711, no. February 2016, pp. 1–7, 2016, doi: 10.1063/1.4941634.
- [54] S. N. Kwon, M. Y. Song, and H. R. Park, 'Electrochemical properties of LiNiO<sub>2</sub> substituted by Al or Ti for Ni via the combustion method', *Ceramics International*, vol. 40, no. 9 PART A, pp. 14141–14147, 2014, doi: 10.1016/j.ceramint.2014.05.149.
- [55] J. Cho, 'LiNi<sub>0.74</sub>Co<sub>0.26</sub>', no. 14, pp. 3089–3094, 2000.
- [56] M. Eilers-Rethwisch *et al.*, 'Comparative study of Sn-doped Li[Ni<sub>0.6</sub>Mn<sub>0.2</sub>Co<sub>0.2-x</sub>Sn<sub>x</sub>]O<sub>2</sub> cathode active materials (x = 0–0.5) for lithium ion batteries regarding electrochemical performance and structural stability', *Journal of Power Sources*, vol. 397, no. June, pp. 68–78, 2018, doi: 10.1016/j.jpowsour.2018.06.072.
- [57] P. Mohan and G. P. Kalaigan, 'Structure and electrochemical performance of LiFe<sub>x</sub>Ni<sub>1-x</sub>O<sub>2</sub> (0.00 ≤ x ≤ 0.20) cathode materials for rechargeable lithium-ion batteries', *Journal of Electroceramics*, vol. 31, no. 1–2, pp. 210–217, 2013, doi: 10.1007/s10832-013-9815-y.
- [58] G. Prado, E. Suard, L. Fournes, and C. Delmas, 'Cationic distribution in the Li(1-z)(Ni(1-y)Fe(y))(1+z)O<sub>2</sub> electrode materials', *Journal of Materials Chemistry*, vol. 10, no. 11, pp. 2553–2560, 2000, doi: 10.1039/b002975k.
- [59] L. Croguennec, E. Suard, P. Willmann, and C. Delmas, 'Structural and electrochemical characterization of the LiNi<sub>1-y</sub>Ti<sub>y</sub>O<sub>2</sub> electrode materials obtained by direct solid-state reactions', *Chemistry of Materials*, vol. 14, no. 5, pp. 2149–2157, 2002, doi: 10.1021/cm011265v.
- [60] D. W. Jun, C. S. Yoon, U. H. Kim, and Y. K. Sun, 'High-Energy Density Core-Shell Structured Li[Ni<sub>0.95</sub>Co<sub>0.025</sub>Mn<sub>0.025</sub>]O<sub>2</sub> Cathode for Lithium-Ion Batteries', *Chemistry of Materials*, vol. 29, no. 12, pp. 5048–5052, 2017, doi: 10.1021/acs.chemmater.7b01425.
- [61] Y. K. Sun, S. T. Myung, M. H. Kim, J. Prakash, and K. Amine, 'Synthesis and characterization of Li[(Ni<sub>0.8</sub>Co<sub>0.1</sub>Mn<sub>0.1</sub>)<sub>0.8</sub>(Ni<sub>0.5</sub>Mn<sub>0.5</sub>)<sub>0.2</sub>]O<sub>2</sub> with the microscale core-shell structure as the positive electrode material for lithium batteries', *Journal of the American Chemical Society*, vol. 127, no. 38, pp. 13411–13418, 2005, doi: 10.1021/ja053675g.
- [62] Y. Sun, S. Myung, B.-C. Park, and K. Amine, 'Synthesis of Spherical Nano- to Microscale Core - Shell Particles Applications to Lithium Batteries', *Chemistry of Materials*, no. 5, pp. 5159–5163, 2006.
- [63] J. Li, R. Doig, J. Camardese, K. Plucknett, and J. R. Dahn, 'Measurements of Interdiffusion Coefficients of Transition Metals in Layered Li-Ni-Mn-Co Oxide Core-Shell Materials during Sintering Measurements of Interdiffusion Coefficients of Transition Metals in Layered Li-Ni-Mn-Co Oxide Core-Shell Materials during S', 2015, doi: 10.1021/acs.chemmater.5b03499.
- [64] Y. K. Sun *et al.*, 'Nanostructured high-energy cathode materials for advanced lithium batteries', *Nature Materials*, vol. 11, no. 11, pp. 942–947, 2012, doi: 10.1038/nmat3435.
- [65] X. Wang, Y. Ding, Y. Deng, and Z. Chen, 'Ni-Rich / Co-Poor Layered Cathode for Automotive Li-Ion Batteries : Promises and Challenges', vol. 1903864, pp. 1–28, 2022, doi: 10.1002/aenm.201903864.
- [66] M. G. Kim and J. Cho, 'Reversible and high-capacity nanostructured electrode materials for li-ion batteries', *Advanced Functional Materials*, vol. 19, no. 10, pp. 1497–1514, 2009, doi: 10.1002/adfm.200801095.
- [67] J. Cho, T. J. Kim, Y. J. Kim, and B. Park, 'High-performance ZrO<sub>2</sub>-coated LiNiO<sub>2</sub> cathode material', *Electrochemical and Solid-State Letters*, vol. 4, no. 10, pp. 160–162, 2001, doi: 10.1149/1.1398556.
- [68] J. Kang and B. Han, 'First-principles study on the thermal stability of LiNiO<sub>2</sub> materials coated by amorphous Al<sub>2</sub>O<sub>3</sub> with atomic layer thickness', *ACS Applied Materials and Interfaces*, vol. 7, no. 21, pp. 11599–11603, 2015, doi: 10.1021/acsami.5b02572.
- [69] S. H. Lee, G. J. Park, S. J. Sim, B. S. Jin, and H. S. Kim, 'Improved electrochemical performances of LiNi<sub>0.8</sub>Co<sub>0.1</sub>Mn<sub>0.1</sub>O<sub>2</sub> cathode via SiO<sub>2</sub> coating', *Journal of Alloys and Compounds*, vol. 791, pp. 193–199, 2019, doi: 10.1016/j.jallcom.2019.03.308.
- [70] S. Zhao *et al.*, 'Annealing effects of TiO<sub>2</sub> coating on cycling performance of Ni-rich cathode material LiNi<sub>0.8</sub>Co<sub>0.1</sub>Mn<sub>0.1</sub>O<sub>2</sub> for lithium-ion battery', *Materials Letters*, vol. 265, p. 127418, 2020, doi: 10.1016/j.matlet.2020.127418.
- [71] I. Azcarate, W. Yin, C. Méthivier, F. Ribot, C. Laberty-Robert, and A. Grimaud, 'Assessing the Oxidation Behavior of EC:DMC Based Electrolyte on Non-Catalytically Active Surface', *Journal of The Electrochemical Society*, vol. 167, no. 8, p. 080530, 2020, doi: 10.1149/1945-7111/ab8f57.
- [72] B. L. D. Rinkel, D. S. Hall, I. Temprano, and C. P. Grey, 'Electrolyte oxidation pathways in lithium-ion batteries', *Journal of the American Chemical Society*, vol. 142, no. 35, pp. 15058–15074, 2020, doi: 10.1021/jacs.0c06363.
- [73] J. Langdon, R. Sim, and A. Manthiram, 'Gas Generation in Lithium Cells with High-Nickel Cathodes and Localized High-Concentration Electrolytes', *ACS Energy Letters*, vol. 7, no. 8, pp. 2634–2640, 2022, doi: 10.1021/acsenergylett.2c01444.
- [74] M. Moshkovich, M. Cojocaru, H. E. Gottlieb, and D. Aurbach, 'The study of the anodic stability of alkyl carbonate solutions by in situ FTIR spectroscopy, EQCM, NMR and MS', *Journal of Electroanalytical Chemistry*, vol. 497, no. 1–2, pp. 84–96, 2001, doi: 10.1016/S0022-0728(00)00457-5.
- [75] O. C. Harris, S. E. Lee, C. Lees, and M. Tang, 'Review: Mechanisms and consequences of chemical cross-talk in advanced Li-ion batteries', *JPhys Energy*, vol. 2, no. 3, 2020, doi: 10.1088/2515-7655/ab8b68.
- [76] R. Jung, M. Metzger, F. Maglia, C. Stinner, and H. A. Gasteiger, 'Chemical versus electrochemical electrolyte oxidation

- on NMC111, NMC622, NMC811, LNMO, and conductive carbon', *Journal of Physical Chemistry Letters*, vol. 8, no. 19, pp. 4820–4825, 2017, doi: 10.1021/acs.jpcclett.7b01927.
- [77] R. Jung, M. Metzger, F. Maglia, C. Stinner, and H. A. Gasteiger, 'Oxygen Release and Its Effect on the Cycling Stability of  $\text{LiNi}_x\text{Mn}_y\text{Co}_z\text{O}_2$  (NMC) Cathode Materials for Li-Ion Batteries', *Journal of The Electrochemical Society*, vol. 164, no. 7, pp. A1361–A1377, 2017, doi: 10.1149/2.0021707jes.
- [78] S. Sharifi-Asl, J. Lu, K. Amine, and R. Shahbazian-Yassar, 'Oxygen Release Degradation in Li-Ion Battery Cathode Materials: Mechanisms and Mitigating Approaches', *Advanced Energy Materials*, vol. 9, no. 22, pp. 1–19, 2019, doi: 10.1002/aenm.201900551.
- [79] A. T. S. Freiberg, M. K. Roos, J. Wandt, R. De Vivie-Riedle, and H. A. Gasteiger, 'Singlet Oxygen Reactivity with Carbonate Solvents Used for Li-Ion Battery Electrolytes', *Journal of Physical Chemistry A*, vol. 122, no. 45, pp. 8828–8839, 2018, doi: 10.1021/acs.jpca.8b08079.
- [80] G. Amatucci, A. Du Pasquier, A. Blyr, T. Zheng, and J. M. Tarascon, 'The elevated temperature performance of the  $\text{LiMn}_2\text{O}_4/\text{C}$  system: Failure and solutions', *Electrochimica Acta*, vol. 45, no. 1–2, pp. 255–271, 1999, doi: 10.1016/S0013-4686(99)00209-1.
- [81] A. Du Pasquier *et al.*, 'Mechanism for Limited 55°C Storage Performance of  $\text{Li}_{1.05}\text{Mn}_{1.95}\text{O}_4$  Electrodes', *Journal of The Electrochemical Society*, vol. 146, no. 2, pp. 428–436, 1999, doi: 10.1149/1.1391625.
- [82] J. A. Gilbert, I. A. Shkrob, and D. P. Abraham, 'Transition Metal Dissolution, Ion Migration, Electrocatalytic Reduction and Capacity Loss in Lithium-Ion Full Cells', *Journal of The Electrochemical Society*, vol. 164, no. 2, pp. A389–A399, 2017, doi: 10.1149/2.1111702jes.
- [83] H. R. Morin *et al.*, 'Transition-Metal Dissolution from NMC-Family Oxides: A Case Study', *ACS Applied Energy Materials*, vol. 3, no. 3, pp. 2565–2575, 2020, doi: 10.1021/acsaem.9b02277.
- [84] D. R. Gallus *et al.*, 'The influence of different conducting salts on the metal dissolution and capacity fading of NCM cathode material', *Electrochimica Acta*, vol. 134, pp. 393–398, 2014, doi: 10.1016/j.electacta.2014.04.091.
- [85] A. Jarry *et al.*, 'The Formation Mechanism of Fluorescent Metal Complexes at the  $\text{Li}_x\text{Ni}_{0.5}\text{Mn}_{1.5}\text{O}_4$ - $\delta$ /Carbonate Ester Electrolyte Interface', *Journal of the American Chemical Society*, vol. 137, no. 10, pp. 3533–3539, 2015, doi: 10.1021/ja5116698.
- [86] Z. Ruff, C. Xu, and C. P. Grey, 'Transition Metal Dissolution and Degradation in NMC811-Graphite Electrochemical Cells', *Journal of The Electrochemical Society*, vol. 168, no. 6, p. 060518, 2021, doi: 10.1149/1945-7111/ac0359.
- [87] S. R. Gowda, 'Oxidation state of cross-over manganese species on the graphite electrode of lithium-ion cells', *Physical Chemistry Chemical Physics*, vol. 16, no. 15, pp. 6898–6902, 2014, doi: 10.1039/c4cp00764f.
- [88] C. Delacourt *et al.*, 'Effect of Manganese Contamination on the Solid-Electrolyte-Interphase Properties in Li-Ion Batteries', *Journal of The Electrochemical Society*, vol. 160, no. 8, pp. A1099–A1107, 2013, doi: 10.1149/2.035308jes.
- [89] C. Zhan, X. Qiu, J. Lu, and K. Amine, 'Tuning the Mn Deposition on the Anode to Improve the Cycle Performance of the Mn-Based Lithium Ion Battery', *Advanced Materials Interfaces*, vol. 3, no. 11, pp. 1–6, 2016, doi: 10.1002/admi.201500856.
- [90] J. Yang *et al.*, 'Electrolytes Polymerization-Induced Cathode-Electrolyte-Interphase for High Voltage Lithium-Ion Batteries', *Advanced Energy Materials*, vol. 11, no. 39, pp. 1–11, 2021, doi: 10.1002/aenm.202101956.
- [91] C. Zhan, T. Wu, J. Lu, and K. Amine, 'Dissolution, migration, and deposition of transition metal ions in Li-ion batteries exemplified by Mn-based cathodes-A critical review', *Energy and Environmental Science*, vol. 11, no. 2, pp. 243–257, 2018, doi: 10.1039/c7ee03122j.
- [92] O. C. Harris, Y. Lin, Y. Qi, K. Leung, and M. H. Tang, 'How Transition Metals Enable Electron Transfer through the SEI: Part I. Experiments and Butler-Volmer Modeling', *Journal of The Electrochemical Society*, vol. 167, no. 1, p. 013502, 2020, doi: 10.1149/2.0022001jes.
- [93] K. Leung, 'First-Principles Modeling of Mn(II) Migration above and Dissolution from  $\text{Li}_x\text{Mn}_2\text{O}_4$  (001) Surfaces', *Chemistry of Materials*, vol. 29, no. 6, pp. 2550–2562, 2017, doi: 10.1021/acs.chemmater.6b04429.
- [94] T. Joshi, K. Eom, G. Yushin, and T. F. Fuller, 'Effects of Dissolved Transition Metals on the Electrochemical Performance and SEI Growth in Lithium-Ion Batteries', *Journal of The Electrochemical Society*, vol. 161, no. 12, pp. A1915–A1921, 2014, doi: 10.1149/2.0861412jes.
- [95] S. Solchenbach, G. Hong, A. T. S. Freiberg, R. Jung, and H. A. Gasteiger, 'Electrolyte and SEI Decomposition Reactions of Transition Metal Ions Investigated by On-Line Electrochemical Mass Spectrometry', *Journal of The Electrochemical Society*, vol. 165, no. 14, pp. A3304–A3312, 2018, doi: 10.1149/2.0511814jes.
- [96] S. Klein *et al.*, 'Understanding the Outstanding High-Voltage Performance of NCM523|Graphite Lithium Ion Cells after Elimination of Ethylene Carbonate Solvent from Conventional Electrolyte', *Advanced Energy Materials*, vol. 11, no. 14, 2021, doi: 10.1002/aenm.202003738.
- [97] S. Klein *et al.*, 'Exploiting the Degradation Mechanism of NCM523|Graphite Lithium-Ion Full Cells Operated at High Voltage', *ChemSusChem*, vol. 14, no. 2, pp. 595–613, 2021, doi: 10.1002/cssc.202002113.
- [98] U. R. Koleti, T. Q. Dinh, and J. Marco, 'A new on-line method for lithium plating detection in lithium-ion batteries', *Journal of Power Sources*, vol. 451, no. November 2019, p. 227798, 2020, doi: 10.1016/j.jpowsour.2020.227798.
- [99] V. Zinth *et al.*, 'Lithium plating in lithium-ion batteries at sub-ambient temperatures investigated by in situ neutron diffraction', *Journal of Power Sources*, vol. 271, pp. 152–159, 2014, doi: 10.1016/j.jpowsour.2014.07.168.
- [100] C. von Lüders *et al.*, 'Lithium plating in lithium-ion batteries investigated by voltage relaxation and in situ neutron diffraction', *Journal of Power Sources*, vol. 342, pp. 17–23, 2017, doi: 10.1016/j.jpowsour.2016.12.032.

- [101] T. Waldmann, M. Wilka, M. Kasper, M. Fleischhammer, and M. Wohlfahrt-Mehrens, 'Temperature dependent ageing mechanisms in Lithium-ion batteries - A Post-Mortem study', *Journal of Power Sources*, vol. 262, pp. 129–135, 2014, doi: 10.1016/j.jpowsour.2014.03.112.
- [102] X. G. Yang and C. Y. Wang, 'Understanding the trilemma of fast charging, energy density and cycle life of lithium-ion batteries', *Journal of Power Sources*, vol. 402, no. August, pp. 489–498, 2018, doi: 10.1016/j.jpowsour.2018.09.069.
- [103] L. Madec and L. D. Ellis, 'Exploring Interactions between Electrodes in Li[Ni x Mn y Co 1-xy ]O 2 /Graphite Cells through Electrode/Electrolyte Interfaces Analysis ', *Journal of The Electrochemical Society*, vol. 164, no. 14, pp. A3718–A3726, 2017, doi: 10.1149/2.1011714jes.
- [104] J. C. Burns *et al.*, 'Predicting and Extending the Lifetime of Li-Ion Batteries', *Journal of The Electrochemical Society*, vol. 160, no. 9, pp. A1451–A1456, 2013, doi: 10.1149/2.060309jes.
- [105] Y. Q. Chen *et al.*, 'An electrolyte additive with boron-nitrogen-oxygen alkyl group enabled stable cycling for high voltage LiNi<sub>0.5</sub>Mn<sub>1.5</sub>O<sub>4</sub> cathode in lithium-ion battery', *Journal of Power Sources*, vol. 477, no. August, p. 228473, 2020, doi: 10.1016/j.jpowsour.2020.228473.
- [106] J. Ahn, J. Im, H. Seo, S. Yoon, and K. Y. Cho, 'Enhancing the cycling stability of Ni-rich LiNi<sub>0.83</sub>Co<sub>0.11</sub>Mn<sub>0.06</sub>O<sub>2</sub> cathode at 4.5 V via 2,4-difluorobiphenyl additive', *Journal of Power Sources*, vol. 512, no. June, p. 230513, 2021, doi: 10.1016/j.jpowsour.2021.230513.
- [107] Y. Zheng *et al.*, 'Construction of a Stable LiNi<sub>0.8</sub>Co<sub>0.1</sub>Mn<sub>0.1</sub>O<sub>2</sub> (NCM811) Cathode Interface by a Multifunctional Organosilicon Electrolyte Additive', *ACS Applied Energy Materials*, vol. 3, no. 3, pp. 2837–2845, 2020, doi: 10.1021/acsaem.9b02486.
- [108] N. Von Aspern *et al.*, 'Fluorinated Cyclic Phosphorus(III)-Based Electrolyte Additives for High Voltage Application in Lithium-Ion Batteries: Impact of Structure-Reactivity Relationships on CEI Formation and Cell Performance', *ACS Applied Materials and Interfaces*, vol. 11, no. 18, pp. 16605–16618, 2019, doi: 10.1021/acsaami.9b03359.
- [109] Z. Chen *et al.*, 'Borate electrolyte additives for high voltage lithium nickel manganese oxide electrode: A comparative study', *Electrochimica Acta*, vol. 249, pp. 353–359, 2017, doi: 10.1016/j.electacta.2017.08.027.
- [110] X. Zuo, C. Fan, J. Liu, X. Xiao, J. Wu, and J. Nan, 'Effect of tris(trimethylsilyl)borate on the high voltage capacity retention of LiNi<sub>0.5</sub>Co<sub>0.2</sub>Mn<sub>0.3</sub>O<sub>2</sub>/graphite cells', *Journal of Power Sources*, vol. 229, pp. 308–312, 2013, doi: 10.1016/j.jpowsour.2012.12.056.
- [111] Q. Liu *et al.*, 'Synergy Effect of Trimethyl Borate on Protecting High-Voltage Cathode Materials in Dual-Additive Electrolytes', *ACS Applied Materials and Interfaces*, vol. 13, no. 18, pp. 21459–21466, 2021, doi: 10.1021/acsaami.1c04389.
- [112] F. Zhang *et al.*, 'Synergistic effect of sulfolane and lithium Difluoro(oxalate)borate on improvement of compatibility for LiNi<sub>0.8</sub>Co<sub>0.15</sub>Al<sub>0.05</sub>O<sub>2</sub> electrode', *Electrochimica Acta*, vol. 337, p. 135727, 2020, doi: 10.1016/j.electacta.2020.135727.
- [113] M. Mao, B. Huang, Q. Li, C. Wang, Y. B. He, and F. Kang, 'In-situ construction of hierarchical cathode electrolyte interphase for high performance LiNi<sub>0.8</sub>Co<sub>0.1</sub>Mn<sub>0.1</sub>O<sub>2</sub>/Li metal battery', *Nano Energy*, vol. 78, no. July, p. 105282, 2020, doi: 10.1016/j.nanoen.2020.105282.
- [114] Y. Zhu, Y. Li, M. Bettge, and D. P. Abraham, 'Positive Electrode Passivation by LiDFOB Electrolyte Additive in High-Capacity Lithium-Ion Cells', *Journal of The Electrochemical Society*, vol. 159, no. 12, pp. A2109–A2117, 2012, doi: 10.1149/2.083212jes.
- [115] T. Deng *et al.*, 'Designing In-Situ-Formed Interphases Enables Highly Reversible Cobalt-Free LiNiO<sub>2</sub> Cathode for Li-ion and Li-metal Batteries', *Joule*, vol. 3, no. 10, pp. 2550–2564, 2019, doi: 10.1016/j.joule.2019.08.004.
- [116] X. Li *et al.*, 'Effects of Imide-Orthoborate Dual-Salt Mixtures in Organic Carbonate Electrolytes on the Stability of Lithium Metal Batteries', *ACS Applied Materials and Interfaces*, vol. 10, no. 3, pp. 2469–2479, 2018, doi: 10.1021/acsaami.7b15117.
- [117] Z. A. Zhang, X. X. Zhao, B. Peng, Y. Q. Lai, Z. Y. Zhang, and J. Li, 'Mixed salts for lithium iron phosphate-based batteries operated at wide temperature range', *Transactions of Nonferrous Metals Society of China (English Edition)*, vol. 25, no. 7, pp. 2260–2265, 2015, doi: 10.1016/S1003-6326(15)63839-0.
- [118] K. Park, S. Yu, C. Lee, and H. Lee, 'Comparative study on lithium borates as corrosion inhibitors of aluminum current collector in lithium bis(fluorosulfonyl)imide electrolytes', *Journal of Power Sources*, vol. 296, pp. 197–203, 2015, doi: 10.1016/j.jpowsour.2015.07.052.
- [119] J. Xu, 'Critical Review on cathode–electrolyte Interphase Toward High-Voltage Cathodes for Li-Ion Batteries', *Nano-Micro Letters*, vol. 14, no. 1, pp. 1–22, 2022, doi: 10.1007/s40820-022-00917-2.
- [120] X. Fan *et al.*, 'Non-flammable electrolyte enables li-metal batteries with aggressive cathode chemistries', *Nature Nanotechnology*, vol. 13, no. 8, pp. 715–722, 2018, doi: 10.1038/s41565-018-0183-2.
- [121] T. Achiha *et al.*, 'Thermal Stability and Electrochemical Properties of Fluorine Compounds as Nonflammable Solvents for Lithium-Ion Batteries', *Journal of The Electrochemical Society*, vol. 157, no. 6, p. A707, 2010, doi: 10.1149/1.3377084.
- [122] Z. Yu *et al.*, 'Tuning Fluorination of Linear Carbonate for Lithium-Ion Batteries', *Journal of The Electrochemical Society*, vol. 169, no. 4, p. 040555, 2022, doi: 10.1149/1945-7111/ac67f5.
- [123] C. C. Su *et al.*, 'Principle in developing novel fluorinated sulfone electrolyte for high voltage lithium-ion batteries', *Energy and Environmental Science*, vol. 14, no. 5, pp. 3029–3034, 2021, doi: 10.1039/d0ee03890c.
- [124] R. Chen *et al.*, 'An investigation of functionalized electrolyte using succinonitrile additive for high voltage lithium-ion batteries', *Journal of Power Sources*, vol. 306, pp. 70–77, 2016, doi: 10.1016/j.jpowsour.2015.10.105.
- [125] S. Y. Park *et al.*, 'Ni-Ion-Chelating Strategy for Mitigating the Deterioration of Li-Ion Batteries with Nickel-Rich Cathodes',

- Advanced Science*, vol. 2205918, pp. 1–12, 2022, doi: 10.1002/advs.202205918.
- [126] A. Banerjee, B. Ziv, Y. Shilina, S. Luski, D. Aurbach, and I. C. Halalay, 'Improving Stability of Li-Ion Batteries by Means of Transition Metal Ions Trapping Separators', *Journal of The Electrochemical Society*, vol. 163, no. 6, pp. A1083–A1094, 2016, doi: 10.1149/2.0081607jes.
- [127] A. Banerjee, B. Ziv, S. Luski, D. Aurbach, and I. C. Halalay, 'Increasing the durability of Li-ion batteries by means of manganese ion trapping materials with nitrogen functionalities', *Journal of Power Sources*, vol. 341, pp. 457–465, 2017, doi: 10.1016/j.jpowsour.2016.12.036.
- [128] J. G. Han, K. Kim, Y. Lee, and N. S. Choi, 'Scavenging Materials to Stabilize LiPF<sub>6</sub>-Containing Carbonate-Based Electrolytes for Li-Ion Batteries', *Advanced Materials*, vol. 31, no. 20, 2019, doi: 10.1002/adma.201804822.
- [129] H. Liu, A. J. Naylor, A. S. Menon, W. R. Brant, K. Edström, and R. Younesi, 'Understanding the Roles of Tris(trimethylsilyl) Phosphite (TMSPi) in LiNi<sub>0.8</sub>Mn<sub>0.1</sub>Co<sub>0.1</sub>O<sub>2</sub> (NMC811)/Silicon–Graphite (Si–Gr) Lithium-Ion Batteries', *Advanced Materials Interfaces*, vol. 7, no. 15, 2020, doi: 10.1002/admi.202000277.
- [130] Y. Yamada and A. Yamada, 'Review—Superconcentrated Electrolytes for Lithium Batteries', *Journal of The Electrochemical Society*, vol. 162, no. 14, pp. A2406–A2423, 2015, doi: 10.1149/2.0041514jes.
- [131] W. R. McKinnon and J. R. Dahn, 'How to Reduce the Cointercalation of Propylene Carbonate in Li x ZrS<sub>2</sub> and Other Layered Compounds', *Journal of The Electrochemical Society*, vol. 132, no. 2, pp. 364–366, 1985, doi: 10.1149/1.2113839.
- [132] O. Borodin, J. Self, K. A. Persson, C. Wang, and K. Xu, 'Uncharted Waters: Super-Concentrated Electrolytes', *Joule*, vol. 4, no. 1, pp. 69–100, 2020, doi: 10.1016/j.joule.2019.12.007.
- [133] Z. Inaba, Minoru & TOMIYASU, Hanako & Tasaka, Akimasa & JEONG, Soon-Ki & IRIYAMA, Yasutoshi & Abe, Takeshi & OGUMI, 'Surface Film Formation on Graphite Negative Electrode at Elevated Temperatures.' *Electrochemistry*, p. 71. N°12, 2003, doi: 10.5796/electrochemistry.71.1132.
- [134] S. K. Jeong, M. Inaba, Y. Iriyama, T. Abe, and Z. Ogumi, 'Interfacial reactions between graphite electrodes and propylene carbonate-based solutions: Electrolyte-concentration dependence of electrochemical lithium intercalation reaction', *Journal of Power Sources*, vol. 175, no. 1, pp. 540–546, 2008, doi: 10.1016/j.jpowsour.2007.08.065.
- [135] Y. Yamada *et al.*, 'Unusual stability of acetonitrile-based superconcentrated electrolytes for fast-charging lithium-ion batteries', *Journal of the American Chemical Society*, vol. 136, no. 13, pp. 5039–5046, 2014, doi: 10.1021/ja412807w.
- [136] S. K. Jeong *et al.*, 'Suppression of dendritic lithium formation by using concentrated electrolyte solutions', *Electrochemistry Communications*, vol. 10, no. 4, pp. 635–638, 2008, doi: 10.1016/j.elecom.2008.02.006.
- [137] L. Suo, Y. S. Hu, H. Li, M. Armand, and L. Chen, 'A new class of Solvent-in-Salt electrolyte for high-energy rechargeable metallic lithium batteries', *Nature Communications*, vol. 4, pp. 1–9, 2013, doi: 10.1038/ncomms2513.
- [138] J. Qian *et al.*, 'High rate and stable cycling of lithium metal anode', *Nature Communications*, vol. 6, 2015, doi: 10.1038/ncomms7362.
- [139] K. Matsumoto, K. Inoue, K. Nakahara, R. Yuge, T. Noguchi, and K. Utsugi, 'Suppression of aluminum corrosion by using high concentration LiTFSI electrolyte', *Journal of Power Sources*, vol. 231, pp. 234–238, 2013, doi: 10.1016/j.jpowsour.2012.12.028.
- [140] Y. Yamada, C. H. Chiang, K. Sodeyama, J. Wang, Y. Tateyama, and A. Yamada, 'Corrosion Prevention Mechanism of Aluminum Metal in Superconcentrated Electrolytes', *ChemElectroChem*, vol. 2, no. 11, pp. 1687–1694, 2015, doi: 10.1002/celec.201500235.
- [141] D. W. McOwen, D. M. Seo, O. Borodin, J. Vatamanu, P. D. Boyle, and W. A. Henderson, 'Concentrated electrolytes: Decrypting electrolyte properties and reassessing Al corrosion mechanisms', *Energy and Environmental Science*, vol. 7, no. 1, pp. 416–426, 2014, doi: 10.1039/c3ee42351d.
- [142] T. Ma *et al.*, 'Revisiting the Corrosion of the Aluminum Current Collector in Lithium-Ion Batteries', *Journal of Physical Chemistry Letters*, vol. 8, no. 5, pp. 1072–1077, 2017, doi: 10.1021/acs.jpcllett.6b02933.
- [143] N. Dubouis *et al.*, 'Extending insertion electrochemistry to soluble layered halides with superconcentrated electrolytes', *Nature Materials*, vol. 20, no. 11, pp. 1545–1550, 2021, doi: 10.1038/s41563-021-01060-w.
- [144] J. Wang, Y. Yamada, K. Sodeyama, C. H. Chiang, Y. Tateyama, and A. Yamada, 'Superconcentrated electrolytes for a high-voltage lithium-ion battery', *Nature Communications*, vol. 7, no. May, pp. 1–9, 2016, doi: 10.1038/ncomms12032.
- [145] W. Liu, J. Li, W. Li, H. Xu, C. Zhang, and X. Qiu, 'Inhibition of transition metals dissolution in cobalt-free cathode with ultrathin robust interphase in concentrated electrolyte', *Nature Communications*, vol. 11, no. 1, 2020, doi: 10.1038/s41467-020-17396-x.
- [146] K. Yoshida *et al.*, 'Oxidative-stability enhancement and charge transport mechanism in glyme-lithium salt equimolar complexes', *Journal of the American Chemical Society*, vol. 133, no. 33, pp. 13121–13129, 2011, doi: 10.1021/ja203983r.
- [147] Y. Yamada, M. Yaegashi, T. Abe, and A. Yamada, 'A superconcentrated ether electrolyte for fast-charging Li-ion batteries', *Chemical Communications*, vol. 49, no. 95, pp. 11194–11196, 2013, doi: 10.1039/c3cc46665e.
- [148] S. Chen *et al.*, 'High-Voltage Lithium-Metal Batteries Enabled by Localized High-Concentration Electrolytes', *Advanced Materials*, vol. 30, no. 21, pp. 1–7, 2018, doi: 10.1002/adma.201706102.
- [149] K. Dokko *et al.*, 'Solvate Ionic Liquid Electrolyte for Li–S Batteries', *Journal of The Electrochemical Society*, vol. 160, no. 8, pp. A1304–A1310, 2013, doi: 10.1149/2.111308jes.
- [150] T. Li, Y. Li, Y. Sun, Z. Qian, and R. Wang, 'New Insights on the Good Compatibility of Ether-Based Localized High-Concentration Electrolyte with Lithium Metal', *ACS Materials Letters*, vol. 3, pp. 838–844, 2021, doi: 10.1021/acsmaterialslett.1c00276.

- [151] X. Zhang *et al.*, 'Electrolyte Regulating toward Stabilization of Cobalt-Free Ultrahigh-Nickel Layered Oxide Cathode in Lithium-Ion Batteries', *ACS Energy Letters*, vol. 6, no. 4, pp. 1324–1332, 2021, doi: 10.1021/acsenergylett.1c00374.
- [152] Z. Xu, K. Deng, S. Zhou, Z. Liu, X. Guan, and D. Mo, 'Nonflammable Localized High-Concentration Electrolytes with Long-Term Cycling Stability for High-Performance Li Metal Batteries', *ACS Applied Materials and Interfaces*, 2022, doi: 10.1021/acssami.2c13922.
- [153] C. Niu *et al.*, 'High-energy lithium metal pouch cells with limited anode swelling and long stable cycles', *Nature Energy*, vol. 4, no. 7, pp. 551–559, 2019, doi: 10.1038/s41560-019-0390-6.
- [154] S. Chen *et al.*, 'High-Efficiency Lithium Metal Batteries with Fire-Retardant Electrolytes', *Joule*, vol. 2, no. 8, pp. 1548–1558, 2018, doi: 10.1016/j.joule.2018.05.002.
- [155] X. Cao *et al.*, 'Effects of fluorinated solvents on electrolyte solvation structures and electrode/electrolyte interphases for lithium metal batteries', *Proceedings of the National Academy of Sciences of the United States of America*, vol. 118, no. 9, pp. 1–9, 2021, doi: 10.1073/pnas.2020357118.
- [156] W. W. A. van Ekeren *et al.*, 'A comparative analysis of the influence of hydrofluoroethers as diluents on solvation structure and electrochemical performance in non-flammable electrolytes', *Journal of Materials Chemistry A*, vol. 11, no. 8, pp. 4111–4125, 2023, doi: 10.1039/d2ta08404j.
- [157] J. Langdon, Z. Cui, and A. Manthiram, 'Role of Electrolyte in Overcoming the Challenges of LiNiO<sub>2</sub> Cathode in Lithium Batteries', *ACS Energy Letters*, vol. 6, no. 11, pp. 3809–3816, 2021, doi: 10.1021/acsenergylett.1c01714.
- [158] F. Guo *et al.*, 'Improved Cycling of Li||NMC811 Batteries under Practical Conditions by a Localized High-Concentration Electrolyte', *Small*, 2023, doi: 10.1002/smll.202207290.
- [159] X. Zhang *et al.*, 'Advanced Electrolytes for Fast-Charging High-Voltage Lithium-Ion Batteries in Wide-Temperature Range', *Advanced Energy Materials*, vol. 10, no. 22, pp. 1–11, 2020, doi: 10.1002/aenm.202000368.
- [160] X. Zhang *et al.*, 'Unravelling high-temperature stability of lithium-ion battery with lithium-rich oxide cathode in localized high-concentration electrolyte', *Journal of Power Sources Advances*, vol. 5, no. May, 2020, doi: 10.1016/j.powera.2020.100024.
- [161] Y. Yamada, J. Wang, S. Ko, E. Watanabe, and A. Yamada, 'Advances and issues in developing salt-concentrated battery electrolytes', *Nature Energy*, vol. 4, no. 4, pp. 269–280, 2019, doi: 10.1038/s41560-019-0336-z.
- [162] X. Ren *et al.*, 'High-concentration ether electrolytes for stable high-voltage lithium metal batteries', *ACS Energy Letters*, vol. 4, no. 4, pp. 896–902, 2019, doi: 10.1021/acsenergylett.9b00381.
- [163] X. Ren *et al.*, 'Enabling High-Voltage Lithium-Metal Batteries under Practical Conditions', *Joule*, vol. 3, no. 7, pp. 1662–1676, 2019, doi: 10.1016/j.joule.2019.05.006.
- [164] S. Chen *et al.*, 'Critical Parameters for Evaluating Coin Cells and Pouch Cells of Rechargeable Li-Metal Batteries', *Joule*, vol. 3, no. 4, pp. 1094–1105, 2019, doi: 10.1016/j.joule.2019.02.004.
- [165] 'National Renewable Energy Laboratory - Performances of Photovoltaic Cells', 2021. <https://www.nrel.gov/pv/device-performance.html>.
- [166] Y.-K. Sun, 'An Experimental Checklist for Reporting Battery Performances', *ACS Energy Letters*, vol. 6, no. 6, pp. 2187–2189, 2021, doi: 10.1021/acsenergylett.1c00870.
- [167] J. Li *et al.*, 'Good practice guide for papers on batteries for the Journal of Power Sources', *Journal of Power Sources*, vol. 452, no. February, p. 227824, 2020, doi: 10.1016/j.jpowsour.2020.227824.
- [168] Z. Lin, T. Liu, X. Ai, and C. Liang, 'Aligning academia and industry for unified battery performance metrics', *Nature Communications*, vol. 9, no. 1, pp. 8–12, 2018, doi: 10.1038/s41467-018-07599-8.
- [169] H. Zheng, J. Li, X. Song, G. Liu, and V. S. Battaglia, 'A comprehensive understanding of electrode thickness effects on the electrochemical performances of Li-ion battery cathodes', *Electrochimica Acta*, vol. 71, pp. 258–265, 2012, doi: 10.1016/j.electacta.2012.03.161.
- [170] J. C. Bernard, J. C. Hestenes, K. S. Mayilvahanan, L. E. Marbella, and A. C. West, 'Investigating the Influence of Polymer Binders on Liquid Phase Transport and Tortuosity Through Lithium-Ion Electrodes', *Journal of The Electrochemical Society*, vol. 170, no. 3, p. 030518, 2023, doi: 10.1149/1945-7111/acbf7c.
- [171] D. Andre *et al.*, 'Future generations of cathode materials: An automotive industry perspective', *Journal of Materials Chemistry A*, vol. 3, no. 13, pp. 6709–6732, 2015, doi: 10.1039/c5ta00361j.
- [172] G. Ceder, Y. M. Chiang, D. R. Sadoway, M. K. Aydinol, Y. I. Jang, and B. Huang, 'Identification of cathode materials for lithium batteries guided by first-principles calculations', *Nature*, vol. 392, no. 6677, pp. 694–696, 1998, doi: 10.1038/33647.
- [173] M. D. Radin *et al.*, 'Narrowing the Gap between Theoretical and Practical Capacities in Li-Ion Layered Oxide Cathode Materials', *Advanced Energy Materials*, vol. 7, no. 20, pp. 1–33, 2017, doi: 10.1002/aenm.201602888.
- [174] J. Kasnatscheew *et al.*, 'A Tutorial into Practical Capacity and Mass Balancing of Lithium Ion Batteries', *Journal of The Electrochemical Society*, vol. 164, no. 12, pp. A2479–A2486, 2017, doi: 10.1149/2.0961712jes.
- [175] B. R. Long *et al.*, 'Enabling high-energy, high-voltage lithium-ion cells: Standardization of coin-cell assembly, electrochemical testing, and evaluation of full cells', *35th Annual International Battery Seminar and Exhibit 2018*, vol. 1, no. 14, pp. 112–122, 2018, doi: 10.1149/2.0691614jes.
- [176] A. Smith, P. Stüble, L. Leuthner, A. Hofmann, F. Jeschull, and L. Mereacre, 'Potential and Limitations of Research Battery Cell Types for Electrochemical Data Acquisition', *Batteries and Supercaps*, 2023, doi: 10.1002/batt.202300080.
- [177] V. Murray, D. S. Hall, and J. R. Dahn, 'A Guide to Full Coin Cell Making for Academic Researchers', *Journal of The*

- Electrochemical Society*, vol. 166, no. 2, pp. A329–A333, 2019, doi: 10.1149/2.1171902jes.
- [178] D. L. Wood, J. Li, and C. Daniel, 'Prospects for reducing the processing cost of lithium ion batteries', *Journal of Power Sources*, vol. 275, pp. 234–242, 2015, doi: 10.1016/j.jpowsour.2014.11.019.
- [179] S. J. An, J. Li, Z. Du, C. Daniel, and D. L. Wood, 'Fast formation cycling for lithium ion batteries', *Journal of Power Sources*, vol. 342, pp. 846–852, 2017, doi: 10.1016/j.jpowsour.2017.01.011.
- [180] 'INTERNATIONAL STANDARD - Space systems — Lithium ion battery for space vehicles — Design and verification requirements', *Reference number ISO 17546:2016(E)*, 2016.
- [181] 'INTERNATIONAL STANDARD - Electrically propelled road vehicles — Test specification for lithium-ion traction battery packs and systems', *Reference number ISO 12405-4:2018(E)*, 2018.
- [182] P. M. Attia *et al.*, 'Closed-loop optimization of fast-charging protocols for batteries with machine learning', *Nature*, vol. 578, no. 7795, pp. 397–402, 2020, doi: 10.1038/s41586-020-1994-5.
- [183] K. A. Severson *et al.*, 'Data-driven prediction of battery cycle life before capacity degradation', *Nature Energy*, vol. 4, no. 5, pp. 383–391, 2019, doi: 10.1038/s41560-019-0356-8.
- [184] J. Vetter *et al.*, 'Ageing mechanisms in lithium-ion batteries', *Journal of Power Sources*, vol. 147, no. 1–2, pp. 269–281, 2005, doi: 10.1016/j.jpowsour.2005.01.006.
- [185] D. Aurbach *et al.*, 'Review on electrode-electrolyte solution interactions, related to cathode materials for Li-ion batteries', *Journal of Power Sources*, vol. 165, no. 2, pp. 491–499, 2007, doi: 10.1016/j.jpowsour.2006.10.025.
- [186] J. S. Edge *et al.*, 'Lithium ion battery degradation: what you need to know', *Physical Chemistry Chemical Physics*, vol. 23, no. 14, pp. 8200–8221, 2021, doi: 10.1039/d1cp00359c.
- [187] C. R. Birkl, M. R. Roberts, E. McTurk, P. G. Bruce, and D. A. Howey, 'Degradation diagnostics for lithium ion cells', *Journal of Power Sources*, vol. 341, pp. 373–386, 2017, doi: 10.1016/j.jpowsour.2016.12.011.
- [188] I. Bloom *et al.*, 'Differential voltage analyses of high-power, lithium-ion cells 1. Technique and application', *Journal of Power Sources*, vol. 139, no. 1–2, pp. 295–303, 2005, doi: 10.1016/j.jpowsour.2004.07.021.
- [189] A. J. Smith, J. C. Burns, D. Xiong, and J. R. Dahn, 'Interpreting High Precision Coulometry Results on Li-ion Cells', *Journal of The Electrochemical Society*, vol. 158, no. 10, p. A1136, 2011, doi: 10.1149/1.3625232.
- [190] R. D. Deshpande, P. Ridgway, Y. Fu, W. Zhang, J. Cai, and V. Battaglia, 'The Limited Effect of VC in Graphite/NMC Cells', *Journal of The Electrochemical Society*, vol. 162, no. 3, pp. A330–A338, 2015, doi: 10.1149/2.0221503jes.
- [191] J. Xu, R. D. Deshpande, J. Pan, Y.-T. Cheng, and V. S. Battaglia, 'Electrode Side Reactions, Capacity Loss and Mechanical Degradation in Lithium-Ion Batteries', *Journal of The Electrochemical Society*, vol. 162, no. 10, pp. A2026–A2035, 2015, doi: 10.1149/2.0291510jes.
- [192] D. Atkins *et al.*, 'Understanding Battery Interfaces by Combined Characterization and Simulation Approaches: Challenges and Perspectives', *Advanced Energy Materials*, vol. 12, no. 17, 2022, doi: 10.1002/aenm.202102687.
- [193] J. P. Christophersen, J. E. Soc, J. P. Christophersen, C. D. Ho, C. G. Motloch, and D. Howell, 'Effects of Reference Performance Testing during Aging Using Commercial Lithium-Ion Cells Effects of Reference Performance Testing during Aging Using Commercial Lithium-Ion Cells', 2006, doi: 10.1149/1.2201473.
- [194] H. M. Dahn, A. J. Smith, J. C. Burns, D. A. Stevens, and J. R. Dahn, 'User-Friendly Differential Voltage Analysis Firmware for the Analysis of Degradation Mechanisms in Li-Ion Batteries', *Journal of The Electrochemical Society*, vol. 159, no. 9, pp. A1405–A1409, 2012, doi: 10.1149/2.013209jes.
- [195] M. L. de Souza, M. Duquesnoy, M. Morcrette, and A. A. Franco, 'Electrochemistry Visualization Tool to Support the Electrochemical Analysis of Batteries', *Batteries and Supercaps*, 2022, doi: 10.1002/batt.202200378.
- [196] D. Ansean *et al.*, 'Lithium-Ion Battery Degradation Indicators Via Incremental Capacity Analysis', *IEEE Transactions on Industry Applications*, vol. 55, no. 3, pp. 2992–3002, 2019, doi: 10.1109/TIA.2019.2891213.
- [197] M. Dubarry, C. Truchot, and B. Y. Liaw, 'Cell degradation in commercial LiFePO<sub>4</sub> cells with high-power and high-energy designs', *Journal of Power Sources*, vol. 258, pp. 408–419, 2014, doi: 10.1016/j.jpowsour.2014.02.052.
- [198] P. M. Attia *et al.*, 'Review—"Knees" in Lithium-Ion Battery Aging Trajectories', *Journal of The Electrochemical Society*, pp. 1–93, 2022, doi: 10.1149/1945-7111/ac6d13.
- [199] X. Ma *et al.*, 'Editors' Choice—Hindering Rollover Failure of Li[Ni 0.5 Mn 0.3 Co 0.2 ]O<sub>2</sub>/Graphite Pouch Cells during Long-Term Cycling ', *Journal of The Electrochemical Society*, vol. 166, no. 4, pp. A711–A724, 2019, doi: 10.1149/2.0801904jes.
- [200] T. Boulanger *et al.*, 'Investigation of Redox Shuttle Generation in LFP/Graphite and NMC811/Graphite Cells', *Journal of The Electrochemical Society*, vol. 169, no. 4, p. 040518, 2022, doi: 10.1149/1945-7111/ac62c6.
- [201] S. Buechele *et al.*, 'Identification of Redox Shuttle Generated in LFP/Graphite and NMC811/Graphite Cells', *Journal of The Electrochemical Society*, vol. 170, no. 1, p. 010511, 2023, doi: 10.1149/1945-7111/acaf44.
- [202] G. Yan, D. Alves-Dalla-Corte, W. Yin, N. Madern, G. Gachot, and J.-M. Tarascon, 'Assessment of the Electrochemical Stability of Carbonate-Based Electrolytes in Na-Ion Batteries', *Journal of The Electrochemical Society*, vol. 165, no. 7, pp. A1222–A1230, 2018, doi: 10.1149/2.0311807jes.
- [203] R. Sahore, F. Dogan, and I. D. Bloom, 'Identification of Electrolyte-Soluble Organic Cross-Talk Species in a Lithium-Ion Battery via a Two-Compartment Cell', *Chemistry of Materials*, vol. 31, no. 8, pp. 2884–2891, 2019, doi: 10.1021/acs.chemmater.9b00063.
- [204] F. Omenya, M. Paiss, X. Li, and D. Reed, 'Energy and Power Evolution Over the Lifetime of a Battery', *ACS Energy Letters*, no. 2707–2710, pp. 8–11, 2023, doi: 10.1021/acsenerylett.3c00660.

- [205] L. D. Ellis *et al.*, 'Quantifying, Understanding and Evaluating the Effects of Gas Consumption in Lithium-Ion Cells', *Journal of The Electrochemical Society*, vol. 164, no. 14, pp. A3518–A3528, 2017, doi: 10.1149/2.0191714jes.
- [206] J. Chen, C. Buhmester, and J. R. Dahn, 'Chemical overcharge and overdischarge protection for lithium-ion batteries', *Electrochemical and Solid-State Letters*, vol. 8, no. 1, pp. 1–5, 2005, doi: 10.1149/1.1836119.
- [207] E. Björklund *et al.*, 'Cycle-Induced Interfacial Degradation and Transition-Metal Cross-Over in LiNi<sub>0.8</sub>Mn<sub>0.1</sub>Co<sub>0.1</sub>O<sub>2</sub>-Graphite Cells', *Chemistry of Materials*, vol. 34, no. 5, pp. 2034–2048, 2022, doi: 10.1021/acs.chemmater.1c02722.
- [208] F. Lin *et al.*, 'Surface reconstruction and chemical evolution of stoichiometric layered cathode materials for lithium-ion batteries', *Nature communications*, vol. 5, no. April, p. 3529, 2014, doi: 10.1038/ncomms4529.
- [209] H. H. Ryu, G. T. Park, C. S. Yoon, and Y. K. Sun, 'Microstructural Degradation of Ni-Rich Li[Ni<sub>x</sub>Co<sub>y</sub>Mn<sub>1-x-y</sub>]O<sub>2</sub> Cathodes During Accelerated Calendar Aging', *Small*, vol. 14, no. 45, pp. 1–8, 2018, doi: 10.1002/smll.201803179.
- [210] K. J. Park *et al.*, 'Degradation Mechanism of Ni-Enriched NCA Cathode for Lithium Batteries: Are Microcracks Really Critical?', *ACS Energy Letters*, vol. 4, no. 6, pp. 1394–1400, 2019, doi: 10.1021/acsenergylett.9b00733.
- [211] M. Ebner, F. Geldmacher, F. Marone, M. Stampanoni, and V. Wood, 'X-Ray Tomography of Porous, Transition Metal Oxide Based Lithium Ion Battery Electrodes', *Advanced Energy Materials*, vol. 3, no. 7, pp. 845–850, 2013, doi: 10.1002/aenm.201200932.
- [212] Y. C. K. Chen-Wiegart, Z. Liu, K. T. Faber, S. A. Barnett, and J. Wang, '3D analysis of a LiCoO<sub>2</sub>-Li(Ni<sub>1/3</sub>Mn<sub>1/3</sub>Co<sub>1/3</sub>)O<sub>2</sub> Li-ion battery positive electrode using x-ray nano-tomography', *Electrochemistry Communications*, vol. 28, pp. 127–130, 2013, doi: 10.1016/j.elecom.2012.12.021.
- [213] S. Klein *et al.*, 'Demonstrating Apparently Inconspicuous but Sensitive Impacts on the Rollover Failure of Lithium-Ion Batteries at a High Voltage', *ACS Applied Materials and Interfaces*, vol. 13, no. 48, pp. 57241–57251, 2021, doi: 10.1021/acsaami.1c17408.
- [214] W. M. Dose, C. Xu, C. P. Grey, and M. F. L. De Volder, 'Effect of Anode Slippage on Cathode Cutoff Potential and Degradation Mechanisms in Ni-Rich Li-Ion Batteries', *Cell Reports Physical Science*, vol. 1, no. 11, p. 100253, 2020, doi: 10.1016/j.xcrp.2020.100253.
- [215] M. Petzl, M. Kasper, and M. A. Danzer, 'Lithium plating in a commercial lithium-ion battery - A low-temperature aging study', *Journal of Power Sources*, vol. 275, pp. 799–807, 2015, doi: 10.1016/j.jpowsour.2014.11.065.
- [216] P. Rozier and J. M. Tarascon, 'Review—Li-Rich Layered Oxide Cathodes for Next-Generation Li-Ion Batteries: Chances and Challenges', *Journal of The Electrochemical Society*, vol. 162, no. 14, pp. A2490–A2499, 2015, doi: 10.1149/2.0111514jes.
- [217] L. M. Thompson *et al.*, 'Quantifying Changes to the Electrolyte and Negative Electrode in Aged NMC532/Graphite Lithium-Ion Cells', *Journal of The Electrochemical Society*, vol. 165, no. 11, pp. A2732–A2740, 2018, doi: 10.1149/2.0721811jes.
- [218] S. Klein *et al.*, 'Re-evaluating common electrolyte additives for high-voltage lithium ion batteries', *Cell Reports Physical Science*, vol. 2, no. 8, 2021, doi: 10.1016/j.xcrp.2021.100521.
- [219] C. Zhan *et al.*, 'Mn(II) deposition on anodes and its effects on capacity fade in spinel lithium manganese-carbon systems', *Nature Communications*, vol. 4, no. li, pp. 1–8, 2013, doi: 10.1038/ncomms3437.
- [220] D. R. Vissers *et al.*, 'Role of Manganese Deposition on Graphite in the Capacity Fading of Lithium Ion Batteries', *ACS Applied Materials and Interfaces*, vol. 8, no. 22, pp. 14244–14251, 2016, doi: 10.1021/acsaami.6b02061.
- [221] X. G. Yang and C. Y. Wang, 'Understanding the trilemma of fast charging, energy density and cycle life of lithium-ion batteries', *Journal of Power Sources*, vol. 402, no. September, pp. 489–498, 2018, doi: 10.1016/j.jpowsour.2018.09.069.
- [222] K. Kim, H. Ma, S. Park, and N. S. Choi, 'Electrolyte-Additive-Driven Interfacial Engineering for High-Capacity Electrodes in Lithium-Ion Batteries: Promise and Challenges', *ACS Energy Letters*, vol. 5, no. 5, pp. 1537–1553, 2020, doi: 10.1021/acsenergylett.0c00468.
- [223] D. Zhang *et al.*, 'Lithium hexamethyldisilazide as electrolyte additive for efficient cycling of high-voltage non-aqueous lithium metal batteries', *Nature Communications*, vol. 13, no. 1, 2022, doi: 10.1038/s41467-022-34717-4.
- [224] S. H. Jang, K. J. Lee, J. Mun, Y. K. Han, and T. Yim, 'Chemically-induced cathode–electrolyte interphase created by lithium salt coating on Nickel-rich layered oxides cathode', *Journal of Power Sources*, vol. 410–411, no. November 2018, pp. 15–24, 2019, doi: 10.1016/j.jpowsour.2018.11.008.
- [225] L. Qiao *et al.*, 'Stable non-corrosive sulfonimide salt for 4-V-class lithium metal batteries', *Nature Materials*, vol. 21, no. 4, pp. 455–462, 2022, doi: 10.1038/s41563-021-01190-1.
- [226] D. Degoulange, N. Dubouis, and A. Grimaud, 'Toward the understanding of water-in-salt electrolytes: Individual ion activities and liquid junction potentials in highly concentrated aqueous solutions', *Journal of Chemical Physics*, vol. 155, no. 6, pp. 1–10, 2021, doi: 10.1063/5.0058506.
- [227] A. J. Smith, J. C. Burns, and J. R. Dahn, 'High-precision differential capacity analysis of LiMn<sub>2</sub>O<sub>4</sub>/graphite cells', *Electrochemical and Solid-State Letters*, vol. 14, no. 4, pp. 39–41, 2011, doi: 10.1149/1.3543569.
- [228] Y. Yamada and A. Yamada, 'Superconcentrated electrolytes to create new interfacial chemistry in non-aqueous and aqueous rechargeable batteries', *Chemistry Letters*, vol. 46, no. 8, pp. 1056–1064, 2017, doi: 10.1246/cl.170284.
- [229] L. El Ouatani *et al.*, 'The Effect of Vinylene Carbonate Additive on Surface Film Formation on Both Electrodes in Li-Ion Batteries', *Journal of The Electrochemical Society*, vol. 156, no. 2, p. A103, 2009, doi: 10.1149/1.3029674.
- [230] B. Philippe, R. Dedryveire, M. Gorgoi, H. Rensmo, D. Gonbeau, and K. Edström, 'Improved performances of nanosilicon electrodes using the salt LiFSI: A photoelectron spectroscopy study', *Journal of the American Chemical Society*, vol. 135, no. 26, pp. 9829–9842, 2013, doi: 10.1021/ja403082s.

- [231] R. Dedryvère, L. Gireaud, S. Grugeon, S. Laruelle, J. M. Tarascon, and D. Gonbeau, 'Characterization of lithium alkyl carbonates by X-ray photoelectron spectroscopy: Experimental and theoretical study', *Journal of Physical Chemistry B*, vol. 109, no. 33, pp. 15868–15875, 2005, doi: 10.1021/jp051626k.
- [232] Z. D. Li *et al.*, 'Trimethyl phosphite as an electrolyte additive for high-voltage lithium-ion batteries using lithium-rich layered oxide cathode', *Journal of Power Sources*, vol. 240, pp. 471–475, 2013, doi: 10.1016/j.jpowsour.2013.04.038.
- [233] H. Y. Xu, S. Xie, Q. Y. Wang, X. L. Yao, Q. S. Wang, and C. H. Chen, 'Electrolyte additive trimethyl phosphite for improving electrochemical performance and thermal stability of LiCoO<sub>2</sub> cathode', *Electrochimica Acta*, vol. 52, no. 2, pp. 636–642, 2006, doi: 10.1016/j.electacta.2006.05.043.
- [234] H. Zhang *et al.*, '1,3,5-Trifluorobenzene and fluorobenzene co-assisted electrolyte with thermodynamic and interfacial stabilities for high-voltage lithium metal battery', *Energy Storage Materials*, vol. 48, no. February, pp. 393–402, 2022, doi: 10.1016/j.ensm.2022.03.034.

# **RESUME DE THESE EN FRANCAIS**



Atteindre la neutralité carbone d'ici 2050 représente un défi ambitieux, et les batteries Li-ion jouent un rôle clé. Au cours des trois dernières décennies, d'importants progrès ont été réalisés dans la chimie et la conception des cellules, faisant des batteries Li-ion une solution pertinente, en particulier dans le domaine de la mobilité. La tendance actuelle vise à produire des batteries à haute densité d'énergie en utilisant des matériaux riches en nickel. Cependant, ces matériaux sont très réactifs, surtout à des tensions de fonctionnement élevées, et il est donc essentiel de les stabiliser efficacement pour tirer parti de leur haute énergie. Bien que des avancées telles que le dopage chimique, l'optimisation des électrolytes ou le revêtement des particules aient considérablement amélioré les performances de ces matériaux, ce travail reste fastidieux, car les outils d'analyse des dégradations ne sont pas encore totalement optimisés. En effet, les critères d'évaluation les plus couramment utilisés, tels que la capacité de décharge ( $Q_D$ ) et l'efficacité coulombique (EC), ne suffisent pas à comprendre les mécanismes de vieillissement des batteries. Même si les valeurs de  $Q_D$  et EC sont bonnes, des dégradations complexes peuvent avoir lieu et provoquer une défaillance soudaine de la batterie. Néanmoins, en examinant les courbes de cyclage, de nouvelles informations deviennent accessibles, ce qui légitime la nécessité de moderniser les méthodes conventionnelles d'analyse des performances des batteries.

L'objectif de cette thèse de doctorat est de développer des protocoles visant à comprendre les dégradations au sein des batteries Li-ion. Ces protocoles ne se limitent pas seulement à l'analyse, mais englobent l'intégralité du processus de test, incluant la standardisation de l'assemblage des cellules et la mise en place de protocoles de cyclage adaptés.

Avant d'entamer l'analyse des performances des batteries, la première étape consiste à assurer de la pertinence et de la reproductibilité des données mesurées. Ainsi, nous avons entrepris de standardiser et d'optimiser l'assemblage des piles bouton, un format de batterie convenant à des tests en recherche académique, afin d'obtenir une base de données fiable pour nos analyses. Cette démarche a nécessité une réflexion approfondie sur des aspects tels que le volume d'électrolyte et la pression interne des cellules. Nous avons notamment démontré que le volume idéal d'électrolyte est atteint lorsqu'il remplit quatre fois la porosité du séparateur et des

électrodes, garantissant ainsi un équilibre entre la conductivité ionique et la durabilité des performances. De plus, la pression interne optimale est obtenue en utilisant une hauteur totale adaptée des composants avant le sertissage de la cellule. Au final, tous ces ajustements ont grandement amélioré la reproductibilité des résultats. Une fois la reproductibilité assurée, nous avons étudié l'influence des conditions de cyclage sur les performances des batteries. Cela a inclus l'examen de l'impact des premiers cycles de formation et des effets des différentes conditions de cyclage : limite en voltage, courant, maintien du voltage etc. Il est important de noter que le processus d'optimisation a été spécifiquement conçu pour le format de cellule bouton, et une adaptation serait nécessaire pour le mettre en œuvre dans des environnements industriels utilisant des cellules de type 18650 ou « pouch ».

Le deuxième objectif est de mettre en place les protocoles d'analyse afin d'assurer une compréhension approfondie des processus de dégradation. Ces protocoles reposent principalement sur l'analyse des capacités absolues des cellules ainsi que sur l'exploitation des courbes dérivées  $dV/dQ$  et  $dQ/dV$ . En combinant ces analyses, il est possible de déterminer où se produisent les dégradations, quels mécanismes sont impliqués et d'en quantifier leurs effets. Les analyses sont si précises qu'elles permettent d'expliquer des phénomènes complexes tels que les accélérations ou les ralentissements des vitesses de dégradation, en particulier le phénomène de mort subite, souvent causé par des dégradations croisées appelées "crosstalk". Grâce à ces workflows, nous avons pu identifier avec succès certains type de crosstalks.

Le cas de crosstalk le plus répandu est la dissolution des métaux de transition depuis l'électrode positive jusqu'à l'électrode négative. Grâce aux protocoles d'analyse, nous avons pu différencier les effets de ces métaux sur l'électrode négative entre un dépôt de lithium métallique ou la dégradation de l'électrolyte. Un autre type de crosstalk est le décalage progressif de la fenêtre des tensions de cyclage, pouvant atteindre plusieurs millivolts. Ce décalage amène l'électrode positive à fonctionner à un potentiel plus élevé, ce qui peut déclencher de nouvelles dégradations.

Il est important de noter que toutes ces procédures d'analyse sont transposables à tous types de batteries, y compris les batteries à ions sodium ou les batteries tout solide sans anode. Cependant, le concept d'inventaire de lithium ne sera

pas applicable aux batteries utilisant des anodes métalliques, car elles bénéficient d'un réservoir d'ions lithium semi-infini.

Les deux premiers chapitres objectifs de thèses sont volontairement très orientés pour des applications industrielles. En effet, obtenir des performances répétables et analyser de façon fiable les dégradations sont un enjeu majeur pour les industries. C'est un gain de temps non négligeable pour le département R&D visant à optimiser les compositions d'électrolyte et fonctionnement des matériaux à haut voltage par exemple.

Les études suivantes visent à tester ces protocoles dans des cas concrets. La première étude s'est concentrée sur l'effet des hautes tensions de cyclage sur les cellules graphite/LiNiO<sub>2</sub>. Comme attendu, à mesure que la tension augmente, les dégradations et la perte de capacité deviennent plus prononcées et l'analyse des courbes dV/dQ permet de mettre en évidence que la principale cause de dégradation provient de la dégradation de l'électrolyte à l'interface du graphite, formant la "Solide Electrolyte Interphase" ou SEI. Cette croissance du SEI entraîne une perte de lithium et, par conséquent, une diminution des performances.

Nous avons également démontré que la croissance de la SEI se stabilise à des tensions faibles et modérées, soit à 4,2 V et 4,5 V respectivement, mais devient incontrôlable à des tensions élevées, à 4,8 V. De plus, notre étude a révélé que la teneur en nickel dans la SEI augmente avec la tension ce qui déstabilise cette dernière. En effet, le nickel agit comme un catalyseur, entraînant une décomposition supplémentaire de l'électrolyte et une augmentation de la perte de lithium. Une analyse complémentaire a révélé que le dépôt de nickel sur le graphite favorise les mécanismes de dégradation associés à la croissance de la SEI, plutôt que le dépôt de lithium, ce qui diffère des observations précédentes dans la littérature. De plus, nos conclusions s'appliquent également au cobalt et au manganèse.

Dans une phase ultérieure, nous prévoyons de tester l'effet d'une membrane chélatante pour capturer les métaux libérés par l'électrode positive dans l'électrolyte, ou d'explorer l'utilisation d'additifs afin de limiter la dissolution des métaux.

En conclusion, cette étude fournit un modèle permettant de comprendre les effets de la dissolution des métaux de transition et d'en évaluer les impacts sur la SEI.

Afin de stabiliser les cellules à haut voltage, nous avons ensuite étudié les électrolytes hautement concentrés (HCE) dans les cellules graphite/NMC811. Les HCE sont réputés pour améliorer les performances en favorisant la formation de SEI robustes et minces. Ayant testé les HCE, il a été montré que les cellules avaient une meilleure rétention de capacité au cours des 250 premiers cycles comparés à un électrolyte conventionnel. Cependant les cellules subissaient des dégradations significatives par la suite.

Grâce aux protocoles d'analyse utilisés, nous avons identifié une réaction d'oxydation parasite à l'électrode positive, liée à l'oxydation du solvant, le diméthyl carbonate (DMC). Cette oxydation a ensuite été confirmée par des mesures UV-visible. La capacité supplémentaire résultant de cette oxydation est compensée au niveau de l'électrode négative par une lithiation plus importante du graphite, jusqu'à ce qu'elle soit totalement remplie de lithium. À ce stade, le dépôt de lithium métallique se produit, comme révélé par l'apparition de pics caractéristiques sur les courbes  $dQ/dV$ . Ce dépôt de lithium métallique est à l'origine du phénomène de mort subite de la cellule à partir du 250<sup>e</sup> cycle. En effet, le lithium métallique commence à réagir de manière excessive avec l'électrolyte, ce qui a été confirmé par XPS, entraînant des pertes importantes de lithium. Afin de réduire les effets néfastes du lithium métallique, un additif appelé "vinylene carbonate" (VC) a été introduit dans le HCE. Celui-ci se décompose à l'interface négative, stabilisant ainsi l'électrode en graphite et limitant les conséquences néfastes du lithium métallique. Cependant, cet additif n'a pas pu arrêter l'oxydation parasite du DMC.

Une autre approche pour limiter l'oxydation parasite consiste à diluer le HCE en utilisant un éther fluoré, créant ainsi un troisième type d'électrolyte appelé LHCE (HCE Localement Dilué). Ce type d'électrolyte présente des performances plus élevées avec des réactions parasites moins prononcées, et plus de 82% de la capacité initiale est conservée à 4,4 V après 500 cycles. Dans notre quête d'optimisation, nous avons testé différents additifs, mais ils n'ont pas donné de résultats concluants. Seul le VC a montré une stabilisation prometteuse de l'interface négative, mais seulement après un cyclage prolongé, suggérant que cet additif pourrait être pertinent pour les cycles à long terme, notamment après 500 cycles. Cependant, nos résultats suggèrent qu'une

concentration en masse de 2% d'additif pourrait être excessive pour cette application, et une optimisation supplémentaire dans ce domaine est nécessaire.

De plus, les additifs testés pour améliorer la SEI sont similaires à ceux couramment utilisés dans les électrolytes commerciaux et pourraient ne pas être adaptés au HCE ou au LHCE qui présentent des propriétés spécifiques de solvatation. Il est donc nécessaire d'explorer des additifs spécifiquement conçus pour le HCE ou le LHCE afin d'optimiser leur performance.

En conclusion, ces travaux de thèse apportent des outils pour améliorer la compréhension des dégradations dans les batteries. Ces protocoles d'analyse ont notamment permis de mettre en évidence des dégradations subtiles, telles qu'une oxydation parasite entraînant un dépôt de lithium sur l'autre électrode. Ces méthodes ouvrent la voie vers une détection améliorée des phénomènes de dégradation, ce qui permettra d'optimiser de manière efficace les futures générations de batteries.



## Mise en Evidence des Schémas de Dégradation des Batteries Li-ion grâce à des Procédures d'Analyse Electrochimique.

Abstract :

La chimie des électrodes positives dans les batteries Li-ion a évolué, au cours des vingt dernières années, autour d'une famille d'oxydes lamellaires à base de nickel, manganèse et cobalt, connus sous le nom de phases NMC. En mettant l'accent sur l'autonomie des batteries, les recherches visent à accroître la densité énergétique de ces matériaux en augmentant leur fraction de nickel et leur tension de fonctionnement. Cependant, à des teneurs en nickel supérieures à 80% et une tension de 4.2 V, les phases NMC sont sujettes à une série de dégradations physico-chimiques impliquant le matériau ainsi que son interface avec l'électrolyte. Des dégradations structurales, l'oxydation de l'électrolyte ou la dissolution des métaux de transition sont autant d'exemples illustrant la variété des dégradations en jeu. Pire encore, ces dégradations peuvent en déclencher d'autres, et au final, c'est toute la cellule qui se retrouve impactée, pouvant conduire à une chute brutale de la capacité de la batterie, phénomène appelé « emballement ». Imprévisible et soudain, les emballlements sont difficiles à expliquer avec les descripteurs classiques de performance tels que la capacité en décharge ou l'efficacité coulombique. L'objectif de cette thèse est de développer des protocoles d'analyse combinant des techniques électrochimiques afin d'expliquer la nature des dégradations en jeu, c'est-à-dire leurs mécanismes, leurs localisations, et le tout de manière quantitative. Ces techniques se basent principalement sur l'analyse du glissement des capacités en fin de charge et décharge, ainsi que les dérivées  $dV/dQ$  et  $dQ/dV$ . Avant la mise en place de ces techniques, le travail préliminaire consistait à assurer la qualité des mesures électrochimiques grâce à la standardisation des méthodes d'assemblage des cellules et des méthodes de test. Une fois les données générées répétables, les protocoles d'analyse mis en place ont permis, entre autres, d'étudier les effets de la dissolution du nickel sur l'électrode de graphite ou de mettre en évidence des dégradations inattendues lors de l'utilisation d'un électrolyte super concentré en sel de lithium, bien que reconnu pour sa haute stabilité. Les compositions d'électrolytes ont donc pu être ajustées, ce qui a augmenté la durée de vie des batteries. En résumé, ces protocoles améliorent la compréhension des dégradations et permettent d'optimiser au mieux les conditions de fonctionnement des batteries Li-ion. Cela ouvre la voie vers la stabilisation des interfaces et le développement de nouvelles chimies.

Mots clés : Electrochimie, Batterie Li-ion, Standardisation, Protocole d'analyse, Interfaces liquide/solide, Dégradation

# Unraveling Degradation Patterns in Li-ion Batteries through Electrochemical Analysis Procedures

## Abstract:

For the past twenty years, the chemistry of positive electrodes in Li-ion batteries has predominantly focused on a group of layered oxides composed of nickel, manganese, and cobalt, commonly referred to as NMC phases. The primary goal of research has been to enhance the energy density of these materials by increasing their nickel content and operating voltage. However, once the nickel content surpasses 80% and the voltage reaches 4.2 V, the NMC phases become susceptible to a range of physicochemical degradations involving both the material itself and its interaction with the electrolyte. Structural degradation, electrolyte oxidation, and the dissolution of transition metals exemplify the various mechanisms at play. Furthermore, these deteriorations can trigger additional ones, ultimately affecting the entire battery cell and causing a sudden decline in battery capacity referred to as “rollover”. The unpredictable and abrupt nature of rollover poses challenges for conventional performance indicators like discharge capacity ( $Q_D$ ) or coulombic efficiency in explaining them. The objective of this thesis is to develop analysis protocols that combine electrochemical techniques to comprehensively elucidate the chemistry underlying these deteriorations. This includes understanding the nature of the deterioration, its localization within the battery, and most importantly, quantifying its impact. These techniques primarily rely on observing the capacity slippages, as well as analyzing the derivatives  $dV/dQ$  and  $dQ/dV$ . To implement these techniques, the initial step involved ensuring the accuracy of the electrochemical measurements by standardizing the assembly and testing methods. Once reliable and high-quality data were obtained, the protocols facilitated the examination of the effects of nickel dissolution on the graphite electrode, revealing unforeseen deteriorations that occurred when using a highly concentrated electrolyte, despite its recognized high stability. Consequently, adjustments to the electrolyte compositions could be made to mitigate deteriorations and extend the battery's lifespan. In summary, these protocols significantly contribute to our understanding of deteriorations and enable the optimization of operating conditions for Li-ion batteries. This advancement allows for stabilizing interfaces and materials, as well as fostering the development of novel chemical approaches in battery technology.

Keywords: Electrochemistry, Li-ion battery, Standardization, Analysis protocol, Liquid/solid interfaces, Degradation